KAIST Research Series

Chun T. Rim

Phasor Power Electronics

KAIST

Springer

KAIST Research Series

Series editors

More information about this series at http://www.springer.com/series/11753

Chun T. Rim

Phasor Power Electronics

Springer

Chun T. Rim
Department of Nuclear and Quantum
Engineering
KAIST
Daejeon
Korea, Republic of (South Korea)

ISSN 2214-2541 ISSN 2214-255X (electronic)
KAIST Research Series
ISBN 978-981-10-0535-0 ISBN 978-981-10-0536-7 (eBook)
DOI 10.1007/978-981-10-0536-7

Library of Congress Control Number: 2016935210

Printed on acid-free paper

This Springer imprint is published by Springer Nature
The registered company is Springer Science+Business Media Singapore Pte Ltd.

Preface

Since the start of the twentieth century, modern society has been utilizing electric power for maintaining civil systems such as transportation, communications, factories, houses, and commercial buildings. Power electronics has recently been an active area because of electric vehicles, renewable energies, smart grids, mobile devices, light emitting diodes (LEDs), and wireless power transfer (WPT) technology. Power supplies and switching converters are a requisite for modern devices and most electric systems. More efficient, lower weight, compact, and cheaper power solutions are highly sought by consumers, and power electronics deals with these challenging issues.

It is well known that all switching converters are time varying and equivalent to switched transformers, which I first proved in general about 30 years ago. Although there were the well-known R.D. Middlebrook's state-space averaging techniques and Peter Wood's existence function techniques, they are valid only for DC-DC converter analyses and static analyses of converters, respectively. I wondered at that time why we still did not have a general technique valid for the static and dynamic analyses of any converters.

After studying this problem for several years during my Ph.D. candidate period, I found that power electronics is a unique field among electronic engineering areas in that it always involves time-varying characteristics of converters without any exception. A linear power electronic circuit containing power switches even becomes nonlinear when a power switch operates in the discontinuously conduction mode, which means that the inductor current or capacitor voltage spontaneously becomes zero during a switching period. Therefore, nonlinear time-varying systems are abundant in switching converters, which require a special modeling technique to make the complex nature of the switching converter simple and easy to handle.

There are many books on power electronics that explain how the switching converters operate, and they provide some analytical results and design guidelines. Except for the state averaging and existence function techniques, most books deal with piecewise linear circuit models; hence, mathematical results derived from the models become too complicated to be used in practice. Until now, there is no such

book that generally and systematically deals with the time-varying switching system, transforming it into an equivalent time-invariant circuit. Neither cumbersome equations nor matrix manipulations are needed by the techniques introduced in this book, which are collectively referred to as 'phasor transformation'.

This book starts with the introduction of the philosophy of power electronics and fundamental knowledge and background of modern power electronics. The switched transformer concept, which is applicable to any switching converter, is introduced and it is shown that DC-DC converter analyses are so straightforward that little equational manipulations are needed. Then the phasor transformation techniques are comprehensively explained in three parts. Single phase and multi-phase AC systems are dealt with through the single phase phasor transformation and circuit DQ transformation, respectively. A general unified phasor transformation is then introduced for the static and dynamic cases. Each part provides readers with corresponding application examples.

As an inventor of the switched transformer model and phasor transformation models in power electronics, I feel that these models are the most fundamental and powerful theories to deal with power electronics with great ease. Throughout my research and developments on practical applications of power electronics during the past three decades, I have also become familiar with the most advanced LED drivers and WPT technologies. I have led a team to develop the WPT systems of the On-Line Electric Vehicles (OLEVs), which were the first of their kind to be commercialized in the world. My students and I have researched the longest distance WPT of 10 W at 10 m and developed several innovative WPT products including the world's first free space charging mobile device that is plate type with six degrees of freedom. I have included some of these research issues in this book, which vividly shows the practical application of the proposed theories to industries. In this way, this book covers from the ultimately basic concepts to the most advanced state-of-the-art technologies. The usefulness of this book, however, depends on how frequently readers apply it in their engineering problem solving. The intention of writing this book is to provide know-how to beginners, newcomers, and experienced power electronics engineers who want to find an appropriate model and to analyze the switching converter systematically. This book can be used as a textbook for graduate students who major in power electronics or as a reference book of higher level undergraduate students.

I would like to thank Prof. Gyu H. Cho at KAIST for his outstanding leadership in developing a circuit-based unified general method to analyze and design complicated electronic circuits very easily without any equations. My work on modeling power electronics was significantly motivated by Prof. Cho's ideas on electronic circuits. Furthermore, he persistently encouraged research on this unified general modeling of power electronics, which is a sort of high-risk-high-return research. It is always challenging to study unknown areas, especially the development of a theory in an engineering field. Now I can say the following words:

A circuit is more powerful than equations.

I would also like to thank Mr. Seog Y. Jeong, Ji H. Kim, and Gi C. Jang for their great help in preparing the manuscript of this book. I appreciate very much Springer for its decision to publish this book. Without this help, this book would not have appeared.

As a teacher at a university now, I am very happy to share my experience of struggling throughout my life with worldwide friends to find appropriate switching converter models.

January 2016 Chun T. Rim

Contents

Part I
Introduction to Power Electronics

This part introduces the very basic knowledge of power electronics. The most fundamental principles of power electronics are explained first: the philosophy of power electronics. A few important principles of power electronics, which are the 'key principles' of power electronics, follow.

Chapter 1
The Philosophy of Power Electronics

This chapter explains why power electronics is so special and difficult to understand. A state equation is obtained for a switching converter example and generally compared with conventional systems. However, general unified approaches for understanding and analysis of power circuits are deliberately sought in this book as an extension of similar works done in electronic circuits, which were believed to be very complicated and formidable to handle.

Since electronics switches such as transistors and diodes are used to control power, power electronics has become an important area of electronics. As electronic switches started being used in power circuits, engineers realized that the switching power circuits are quite different from conventional electric circuits. The characteristics of switching power circuits that confound engineers are time-varying nature and AC (alternating current) circuit dynamics, as shown in Fig. 1.1. In this chapter, these unique features of power electronics are explained as an introduction to power electronics.

I like power electronics because it is a kind of 3D work, i.e., diversified, dangerous, and difficult. To be a power electronics expert, one should know not only electronics such as electric circuit theory, micro-electronics, control, signal processing, semi-conductor, and electricity but also mechanics and materials. There are unique characteristics in electrical engineering because the control, communications, image processing, and software engineering may not be so diversified compared with power electronics. Moreover, power electronics deals with high voltage and large current as the conventional electrical engineering is doing; as such, it is dangerous when performing experiments and development. Power electronics may be one of the most difficult engineering fields, on par with radio frequency engineering and fluid mechanics, from my experience. However, a power electronic circuit looks simple compared to a conventional analog filter or an electronic circuit. Actually, this apparently simple power electronic circuit makes it more difficult to analyze and design of it, which is the reason why many electric engineers who are now familiar with power electronics have trouble handling power electronic circuits.

C.T. Rim, *Phasor Power Electronics*, KAIST Research Series,
DOI 10.1007/978-981-10-0536-7_1

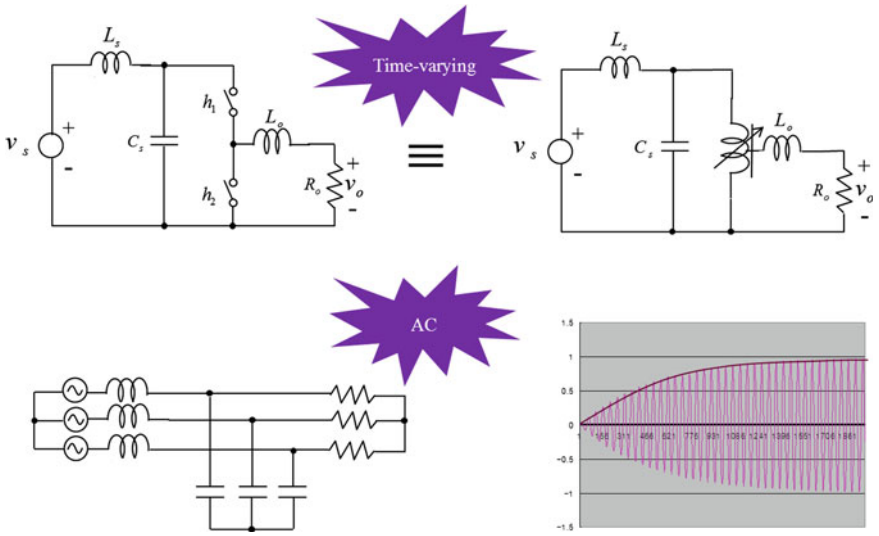

Fig. 1.1 Time-varying and AC characteristics of power electronics that give engineers a headache

1.1 All Switching Converter Is Time-Varying, Which Makes Power Electronics so Unique and Difficult to Learn

Let me give you an example of analyzing a boost converter, as shown in Fig. 1.2, which is one of the most basic switching converters in power electronics. (The name, 'boost' stems from the fact that the output voltage of the boost converter is always higher than the input voltage.) What is the output voltage of the converter when the switch Q_c is ideally turned on and off periodically with a turn-on duty ratio of $d = 0.7$ assuming all other circuit parameters are given?

If you are familiar with electronic circuit analysis, you may find the answer by setting up piecewise state equations for each switching state, as shown in Fig. 1.3.

$$L\frac{di_s}{dt} = v_S \quad C\frac{dv_0}{dt} - \frac{v_0}{R_L} \quad \text{for} \quad kT < t < kT + d \cdot T, \quad k = 0, 1, 2, \ldots \quad \text{(S1)} \quad \text{(1.1a)}$$

$$L\frac{di_s}{dt} = v_S - v_0 \quad C\frac{dv_0}{dt} = i_S - \frac{v_0}{R_L} \quad \text{for} \quad kT < d \cdot T < t < (k+1)T, \quad k = 0, 1, 2, \ldots \quad \text{(S2)} \quad \text{(1.1b)}$$

As you solve the state equations of S1 circuit and apply the final values of the circuit to the initial conditions of S2 circuit, you can determine the whole voltages and currents of the circuit for a period. As you repeat this process for the

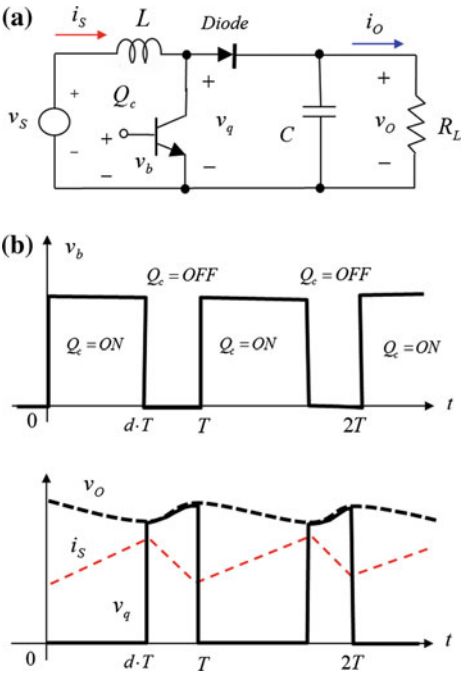

Fig. 1.2 The behavior of a boost converter in continuous conduction mode (CCM). **a** A simplified circuit diagram. **b** Its switching waveforms in the steady state

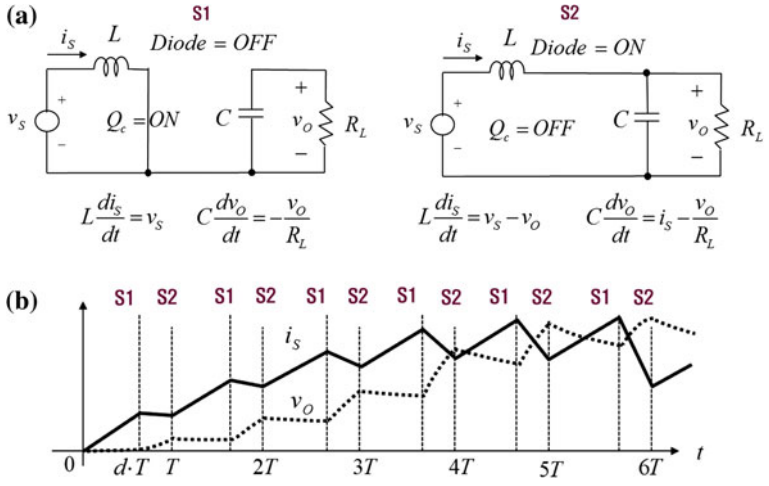

Fig. 1.3 Piecewise analysis of a boost converter in the CCM. **a** Two piecewise circuits S1 and S2 of Fig. 1.2. **b** The dynamic state variables for the first six periods when the initial conditions are zeroes

consecutive periods, you can determine the values of any states, as shown in the bottom diagram of Fig. 1.3. For simplicity of discussion, it is assumed that all the switch currents are continuously conducting throughout the operation, which is called continuous conduction mode (CCM) in power electronics.

Question 1

1. Can you solve (1.1) for a period, assuming zero initial conditions?
2. Apply the solution of (1.1) to the next period.
3. Think about how to obtain the steady state solution.

It looks like we now have a complete solution for the boost converter because we know all the circuit information for given circuit parameters. However, you will readily recognize that there are quite a few cases where you can make designs based on the state equations and the solutions. If you try to repeat the process for the first three consecutive periods, you will find that the solution in the analytic form is hardly possible to deal with. It is too complicated and its complexity increases as the number of periods increases. There is no hope of finding the steady state condition in this way.

For the control of this switching converter, you need the average values of voltage and current which has lots of switching ripples. As you filter out the switching ripples with a finite bandwidth, you will get the response of the filters instead of the original signals, which results in a slow system response. In this way, the switching behavior of a converter makes it very difficult to analyze and control a power electronic circuit composed of a converter and its controller.

We can say that power electronics is a unique engineering field that deals with non-linear time-varying switching systems. All switching converters, without exception, are time-varying systems because their circuit configurations are repeatedly changed in time by electronic switches, as can be seen from Fig. 1.3. Equation (1.1) can be rewritten in a state equation form, as follows:

$$\dot{\boldsymbol{x}} = \boldsymbol{A}_1\boldsymbol{x} + \boldsymbol{B}_1\boldsymbol{u} \quad \text{for} \quad kT < t < kT + d \cdot T, \quad k = 0, 1, 2, \ldots \tag{1.2a}$$

$$\dot{\boldsymbol{x}} = \boldsymbol{A}_2\boldsymbol{x} + \boldsymbol{B}_2\boldsymbol{u} \quad \text{for} \quad kT + d \cdot T < t < (k+1)T, \quad k = 0, 1, 2, \ldots \tag{1.2b}$$

where state $\boldsymbol{x}$, input $\boldsymbol{u}$, and linear time-invariant (LTI) matrices $\boldsymbol{A}_1$, $\boldsymbol{B}_1$, $\boldsymbol{A}_2$, $\boldsymbol{B}_2$ are defined as

$$\begin{aligned} \boldsymbol{x} &\equiv \begin{Bmatrix} i_S \\ v_O \end{Bmatrix}, \quad \boldsymbol{u} \equiv v_S, \quad \boldsymbol{A}_1 \equiv \begin{Bmatrix} 0 & 0 \\ 0 & -\frac{1}{CR_L} \end{Bmatrix}, \\ \boldsymbol{B}_1 &\equiv \begin{Bmatrix} \frac{1}{L} \\ 0 \end{Bmatrix}, \quad \boldsymbol{A}_2 \equiv \begin{Bmatrix} 0 & -\frac{1}{L} \\ \frac{1}{C} & -\frac{1}{CR_L} \end{Bmatrix}, \quad \boldsymbol{B}_2 \equiv \begin{Bmatrix} \frac{1}{L} \\ 0 \end{Bmatrix}. \end{aligned} \tag{1.3}$$

In order to unify the two LTI equations of (1.2) into a single equation, an existence function, which was adopted first by Peter Wood, is used as follows:

$$d(t) = 1 \quad \text{for } kT < t < kT + d \cdot T, \quad k = 0, 1, 2, \ldots \tag{1.4a}$$

$$d(t) = 0 \quad \text{for } kT + d \cdot T < t < (k+1)T, \quad k = 0, 1, 2, \ldots, \tag{1.4b}$$

which results in the following unified single equation.

$$\begin{aligned} \dot{\boldsymbol{x}} &= (\boldsymbol{A}_1\boldsymbol{x} + \boldsymbol{B}_1\boldsymbol{u})d(t) + (\boldsymbol{A}_2\boldsymbol{x} + \boldsymbol{B}_2\boldsymbol{u})d'(t) \\ &= \{\boldsymbol{A}_1 d(t) + \boldsymbol{A}_2 d'(t)\}\boldsymbol{x} + \{\boldsymbol{B}_1 d(t) + \boldsymbol{B}_2 d'(t)\}\boldsymbol{u}, \\ &= \boldsymbol{A}(t)\boldsymbol{x} + \boldsymbol{B}(t)\boldsymbol{u} \end{aligned} \tag{1.5}$$

where the time-varying matrices $\boldsymbol{A}(t), \boldsymbol{B}(t)$ and the complementary existence function $d'(t)$ are defined as follows:

$$\begin{aligned} \boldsymbol{A}(t) &\equiv \boldsymbol{A}_1 d(t) + \boldsymbol{A}_2 d'(t) \\ \boldsymbol{B}(t) &\equiv \boldsymbol{B}_1 d(t) + \boldsymbol{B}_2 d'(t) \\ d'(t) &\equiv 1 - d(t). \end{aligned} \tag{1.6}$$

In general, the state equation and output equation of a switching converter can be described as follows:

$$\dot{\boldsymbol{x}} = \boldsymbol{A}(t)\boldsymbol{x} + \boldsymbol{B}(t)\boldsymbol{u} \tag{1.7a}$$

$$y = \boldsymbol{C}(t)\boldsymbol{x} + \boldsymbol{D}(t)\boldsymbol{u}. \tag{1.7b}$$

In (1.4b), $\boldsymbol{C}(t), \boldsymbol{D}(t)$ are time-varying matrices, which are quite useful for describing a converter with no energy storage elements such as inductors and capacitors; therefore, in this case there are no state variables but an ideal voltage or current source with switches. The number of piecewise LTI circuits in a switching period T is not necessarily two, as shown in Fig. 1.3, and can be arbitrary in general.

As identified from (1.6), the system matrices $\boldsymbol{A}(t), \boldsymbol{B}(t)$ are not non-linear even though they are time-varying as long as the piecewise circuits are LTI.

A switching system, which is typically composed of switching converters, filters, controllers, power sources, and loads, can be compared to an ordinary non-switching system in the state equation domain, as shown in Fig. 1.4. An ordinary system can be represented by the LTI state equation and output equation, where the input may be a power source and the disturbance may be the change of system parameters. In contrast, a switching system can be represented by the time-varying state equation and output equation, where the input is typically the duty ratio and the disturbance is a change of the power source. The duty ratio d is defined from (1.4) as follows:

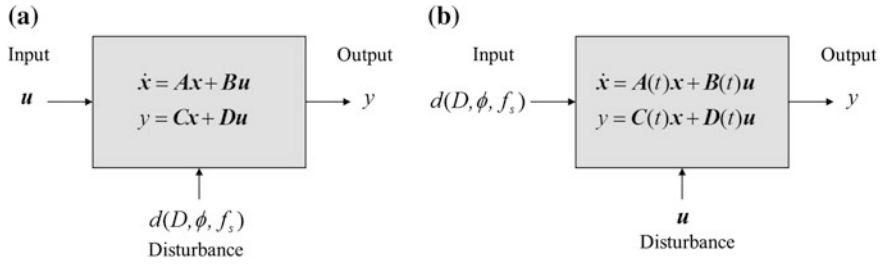

Fig. 1.4 Comparison of a switching system and an ordinary system. **a** An ordinary system. **b** A linear switching system

$$d = d_0 \equiv \frac{1}{T}\int_{kT}^{(k+1)T} d(t)dt \quad \text{for } kT < t < (k+1)T, \quad k = 0, 1, 2, \ldots. \tag{1.8}$$

Contrary to an ordinary non-switching system, a switching system is often controlled by the duty ratio, which is often regarded as the disturbance in the ordinary system. In general, the existence function $d(t)$ of (1.4) can be decomposed in Fourier series to DC and multiple sinusoids with its amplitude, phase, and angular frequency as follows:

$$d(t) = d_0 + d_1 \sin(\omega_s t + \phi_1) + d_2 \sin(2\omega_s t + \phi_2) + \cdots \tag{1.9}$$

The DC and first AC component, which are often referred to as 'fundamental components,' are of prime importance, whereas the remaining are referred to as 'harmonic components.' Depending on the application, the DC or AC components are selected by power filters. The switching frequency or a period T is not necessarily constant and may vary in time, as follows:

$$\omega_s \equiv 2\pi f_s = \frac{2\pi}{T}. \tag{1.10}$$

Similarly, the amplitude and phase of a fundamental component may vary in time. $D = d_0$ for a DC power system, and $D = d_1$ and $\phi = \phi_1$ for an AC power system. In general, a switching system can be controlled by the existence function, which controls the amplitude, phase, and frequency D, ϕ, f_s, as shown in Fig. 1.4.

Question 2

1. Can you find a Fourier series expansion of the existence function $d(t)$ in Fig. 1.2 of the form of (1.9)?
2. Determine D, ϕ, f_s from (1.1).

It can be said that a switching system composed of linear circuit components, operating in the CCM, is linear with respect to (w.r.t.) $\boldsymbol{u}$ and y. Unfortunately, this is

not true in general w.r.t. the input parameters d, f_s and the output y of the switching system. Therefore, the term 'a linear switching system' in this book means that the system is linear w.r.t. only $\boldsymbol{u}$ and y. Even though the meaning of 'linear' is narrow, it is still very useful because it enables us to find a general unified modeling technique, which would be impossible for a non-linear system.

1.2 A Switching Converter May Even Be Nonlinear but Fortunately It Is Linear in Many Cases

A switching converter becomes non-linear if its circuit elements are non-linear or its switches operate in the discontinuous conduction mode (DCM), which means that at least one of the switch currents eventually becomes zero, as shown in Fig. 1.5. The same circuit of Fig. 1.2 becomes DCM when the inductor current becomes zero, as shown in Fig. 1.5a. This occurs when the duty ratio in the steady state, i.e., $d = D$, becomes small or the load resistance is large. At $t = t_0$, the current i_s becomes zero, and then an open circuit S3 is generated, as shown in Fig. 1.5b. You may find the boundary condition between the CCM and DCM, which is called the boundary conduction mode (BDM), by letting $t_0 = T$.

$$L\frac{di_S}{dt} = v_S \quad C\frac{dv_o}{dt} = -\frac{v_o}{R_L} \quad \text{for } kT < t < kT + d \cdot T, \quad k = 0, 1, 2, \ldots \quad \text{(S1)} \tag{1.11a}$$

$$L\frac{di_S}{dt} = v_S - v_o \quad C\frac{dv_o}{dt} = i_S - \frac{v_o}{R_L} \quad \text{for } kT + d \cdot T < t < kT + t_0, \quad k = 0, 1, 2, \ldots \quad \text{(S2)} \tag{1.11b}$$

$$i_S = 0 \quad C\frac{dv_o}{dt} = -\frac{v_o}{R_L} \quad \text{for } kT + t_0 < t < (k+1)T, \quad k = 0, 1, 2, \ldots \quad \text{(S3)} \tag{1.11c}$$

Question 3

1. Determine t_0 assuming that the output voltage changes little during a period.
2. Plot the boundary condition $t_0 = T$ w.r.t. D and R_L.

The boundary condition of the time t_0 is not fixed but rather is a complicated function of circuit and control parameters such as L, C, R_L, d, f_s, and v_s. Therefore, the system matrices in the DCM become as follows:

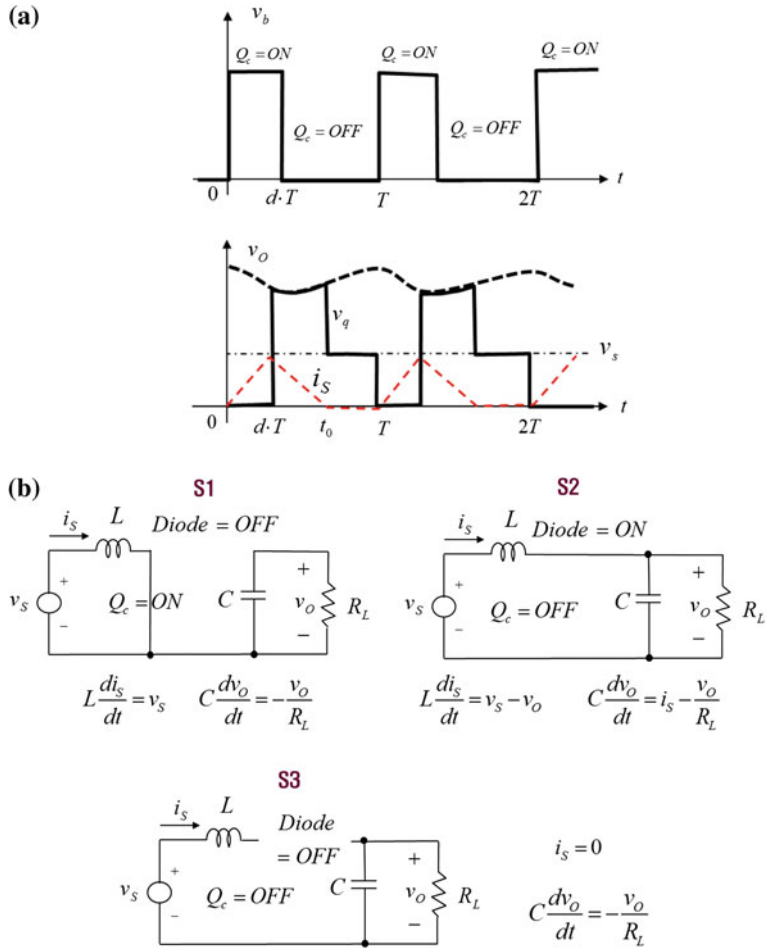

Fig. 1.5 The behavior of a boost converter in DCM. **a** The switching waveforms in the steady state. **b** Three piecewise circuits S1, S2, and S2 of Fig. 1.2

$$\begin{aligned} \boldsymbol{A}(t) &\equiv \boldsymbol{A}_1 d_1(t) + \boldsymbol{A}_2 d_2(t) + \boldsymbol{A}_3 d_3(t) \\ \boldsymbol{B}(t) &\equiv \boldsymbol{B}_1 d_1(t) + \boldsymbol{B}_2 d_2(t) + \boldsymbol{B}_3 d_3(t) \\ d_1(t) &\equiv d(t), \quad d_1(t) + d_2(t) + d_3(t) = 1 \end{aligned} \quad , \tag{1.12}$$

where the system matrices $\boldsymbol{A}_1, \boldsymbol{A}_2, \boldsymbol{A}_3, \boldsymbol{B}_1, \boldsymbol{B}_2, \boldsymbol{B}_3$ are the LTI system matrices for the piecewise equivalent circuits of S1, S2, and S3, respectively. The values of existence functions $d_1(t), d_2(t), d_3(t)$ become unity only for their corresponding periods of S1, S2, and S3, as similarly defined as (1.4). An important fact is that the period of $d_1(t)$ is independently controlled by $d(t)$ but the periods of $d_2(t)$ and $d_3(t)$ are influenced by t_0, which is variable by the state variables i_s and v_o. This means

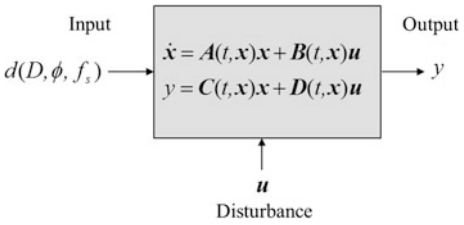

Fig. 1.6 A switching system that becomes nonlinear in the DCM

that the system matrices of the state equation and output equation become a function of states as follows:

$$\dot{\boldsymbol{x}} = \boldsymbol{A}(t,\boldsymbol{x})\boldsymbol{x} + \boldsymbol{B}(t,\boldsymbol{x})\boldsymbol{u} \tag{1.13a}$$

$$y = \boldsymbol{C}(t,\boldsymbol{x})\boldsymbol{x} + \boldsymbol{D}(t,\boldsymbol{x})\boldsymbol{u}. \tag{1.13b}$$

As identified from (1.13), the system is no longer linear even w.r.t. $\boldsymbol{u}$ and y. (You can check the linearity of a system in general by providing two independent input variables to system equations, and then the output will be the same as the sum of two output of each input variable if it is a linear system.)

Therefore, a switching converter (or a switching system) operating in the DCM is nonlinear in all respects, as shown in Fig. 1.6. As discussed above, a switching system with LTI circuit components only becomes linear or nonlinear depending on the operating conditions, where the BDM condition on t_0 determines the boundary. Fortunately, converters are very often designed to operate in the CCM because it is easy to control and the dynamic system performances tend to be better than the DCM.

Except for the cases otherwise specified, all the circuit parameters are assumed to be linear throughout this book, because the switching system is already complicated enough, as proved so far for one of the simplest basic converters, shown in Fig. 1.2.

1.3 Converters Are Crucial for Matching Various Sources with Loads

The purpose of power electronics is to change amplitudes, frequencies, or phases of the power source by electronic switches. Hence, all switching power converters are time-varying systems, which is quite different from conventional time-invariant systems, as discussed in the previous chapter. In general, the power system in power electronics is composed of the power source, input filter, converter, output filter, load, and controller, as shown in Fig. 1.7. The power source can be one of the DC power supplies, DC energy storages, high voltage DC transmission (HVDC) systems, 50/60 Hz single phase (1Φ) AC powers, and three phase (3Φ) AC powers, as shown in Fig. 1.8. The load can be one of the home appliances, DC motors,

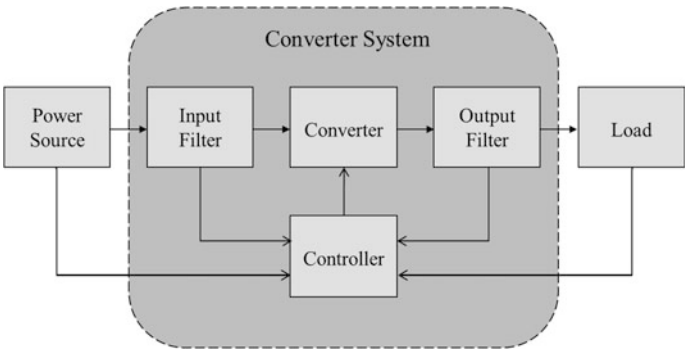

Fig. 1.7 The configuration of a general power system in power electronics

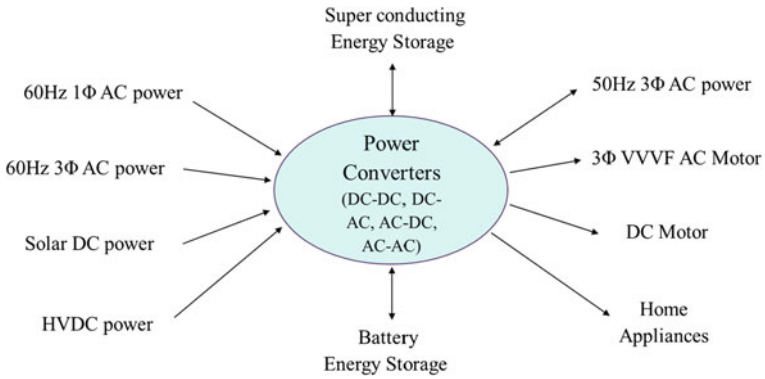

Fig. 1.8 The need for power converters is to match different sources and loads relative to each other

variable-voltage variable-frequency (VVVF) AC motors, and other powers such as DC powers and AC powers. The converter, often referred to as a 'power converter' to distinguish it from a signal converter, is used due to the mismatches between various sources and loads. The converter is either a switching converter as discussed so far or a linear regulator, which is not widely used due to large power loss. Depending on the input and output power types, various converters such as DC-DC (switching regulators), DC-AC (inverters), or AC-DC (rectifiers), AC-AC (cycloconverters) converters are used. Note that the power source is not necessarily providing power and that the load is not necessarily receiving power. The power flow can be arbitrary in general, and any power source can be regarded as a load and vice versa. The input and output filters in power electronics mitigate high order harmonic currents and voltages generated from the converter as well as the power source and load. These filters are usually passive type filters composed of inductors, capacitors, and resistors, which are very often avoided because of power loss. The

filters can be made of a converter, which is called an active filter. The controller collects information from all the components of a power system and processes the information to appropriately control the converter. The controller can be either a digital processor or an analog controller. A 'converter system' consisting of the converter, input/output filters, and controller in this book is also often called a 'converter'. Therefore, it is important to pay attention to the use of 'converter' regarding the intended meaning.

1.4 The Dynamic Characteristics of AC Circuits Are Another Challenging Issue in Power Electronics

As shown in Fig. 1.1, the transient state response of the three phase RLC circuits with three phase balanced (the phase difference between each phase is equal and the amplitude is the same each other) sources is a sinusoidal waveform, whose envelope is asymptotically increasing to the steady state. The static behavior of an AC circuit can be easily analyzed by the well-known phasor analysis; however, the dynamic behavior of an AC circuit is completely different from the static behavior. There was no available theory, often called 'modeling' in power electronics, until I proposed the 'phasor transformation' in 1990.

The simulation results shown in Fig. 1.1 are an actual response I made, which has an exponential envelope characteristic. It is strange that the 3rd order system per phase, i.e., the RLC circuit, is a 9th order system as a total system, but looks like a first order system in its output voltage response. Moreover, this is not always true because the system order of the envelope characteristics may look like a 2nd order system. There must be a sufficient explanation with a simple model if possible.

In general, AC waveforms are everywhere in the universe, and they stem from oscillation phenomena such as rotating electrons around nuclei, oscillating swings, ringing bells, fluctuating bridges, orbiting satellites around Earth, and radiating X-rays from the center of a black hole in a galaxy. In most modern physics and engineering, the oscillation phenomena are dealt with in static ways and dynamics in the time domain are seldom considered due to the difficulties of handling the dynamic AC characteristics (Fig. 1.9).

The AC characteristic is different from the time-varying nature of switching power circuits. The AC characteristic may come from AC sources, AC loads, and AC switching converters, whereas the time-varying characteristic comes only from any switching converter. They must be dealt with separately and sometimes together, which will be discussed in the subsequent chapters.

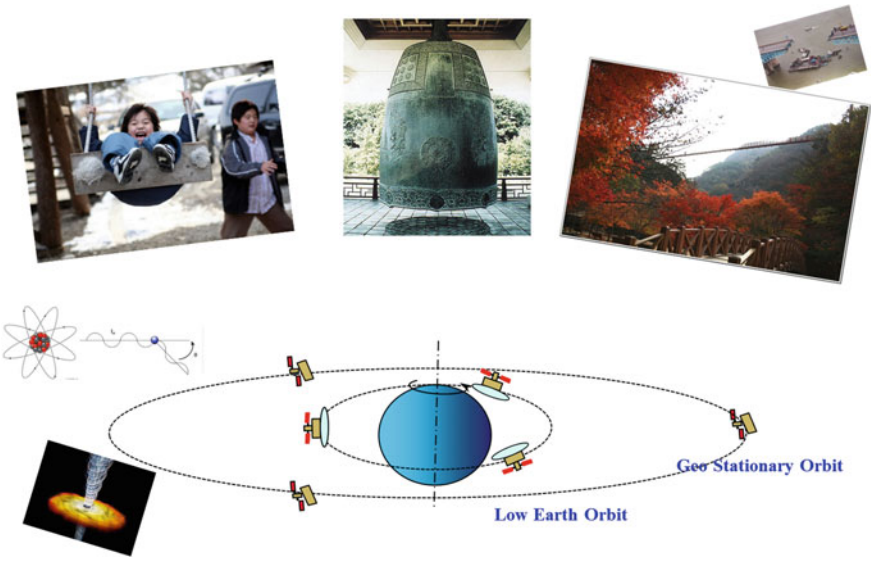

Fig. 1.9 Oscillation phenomenon in the universe from an atom to a galaxy

1.5 Power Electronics Deals with the Unseen, Untouchable, Unbounded, and Inseparable Natures

Power electronics is a kind of electronics. Therefore, the nature of electronics is also found in power electronics as follows:

- **Unseen**: Parameters such as voltage, current, impedance, frequency, and phase cannot be directly seen. This is why we need measuring instruments such as oscilloscopes, multi-meters, and function generators.
- **Untouchable**: Most devices and energy media such as μ-chip, power line, LED light, and plasma cannot be directly touched. This is why we need various sensors such as probes, microscopes, and temperature sensors.
- **Unbounded**: Transmitting power and signal often involves an unlimited range of magnetic field, microwave (M/W), and laser communication.
- **Inseparable**: The circuit, system, network, and system of systems in electronics are closely related to each other and it is quite difficult to separate the operation of a part from other parts.

The above four natures of electronics are not well identified in other fields such as mechanics and construction engineering. The four natures are not easily overcome by common sense, but they must be familiarized by endless practice and experiments until one feels the unseen and untouchable by heart. This is why electronics as well as power electronics are so difficult to learn, which will be your privileged knowledge once you surmount the obstacles you encounter.

Fig. 1.10 Power electronics is one of the most popular and large areas in the IEEE society

Among a hundred of IEEE societies, there are at least 8 societies directly related with power electronics (marked as red) and 19 societies where power electronics related technical issues (marked as blue) are often published, as shown in Fig. 1.10. This is roughly a quarter of all IEEE societies, which means that power electronics is an extremely influential area with many challenging technical issues. It is amazing that nearly every modern electric device and equipment has power systems inside it, and the requirements of each power system differ from each other because of various applications.

1.6 Why Do We Need Theories, Simulations, and Experiments?

I have met many people including engineers who talk about the importance of experiments. Not necessarily to talk about, to have experiments is a vital process to validate a design and to check the reliable operation under certain conditions. One of the problems I found is that many people underestimate the importance of theories. A theory is a good tool to understand the whole principle of a system, especially when a system is very difficult to handle. Because a switching power system is inherently time-varying and sometimes nonlinear with lots of harmonics noises, a good theory or model is crucial for designing and controlling the system.

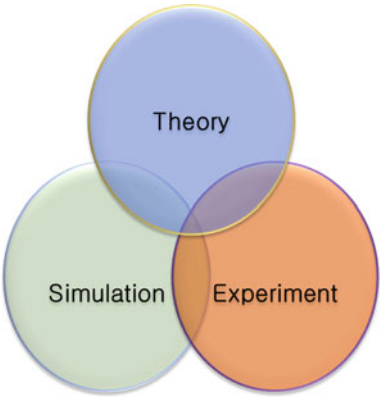

Fig. 1.11 The trinitas of theory, simulation, and experiment

Furthermore, the optimum design and tolerance assessment for extreme cases can be done only by theories and cannot be verified by a finite number of experiments with constrained practical conditions. Cost and time are also problems that limit experiments, and this is why computer simulation is also preferred in power electronics.

For a generalized understanding of phenomena, detailed descriptions are inevitably omitted from a theory, which becomes the limitation of the theory. Simulation also has limitations such as lack of confidence of its results and the absence of physical insight. Therefore, using theory, simulation, and experiment is very helpful for a thorough understanding and optimum design of a system. It is highly desirable for the results of theory, simulation, and experiment to be a trinitas, as shown in Fig. 1.11. For the validity of a design, at least two of the three results should be within reasonable error. A good combination may be either 'theory-experiment' or 'simulation-experiment'.

1.7 Good Power Electronics Engineers Do not Rely on Complicated Equations; Instead, a Smart Equivalent Circuit Is Enough

In this chapter, I have explained why power electronics is so special and why it is so difficult to deal with. However, I would like to give you hope that we can overcome the 3D of power electronics if we can find an equivalent power circuit that can be easily analyzed.

There is already a very good example in the area of electronic circuits, which were believed to be one of the most complicated problems to solve in electronics. In the late 1970s, Dr. Gyu H. Cho, a professor with the Department of Electrical and

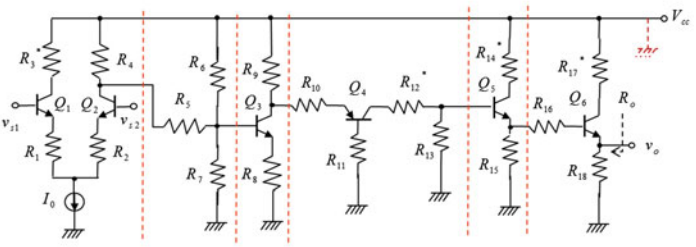

$$|A_v| = \frac{R_4}{R_1 + r_{e1} + R_2 + r_{e2}} \cdot \frac{R_6 \,//\, R_7}{R_4 + R_5 + R_6 \,//\, R_7} \cdot \frac{R_9}{R_8 + r_{e3} + \{(R_4 + R_5) \,//\, R_6 \,//\, R_7\} / \beta_3}$$

$$\frac{R_{13}}{R_9 + R_{10} + r_{e4} + R_{11} / \beta_4} \cdot \frac{R_{15}}{R_{15} + r_{e5} + R_{13} / \beta_5} \cdot \frac{R_{18}}{R_{18} + r_{e6} + \{R_{16} + R_{15} \,//\, (r_{e5} + R_{13} / \beta_5)\} / \beta_6}$$

$$\frac{A_v}{|A_v|} = (+)(+)(-)(+)(+)(+) = (-), \quad R_o = R_{18} \,//\, \left[r_{e6} + \{R_{16} + R_{15} \,//\, (r_{e5} + R_{13} / \beta_5)\} / \beta_6\right]$$

Fig. 1.12 Cho Formula in electronic circuits, which requires no equations for analysis and design

Electronics at KAIST, developed an analytical technique for analyzing and designing very complicated electronic circuits with great ease, as shown in Fig. 1.12.

For any kind of circuit, regardless of how complicated, we can obtain analytical results such as small signal gains, input impedances, output impedances, loop gains of feedback amplifiers, and cut-off frequencies without setting up any equations. It took several hours or even days to analyze the integrated circuit (IC) amplifier of Fig. 1.12 by a conventional equational based approach, but it takes a minute by the Cho Formula (abbreviated as 'Cho-Form'), which is mainly because of the time for writing solutions by hand. The new method is based on a circuit based approach; hence, physical insights such as the impedance concept and Thevenin equivalent circuit concept are fruitfully provided. With the Cho-Form, not only the analysis but also the design of ICs becomes possible, which has greatly contributed to the advance of modern electronic engineering during the past few decades. If you want to know the details of the Cho-Form, please refer to the book, "Gyu-Hyeong Cho, *Advanced Electronic Circuits*, Hong-Reung Publisher, 2008." I am afraid that the book is written in Korean and an English version has not appeared yet.

I have carried out similar works in power electronics throughout my carreer, as shown in Fig. 1.13. The switching power circuits of time-varying and AC are transformed to non-switching ordinary circuits of LTI and DC by four circuit transformation techniques that I developed. The 'DC-AC' of Fig. 1.13 includes both DC-AC converters and AC-DC converters. Recently, they have been combined with a unified general phasor transformation, which is applicable to any type of linear converter.

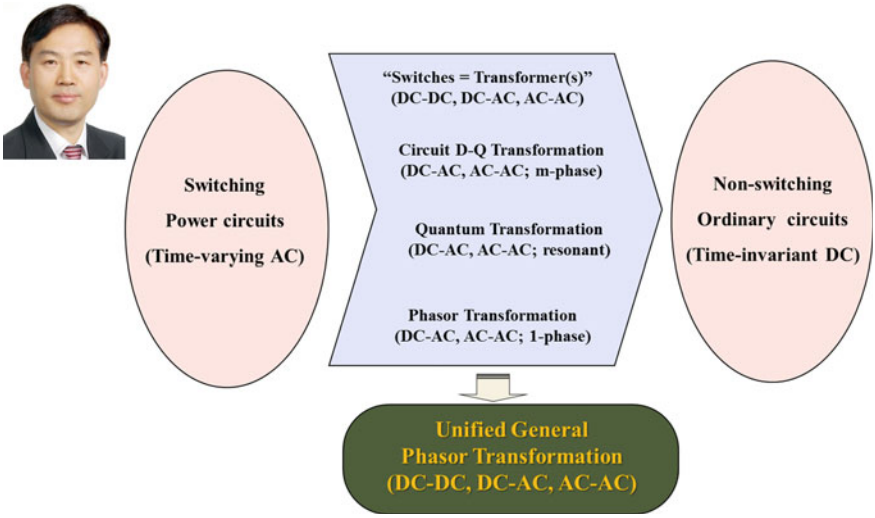

Fig. 1.13 Rim Formula in switching power circuits, which also requires no equations for analysis and design

Throughout the rest of this book, the time-varying nature and AC dynamics of switching power systems will be explored and the Rim Formula, which includes powerful modeling techniques, shall be provided for the readers.

Chapter 2
Key Principles of Power Converters

This chapter explains how linear regulators and switching converters are adopted in power processing from the very basic principles of power circuits. The switching process is dealt with and switching losses, efficiency, and snubber circuits are introduced. The concepts of continuous conduction and discontinuous conduction modes are explained.

A converter, also quite often referred to as a 'switching converter' or 'power converter' to distinguish it from a signal converter, is composed of inductors (L), capacitors (C), resistors (R), transformers (T), and semiconductor switches (S), as shown in Fig. 2.1. It can be said that the purpose of a 'modern' converter is to convert and control power by semiconductor switches. Note that 'old' converters in the early 20th century were not made of semiconductor switches but rather electro-mechanical machines or electronic vacuum tube switches.

In this chapter, a few key principles for understanding the converter are provided from the very basic idea. Ideally, a converter

1. changes power without any power loss, i.e., power efficiency is 100 %,
2. takes zero response time with no transient overshoot, i.e., its operation is quite fast and stable,
3. has no harmonics and ripples,
4. is involved in no faults, i.e., it is maintenance free and has infinite lifetime,
5. has minimum size, weight, and cost,
6. operates in all-weather environments under harsh conditions.

Of course, there is no such ideal converter, and power electronic engineers are struggling to make converters close to it. More often, finding a suitable trade-off between the above mentioned six requirements is a practical issue that engineers encounter. More specifically, choosing the configuration of a converter and determining the parameters of circuit components, often called 'design', are major jobs for engineers.

C.T. Rim, *Phasor Power Electronics*, KAIST Research Series,
DOI 10.1007/978-981-10-0536-7_2

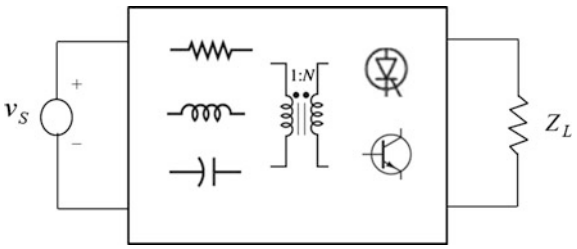

Fig. 2.1 A converter is composed of LCR and TS in general

2.1 Evolution of Power Converters

2.1.1 Why Do We Need Power Control?

Let's see why we should control the power with a DC power circuit, as shown in Fig. 2.2. There are at least three cases where we need to control the power. First, the battery output voltage changes by aging, as shown in Fig. 2.2a. Many loads do not permit this voltage drop; then, we should have a countermeasure to address this problem. Second, the output voltage of a battery changes as the load current

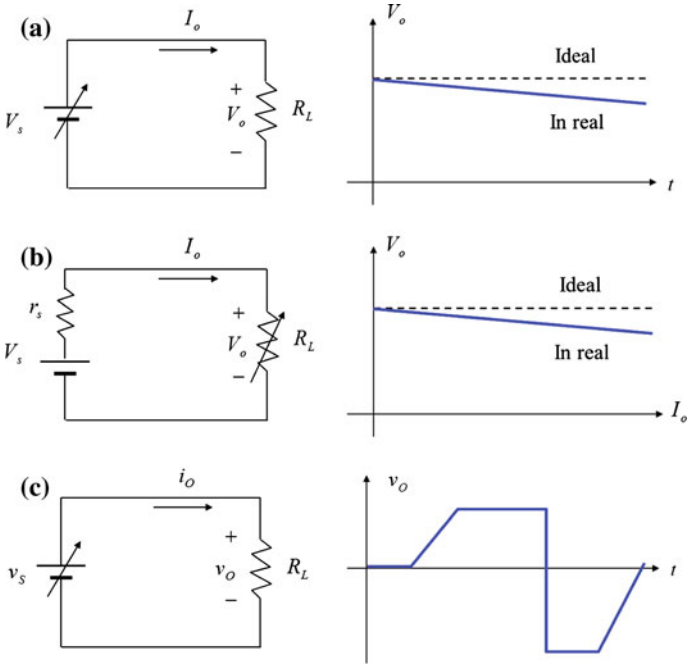

Fig. 2.2 The reasons why we need power control in a power system. **a** A battery voltage changes by aging. **b** The output voltage changes as the load current increases. **c** We want to vary the output as desired

increases, as shown in Fig. 2.2b. This voltage drop is inevitable due to the finite value of the internal resistance of the battery, which is of course not permitted for a voltage sensitive load. The third case is that we want to vary the output dynamically as desired, as shown in Fig. 2.2c. It is remarkable to see that the need for power control comes from the power source, load, and converter. This means that every component of a power system can be a source of problems that should be solved.

2.1.2 *We Can Control the Power by a Time-Varying Resistor*

Let's start with a very simple idea of controlling output power by a controllable variable resistor, as shown in Fig. 2.3. As the source voltage v_S fluctuates randomly, we need to control the resistor R_c so that the output voltage v_O can be regulated as desired. It is straightforwardly found that the DC (direct current) gain, often referred to as 'large signal gain', is as follows:

$$G_v \equiv \frac{v_O}{v_S} = \frac{R_L}{R_c + R_L}. \tag{2.1}$$

$R_c(t)$, which is now time-varying, can then be determined for given DC gain as follows:

$$R_c(t) = R_L\left(\frac{1}{G_v} - 1\right) = R_L\left(\frac{v_S}{v_O} - 1\right). \tag{2.2}$$

As identified from (2.2), v_O cannot be larger than v_S so far as $R_c(t)$ is non-negative, and the power control system involves inherent power loss in $R_c(t)$. Therefore, this type of converter can be applicable to voltage step-down conversion applications where power efficiency is not a serious problem.

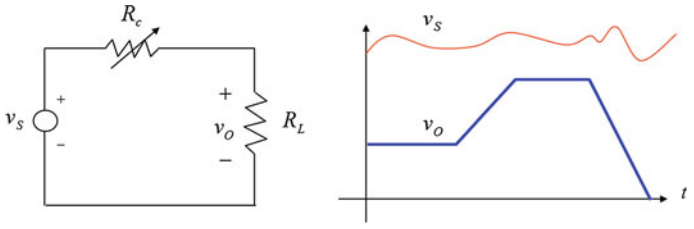

Fig. 2.3 An idea for controlling output power by a variable resistor

2.1.3 We Can Control the Power by a Power Transistor in Linear Mode

The ideal of controllable resistor can be implemented by using a transistor, as shown in Fig. 2.4. The output voltage can be determined by a simple equation, considering non-saturation conditions for the transistor, as follows:

$$v_O = v_Q - v_\gamma \quad \text{for} \quad v_S - v_O \geq v_\sigma \cong 0.2 \quad \because v_Q = v_O + v_\gamma \cong v_O + 0.7. \tag{2.3}$$

As identified from (2.3), the output voltage can be arbitrarily controlled under the restricted conditions of non-saturation. A very popular application is the linear regulator, where the output voltage is usually kept constant to a certain specified value, as shown in Fig. 2.4 as a dotted line. Feedback control is very often used in practice to achieve an accurate voltage regulation regardless of source voltage variation and load current change. Another application is the power amplifier, where the output voltage quickly follows the wanted voltage waveform, as shown in Fig. 2.4 as a bold line.

Over current protection for a small R_L, over voltage protection against high input voltage or output voltage due to inductive load characteristics, and over temperature protection for the power transistor are needed for practical applications. This is why we need a power control integrated circuit (IC) in power electronics.

Question 1

1. Determine the maximum amplitude of a sinusoidal output voltage of a power amplifier for a fixed V_s.
2. Calculate the power efficiency of the power amplifier for the maximum amplitude case of (1).

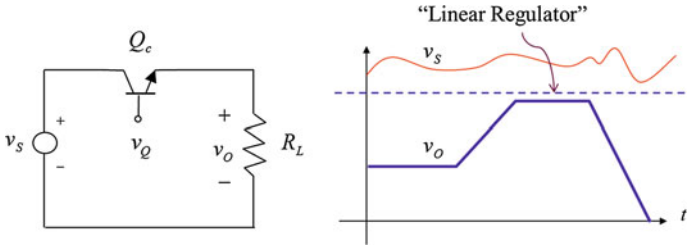

Fig. 2.4 An implementation example of the controllable resistor of Fig. 2.3

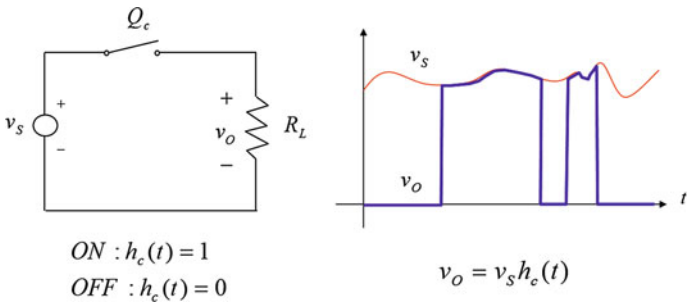

Fig. 2.5 An ideal power switch for controlling output power without any power loss

2.1.4 We Can Control the Power by a Power Transistor in Switching Mode

An innovative way of controlling output power without any power loss is to use an ideal power switch, as shown in Fig. 2.5. When the power switch is ON, then the voltage drop of the ideal power switch is zero. When the power switch is OFF, then the current of the ideal power switch is zero. Therefore, the power loss in the ideal switch becomes always zero, which results in 100 % power efficiency.

The idea of controlling power by an ideal power switch can be implemented by a power transistor, operating in switching mode, as shown in Fig. 2.6. Similar to the controllable resistor case, voltage step-down conversion is only possible and square wave type output voltage is obtained for this power switch method.

Furthermore, this switch mode power transistor is seldom used without proper measures in practice because of the leakage inductance, which exists for any power line of the order of 1 μH/m for 1 nH/mm. For example, a 10 cm power line has 0.1 μH, which may destroy a power transistor of 1000 V voltage rating. One way of avoiding this unwanted high induced voltage from the leakage inductance is to use a power diode, as shown in Fig. 2.7. As soon as the ideal transistor is turned on or off, the ideal diode is turned off and on, which provides an alternative current path so that the current of the leakage inductor can be continuous. In this way, the

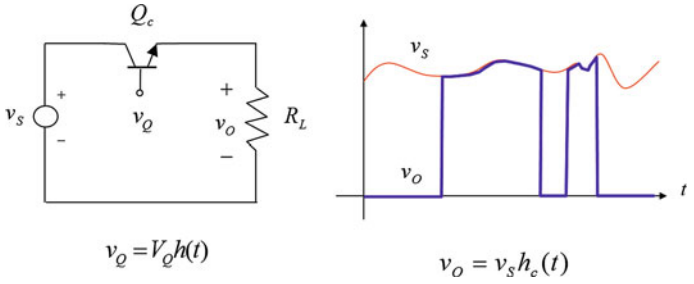

Fig. 2.6 Implementation of the ideal power switch of Fig. 2.5

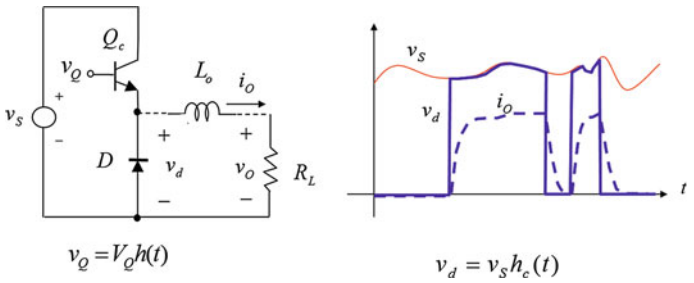

Fig. 2.7 A possible way of protecting the power transistor from the leakage inductance using a power diode

collector-emitter voltage stress of the transistor is safely constrained within the source voltage. The output current is accordingly determined by the leakage inductance and load, as depicted in Fig. 2.7.

The transistor-diode pair is referred to as a 'switch cell' because the switches do not operate separately but rather they operate like a system. Even though the switch mode transistor-diode pair is safely operating, this power circuit is not widely used except for a simple on/off control of power where large switching noise is not a problem in practice.

2.1.5 *A Switching Converter with Input and Output Filters Is a Viable Solution*

Instead of leakage inductance, a lumped inductor can be attached the switch cell. The switch cell with a filter can be called a basic 'converter', as shown in Fig. 2.8.

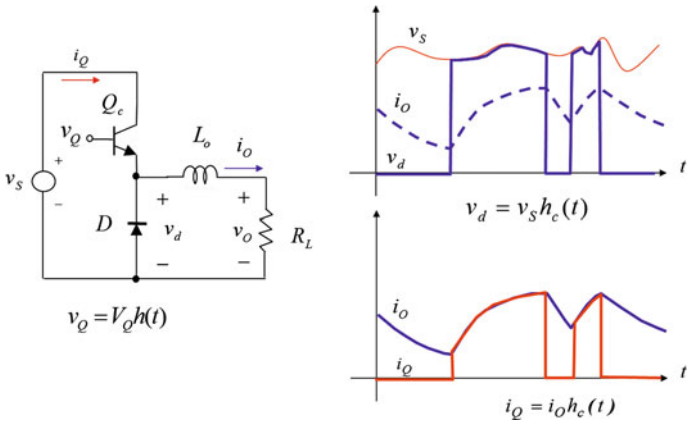

Fig. 2.8 A basic converter with an output inductor only

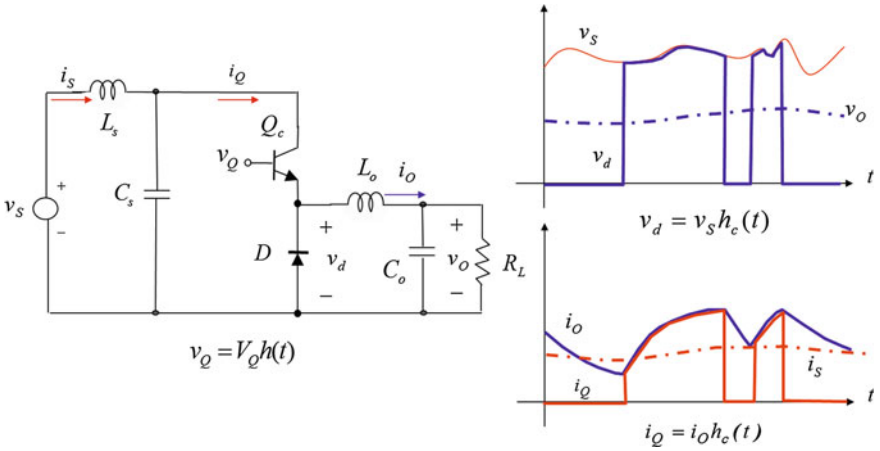

Fig. 2.9 A buck converter with input and output LC filters

Now, the output current can be continuous and the load voltage becomes smooth. One of the problems of this converter is that the input current i_Q contains large switching current, as shown in Fig. 2.8.

Therefore, we need to add an input filter to mitigate the switching harmonic current, and we need to strengthen the output filter as well, as shown in Fig. 2.9. The input and output LC filters eliminate the switching voltage and current generated from the switch cell. The step-down converter, as shown in Figs. 2.8 and 2.9, is called a buck converter when it is used in DC-DC power conversion, which is regarded as the most fundamental converter. Now we have smooth voltage and current waveforms of both source and load sides.

A remaining problem is that the system becomes too complicated, and consequently the design of circuit parameters and control of the system are not easy. For example, the system order of the buck converter of Fig. 2.9 is four, and it is not a simple task to find the dynamic (transient state response) and static (steady state response) solutions by 4 × 4 matrix manipulations. Note that the buck converter of Fig. 2.9 is one of the simplest converters, and the system order tends to be even higher than ten and the system is even time-varying. Of course, you do not have to worry about these problems. To make the complicated nature of the power circuit simple is the purpose of this book. An easy way of solving the problems will be provided for you.

2.1.6 *What Are Allowable Switches and What Are not Allowed?*

Concerning the switches in a switch cell, each switch must be of appropriate type to cope with the voltage and current directions of the source and load. Let me show

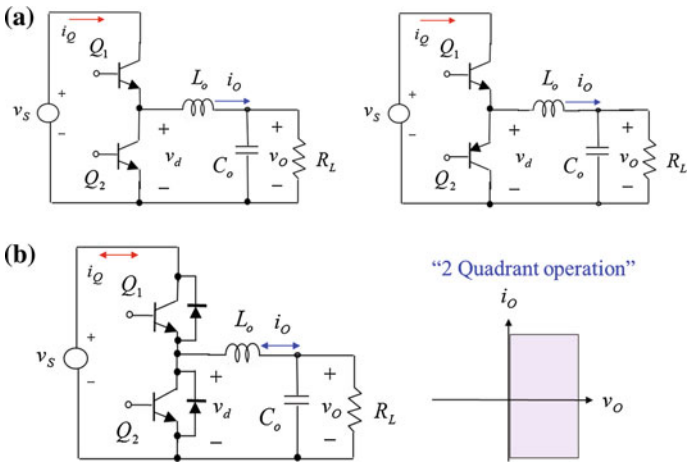

Fig. 2.10 Prohibited and permitted topologies of the buck converter example. **a** Prohibited topologies. **b** Permitted topology

you the configuration of a converter, also referred to as the 'topology', for the buck converter example. As shown in Fig. 2.10, the current flow of an inductor and the voltage polarity of a capacitor in the power circuit do not change in a period. The switch cell should cope with these properties; i.e., the switches Q_1 and Q_2 should provide the same output current direction at once. The switch Q_2 of Fig. 2.10a cannot provide forward current, and hence continuous output current flow is not guaranteed. However, the switch cell of Fig. 2.10b provides either positive or negative directions of output current flow at once, which is called as 'two quadrant operation' in power electronics. If the switch cell of Fig. 2.10b provides the step down voltage conversion function for the negative polarity of voltage, then it is called 'four quadrant operation'. This type of converter is called a 'chopper' if it is used in AC-AC power conversion. Of course, the converters in Figs. 2.8 and 2.9 are for DC-DC applications because the voltage and current flow of the switch cell can be unidirectional only with the proposed transistor-diode pair. For the chopper applications, the switch cell should be made of bidirectional switches, which operate for both directions of voltage and current.

2.2 Understanding the Operation of Converters

Various aspects of the operation of converters are explained below.

2.2.1 CCM and DCM Analyses for an Ideal Switch Cell

The piecewise LTI circuit analysis, as introduced for the boost converter example in the previous chapter, will be briefly introduced for the buck converter example to see the similarities and differences between the two converters. For simplicity, a buck converter with an output LC filter is selected this time. Drawing piecewise LTI circuits is a good start for analyzing a converter even though it cannot show all features of the operation of a converter, as discussed in the previous chapter. The LTI circuits for the CCM and DCM are two and three, respectively, as shown in Figs. 2.11 and 2.12.

At the beginning of the analysis, usually parasitic circuit elements such as internal resistances in switches, inductors, and capacitors, parasitic capacitances in inductors, and parasitic inductances in capacitors are neglected. Moreover, the source voltage and output voltage are assumed to be perfectly constant; i.e., the output capacitance is large enough so that there is no switching ripple voltage in the output. The system is also assumed to be in the steady state; of course, this is not true and the dynamic response should be explored in many cases for practical applications.

The inductor current becomes a straight line and the positive change of S1 becomes the same as the negative change of S2 in the steady state for the CCM case of Fig. 2.11, as follows:

$$\Delta I_o \cong \frac{V_s - V_o}{L_o} DT \cong \frac{V_o}{L_o}(1-D)T, \tag{2.4}$$

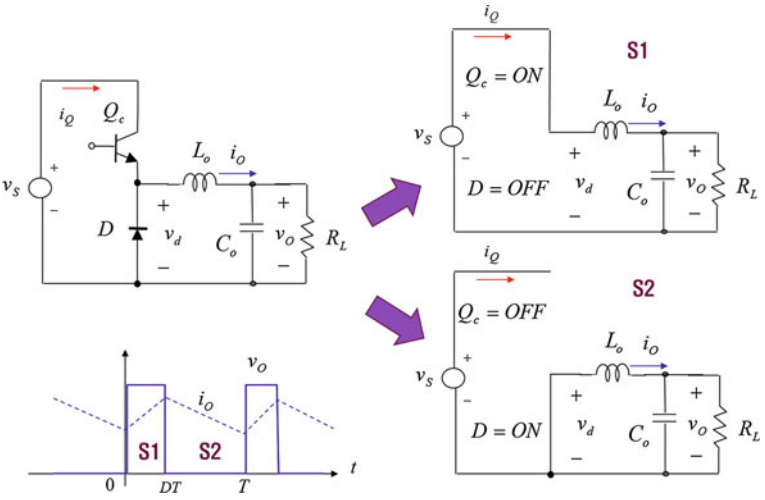

Fig. 2.11 Piecewise LTI circuits for the CCM operating buck converter

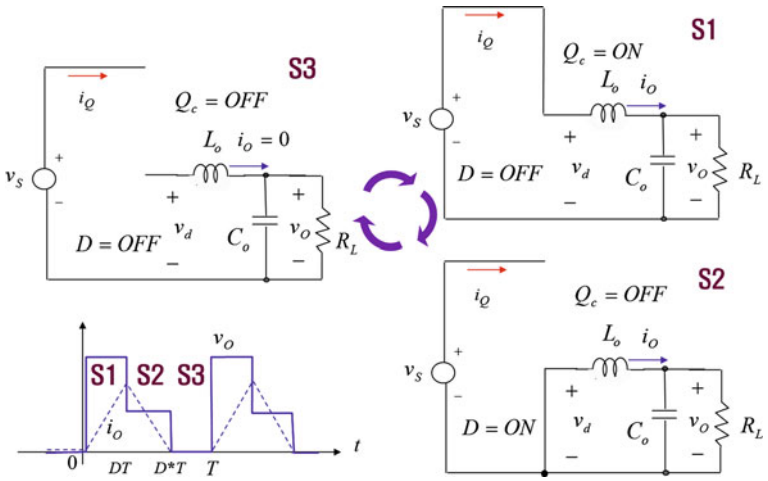

Fig. 2.12 Piecewise LTI circuits for the DCM operating buck converter

which results in a very simple DC gain.

$$G_V \equiv \frac{V_o}{V_s} \cong \mathrm{D}. \tag{2.5}$$

We need one more equation to determine the unknown variables in (2.4), which is the following output equation:

$$V_o = I_o R_L \quad \text{or} \quad I_o = V_o/R_L \cong DV_s/R_L. \tag{2.6}$$

Then the minimum and maximum values of the inductor current become as follows:

$$I_{o,min} = I_o - \Delta I_o/2, \quad I_{o,max} = I_o + \Delta I_o/2. \tag{2.7}$$

From (2.7), $I_{o,max}$ is used to determine the inductor current rating to withstand magnetic saturation, whereas $I_{o,min}$ is used to determine the boundary condition between the CCM and DCM as follows:

$$I_{o,min} = I_o - \Delta I_o/2 = 0 \quad \rightarrow \quad D_{BCM} = 1 - \frac{2L_o}{R_L T}. \tag{2.8}$$

As identified from (2.8), no BCM exists for the large L_o or small R_L for a given T which eventually makes D_{BCM} negative. In case the BCM exists, the buck converter operates in the CCM when $D > D_{BCM}$ and operates in the DCM when $D < D_{BCM}$.

In the DCM, the inductor current becomes zero at the time of D^*T, and (2.4) is slightly changed as follows:

$$\Delta I_o \cong \frac{V_s - V_o}{L_o} DT \cong \frac{V_o}{L_o}(D^* - D)T. \tag{2.9}$$

The output equation becomes, considering the average output current becomes the same as the load current, as follows:

$$I_o = \frac{V_o}{R_L} = \frac{\Delta I_o}{2} D^*. \tag{2.10}$$

From (2.9) and (2.10), the duty ratio of conduction D^* is determined.

$$D^* = \frac{L_o}{R_L T} + D. \tag{2.11}$$

Applying (2.11) to (2.9) results in a slightly complicated DC gain for the DCM as follows:

$$G_V \equiv \frac{V_o}{V_s} \cong \frac{K}{1+K}, \quad \because K \equiv D^* D \frac{R_L T}{2L_o^2}. \tag{2.12}$$

Even though we have assumed the simplest case, the analyses of the most basic buck converter are not so simple. Actually, there are many more analysis and design issues to consider.

2.2.2 *Practical Switching Characteristics of a Switching Cell*

All practical power switches have finite on and off switching times, which results in temporary open or off circuits, as shown in Fig. 2.13. At the turn off timing of the transistor Q_c, the diode D is not yet turned on until the diode voltage v_d becomes negative, while the Q_c is about to turn off. If the Q_c is forcefully turned off before the D is turned on, an open circuit (A case) may occur. At the instant of turn on timing of Q_c, the D was conducting; hence, a short circuit (B case) may occur if the Q_c is forcefully turned on. Of course these open and circuits are theoretically not allowed, but practical switches with finite switching times are exposed to the danger of failures due to the high open voltage (A case) or large short current (B case) if not properly operated.

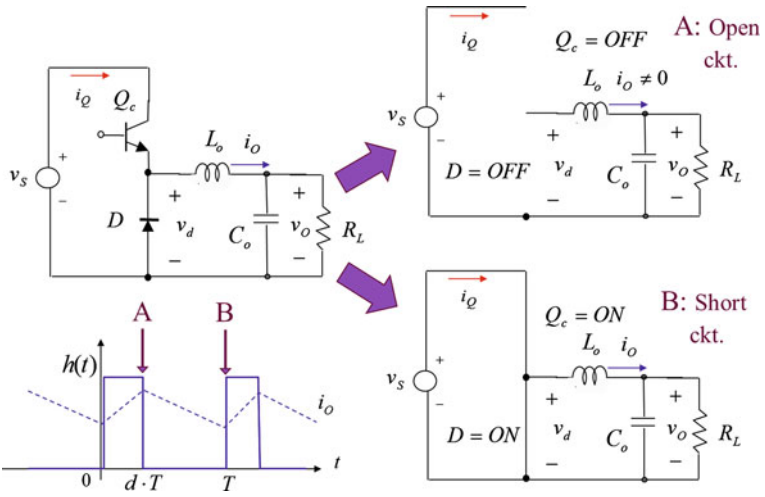

Fig. 2.13 Practical switches may be in danger of open or short circuit due to finite switching times

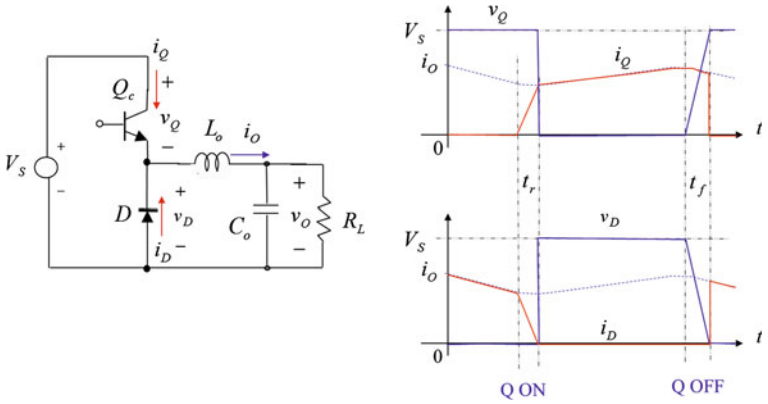

Fig. 2.14 Switching waveforms of a switch cell with finite switching times for an inductive load

As shown in Fig. 2.14, the switching waveforms of a switch cell with finite switching times can be drawn for an inductive load assuming an ideal DC source and load voltages. If the turn-on current and turn-off voltage of Q_c are of straight line change, then the circuit can be analyzed considering the following conditions:

$$v_Q + v_D = V_S \tag{2.13a}$$

$$i_Q + i_D = i_O. \tag{2.13b}$$

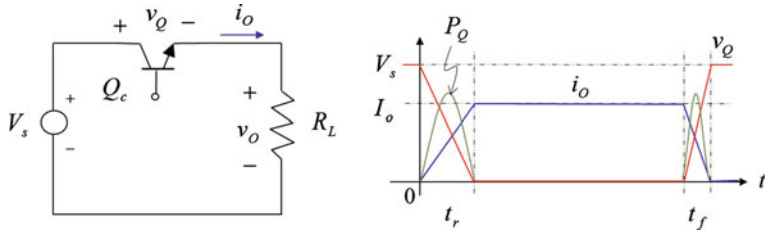

Fig. 2.15 Switching waveforms of a switch cell with finite switching times for a resistive load

The power loss during switching, called switching loss, can be calculated as follows:

$$P_{sw} = P_Q = \frac{1}{T}\int_0^T v_Q i_Q dt \cong \frac{V_s I_o}{2}\frac{t_r + t_f}{T}$$

$$\because \int_0^{t_r} v_Q i_Q dt \cong \int_0^{t_r} V_s (I_o t/t_r) dt = V_s I_o t_r/2$$

$$\because \int_0^{t_f} v_Q i_Q dt \cong \int_0^{t_f} V_s (1 - t/t_f) I_o dt = V_s I_o t_f/2\,. \tag{2.14}$$

Note that the switching loss of the diode is zero because either the voltage or current of the diode becomes zero during the on and off switching periods. Therefore, the switching loss in the transistor P_Q is the same as the total switching loss P_{sw} of the switch cell in this case. Furthermore, we have not considered the conduction loss of the switches yet. As noticed from (2.14), the switching loss highly depends on the switching waveforms of the switch voltage and current, which is referred as switching trajectory.

Another switching case for a resistive load with finite switching times is shown in Fig. 2.15, where both the voltage and current of the transistor are assumed to vary simultaneously in straight lines.

The switching loss can be calculated as follows:

$$P_Q = \frac{1}{T}\int_0^T v_Q i_Q dt \cong \frac{V_s I_o}{6}\frac{t_r + t_f}{T}$$

$$\because \int_0^{t_r} v_Q i_Q dt \cong \int_0^{t_r} (V_s - I_o R_L t/t_r)(I_o t/t_r) dt = V_s I_o t_r/6\,. \tag{2.15}$$

Comparing (2.15) to (2.14), the resistive load has three times less switching loss than the inductive load. The power efficiency of the converters, often referred to as 'efficiency', can be calculated from (2.14) and (2.15) as follows:

$$\eta \equiv \frac{P_o}{P_s} = \frac{P_o}{P_o + P_{sw}} = \frac{1}{1 + P_{sw}/P_o} \tag{2.16}$$

Applying the general efficiency equation of (2.16) to the inductive and resistive switching cases results in the following.

$$\eta_L = \frac{1}{1 + \frac{V_s I_o}{2}\frac{t_r + t_f}{T}\frac{1}{V_o I_o}} = \frac{1}{1 + \frac{t_r + t_f}{2T}\frac{1}{G_V}} \cong \frac{1}{1 + \frac{t_r + t_f}{2T}\frac{1}{D + t_f/(2T)}} = \frac{1}{1 + \frac{t_r + t_f}{2TD + t_f}} \tag{2.17a}$$

$$\eta_R \cong \frac{1}{1 + \frac{V_s I_o}{6}\frac{t_r + t_f}{T}\frac{1}{V_s I_o D}} = \frac{1}{1 + \frac{t_r + t_f}{6T}\frac{1}{D}} \tag{2.17b}$$

As noticed from (2.17a, 2.17b), the efficiency highly depends not only on the switching times and load types but also the duty ratio, which should be considered in cases where higher efficiency is required.

So far, it has been assumed in this section that there is no parasitic inductance and capacitance in a switch. In practice, switches in a switch cell involve lots of parasitics, which play important roles in every switching, as shown in Fig. 2.16. For the turn-on process of a switch cell, as denoted by S1, both the transistor and diode

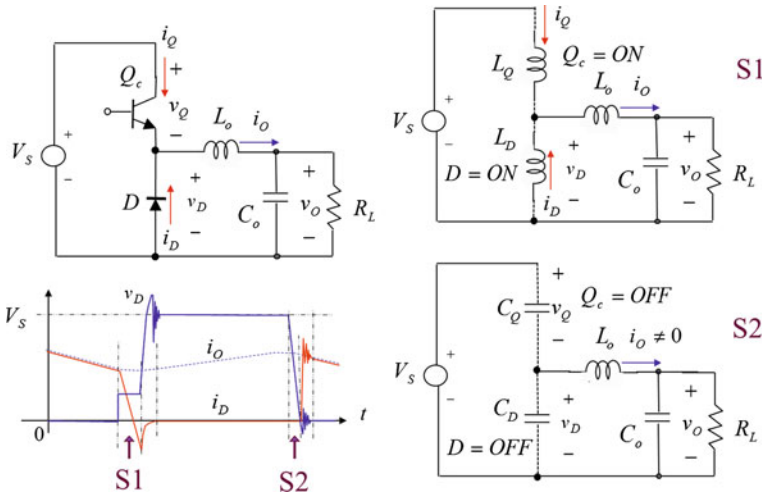

Fig. 2.16 Practical switching on/off processes, where switches involve parasitic inductances and capacitances

are turned on and a short circuit is established. The parasitic inductances of the switches L_Q and L_D then mainly determine the slope of current i_D until the reverse recovery of the diode ceases. Just after the reverse recovery process, a non-linear parasitic capacitance of the diode of a few pF gives rise to resonant ringing together with the parasitic inductances, which is typically a few MHz damping sinusoidal waveform.

Question 2

Can you try to analyze the parasitic resonant ringing phenomena?

For the turn-off process of the switch cell, as denoted by S2, both the transistor and diode are turned off and an open circuit is established. Then, the parasitic capacitances of the switches C_Q and C_D mainly determine the slope of the voltage v_D until the reverse recovery of the diode ceases. As soon as the diode is turned on, the parasitic inductance L_D gives rise to another resonant ringing together with the parasitic capacitances.

As I have explained a few aspects of a practical switching phenomenon, the switching process is never simple and easy to handle. But this switching process is quite important, perhaps the most important aspect, in the design of a switching converter because it determines the switching loss, power efficiency, and reliability of the switching converter. In particular, the switching trajectory determines the reliability of each switch because the junction temperature of a switch increases due to the switching loss. Therefore, the circuit fabrication of a switch cell should be very compact in size and length to reduce the parasitic inductances, and the selection of switches must be made considering the parasitic capacitances in order to have fast switching or less switching loss. Much more detailed analyses and measurements should be made in practice to build a long lasting reliable converter, which are left for practice.

2.2.3 Snubber Circuits Are Often Used to Improve Switching Characteristics

The reliability of switching devices in a converter is highly determined by the switching characteristics as mentioned above. One of the switching problems is the over voltage that arises from parasitic ringing, which should be mitigated or constrained. Another important switching problem is the large slope of the reverse recovery current of a diode, which results in high voltage spikes or breakdown of the main switch such as a transistor and silicon controlled rectifier (SCR). Two example snubber circuits are illustrated for an inductive load, as shown in Fig. 2.17.

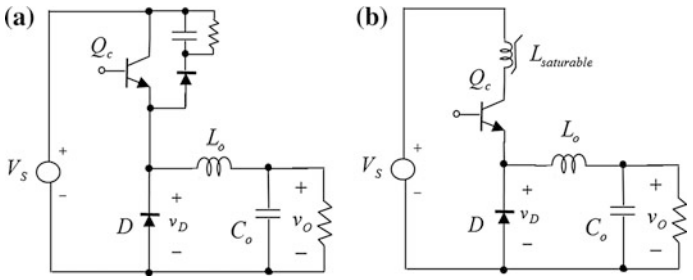

Fig. 2.17 Snubber circuits for an inductive load, protecting switches and improving switching characteristics. **a** For over voltage protection. **b** For *di*/*dt* limit

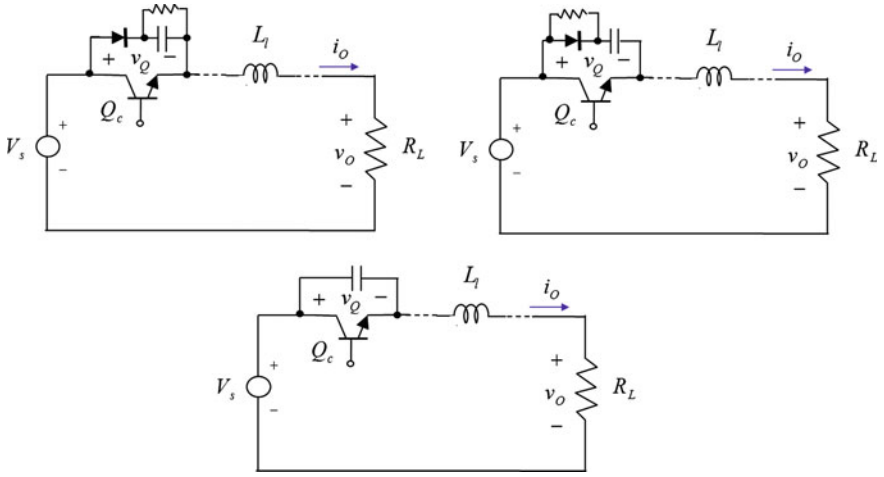

Fig. 2.18 Snubber circuits for a resistive load, protecting the switch from a stray inductance

As explained for the single switch resistor case of Fig. 2.6, the line inductance L_l may give rise to a high voltage spike when the transistor is turned off, and the snubber circuits, as shown in Fig. 2.18, can protect the switch from voltage breakdown.

Part II
Switching Converters as Electronic Transformers

In this part, a few important conventional modeling techniques are introduced, and the properties of switches as transformers are strictly proved in general and then extended to all switching converters.

Chapter 3
Conventional Models

Dealing with switches has been an important issue in power electronics since they can turn linear time-invariant systems into nonlinear time-varying systems. Simplifying or eliminating switching action is the main problem in modeling switching systems. One successful method is the state-space averaging technique. This approach was well-established for DC-DC converters by R.D. Middlebrook. Another useful model is the existence function model developed by Peter Wood, which can be applicable to the steady state analyses of AC converters (DC-AC, AC-DC, and AC-AC converters). A quite general unified approach called the discrete state equation model was proposed by J.G. Kassakian, but it is not easy to apply in practice. These conventional models are explained in this chapter, and you will see their strengths and weaknesses, which will show the need for a general unified but simple and easy model.

3.1 State Space Average Model

3.1.1 One of the Most Powerful and Simple Methods for Eliminating Time-Varying Nature of DC-DC Converters

About 40 years ago, R.D. Middlebrook developed a general unified modeling technique for DC-DC switching converters called the 'state space average model' [1, 2]. The basic idea is to take an average over the time-varying state equation of a switching converter. Let me explain using a buck converter with an ideal switching cell and LC output filter, as shown in Fig. 3.1.

Assuming that the converter is operating in the CCM, there are two operating modes of the converter, S1 and S2, which result in two LTI state equations as follows:

C.T. Rim, *Phasor Power Electronics*, KAIST Research Series,
DOI 10.1007/978-981-10-0536-7_3

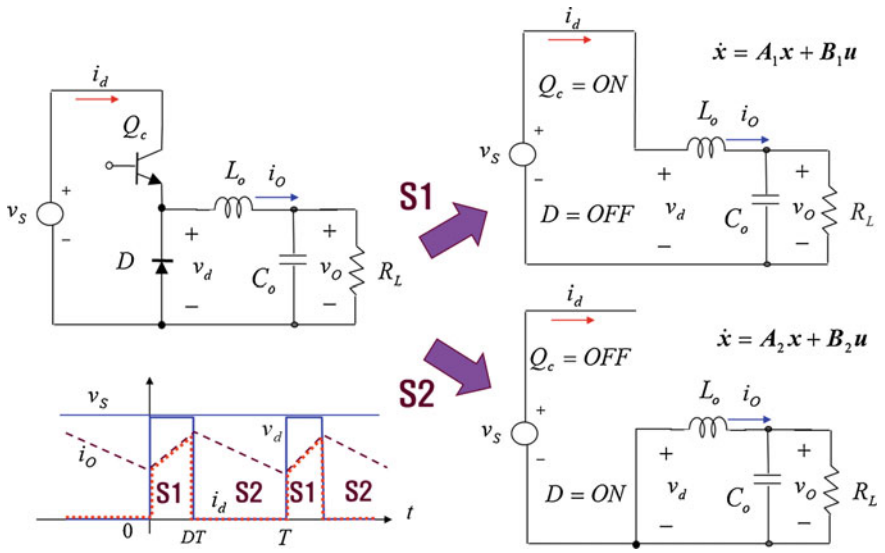

Fig. 3.1 Piecewise equivalent LTI circuits for a buck converter and their state equations

$$\dot{\boldsymbol{x}} = \boldsymbol{A}_1\boldsymbol{x} + \boldsymbol{B}_1\boldsymbol{u} \quad \text{for } kT < t < kT + d \cdot T,\ k = 0, 1, 2, \ldots : \text{S1} \tag{3.1a}$$

$$\dot{\boldsymbol{x}} = \boldsymbol{A}_2\boldsymbol{x} + \boldsymbol{B}_2\boldsymbol{u} \quad \text{for } kT + d \cdot T < t < (k+1)T,\ k = 0, 1, 2, \ldots : \text{S2}, \tag{3.1b}$$

where state $\boldsymbol{x}$, input $\boldsymbol{u}$, and linear time-invariant matrices $\boldsymbol{A}_1$, $\boldsymbol{B}_1$, $\boldsymbol{A}_2$, $\boldsymbol{B}_2$ are defined to be

$$\boldsymbol{x} \equiv \begin{Bmatrix} i_O \\ v_O \end{Bmatrix}, \boldsymbol{u} \equiv v_S, \boldsymbol{A}_1 \equiv \begin{Bmatrix} 0 & -\frac{1}{L_o} \\ \frac{1}{C_o} & -\frac{1}{C_o R_L} \end{Bmatrix}, \boldsymbol{B}_1 \equiv \begin{Bmatrix} \frac{1}{L_o} \\ 0 \end{Bmatrix}, \boldsymbol{A}_2 \equiv \begin{Bmatrix} 0 & -\frac{1}{L_o} \\ \frac{1}{C_o} & -\frac{1}{C_o R_L} \end{Bmatrix},$$
$$\boldsymbol{B}_2 \equiv \begin{Bmatrix} 0 \\ 0 \end{Bmatrix}. \tag{3.2}$$

Similar with the boost converter case of the previous part, a combined time-varying state equation is obtained as follows:

$$\begin{aligned} \dot{\boldsymbol{x}} &= (\boldsymbol{A}_1\boldsymbol{x} + \boldsymbol{B}_1\boldsymbol{u})d(t) + (\boldsymbol{A}_2\boldsymbol{x} + \boldsymbol{B}_2\boldsymbol{u})d'(t) \\ &= \boldsymbol{A}(t)\boldsymbol{x} + \boldsymbol{B}(t)\boldsymbol{u} \end{aligned}, \tag{3.3}$$

where the duty function is

$$d(t) = 1 \quad \text{for } kT < t < kT + d \cdot T,\ k = 0, 1, 2, \ldots \tag{3.4a}$$

$$d(t) = 0 \quad \text{for } kT + d \cdot T < t < (k+1)T, \quad k = 0, 1, 2, \ldots, \tag{3.4b}$$

and time-varying matrices are

$$\begin{aligned} \boldsymbol{A}(t) &\equiv \boldsymbol{A}_1 d(t) + \boldsymbol{A}_2 d'(t) \\ \boldsymbol{B}(t) &\equiv \boldsymbol{B}_1 d(t) + \boldsymbol{B}_2 d'(t) \\ d'(t) &\equiv 1 - d(t) \end{aligned} . \tag{3.5}$$

Taking an average over a period T, we can obtain another state equation, called the state space average model, as follows:

$$\begin{aligned} \dot{\bar{\boldsymbol{x}}} &\cong \overline{(\boldsymbol{A}_1 \boldsymbol{x} + \boldsymbol{B}_1 \boldsymbol{u})} D + \overline{(\boldsymbol{A}_2 \boldsymbol{x} + \boldsymbol{B}_2 \boldsymbol{u})} D' \\ &= (\boldsymbol{A}_1 D + \boldsymbol{A}_2 D')\bar{\boldsymbol{x}} + (\boldsymbol{B}_1 D + \boldsymbol{B}_2 D')\bar{\boldsymbol{u}} \\ &\equiv \boldsymbol{A}_0 \bar{\boldsymbol{x}} + \boldsymbol{B}_0 \bar{\boldsymbol{u}} \end{aligned} . \tag{3.6}$$

The averaged variables and matrices are defined as follows:

$$\begin{aligned} \bar{\boldsymbol{x}} &\equiv \tfrac{1}{T}\int_t^{t+T} \boldsymbol{x}(t)dt, \bar{\boldsymbol{u}} \equiv \tfrac{1}{T}\int_t^{t+T} \boldsymbol{u}(t)dt \\ \boldsymbol{A}_0 &\equiv \tfrac{1}{T}\int_0^{T} \boldsymbol{A}(t)dt, \boldsymbol{B}_0 \equiv \tfrac{1}{T}\int_0^{T} \boldsymbol{B}(t)dt \end{aligned} . \tag{3.7}$$

The averaged variables are drawn in Fig. 3.2 with an averaged circuit, which is reconstructed from (3.6).

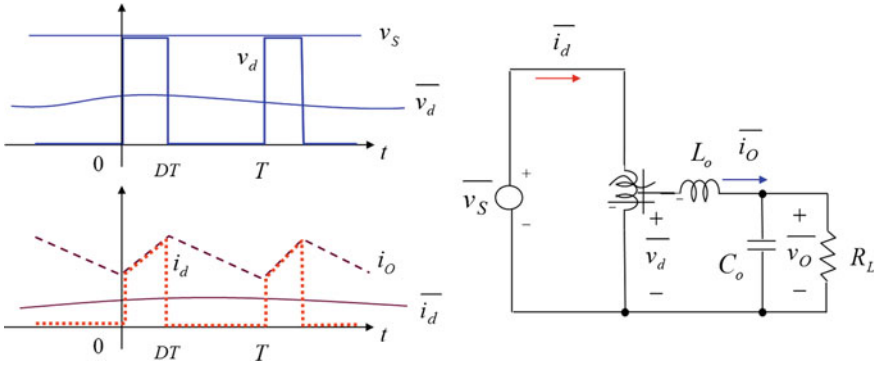

Fig. 3.2 Averaged waveforms and an averaged circuit of Fig. 3.1

3.1.2 The State Average Model Is not an Exact but Rather an Approximate Model

Note that all the variables in Fig. 3.2 are different from those in Fig. 3.1, which are correlated with each other through (3.7). In other words, there is no guarantee that the averaged circuit of Fig. 3.2 gives us the exact averaged values of the time-varying state equation of (3.3) or the original switching circuit of Fig. 3.1. Actually, the validity of the state average model of (3.6) has never been rigorously verified by R.D. Middlebrook so far as I know, even though the technique is very well known and widely used with fruitful results. It is a bold assumption that the averaged state equation of (3.6) will give arise to a correct solution of the time-varying state equation of (3.3).

As R.D. Middlebrook explained, the state space average model is an approximate model, whose conditions for exactness and mismatching errors are not fully identified. There are a few studies that describe the errors of the state average model for a specific converter.

Now let's generally identify the background theory underlying the state space averaging. The time-varying state equation of (3.3) can be expanded in Fourier series as follows:

$$\begin{aligned}\dot{\boldsymbol{x}} &= \boldsymbol{A}(t)\boldsymbol{x} + \boldsymbol{B}(t)\boldsymbol{u} \\ &= \sum_{k=-\infty}^{\infty} \boldsymbol{A}_k \mathrm{e}^{jk\omega t}\boldsymbol{x} + \sum_{k=-\infty}^{\infty} \boldsymbol{B}_k \mathrm{e}^{jk\omega t}\boldsymbol{u}\end{aligned}, \tag{3.8}$$

where the Fourier coefficient matrices are defined

$$\boldsymbol{A}_k = \frac{1}{T}\int_0^T \boldsymbol{A}(t)\mathrm{e}^{-jk\omega t}dt,\ \boldsymbol{B}_k = \frac{1}{T}\int_0^T \boldsymbol{B}(t)\mathrm{e}^{-jk\omega t}dt. \tag{3.9}$$

As identified from (3.9), the DC terms of $\boldsymbol{A}_k$ and $\boldsymbol{B}_k$ are $\boldsymbol{A}_0$ and $\boldsymbol{B}_0$ of (3.7); hence, it can be said that the state space averaging is an approximated form of the state equation expanded in Fourier series. The AC terms of $\boldsymbol{A}_k$ and $\boldsymbol{B}_k$ that correspond to the non-zero k are the source of error of the state space averaging.

If a solution of closed form is available, then the Fourier state equation of (3.8) can **be** a general unified modeling technique. A possible trial would be to put the state and input variables as follows:

$$\boldsymbol{x} = \sum_{k=-\infty}^{\infty} \boldsymbol{X}_k(t)\mathrm{e}^{jk\omega t}, \boldsymbol{u} = \sum_{k=-\infty}^{\infty} \boldsymbol{U}_k(t)\mathrm{e}^{jk\omega t}. \tag{3.10}$$

Applying (3.10) to (3.8) results in

$$\begin{aligned}\dot{\boldsymbol{x}} &= \sum_{k=-\infty}^{\infty}\left\{\dot{\boldsymbol{X}}_k(t)\mathrm{e}^{jk\omega t}+jk\omega\boldsymbol{X}_k(t)\mathrm{e}^{jk\omega t}\right\} = \sum_{k=-\infty}^{\infty}\left\{\dot{\boldsymbol{X}}_k(t)+jk\omega\boldsymbol{X}_k(t)\right\}\mathrm{e}^{jk\omega t} \\ &= \sum_{k=-\infty}^{\infty}\boldsymbol{A}_k\mathrm{e}^{jk\omega t}\sum_{k=-\infty}^{\infty}\boldsymbol{X}_k(t)\mathrm{e}^{jk\omega t}+\sum_{k=-\infty}^{\infty}\boldsymbol{B}_k\mathrm{e}^{jk\omega t}\sum_{k=-\infty}^{\infty}\boldsymbol{U}_k(t)\mathrm{e}^{jk\omega t} \\ &= \sum_{m=-\infty}^{\infty}\sum_{n=-\infty}^{\infty}\boldsymbol{A}_m\boldsymbol{X}_n(t)\mathrm{e}^{j(m+n)\omega t}+\sum_{m=-\infty}^{\infty}\sum_{n=-\infty}^{\infty}\boldsymbol{B}_m\boldsymbol{U}_n(t)\mathrm{e}^{j(m+n)\omega t}\end{aligned} \tag{3.11}$$

By equating the left term with the right term of (3.11), it is possible to obtain the k-th state equation as follows:

$$\dot{\boldsymbol{X}}_k(t)+jk\omega\boldsymbol{X}_k(t) = \sum_{m=-\infty}^{\infty}\sum_{n=-\infty}^{\infty}\left\{\boldsymbol{A}_m\boldsymbol{X}_n(t)+\boldsymbol{B}_m\boldsymbol{U}_n(t)\right\} \quad \text{for } k=m+n. \tag{3.12}$$

For the DC-DC converter case, i.e., k = 0, (3.12) becomes as follows:

$$\begin{aligned}\dot{\boldsymbol{X}}_0(t) = {} & \boldsymbol{A}_0\boldsymbol{X}_0(t)+\boldsymbol{B}_0\boldsymbol{U}_0(t)+\boldsymbol{A}_1\boldsymbol{X}_{-1}(t)+\boldsymbol{B}_1\boldsymbol{U}_{-1}(t)+\boldsymbol{A}_{-1}\boldsymbol{X}_1(t) \\ & +\boldsymbol{B}_{-1}\boldsymbol{U}_1(t)+\boldsymbol{A}_2\boldsymbol{X}_{-2}(t)+\boldsymbol{B}_2\boldsymbol{U}_{-2}(t)+\cdots.\end{aligned} \tag{3.13}$$

As is evident from (3.13) that a Fourier state equation involves an infinite number of other state variables, it is impossible to have a general solution of closed form in this way. In case the AC terms of the system matrices are negligible, (3.13) can be approximated as follows:

$$\dot{\boldsymbol{X}}_0(t) \cong \boldsymbol{A}_0\boldsymbol{X}_0(t)+\boldsymbol{B}_0\boldsymbol{U}_0(t), \tag{3.14}$$

which is of the same form of the state space averaging of (3.6).

3.1.3 The Merits and Demerits of the State Average Model

Despite the theoretical limitations of the state space averaging, the technique has been loved by power electronics engineers so far because of its straightforward way of modeling with lots of physical insight. The strengths and drawbacks of the state space average model can be summarized as follows:

- Valid for DC-DC converters only
- Useful for DC & AC analyses
- Valid for ideal switching only
- Not used for harmonic analysis

- Not a circuit oriented model
- Needs complex matrix manipulation

The DC analyses of a converter involve DC transfer gain of voltage or current, power loss, power efficiency, and power factor, whereas the AC analyses involve small signal transfer functions w.r.t. duty ratios and source voltage, etc., impedances, and frequency responses of a converter. Even though an equivalent circuit for an AC small signal is drawn from a state space average model, the state space modeling highly relies on complicated matrix manipulation to derive solutions. For instance, the state space averaged equation is resolved into the DC terms (steady state large signals) and AC terms (transient small signals) as follows:

$$\dot{\bar{\boldsymbol{x}}} \equiv \dot{\boldsymbol{X}} + \dot{\hat{\boldsymbol{x}}} = \dot{\hat{\boldsymbol{x}}} = \boldsymbol{A}_0(\boldsymbol{X} + \hat{\boldsymbol{x}}) + \boldsymbol{B}_0(\boldsymbol{U} + \hat{\boldsymbol{u}}), \tag{3.15}$$

which results in the following DC and AC solutions.

$$0 = \boldsymbol{A}_0\boldsymbol{X} + \boldsymbol{B}_0\boldsymbol{U} \quad \rightarrow \quad \boldsymbol{X} = \boldsymbol{A}_0^{-1}\boldsymbol{B}_0\boldsymbol{U}, \tag{3.16a}$$

$$\dot{\hat{\boldsymbol{x}}} = \boldsymbol{A}_0\hat{\boldsymbol{x}} + \boldsymbol{B}_0\hat{\boldsymbol{u}} \quad \rightarrow \quad \hat{\boldsymbol{X}}(s) = (s\boldsymbol{I} - \boldsymbol{A}_0)^{-1}\hat{\boldsymbol{U}}(s). \tag{3.16b}$$

As seen from (3.16a, b), complicated matrix inversions and multiplications are inevitable for the state space models, which can be hardly applicable in practice to a converter whose system order is higher than 4. Even though computer aided solutions are available for higher order systems, no physical insight can be obtained in this way.

Question 1

1. What happens to the average state equation if an LC filter is attached to the source side or load side of the circuit in Fig. 3.2?
   → A new state equation should be set up for a different circuit configuration even though we already know the state equations of both circuits. This is a quite cumbersome and tedious work in practice, whereas circuit domain work is very simple and intuitive if an equivalent LTI circuit of a converter is known.
2. Is there any general rule in the state space average model concerning circuit attachment and detachment?

3.2 Existence Function Model

Peter Wood proposed the existence function model as a general solution for a converter consisting of ideal switches and sources only, as shown in Fig. 3.3 [3]. The dependent voltage and current of the converter are determined by the existence functions and ideal sources as follows:

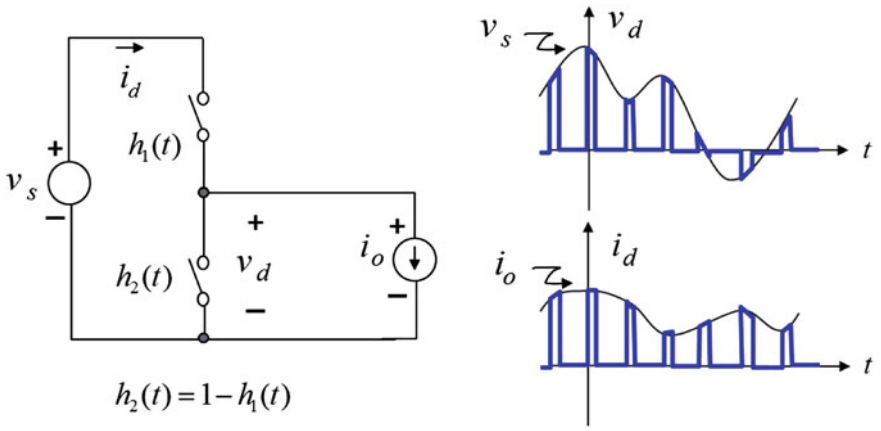

Fig. 3.3 Existence function model and its switching waveforms

$$\begin{aligned} v_d &= h_1(t)v_s \\ i_d &= h_1(t)i_o \end{aligned}. \tag{3.17}$$

In general, the dependent variables of (3.17) can be described as a special form of an output equation as follows:

$$\boldsymbol{y} = \boldsymbol{D}(t)\boldsymbol{u}. \tag{3.18}$$

Applying Fourier series expansion to (3.18) results in

$$\boldsymbol{y} = \sum_{k=-\infty}^{\infty} \boldsymbol{D}_k \mathrm{e}^{jk\omega t} \sum_{k=-\infty}^{\infty} \boldsymbol{U}_k \mathrm{e}^{jk\omega t} = \sum_{m=-\infty}^{\infty} \sum_{n=-\infty}^{\infty} \boldsymbol{D}_m \boldsymbol{U}_n \mathrm{e}^{j(m+n)\omega t}. \tag{3.19}$$

Note from (3.19) that the coefficient matrices are no longer time-varying because the existence function model does not deal with the transient response of a switching converter. The phasor of the k-th frequency component can be determined once the source variables and existence functions are given. Different from the Fourier state equation of (3.12), the existence function model of (3.19) gives us a straightforward solution.

The merits and demerits of the existence function model can be summarized as follows:

- Generally applicable to DC converters (DC-DC) and AC converters (DC-AC, AC-DC, AC-AC)
- Useful for DC analyses only
- Useful for harmonic analysis
- Valid for ideal switching and linear switching cases (CCM) only
- Not a circuit oriented model

3.3 Discrete State Equation Model

I would like to introduce one more general unified model, which was believed to be so general that it can solve most time-varying switching converter problems. The time-varying state equation of (3.3) is composed of several LTI state equations; hence, a consecutive application of the LTI state equations may result in a closed form time-invariant discrete state equation that leads to a general solution [4, 5]. Assume that the switching converter is described by n consecutive LTI state equations as follows:

$$\begin{aligned}\dot{\boldsymbol{x}} &= \boldsymbol{A}(t)\boldsymbol{x} + \boldsymbol{B}(t)\boldsymbol{u} \\ &= \sum_{m=1}^{n} \boldsymbol{A}_m d_m(t)\boldsymbol{x} + \sum_{m=1}^{n} \boldsymbol{B}_m d_m(t)\boldsymbol{u}\end{aligned}, \tag{3.20}$$

where $\boldsymbol{A}_m$ and $\boldsymbol{B}_m$ are the LTI system matrices, and $d_m(t)$ is the m-th duty ratio function in a period that becomes 1 for its period and 0 for others. For example, the boost-converter operating in the DCM, as depicted in (3.12) of Ch. 1, has three LTI matrices as follows:

$$\begin{aligned}\boldsymbol{A}(t) &\equiv \boldsymbol{A}_1 d_1(t) + \boldsymbol{A}_2 d_2(t) + \boldsymbol{A}_3 d_3(t) \\ \boldsymbol{B}(t) &\equiv \boldsymbol{B}_1 d_1(t) + \boldsymbol{B}_2 d_2(t) + \boldsymbol{B}_3 d_3(t)\end{aligned}. \tag{3.21}$$

The state values for the example of (3.21) at the end time of each duty function of a period T can be found as follows:

$$\begin{aligned}\boldsymbol{x}_1 &= e^{\boldsymbol{A}_1 d_1 T}\boldsymbol{x}_0 + \int_0^{d_1 T} \boldsymbol{B}_1 \boldsymbol{u}(t)\mathrm{d}t \\ \boldsymbol{x}_2 &= e^{\boldsymbol{A}_2 d_2 T}\boldsymbol{x}_1 + \int_{d_1 T}^{(d_1+d_2)T} \boldsymbol{B}_2 \boldsymbol{u}(t)\mathrm{d}t \\ \boldsymbol{x}_3 &= e^{\boldsymbol{A}_3 d_3 T}\boldsymbol{x}_2 + \int_{(d_1+d_2)T}^{(d_1+d_2+d_3)T} \boldsymbol{B}_3 \boldsymbol{u}(t)\mathrm{d}t\end{aligned}, \tag{3.22}$$

which can be rewritten as

$$\begin{aligned}\boldsymbol{x}_3 &= e^{\boldsymbol{A}_3 d_3 T}\left\{e^{\boldsymbol{A}_2 d_2 T}\boldsymbol{x}_1 + \int_{d_1 T}^{(d_1+d_2)T} \boldsymbol{B}_2 \boldsymbol{u}(t)\mathrm{d}t\right\} + \int_{(d_1+d_2)T}^{(d_1+d_2+d_3)T} \boldsymbol{B}_3 \boldsymbol{u}(t)\mathrm{d}t \\ &= e^{(\boldsymbol{A}_2 d_2 + \boldsymbol{A}_3 d_3)T}\boldsymbol{x}_1 + e^{\boldsymbol{A}_3 d_3 T}\int_{d_1 T}^{(d_1+d_2)T} \boldsymbol{B}_2 \boldsymbol{u}(t)\mathrm{d}t + \int_{(d_1+d_2)T}^{(d_1+d_2+d_3)T} \boldsymbol{B}_3 \boldsymbol{u}(t)\mathrm{d}t \\ &= e^{(\boldsymbol{A}_2 d_2 + \boldsymbol{A}_3 d_3)T}\left\{e^{\boldsymbol{A}_1 d_1 T}\boldsymbol{x}_0 + \int_0^{d_1 T} \boldsymbol{B}_1 \boldsymbol{u}(t)\mathrm{d}t\right\} + e^{\boldsymbol{A}_3 d_3 T}\int_{d_1 T}^{(d_1+d_2)T} \boldsymbol{B}_2 \boldsymbol{u}(t)dt + \int_{(d_1+d_2)T}^{(d_1+d_2+d_3)T} \boldsymbol{B}_3 \boldsymbol{u}(t)\mathrm{d}t \\ &= e^{(\boldsymbol{A}_1 d_1 + \boldsymbol{A}_2 d_2 + \boldsymbol{A}_3 d_3)T}\boldsymbol{x}_0 + e^{(\boldsymbol{A}_2 d_2 + \boldsymbol{A}_3 d_3)T}\int_0^{d_1 T} \boldsymbol{B}_1 \boldsymbol{u}(t)\mathrm{d}t + e^{\boldsymbol{A}_3 d_3 T}\int_{d_1 T}^{(d_1+d_2)T} \boldsymbol{B}_2 \boldsymbol{u}(t)\mathrm{d}t + \int_{(d_1+d_2)T}^{(d_1+d_2+d_3)T} \boldsymbol{B}_3 \boldsymbol{u}(t)\mathrm{d}t \\ &\equiv \boldsymbol{A}_d \boldsymbol{x}_0 + \boldsymbol{w}_0\end{aligned}. \tag{3.23}$$

For simplicity, two LTI matrices are introduced in (3.23), which are valid for a period as follows:

$$\begin{aligned}\boldsymbol{A}_d &= e^{(\boldsymbol{A}_1 d_1 + \boldsymbol{A}_2 d_2 + \boldsymbol{A}_3 d_3)T} \\ \boldsymbol{w}_0 &= e^{(\boldsymbol{A}_2 d_2 + \boldsymbol{A}_3 d_3)T} \int_0^{d_1 T} \boldsymbol{B}_1 \boldsymbol{u}(t)dt + e^{\boldsymbol{A}_3 d_3 T} \int_{d_1 T}^{(d_1+d_2)T} \boldsymbol{B}_2 \boldsymbol{u}(t)dt \\ &\quad + \int_{(d_1+d_2)T}^{(d_1+d_2+d_3)T} \boldsymbol{B}_3 \boldsymbol{u}(t)dt\end{aligned} . \tag{3.24}$$

In general, the nth state value of the kth period becomes the first state value of the $(k+1)$th period; hence, we can obtain the following discrete state equation.

$$\boldsymbol{x}(k+1) = \boldsymbol{x}_m = \boldsymbol{A}_d \boldsymbol{x}(k) + \boldsymbol{w}(k), \tag{3.25}$$

where

$$\begin{aligned}\boldsymbol{A}_d &= e^{\sum_{m=1}^{n} \boldsymbol{A}_m d_m T} \\ \boldsymbol{w}_0 &= e^{\sum_{m=2}^{n} \boldsymbol{A}_m d_m T} \int_0^{d_1 T} \boldsymbol{B}_1 \boldsymbol{u}(t)dt + e^{\sum_{m=3}^{n} \boldsymbol{A}_m d_m T} \int_{d_1 T}^{(d_1+d_2)T} \boldsymbol{B}_2 \boldsymbol{u}(t)dt + \cdots \\ &\quad + \int_{(1-d_n)T}^{T} \boldsymbol{B}_n \boldsymbol{u}(t)dt\end{aligned} . \tag{3.26}$$

It is a formidable work to obtain matrices (3.24) or (3.26) even for a second order system. It seems to be ideal that the discrete equation of (3.25) is LTI and generally applicable to any converter including nonlinear DCM converters. It is difficult to find good applications of this model though, which implies that a model should not only be general unified but also easy to use. The strengths and drawbacks of the discrete state equation model can be summarized as follows:

- Generally applicable to any DC and AC converters
- Valid even for the nonlinear DCM
- Not simple even for DC analyses
- Not applicable to harmonic analysis
- Not a circuit oriented model

Question 2

1. What do you think is the most important aspect in power circuit models among general, unified, and easy?
2. Why are piecewise-LTI-equation-based models still frequently used in power electronics?

→ There should be some advantages in the equation-based models because people are quite accustomed to setting up circuit equations by themselves and the deduction process is traceable step by step. However, it is often impossible to get the time-domain response from the equation. I very often see cases where people apply the Laplace transform to the circuit equation they derived and try to plot in the frequency domain, which is totally incorrect to get the right response. A time-varying system cannot be dealt with in such a way, which is the reason why the models in power electronics should show an equivalent LTI model at the end.

References

1. Middlebrook RD, Cuk S (1976) A general unified approach to modeling switching converter stages. In: IEEE power electronics specialists conference record, pp 18–34
2. Middlebrook RD (1987) Topics in multi-loop regulators and current-mode programming. IEEE Trans Power Electron PE-2(2):109–124
3. Wood P (1979) General theory of switching power converters. In: IEEE power electronics specialists conference record, pp. 3–10
4. Verghese GC, Elbuluk ME, Kassakian JG (1986) A general approach to sampled-data modeling for power electronic circuits. IEEE Trans Power Electron PE-1(2):76–89
5. Verghese G, Mukherji U (1981) Extended averaging and control procedures, In: IEEE power electronics specialists conference record, pp 329–336

Chapter 4
Switched Transformer Model

It would be frustrating for readers that there are not appropriate conventional modeling techniques in power electronics which have the following requirements at the same time:

- Generally applicable to any DC and AC converters
- Unified approach for various converter types
- Valid at least for CCM and for DCM if possible
- Applicable to DC and AC analyses
- Applicable to harmonic analysis
- Exact but can be approximated if necessary
- Available for practical switches with finite switching times and parasitics
- Circuit oriented easy model with lots of physical insight

In this chapter, a strong candidate modeling technique that can meet most of the above requirements is suggested. A lot of this chapter is based on the original paper written by myself [1].

4.1 Introduction to Switched Transformer Models

This switched transformer model is solely conceived by myself since I was a PhD student after thorough reviewing previously developed power electronics modeling techniques [2–11].

4.1.1 A Switch Set in the DC-DC Converter Is a Switched Autotransformer

The fact that the switches in the pulse width modulated (PWM) DC-DC converters are equivalent to transformers is not a news and found in a few papers [7, 9, 10];

C.T. Rim, *Phasor Power Electronics*, KAIST Research Series,
DOI 10.1007/978-981-10-0536-7_4

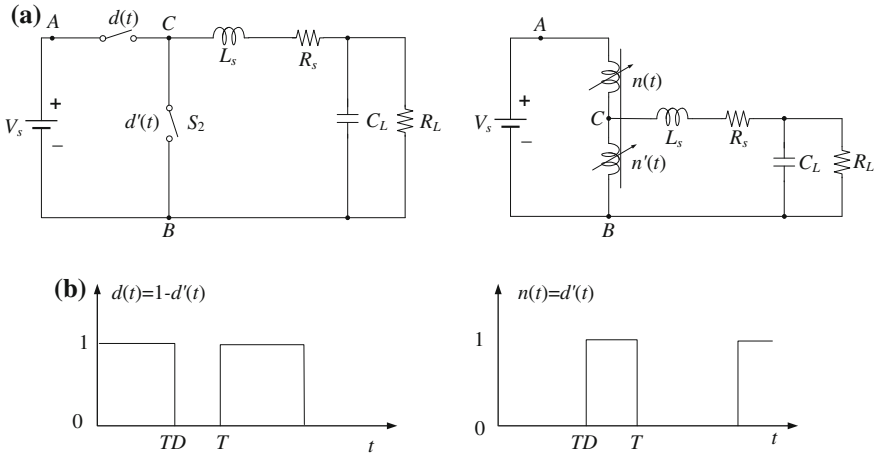

Fig. 4.1 Buck converter example for switched transformers. **a** Original circuit. **b** Switched transformers (A switch set is not an approximated but exact equivalent circuit for a switched transformer.)

however, the equivalence is valid for only the averaged circuit, as explained in the previous chapters. It will be shown here that an ideal switch set is exactly equivalent to a time-varying ideal transformer, as shown in Fig. 4.1.

As an illustrative example, the buck converter shown in Fig. 4.1a is selected, where the two dual switches constitute a switch set. The proof that this switch set is equivalent to the switched transformers, as shown in Fig. 4.1b, can be done as follows.

When the switch S_1 is turned on (that is, $d(t) = 1$) and S_2 is turned off (that is, $d'(t) = 0$), let the upper turn-ratio of the transformer be zero, (that is, $n(t) = 0$) and the lower turn-ratio of the transformer be unity, (that is, $n'(t) = 1$); then, the configurations of the two circuits become identical because the points A and C are connected, and the points B and C are disconnected. Since the inductance of an ideal transformer is infinite, the points B and C are completely disconnected in terms of electric circuit. When S_1 is turned off and S_2 is turned on, the lower turn-ratio is set to zero whereas the upper one is set to unity. The circuit configurations are also the same. So it can be concluded that the switch set is exactly equivalent to the switched transformers whose turn-ratio is defined to be the dual value of the duty ratio of the switch set as follows:

$$n(t) = 1 - d(t) \tag{4.1}$$

In Fig. 4.1, each switch is replaced with its own switched transformer whose turn-ratio is the dual value of the existence function of the switch. At first, it is not easy for readers to accept the fact that the turn-ratio of a transformer can be abruptly

changed, as shown in Fig. 4.1. But you will see that there is no restriction on the turn-ratio of the ideal transformer in the circuit theory. Because a transformer is completely different from an inductor, abrupt change of the turn-ratio as well as discontinuously varying switching voltage and current is allowed for an ideal transformer, which is forbidden for an inductor.

A slight different equivalent circuit for a switch set is the switched autotransformer, where two complementary switched transformers of Fig. 4.1 are combined together into one, as shown in Fig. 4.2.

The dependent voltage and current of Fig. 4.2a are exactly the same as that of Fig. 4.2b, which is an ideal autotransformer, as follows:

$$\begin{aligned} v_d &= v_s h_1(t) \\ i_d &= i_L h_1(t) \end{aligned} . \tag{4.2}$$

Comparing Fig. 4.2 to Fig. 4.1, the switched autotransformer model is found to be exactly equivalent to the complementary switched transformers. Even though the model of Fig. 4.1 is more general, the autotransformer model of Fig. 4.2 is more convenient and will be used in the subsequent steps.

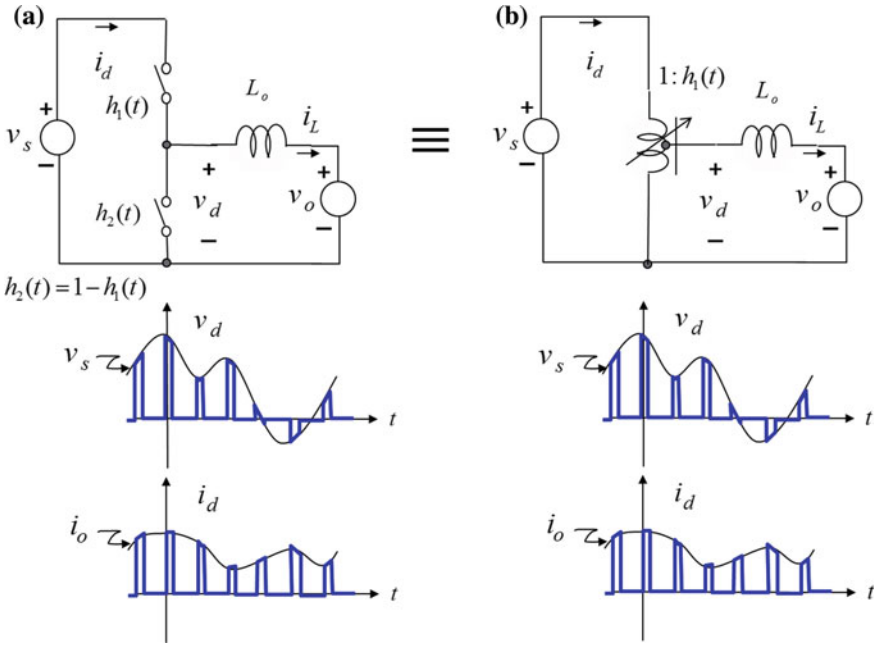

Fig. 4.2 Another buck converter example for a switched autotransformer. **a** Original circuit. **b** Switched autotransformer circuit (The switched autotransformer circuit is equivalent to a switch set regardless of switching patters.)

Question 1

1. Is it really no problem if a pulsating current flows into the ideal transformer in Figs. 4.1b and 4.2b?
   → As identified from (4.2), the current i_d becomes pulsating if the turn-ratio $h_1(t)$ is pulsating. Because there is no inductance in an ideal transformer, even an infinitely large current may flow into the transformer, which is not allowed for an inductor. The physical formation and notation of a transformer looks like two coupled inductors, which makes the power electronics beginner get confused a lot. Please spend enough time to distinguish a transformer from inductors.
2. What is the equivalent circuit of each power switch instead of a set of switches?
   → It is an auto-transformer whose output is grounded to one side and the turn-ratio is the same as the existence function. This idea was suggested by Prof. David Perreault at MIT when I delivered my lecture on the phasor transformation in 2014.

4.1.2 A Switched Transformer Can Be Decomposed to an Ordinary Transformer and Harmonic Sources

The switched autotransformer, also referred more frequently as 'switched transformer', is not an approximated but an exact model for an ideal switch set; however, it is inconvenient in practice because of its time-varying nature. As shown in Fig. 4.3, this switching characteristic of the switched transformer can be removed as follows:

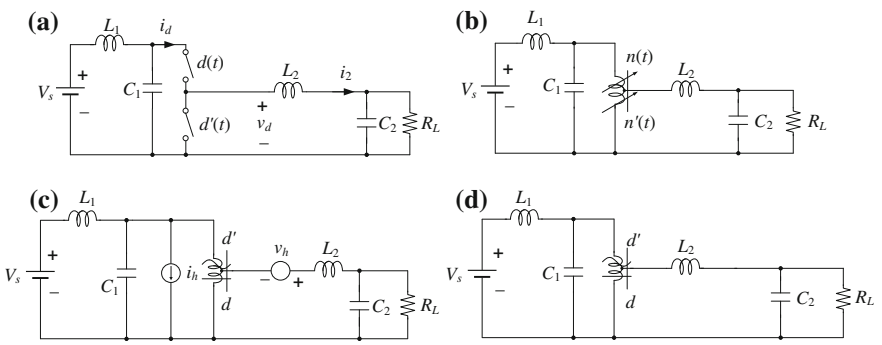

Fig. 4.3 A buck converter with input and output filters, showing harmonic source models. **a** Original circuit. **b** Switched transformer circuit. **c** An equivalent circuit with harmonic sources. **d** Filtered harmonic circuit (The switched transformer model is powerful when it is used in a practical converter with high order filters.)

$$\begin{aligned} v_d &= v_s h_1(t) \equiv v_s\{h_1 + h_h(t)\} = v_s h_1 + v_h \quad \because v_h \equiv v_s h_h(t) \\ i_d &= i_2 h_1(t) \equiv i_2\{h_1 + h_h(t)\} = i_2 h_1 + i_h \quad \because i_h \equiv i_2 h_h(t) \end{aligned} \tag{4.3}$$

In (4.3), h_1 is the average value of the existence function over a period and the dependent variables are decomposed to non-switching terms and harmonic source terms. This equation can be drawn, as shown in Fig. 4.3c, which includes an ordinary autotransformer and harmonic voltage and current sources. Note that there is no approximation in (4.3) and Fig. 4.3c; therefore, they are exactly equivalent to the original circuit of Fig. 4.3a. The harmonic analysis can be done using Fig. 4.3c since the harmonic sources can be calculated from (4.3) and the filtered harmonics can be obtained from the frequency response of the input and output filters just like an ordinary circuit analysis.

The next step is to find an averaged circuit. If the switching frequency is much higher than the cutoff frequencies of the input and output filters, the switched transformer can be simply substituted with the averaged ideal transformer whose turn-ratio is the average of $n(t)$ of Fig. 4.3c, since the switching harmonics are negligible compared to the fundamental components. Finally, the DC model is obtained by eliminating the reactive elements, as shown in Fig. 4.1d. The analysis is straightforward; hence, no additional equation is required.

4.1.3 *DC Analyses of DC Converters Become Possible Without Using Any Equations*

Using the equivalent circuits of the switched transformer, the analyses of a DC-DC converter can be straightforwardly done with the circuit drawing only, as shown in Figs. 4.4, 4.5, 4.6, 4.7, 4.8, and 4.9. The DC model of a buck converter, operating in the steady state, is obtained by eliminating the reactive elements, as shown in Fig. 4.4. The DC voltage gain as well as the average voltages and currents of input and output can be determined with no additional equation.

The procedures for the boost, buck-boost, Cuk, Zeta, and single-ended primary-inductor converter (SEPIC) converters are the same as that already discussed, and thus the resultant equivalent circuits are drawn as in Figs. 4.5, 4.6, 4.7, 4.8, and 4.9, respectively. Clearly, these equivalent transformers turn the complex converter problems into simple RLC circuits including an ordinary transformer.

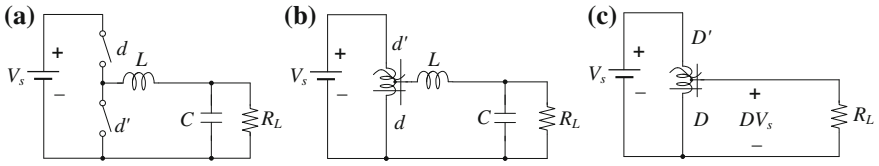

Fig. 4.4 Buck converter example. **a** Original circuit. **b** Averaged circuit. **c** DC circuit

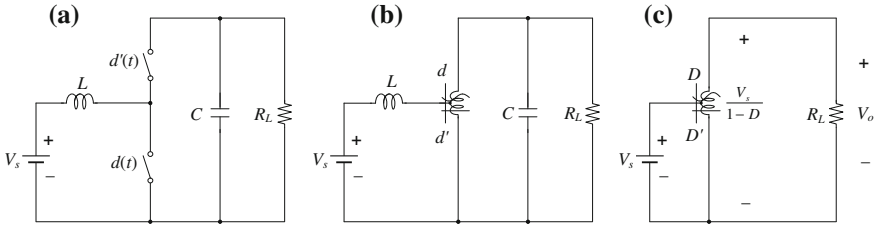

Fig. 4.5 Boost converter example. **a** Original circuit. **b** Averaged circuit. **c** DC circuit (The reason why the output voltage of a boost converter is always boosted up is explained by an autotransformer.)

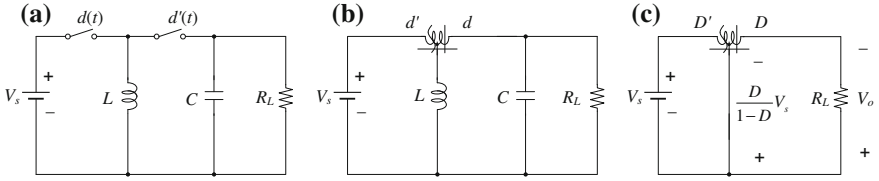

Fig. 4.6 Buck-boost converter. **a** Original circuit. **b** Averaged circuit. **c** DC circuit

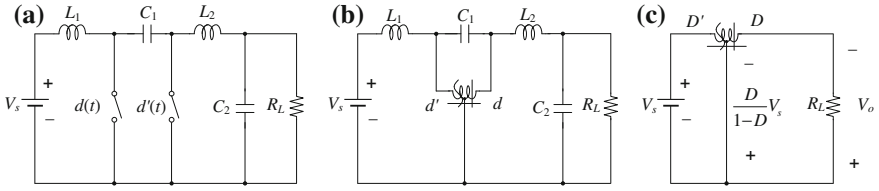

Fig. 4.7 Cuk converter. **a** Original circuit. **b** Averaged circuit. **c** DC circuit (The analysis of a Cuk converter becomes straightforward when the switched transformer model is adopted.)

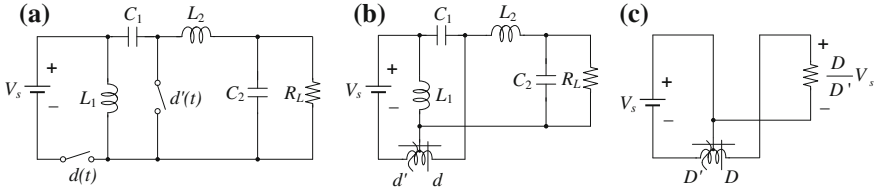

Fig. 4.8 Zeta converter. **a** Original circuit. **b** Averaged circuit. **c** DC circuit

As identified from Figs. 4.4, 4.5, 4.6, 4.7, 4.8, and 4.9, the switch cell in the six basic DC-DC converters plays the same role as an 'electronic transformer'. This is a really good unified approach that apparently different DC converters are inherently all the same each other, and the only difference is the location and configuration of input and output filters.

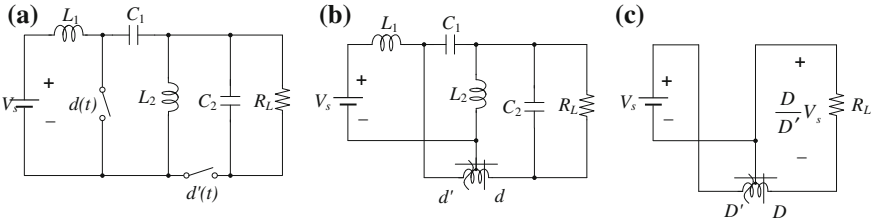

Fig. 4.9 SEPIC converter. **a** Original circuit. **b** Averaged circuit. **c** DC circuit

Practical DC converters often have isolation transformers, which are conventional mechanical transformers, as shown in Fig. 4.10. These converters can be appropriately related with basic circuits; therefore, it is not necessary to analyze these converters with isolation transformers separated from the basic converters.

4.1.4 *Switches in the DC-AC (or AC-DC) Converters Are also Equivalent to Switched Transformers*

It is no longer surprising that the equivalent circuits for the switches in inverters or rectifiers are time-varying transformers. The equivalence of the two circuits can be proved by showing that the external characteristics of both circuits are identical, as done for the DC converters. It is assumed, from now on, that all switches and sources are ideal and balanced, the switches are in the CCM, and switching harmonics are negligible unless otherwise specified. Remember that the electronic transformers as the equivalent circuits of switches are still time-varying.

The dependent voltage and current of the switch sets of Fig. 4.11a are as follows:

$$\begin{aligned} i_s &= i_a d_1 + i_b d_2 + i_c d_3 \\ v_1 &= V_s d_1 \\ v_2 &= V_s d_2 \\ v_3 &= V_s d_3, \end{aligned} \tag{4.4}$$

and those of Fig. 4.11b are

$$\begin{aligned} i_s^* &= i_a d_1 + i_b d_2 + i_c d_3 \\ v_1^* &= V_s d_1 \\ v_2^* &= V_s d_2 \\ v_3^* &= V_s d_3. \end{aligned} \tag{4.5}$$

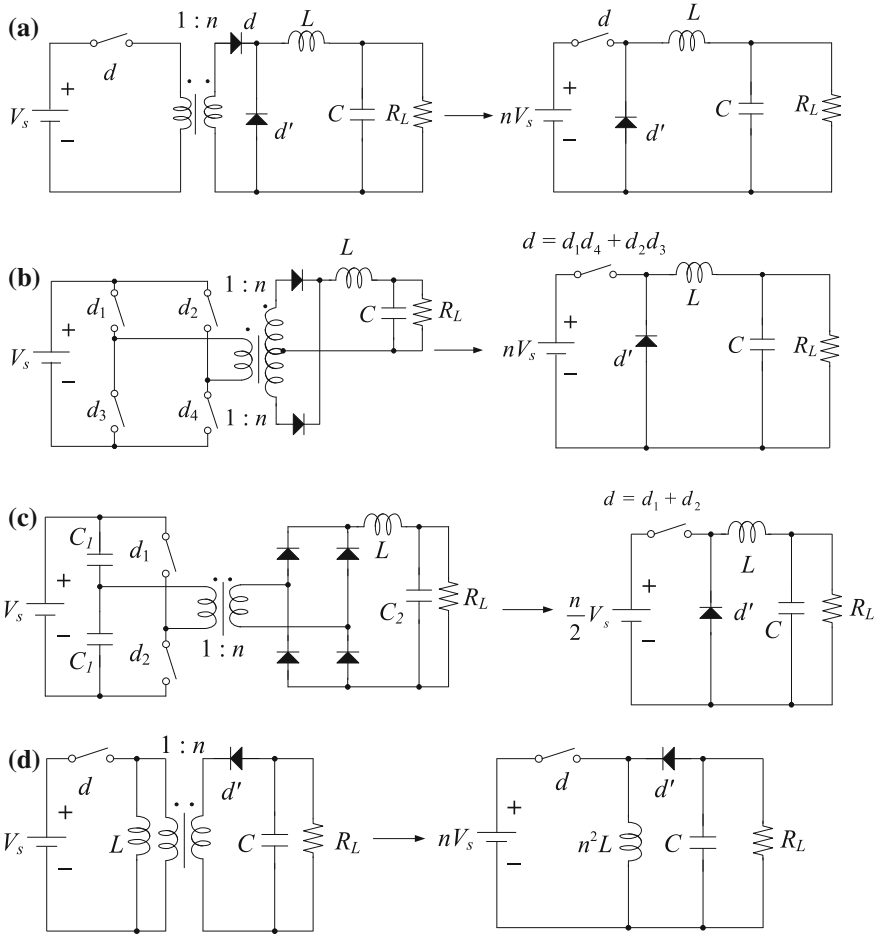

Fig. 4.10 DC converters with an isolation transformer. The *left* circuits are original converters and the *right* circuits are their corresponding basic converters. **a** Forward converter. **b** Push-pull converter. **c** Half-bridge converter. **d** Fly-back converter

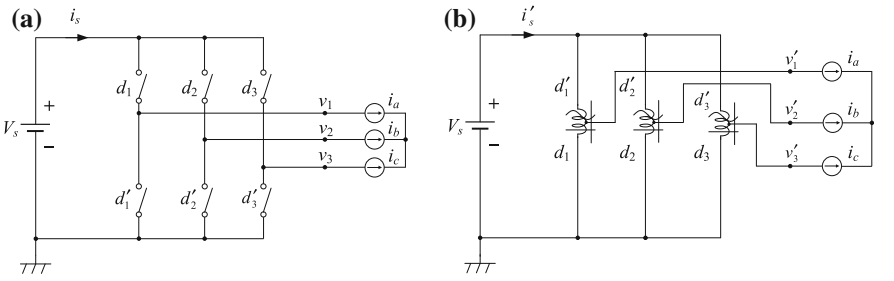

Fig. 4.11 Switches as transformers of VSI. **a** Switching circuit. **b** Transformer circuit

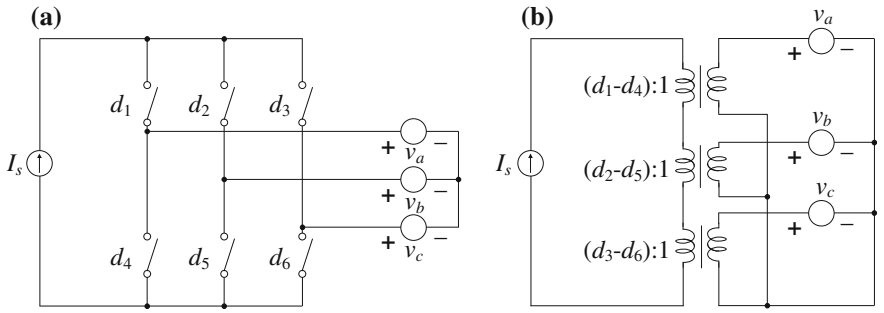

Fig. 4.12 Switches as transformers of CSI. **a** Switching circuit. **b** Transformer circuit

By comparing (4.4) and (4.5), it is found that

$$\begin{aligned} i_s^* &= i_s \\ v_1^* &= v_1 \\ v_2^* &= v_2 \\ v_3^* &= v_{3,} \end{aligned} \tag{4.6}$$

which implies that the two circuits are equivalent so far as the turn-ratios of the transformers are the dual values of the duty functions of corresponding switches. Note that the equivalence is valid not only for the switched transformer but also for the averaged transformer since (4.4)–(4.6) are true for both cases. In a similar procedure, the equivalent circuit for a current-source inverter (CSI) is obtained, as shown in Fig. 4.12.

4.1.5 *Even the Switches in AC-AC Converters Are Equivalent to Electronic Transformers*

A general switching system, which includes an AC-AC converter, is shown in Fig. 4.13a which has m inputs and n outputs. The expected equivalent transformer circuit is depicted in Fig. 4.13b. Then the proof is straightforward as follows. Applying the following relationships to both circuits, it is easily verified that they satisfy the relationships simultaneously:

$$\begin{aligned} \boldsymbol{V}' &= \boldsymbol{D}^{\boldsymbol{T}}\boldsymbol{V} \\ \boldsymbol{I} &= \boldsymbol{D}\boldsymbol{I}', \end{aligned} \tag{4.7}$$

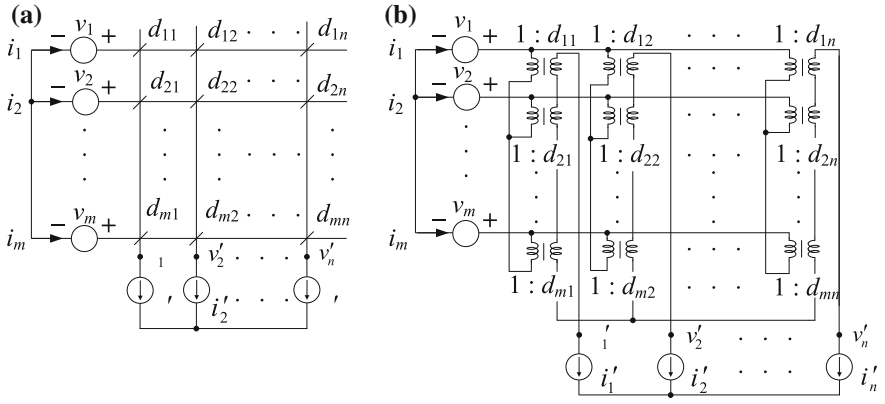

Fig. 4.13 General switches as transformers. **a** General switching system. **b** General time-varying transformer

where

$$\begin{aligned} \boldsymbol{V} &= [v_k]_{m\times 1} \\ \boldsymbol{V}' &= [v'_k]_{n\times 1} \\ \boldsymbol{I} &= [i_k]_{m\times 1} \\ \boldsymbol{I}' &= [i'_k]_{n\times 1} \\ \boldsymbol{D} &= [D_{jk}]_{m\times n} \end{aligned} \tag{4.8}$$

This means that the circuits are equivalent if only the turn-ratios are defined to be the dual values of the duty ratios of the switches. The averaged duty ratio D is the fundamental component of the original switching duty ratio $d(t)$, however, the proof is also valid for the case of $d(t)$ as previously discussed.

4.2 AC Analyses and Harmonic Analyses

4.2.1 A Perturbed Electronic Transformer Makes It Possible to Get the AC Analyses

The AC analyses of a DC converter can be done by perturbing the electronic transformer, which is nonlinear w.r.t. the duty ratio, as shown in Fig. 4.14. The dependent variables of the switch cell can be determined as follows:

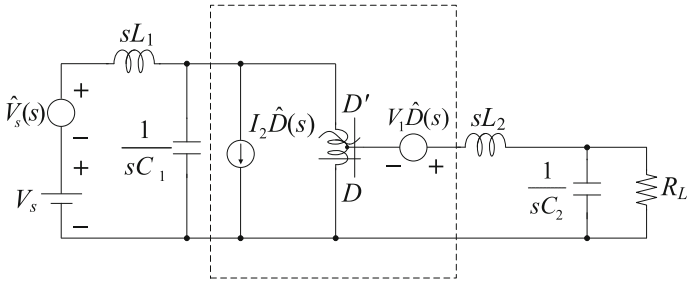

Fig. 4.14 Perturbed buck converter with input and output filters

$$\begin{aligned} v_d &= v_1 d = (V_1 + \hat{v}_1)(D + \hat{d}) = (V_1 + \hat{v}_1)D + V_1\hat{d} + \hat{v}_1\hat{d} \cong (V_1 + \hat{v}_1)D + V_1\hat{d} = v_1 + V_1\hat{d} \\ i_d &= i_2 d = (I_2 + \hat{i}_2)(D + \hat{d}) = (I_2 + \hat{i}_2)D + I_2\hat{d} + \hat{i}_2\hat{d} \cong (I_2 + \hat{i}_2)D + I_2\hat{d} = i_2 + I_2\hat{d} \end{aligned} \tag{4.9}$$

The multiplication of two perturbed terms are omitted from (4.9) because they are very small when the perturbations are small enough.

The circuit reconstruction of (4.9) is done with a transformer of a constant turn-ratio and two voltage and current sources, whose magnitudes are determined by the DC operating conditions.

Removing all the DC variables and the autotransformer from Fig. 4.14, an equivalent AC circuit is obtained, as shown in Fig. 4.15.

The dynamic transfer functions of Fig. 4.15 can be found by a circuit analysis, which requires quite few equations, as follows:

$$\begin{aligned} G_v(s) &= \frac{\hat{V}_o(s)}{\hat{V}_s(s)} = \frac{Z_2 // (Z_3 + Z_4) Z_4 D}{[Z_1 + Z_2 // (Z_3 + Z_4)](Z_3 + Z_4)} \\ G_d(s) &= \frac{\hat{V}_o(s)}{\hat{D}(s)} = \frac{Z_4 V_1}{Z_1 // Z_2 + Z_3 + Z_4} - \frac{Z_1 // Z_2 // (Z_3 + Z_4) Z_4 D I_2}{Z_3 + Z_4} \end{aligned}$$

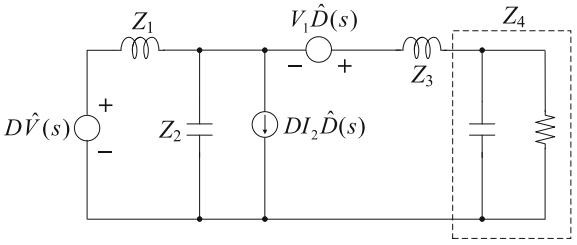

Fig. 4.15 AC equivalent circuit for AC analyses excluding the autotransformer

$$\begin{aligned} Z_1 &= sD^2L_1 \\ Z_2 &= \frac{D^2}{sC_1} \\ Z_3 &= sL_2 \\ Z_4 &= \frac{1}{sC_2} // R_L \end{aligned} \tag{4.10}$$

4.2.2 The Harmonic Analysis Model Is the Same as the AC Perturbed Circuit

It is interesting that the harmonic analysis circuit is the same as the AC perturbed circuit, as shown in Fig. 4.16. The only difference is the values of the sources.

So far the AC analyses and harmonic analysis are shown for DC converters, however, the same procedures and methods can be extended to AC converters, which will be possible together with phasor transformations.

4.2.3 The Switched Transformer Model Can Be Applicable Even to Nonlinear Switching Converters

The fact that the switched transformer model can be applicable to the nonlinear converter in the DCM has not been explained yet. Let me explain now about the extended switched transformer model for a switch cell operating in DCM, as shown in Fig. 4.17. As the inductor current becomes zero, i.e., DCM, the dependent voltage v_d is the same as the output voltage v_o. As shown in Fig. 4.17c, v_d can be decomposed to the transformer secondary voltage v_{d1} and the nonlinear voltage source of v_{d2} as follows:

$$v_d = v_{d1} + v_{d2} \quad \because v_{d1} = h_1 v_s, \quad v_{d2} = \bar{h}_1 \bar{h}_2 v_o. \tag{4.11}$$

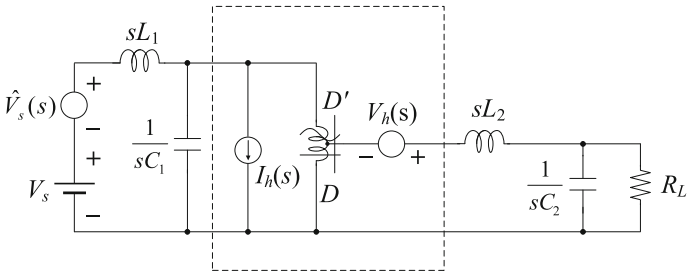

Fig. 4.16 Harmonic analysis circuit, which is the same as the AC equivalent circuit

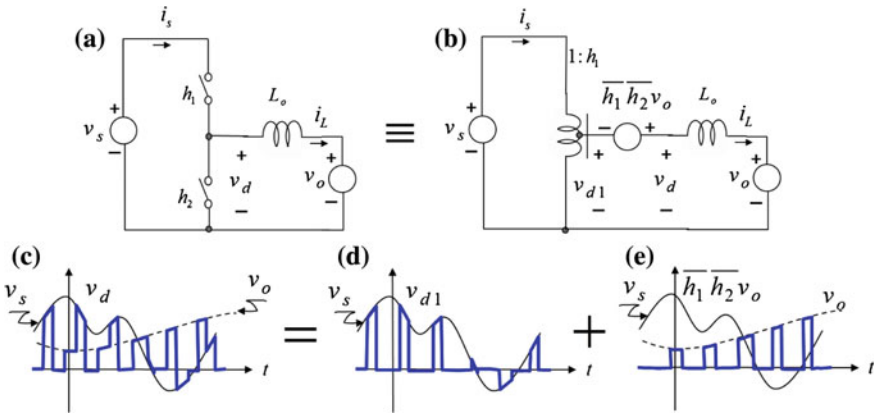

Fig. 4.17 An extended switched transformer model for a switch cell operating in DCM. **a** A switch cell with DCM. **b** Its equivalent transformer model with a nonlinear voltage source. **c** Decomposition of the dependent voltage into the transformer voltage and the nonlinear voltage source

Note from (4.11) that v_{d1} is the same as the secondary voltage of the switched transformer while v_{d2} includes the existence function of h_2, which is controlled by the inductor current. Therefore, the equivalent circuit for a switch cell with DCM is the combination of a linear switching transformer and a nonlinear voltage source, as shown in Fig. 4.17b. In this way, the switched transformer model can be extended to the nonlinear switching DCM case, which can be of course further extended to nonlinear AC converters. This work is left for the proactive readers.

4.2.4 *The Switched Transformer Model Can Be Applicable Even to the Case of Finite Switching Times*

The switched transformer model can be also applicable to the practical switches with finite switching times, as shown in Fig. 4.18.

As shown in Figs. 4.18b, e, the switching function of current d_i is not necessarily the same as the switching function of voltage d_v as follows:

$$i_Q = d_i i_O, \quad v_d = d_v V_s. \tag{4.12}$$

In (4.12), the switching functions d_i and d_v could be either switching waveform or its average one, which is used now. It is necessary to notice that the equivalent switched transformer for the finite switching times has imbalanced dependent turn-ratios between the primary current source and the secondary voltage source, as shown in Fig. 4.18c.

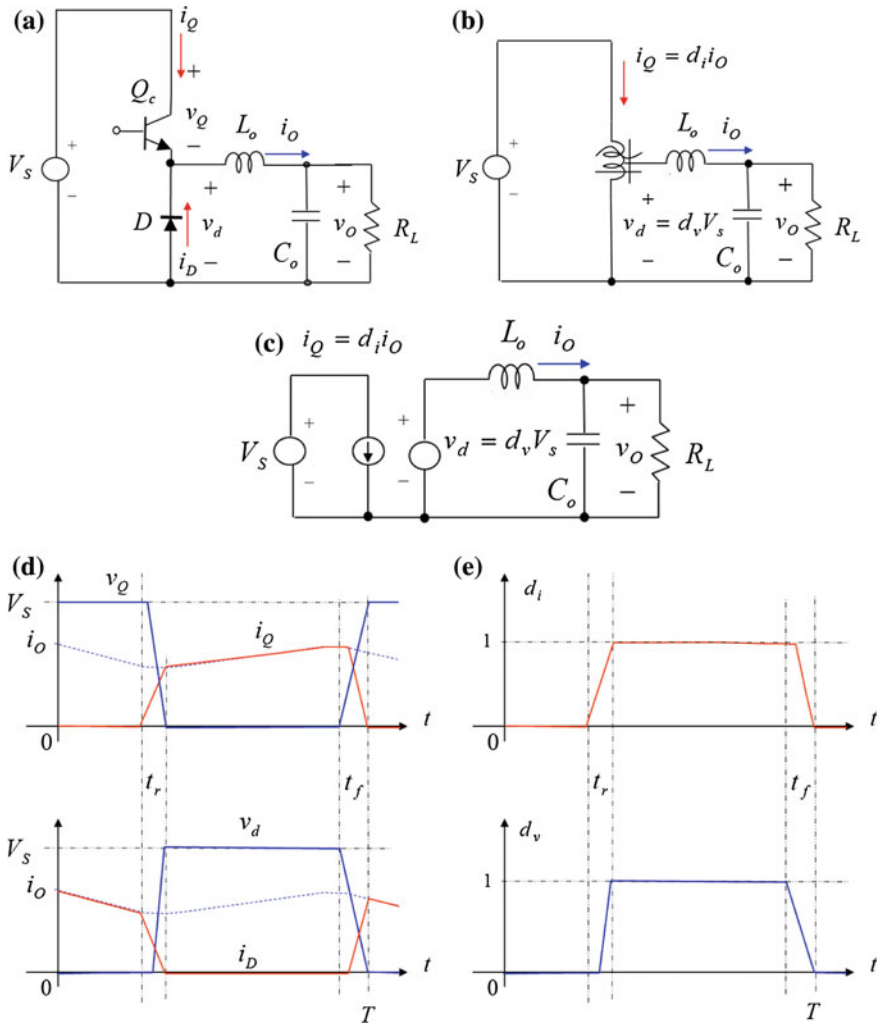

Fig. 4.18 Another extended switched transformer model for a switch cell with finite switching times. **a** The switch cell with finite switching times. **b** Its equivalent switched transformer. **c** Imbalanced sources. **d** Its switching waveforms. **e** The switching functions of current and voltage

The efficiency for a large output inductor can be sought as follows:

$$\eta \equiv \frac{P_o}{P_s} = \frac{V_d I_o}{V_s I_Q} = \frac{(D_v V_s) I_o}{V_s (D_i I_o)} = \frac{D_v}{D_i}. \tag{4.13}$$

It is noteworthy from (4.13) that the efficiency of a switching converter with switching loss only is determined by the ratio of the average switching voltage duty

function and the average switching current duty ratio, which was not shown in any other literatures.

For the inductive switching case, as shown in Fig. 2.14 of Chap. 2, the efficiency (4.13) is identified to be exactly the same as (2.17a) of Chap. 2, as follows:

$$\eta = \frac{D_v}{D_i} = \frac{D + t_f/(2T)}{D + t_r/(2T) + t_f/T} = \frac{1}{1 + \frac{(t_r + t_f)/(2T)}{D + t_f/(2T)}} = \frac{1}{1 + \frac{t_r + t_f}{2TD + t_f}} = \eta_L. \tag{4.14}$$

Question 2

1. Please prove (4.14) using the switching loss calculation of finite switching times.
2. In case highly complicated switching where ringing and high spike switching functions appear, is still (4.13) valid for the case?
   → So far as the inductor current does not fluctuating too much, the efficiency can be simply determined by (4.13).

4.2.5 The Switched Transformer Model Can Deal with Switching Converters with Great Easy and Accurately

It can be summarized that the switched transformer model has the following strengths, which are quite close to the ideal modeling requirements.

- Generally applicable to any DC and AC converters
- Unified approach for various converter types
- Valid not only for CCM but also for DCM
- Applicable to DC and AC analyses
- Applicable to harmonic analysis
- Exact but can be approximated if necessary
- Available for practical switches with finite switching times and parasitics
- Circuit oriented easy model with lots of physical insight

One thing unexplained above is the practical switch with parasitics [12], which is left for proactive readers.

References

1. Rim CT, Hu DY, Cho GH (1990) Transformers as equivalent circuits for switches: general proofs and DQ transformation-based analysis. IEEE Trans Ind Appl: 777–785 (July/Aug)
2. Wood P (1979) General theory of switching power converters. In: IEEE power electronics specialists conference record, pp 3–10

3. Rim CT, Joung GB, Cho GH (1988) A state space modeling of non-ideal DC-DC converters. In: IEEE power electronics specialists conference record, pp 943–950
4. Verghese GC, Elbuluk ME, Kassakian JG (1986) A general approach to sampled-data modeling for power electronic circuits. IEEE Trans Power Electron PE-1(2):76–89
5. Verghese G, Mukherji U (1981) Extended averaging and control procedures. In: IEEE power electronics specialists conference record, pp 329–336
6. Lee FCY, Iwens RP, Yu Y, Triner JE (1979) Generalized computer-aided discrete time-domain modeling and analysis of DC-DC converters. IEEE Trans Ind Electron Contr Instrum IECI-26(2):58–69
7. Middlebrook RD, Cuk S (1976) A general unified approach to modeling switching converter stages. In: IEEE power electronics specialists conference record, pp 18–34
8. Ngo KDT (1986) Low frequency characterization of PWM converter. IEEE Trans Power Electron PE-1(4):223–230
9. Middlebrook RD (1987) Topics in multi-loop regulators and current-mode programming. IEEE Trans Power Electron PE-2(2):109–124
10. Vorperian V, Tymersky R, Lee FCY (1989) Equivalent circuit models for resonant and PWM switches. IEEE Trans Power Electron PE-4(2):205–214
11. Alesina A, Venturini MGB (1981) Solid-state power conversion: a fourier analysis approach to generalized transformer synthesis. IEEE Trans Circuits Syst CAS-28(4):319–330
12. Rim CT, Joung GB, Cho GH (1991) Practical switch-based state-space modeling of DC-DC converters with all parasitics. IEEE Trans Power Electron 6(4):611–617

Part III
Single Phase AC Circuits and Resonant Converters

Phasor transformation, also referred to as phasor modeling, was first brought before the public in 1990, which I had studied for at least four years as a tool to deal with AC circuits, including series resonant converters (SRC) in a unified and general way. This phasor modeling provides explicit and simple equations with fruitful physical insight. For example, in the case that switching frequency deviates from resonant frequency, the SRC is modeled as the first order, and in the case of resonance, the SRC is modeled as the second order.

In this part, the basics of the phasor transformation and its application to the SRC and single phase AC power are explained.

Chapter 5
Basic Phasor Transformation and Application to Series Resonant Converters

In this chapter, the advent of phasor transformation is explained from the background to the application to series resonant converters as an example. The conventional phasor concept that has long been used for nearly a century is found to be a 'static phasor' and a 'dynamic phasor', coined later by other researchers, is introduced here as an extension of the static phasor to a general form of the phasor. A lot of this chapter is based on the original paper of mine [1].

5.1 Background of Phasor Transformation for the SRC

Many researchers [2–8] have shown that the well-known resonant converters are nonlinear switching equations. The complete DC and AC analyses of switching frequency controlled SRC are found in [2, 3]. Several useful curves based on DC analysis, which can be utilized in designing the SRC, are proposed in [4]. The small signal circuit models for AC analysis are suggested in [5–7].

It is worthy to note that the experimental or the simulation output voltage waveforms are very similar to either the first or the second order system responses in a certain operating range and the DC voltage gain curves are similar with resistance-inductance-capacitance (RLC) filter frequency characteristic curves. Therefore, in view of practical applications, it is an important work to find a simplified equivalent circuit of an SRC which can show the simple behaviors though not so accurate for the efficient analysis and design.

Some solutions to the above problem have been given in [9–12]. The diode rectifier and output filter is substituted by an equivalent resistor [9, 10]. So the analysis is drastically simplified by this substitution and the resemblance of resonant converters with RLC filters is well explained in this way. This technique is, however, valid only for the DC analysis and is no longer valid for the AC analysis. On the other hand an approximated small signal model is suggested in a recent paper with good intuition [11].

C.T. Rim, *Phasor Power Electronics*, KAIST Research Series,
DOI 10.1007/978-981-10-0536-7_5

It is thought that the previous models have at least one of the following disadvantages in view of the practical application of them.

1. The equations are not of explicit form.
2. The model is too complex to get physical insights from it.
3. Any rigorous explanation for that the system order changes according to the switching frequency is not provided.
4. DC/AC analyses of frequency [3]/phase [12] control methods are not performed by a unified principle.

In this chapter, a systematic approach based on phasor transformation which gives an equivalent time-invariant circuit that is described as the explicit equations, is suggested. Also the first and second order models of SRC are given. It is further shown that the simulation results based on the proposed model agree with the experimental results.

5.2 Introduction to Phasor Transformation

It is assumed that the SRC shown in Fig. 5.1 is composed of ideal switches and ideal circuit components. Also it is assumed that the converter operates in the continuous conduction mode (CCM) and that the quality factor is sufficiently high enough for the sufficient reduction of harmonic current in the *LC* resonant tank [2, 3]. The switching frequency which is lower than a half of the resonant frequency is not considered due to the difficulties in dealing with the harmonic resonances such as the 3rd and 5th switching harmonics. Though these assumptions arise some error in the analysis result and reduce the generality, these are still useful for the practical application of the SRC models.

5.2.1 Equivalent Transformer Circuit

Since it is proved that a switch set is generally a time-varying transformer [13], an equivalent circuit of Fig. 5.1 can be drawn, as shown in Fig. 5.2 where the switch sets are substituted by their corresponding transformers. The turn-ratios are just the same as the switching functions as shown in Fig. 5.3c. Here the influence of harmonics is ignored since the magnitudes of harmonics are small and these small

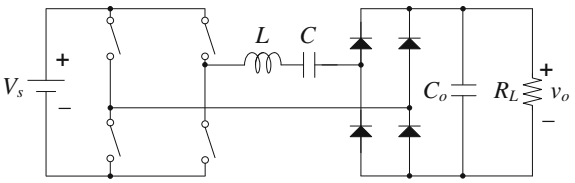

Fig. 5.1 Series resonant converter (SRC)

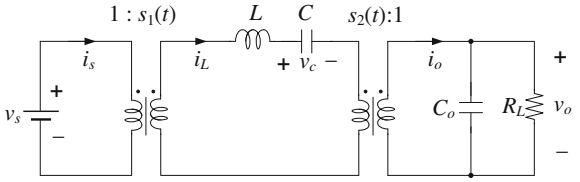

Fig. 5.2 An equivalent transformer circuit

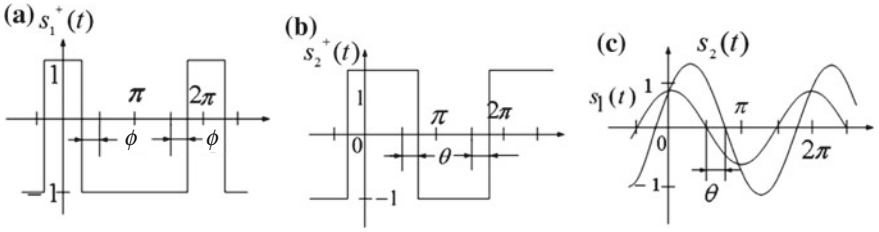

Fig. 5.3 Switching functions. **a** Original $s_1^+(t)$. **b** Original $s_2^+(t)$. **c** Fundamentals of **a** and **b**

harmonics are filtered by the *LC* resonant circuit. The analysis is greatly simplified by this approximation. It should be, however, reminded that this may not be true when the quality factor is small or the switching frequency is much lower than the resonant frequency. The fundamental component, $s_1(t), s_2(t)$ of the original switching functions $s_1^+(t), s_2^+(t)$ are represented as

$$s_1(t) = \frac{4}{\pi}\cos\phi \cdot \cos\omega_s t \tag{5.1a}$$

$$s_2(t) = \frac{4}{\pi}\cos(\omega_s t - \theta), \tag{5.1b}$$

where ϕ is the controlled phase, θ is the diode switch phase delay, and ω_s is the switching frequency. Since the $s_2(t)$ is a function of inductor current, the SRC is described by nonlinear equations and so we cannot directly use the Laplace transformation technique for the analysis of the SRC.

It is noted that no switching element is appeared in Fig. 5.2. The system equation is now analytical, which is a very important basic condition for the following linear transformation.

5.2.2 *Phasor Transformation*

It is well known that the DQ transformation is powerful in the analysis of poly-phase AC systems. The basic principle of the DQ transformation is to find a stationary circuit for a given rotary circuit, which makes it greatly easy to find the

envelopes of rotary variables of a rotary circuit [13]. Unfortunately the powerful DQ transformation cannot be applied to the single phase AC circuits as well as SRC. Up to now, there has been no appropriate transformation which is directly applicable to the analysis of the single phase AC systems.

In this section the way to obtain a stationary circuit for a given rotary one is suggested. Since the conventional phasor represents the magnitude and the phase of a sinusoidal signal in the steady state it cannot represent the signal in the transient state. So a modified phasor which can represent any sinusoidal signal is considered:

$$x(t) = \mathrm{Re}\left\{\sqrt{2}\mathbf{x}(t)\mathrm{e}^{j\omega_s t}\right\}, \tag{5.2}$$

where the $\mathbf{x}(t)$ indicates the complex time-varying variable. None of the $x(t)$ and ω_s, need to be sinusoidal or constant; however, the $\mathbf{x}(t)$ can be non-sinusoidal function when the $x(t)$ is sinusoidal with the frequency of ω_s. In the steady state, $\mathbf{x}(t)$ becomes just the conventional phasor. By applying (5.2) to the time-varying circuit variables appeared in the rotary circuit of Fig. 5.2, a stationary circuit is obtained.

The five basic circuit elements of the single phase AC system, which are inductor, capacitor, transformer, resistor and source, are phasor-transformed, respectively, as follows.

5.2.2.1 Inductor Phasor Transformation

The procedure of the phasor transformation for the inductor is shown in Fig. 5.4. The rotary circuit equation is

$$L\frac{di_L}{dt} = v_L. \tag{5.3}$$

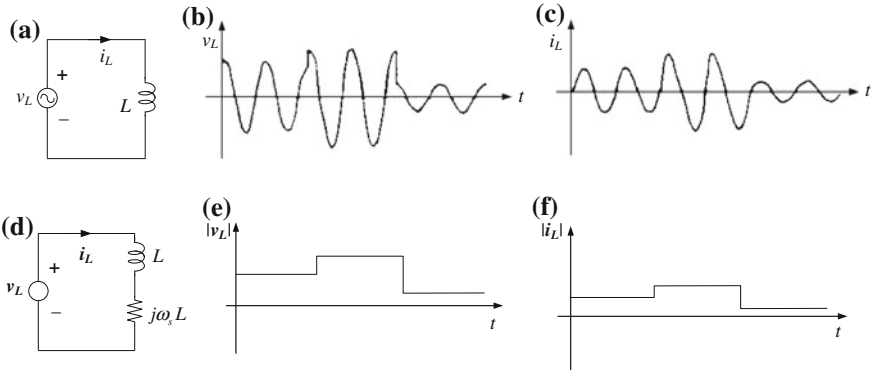

Fig. 5.4 Inductor phasor transformation. **a** Rotary circuit. **b** Rotary voltage. **c** Rotary current. **d** Stationary circuit. **e** Stationary voltage. **f** Stationary current

The phasor transformations of i_L and are v_L are

$$i_L = \mathrm{Re}\left\{\sqrt{2}\boldsymbol{i_L}\mathrm{e}^{j\omega_s t}\right\}$$

and

$$v_L = \mathrm{Re}\left\{\sqrt{2}\boldsymbol{v_L}\mathrm{e}^{j\omega_s t}\right\}, \tag{5.4}$$

respectively. Applying (5.4) to (5.3) results in

$$L\frac{d}{dt}\mathrm{Re}\left\{\sqrt{2}\boldsymbol{i_L}\mathrm{e}^{j\omega_s t}\right\} = \mathrm{Re}\left\{\sqrt{2}\boldsymbol{v_L}\mathrm{e}^{j\omega_s t}\right\} \tag{5.5a}$$

or

$$L\mathrm{Re}\left\{\frac{d\boldsymbol{i_L}}{dt}\mathrm{e}^{j\omega_s t} + j\omega_s\boldsymbol{i_L}\mathrm{e}^{j\omega_s t}\right\} = \mathrm{Re}\left\{\left(L\frac{d\boldsymbol{i_L}}{dt} + j\omega_s\boldsymbol{i_L}\right)\mathrm{e}^{j\omega_s t}\right\} = \mathrm{Re}\left\{\boldsymbol{v_L}\mathrm{e}^{j\omega_s t}\right\}. \tag{5.5b}$$

Equation (5.5a, b) is just equivalent to

$$L\frac{d\boldsymbol{i_L}}{dt} + j\omega_s\boldsymbol{i}_L = \boldsymbol{v}_L. \tag{5.6}$$

The equivalence of (5.5a, b) with (5.6) can be proved as follows.

Theorem

$$\textit{For any}\quad \boldsymbol{x},\boldsymbol{y},\quad \omega_s \neq 0 \qquad \mathrm{Re}\left\{\boldsymbol{x}\mathrm{e}^{j\omega_s t}\right\} = \mathrm{Re}\left\{\boldsymbol{y}\mathrm{e}^{j\omega_s t}\right\}$$
$$\textit{if any only if}\ \boldsymbol{x} = \boldsymbol{y}$$

Proof

$$\mathrm{Re}\left\{\boldsymbol{x}\mathrm{e}^{j\omega_s t}\right\} = \mathrm{Re}\left\{|\boldsymbol{x}|\mathrm{e}^{j\arg(\boldsymbol{x})}\mathrm{e}^{j\omega_s t}\right\} = |\boldsymbol{x}|\mathrm{Re}\left\{\mathrm{e}^{j\arg(\boldsymbol{x})+j\omega_s t}\right\} = |\boldsymbol{y}|\mathrm{Re}\left\{\mathrm{e}^{j\arg(\boldsymbol{y})+j\omega_s t}\right\}$$
$$\leftrightarrow |\boldsymbol{x}| = |\boldsymbol{y}|\ \textit{and}\ \arg(\boldsymbol{x}) = \arg(\boldsymbol{y}) + 2\pi n, n = 0, 1, 2, \ldots$$
$$\leftrightarrow \boldsymbol{x} = \boldsymbol{y} : Q.E.D.$$

It is necessary to make (5.6) be of circuit form for the benefit of well-established circuit analyses techniques as shown in Fig. 5.4d. There exists an imaginary resistor, whose meaning is just conventional inductor impedance in the steady state. However it should not be misunderstood that Fig. 5.4d is no longer valid for in the transient state. The imaginary resistor does not vanish even though it is in the transient state, therefore it's worthy to distinguish this from a conventional reactance.

As can be seen from Fig. 5.4b, c, e, f the stationary circuit can be used to find the envelopes of the sinusoidal waveforms of the rotary circuit. Since the imaginary resistor does not serve the damping, the response needs not to be exponential; in this example there is no time delay.

5.2.2.2 Capacitor Phase Transformation

By a similar procedure with the inductor case, the rotary circuit equation of Fig. 5.5a,

$$C\frac{dv_C}{dt} = i_C \tag{5.7}$$

is changed by the phasor transformation to

$$C\frac{d\boldsymbol{v}_C}{dt} + j\omega C\boldsymbol{v}_C = \boldsymbol{i}_C \tag{5.8}$$

The circuit reconstruction of (5.8) is shown in Fig. 5.5b.

5.2.2.3 Transformer Phasor Transformation

The voltage source single phase inverter as shown in Fig. 5.6a is composed of stationary and rotary parts. Hence the phasor transformation is taken for the rotary part only as

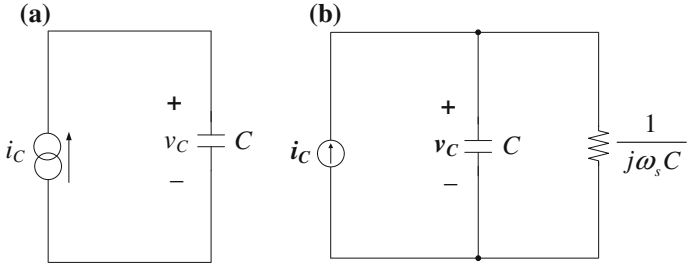

Fig. 5.5 Capacitor phasor transformation. **a** Rotary circuit. **b** Stationary circuit

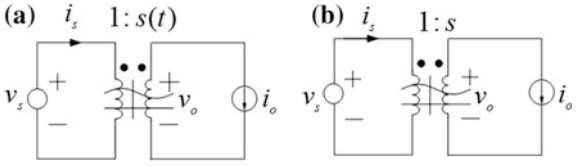

Fig. 5.6 Transformer phasor transformation. **a** Original. **b** Phasor transformed

$$v_o \equiv \mathrm{Re}\left\{\sqrt{2}\boldsymbol{v_o}\mathrm{e}^{j\omega_s t}\right\} \tag{5.9a}$$

$$s(t) \equiv \mathrm{Re}\left\{\sqrt{2}\boldsymbol{s}\mathrm{e}^{j\omega_s t}\right\} \tag{5.9b}$$

$$i_o \equiv \mathrm{Re}\left\{\sqrt{2}\boldsymbol{i_o}\mathrm{e}^{j\omega_s t}\right\} \tag{5.9c}$$

On the other hand the following relations exist in the transformer of Fig. 5.6a:

$$v_0 = s(t)v_s \tag{5.10a}$$

$$i_s = s(t)i_0 \tag{5.10b}$$

Applying (5.9a, b, c)–(5.10a, b) results in

$$v_o = \mathrm{Re}\left\{\sqrt{2}\boldsymbol{v_o}\mathrm{e}^{j\omega_s t}\right\} = \mathrm{Re}\left\{\sqrt{2}\boldsymbol{s}v_s\mathrm{e}^{j\omega_s t}\right\} \tag{5.11a}$$

$$i_s = \mathrm{Re}\left\{\sqrt{2}\boldsymbol{s}\mathrm{e}^{j\omega_s t}\right\} \cdot \mathrm{Re}\left\{\sqrt{2}\boldsymbol{s}v_s\mathrm{e}^{j\omega_s t}\right\} = \mathrm{Re}\{\boldsymbol{s}^*\boldsymbol{i_o}\} + \mathrm{Re}\left\{\boldsymbol{s}\boldsymbol{i_o}\mathrm{e}^{2j\omega_s t}\right\} \tag{5.11b}$$

In (5.11a, b), the symbol, asterisk (*) represents the complex conjugate. As previously proved, (5.11a) becomes

$$\boldsymbol{v_o} = \boldsymbol{s}\boldsymbol{v_s} \tag{5.12a}$$

and (5.11b) can be rewritten as follows considering that the as current of it does not contribute to any voltage change in the source or any energy transfer. Furthermore the frequency of the AC current is so high that this is thoroughly filtered by the adjacent circuits. Therefore,

$$\boldsymbol{i_s} = \boldsymbol{s}^*\boldsymbol{i_o} \tag{5.12b}$$

where a dummy variable i_s whose imaginary part may be arbitrary is introduced as

$$i_s \equiv \mathrm{Re}\{\boldsymbol{i_s}\} \tag{5.12c}$$

Equation (5.12b) may not be true for the parallel resonant converter case where the imaginary current cannot be set to be arbitrary. This cumbersome problem is unsolved until the general unified phasor transformation is introduced in the following chapters. For simplicity, it will not be explained further in this chapter.

The circuit reconstruction based on (5.12a, b, c) is shown in Fig. 5.6b, where an unusual complex turn-ratio is found.

5.2.2.4 Resistor Phasor Transformation

The phasor transformation of a resistor is straightforward since

$$v_R = \mathrm{Re}\left\{\sqrt{2}\boldsymbol{v_R}\mathrm{e}^{j\omega_s t}\right\} = Ri_R = \mathrm{Re}\left\{\sqrt{2}R\boldsymbol{i_R}\mathrm{e}^{j\omega_s t}\right\} \tag{5.13a}$$

or

$$\boldsymbol{v_R} = R\boldsymbol{i_R} \tag{5.13b}$$

5.2.3 *Phasor Transformed SRC*

Since the stationary circuits for individual rotary circuits are now available, the stationary SRC for the rotary SRC of Fig. 5.2 can be drawn as shown in Fig. 5.8 using the results of Figs. 5.4, 5.5, 5.6 and 5.7. Auto-transformers are used now since the turn-ratios never exceed unities. They are determined from (5.1a, b) and (5.9b) as

$$\begin{aligned} \boldsymbol{s}_1 &= \frac{2\sqrt{2}}{\pi}\cos\phi \\ \boldsymbol{s}_2 &= \frac{2\sqrt{2}}{\pi}\mathrm{e}^{-j\theta} \end{aligned} \tag{5.14}$$

Now the circuit shown in Fig. 5.8 is no longer time-varying and all the variables in it are just equivalent to those in Fig. 5.2 with respect to the phasor transformation, (5.2).

It took many steps and discussions in finding this time-invariant circuit, however this procedure can be drastically simplified only if one is get used to this transformation; Fig. 5.8 can be directly drawn from Fig. 5.2 or Fig. 5.1 without any manipulation of equations in case that one knows Figs. 5.4, 5.5, 5.6 and 5.7.

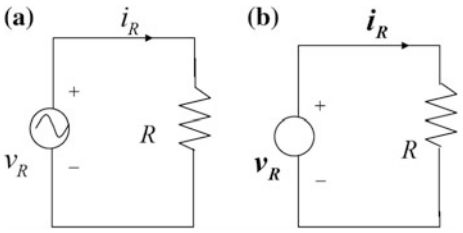

Fig. 5.7 Resistor phasor transformation. **a** Rotary circuit. **b** Stationary circuit

5.3 The Analysis of SRC

5.3.1 DC Analysis

From the phasor transformed circuit of Fig. 5.8, the DC circuit which is utilized in the DC analysis can be obtained by removing the inductor and the capacitors. This stationary circuit should not be confused with the rotary circuit; the inductors of Fig. 5.8 are not substituted by the AC reactances since Fig. 5.8 is not the rotary circuit.

Since the input, output voltages of the two circuits of Figs. 5.2 and 5.9 are identical (note that phasor transformation is not applied to these DC side variables), the DC gain of Fig. 5.9 is the same as that of Fig. 5.2. Then the DC gain is calculated from Fig. 5.9 as

$$G_V \equiv \frac{V_0}{V_s} = \frac{\cos\phi}{\sqrt{1+Q^2\left[\frac{\omega_s}{\omega_r}-\frac{\omega_r}{\omega_s}\right]^2}}, \tag{5.15}$$

where

$$Q = \frac{\pi^2}{8}\frac{\omega_r L}{R_L}, \quad \omega_r = \frac{1}{\sqrt{LC}} \tag{5.16}$$

This confirms the previous simplified DC analyses results where intuitive models are used [9, 10]. There is a little discrepancy between (5.15) and the result of [2], which stems not from the inaccuracy of the phasor transformation but from the neglect of the high order harmonics. Recall that the only approximation used in the phasor transformation is the neglect of the DC side AC current, which does not affect the fundamental components of DC or AC side signals as shown in (5.11b) and (5.12b).

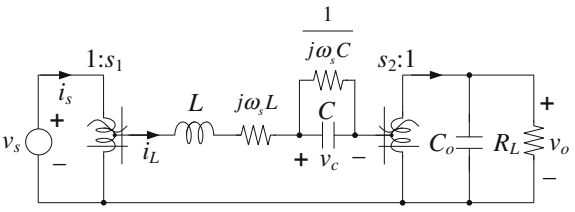

Fig. 5.8 Phasor transformed SRC

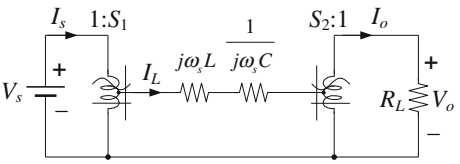

Fig. 5.9 DC circuit for phasor transformed SRC

5.3.2 Variation of System Order

Since Fig. 5.8 is still too complex to analyze, let's simplify it considering the fact that the impedances of imaginary resistors are much larger than those of reactor impedances. This can be justified since the output capacitor is so large that it may govern the overall system response time and, as a result, this time is much larger than a switching period. Under this assumption that $s \ll \omega_s$, it can be seen that

$$\frac{1}{sC + j\omega_s C} = \frac{1}{j\omega_s C\left(1 + \frac{s}{j\omega_s}\right)} \approx \frac{1}{j\omega_s C}\left(1 - \frac{s}{j\omega_s}\right) = \frac{1}{j\omega_s C} + sL\left(\frac{\omega_r}{\omega_s}\right)^2 \tag{5.17}$$

Surprisingly the capacitor is changed to an equivalent inductor, which reduces the system order, as shown in Fig. 5.10a, b. Furthermore it is found that this can be once more simplified as shown in Fig. 5.10c, where the equivalent inductor and imaginary resistors are

$$\begin{aligned} L_{eq} &= L\left\{1 + \left(\frac{\omega_r}{\omega_s}\right)^2\right\} \\ X_{eq} &= \omega_e L\left\{1 - \left(\frac{\omega_r}{\omega_s}\right)^2\right\} \end{aligned} \tag{5.18}$$

The simplified SRC for AC analysis then can be drawn as shown in Fig. 5.11. The reason why the system order changes according to the switching frequency can be explained by Fig. 5.11 and (5.18).

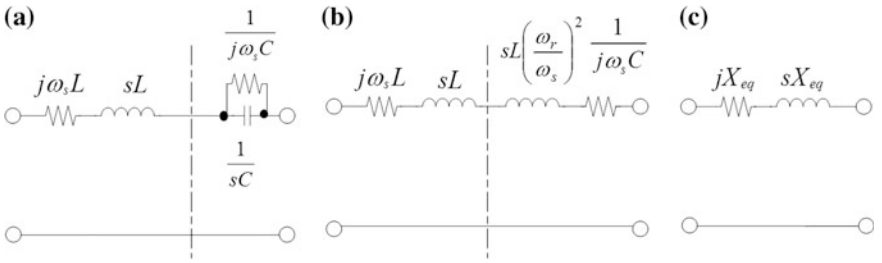

Fig. 5.10 Simplification of phasor transformed resonant tank. **a** Original circuit. **b** Approximated. **c** Simplified

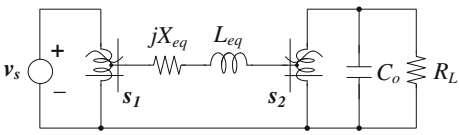

Fig. 5.11 Simplified SRC of Fig. 5.8

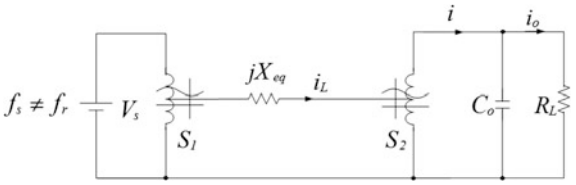

Fig. 5.12 First order model

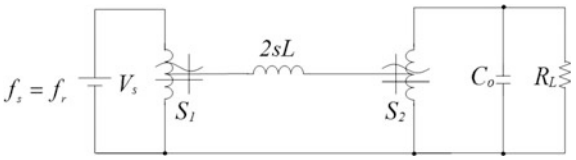

Fig. 5.13 Second order model

As ω_s deviates from ω_r, the absolute of the impedance of the inductor sL_{eq} becomes smaller than that of the imaginary resistor X_{eq}, as seen from (5.18) since the magnitude of the switching frequency is much larger than the inverse of the system response time. This can be justified by the fact that the time constant of an output filter—the products of C_0, and R_L—is several hundred times larger than the switching period in practice. Under this condition the system becomes the first order as shown in Fig. 5.12.

On the other hand as $\omega_{s,}$ is close to ω_r, now X_{eq} becomes smaller than sL_{eq} as seen from (5.18). Under this condition the system becomes second order as shown in Fig. 5.13. Especially when ω_s is identical to ω_r, X_{eq} becomes zero, which is just the case of quantum converter [14, 15].

It is important to determine the boundary switching frequencies ω_b at which the system order changes since this is essential to select a correct model between the two models of Figs. 5.12 and 5.13. Obviously the exact determination of ω_b is impossible since the system order does not change abruptly in practice, however the rough estimation may not be impossible assuming that the equivalent LC resonant circuit impedances of Figs. 5.12 and 5.13 become identical at ω_b. Under this condition the both circuits are physically equivalent.

Since it is observed by the simulation and the experiment that ω_b is very close to ω_r, (5.18) can be approximated as

$$\left|X_{eq}\right| = \left|(\omega_r \pm \omega_d)L\left\{1 - \left(\frac{\omega_r}{\omega_r \pm \omega_d}\right)^2\right\}\right| \approx 2\omega_d L \tag{5.19a}$$

$$\left|sL_{eq}\right| = |s|L\left\{1 + \left(\frac{\omega_r}{\omega_r \pm \omega_d}\right)^2\right\} \approx \frac{2}{\tau_s}L \tag{5.19b}$$

where it is defined as

$$\omega_b = \begin{cases} \omega_r + \omega_d & for\ \omega_s > \omega_r \\ \omega_r - \omega_d & \omega_s < \omega_r \end{cases} \tag{5.19c}$$

τ_s is the system time constant when it is modeled as the first order system and ω_d is the frequency deviation from ω_r.

From the above discussion it can be concluded that

$$\left|X_{eq}\right| = \left|sL_{eq}\right| \quad or \quad \omega_d = \frac{1}{\tau_s} \tag{5.20}$$

This very simple relationship shows that the boundary switching frequency is directly related with the system time constant. And it is found that the SRC is first order at almost everywhere except the very narrow frequency band around ω_r, since τ_s is very much larger than a switching period. This is true in practice since the output filter time constant is so largely designed compared with the switching period that the output voltage ripple may be very small (about 1 % of regulated output voltage). Equation (5.20) will be completed in later by the determination of the value, τ_s.

5.3.3 AC Analysis When ω_s Deviates from ω_r

The first order model as shown in Fig. 5.12 is now analyzed. Since this model is nonlinear due to the non-linear turn-ratio s_2 the small signal perturbations in source voltage, phase, and frequency are to be applied to the first order model to linearize it. Before applying small signal perturbations, let's find an output side equivalent circuit.

The transient current i is determined from Fig. 5.12 and (5.14) as

$$i = \boldsymbol{i_L s_2^*} = \frac{v_s \boldsymbol{s}_1 - v_o \boldsymbol{s}_2}{jX_{eq}} \boldsymbol{s}_2^* = \frac{8}{\pi^2} \frac{v_1 e^{j\theta} - v_o}{jX_{eq}} \tag{5.21a}$$

where

$$v_1 \equiv v_s \cos\phi \tag{5.21b}$$

Since the diode rectifier switching function, s_2 is always synchronized with the resonant tank current i_L the rectified current i should be positive real. So (5.21a, b) can be decomposed to imaginary and real parts as follows:

$$\mathrm{Im}(i) = 0, \quad \mathrm{Re}(i) > 0 \tag{5.22a}$$

or

$$\theta = \begin{cases} +\cos^{-1}\frac{v_0}{v_s\cos\phi} & \omega_s > \omega_r \\ -\cos^{-1}\frac{v_0}{v_s\cos\phi} & \omega_s < \omega_r \end{cases} \tag{5.22b}$$

Equation (5.22a, b) completely determines $\boldsymbol{s}_2$ of (5.14). Applying (5.22a, b) to (5.21a, b) yields

$$i = \frac{8}{\pi^2}\frac{v_s\cos\phi\sin\theta}{X_{eq}} \tag{5.23a}$$

or

$$i = \frac{\sqrt{(v_s\cos\phi)^2 - v_o^2}}{X_e} \tag{5.23b}$$

where

$$X_e = \frac{\pi^2}{8}X_{eq} \tag{5.23c}$$

As discussed above, (5.23b) is a nonlinear function of input/output voltages, hence perturbations are now applied:

$$\hat{i} = \frac{\partial i}{\partial v_1}\left\{\frac{\partial v_1}{\partial v_s}\hat{v}_s + \frac{\partial v_1}{\partial v_\phi}\hat{\phi}\right\} + \frac{\partial i}{\partial v_0}\hat{v}_o + \frac{\partial i}{\partial X_e}\frac{\partial X_e}{\partial \omega_s}\hat{\omega}_s \tag{5.24a}$$

or

$$\begin{aligned}\hat{i} = {} & \frac{1}{X_e}\sqrt{1+\left(\frac{R_L}{X_e}\right)^2}\cos\phi\cdot\hat{v}_s - \frac{V_s}{X_e}\sqrt{1+\left(\frac{R_L}{X_e}\right)^2}\cdot\sin\phi\cdot\hat{\phi} - \frac{R_L}{X_e^2}\hat{v}_o \\ & - \frac{\pi^2}{8}\frac{V_s L_{eq}}{X_e^2}\frac{\hat{\omega}_s}{\sqrt{1+\left(\frac{R_L}{X_e}\right)^2}} \equiv \hat{i}_x - \frac{\hat{v}_0}{R_x}\end{aligned} \tag{5.24b}$$

where the following relations are used:

$$I_o = I = \frac{\sqrt{V_1^2 - V_o^2}}{X_e}, \frac{V_o}{V_1} = \frac{1}{\sqrt{1 + \left(\frac{X_e}{R_L}\right)^2}}, \quad \frac{V_o}{I_o} = R_L, R_x = \frac{X_e^2}{R_L} \tag{5.24c}$$

Since the output voltage perturbation term in (5.24b) is just the expression of a resistor, the perturbed circuit for Fig. 5.12 can be drawn as shown in Fig. 5.14.

The output voltage perturbation is determined by applying (5.24a, b, c) to Fig. 5.14, as follows:

$$\hat{V}_o(s) = \hat{I}_x(s) R_x // R_L \frac{\omega_c}{s + \omega_c} = \frac{\omega_c}{s + \omega_c} \left\{ G_1 \hat{V}_s(s) - G_2 \hat{\phi}(s) - G_3 \hat{\omega}_3(s) \right\}, \tag{5.25a}$$

where

$$G_1 = G_v = \frac{\cos\phi}{\sqrt{1 + \left(\frac{X_e}{R_L}\right)^2}}, G_2 = \frac{V_s \sin\phi}{\sqrt{1 + \left(\frac{X_e}{R_L}\right)^2}}, G_3 = \frac{\pi^2}{8} \frac{V_s L_{eq} R_L}{X_e^2} \left\{ 1 + \left(\frac{R_L}{X_e}\right)^2 \right\}^{-3/2}$$
$$\omega_c = \left\{ 1 + \left(\frac{R_L}{X_e}\right)^2 \right\} \frac{1}{C_o R_L}. \tag{5.25b}$$

The expressions of (5.25a, b) are of explicit and simple forms, which are what we have searched for.

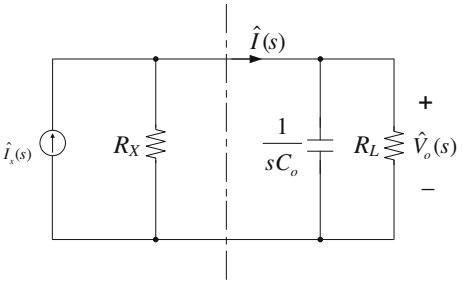

Fig. 5.14 Perturbed first order model

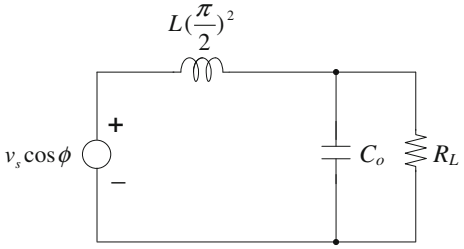

Fig. 5.15 Transformerless second order model

5.3.4 *AC Analysis When ω_s Is Close to ω_r*

Now the second order model as shown in Fig. 5.13 is used for the analysis. The circuit without transformer is drawn as shown in Fig. 5.15 considering the fact that the turn-ratios of (5.14) are all real; this is justified since the θ is zero as can be identified from (5.15) and (5.22b). The AC analysis of this circuit is then straightforward.

$$\hat{V}_o(s) = G_o(s)\left\{\hat{V}_s(s) \cdot \cos\phi - V_s \sin\phi \cdot \hat{\phi}(s)\right\} \tag{5.26a}$$

where

$$G_o(s) = \frac{\omega_n^2}{s^2 + as + \omega_n^2}, \quad a = \frac{1}{C_o R_L}, \quad \omega_n = \frac{2}{\pi\sqrt{LC_o}} \tag{5.26b}$$

The similar result has been also obtained by our previous work [15], as a quantum converter analysis. All SRC control methods such as frequency, phase and time domain ones have been analyzed by a unified principle, the phasor transformation.

5.4 Simulations

Since the proposed model includes several assumptions and approximations, the verification of the model is quite essential. By comparing the exact solution with the response obtained by the proposed model this can be accomplished.

To obtain the exact solution, the following state equation for the original circuit of Fig. 5.1 which is valid not only for CCM but also for discontinuous conduction mode (DCM) is solved numerically:

$$\begin{bmatrix} \dot{i}_L \\ \dot{v}_c \\ \dot{v}_o \end{bmatrix} = \begin{bmatrix} 0 & -\frac{1}{L} & \frac{s_2^+(t)}{L} \\ \frac{1}{C} & 0 & 0 \\ \frac{s_1^+(t)}{C_o} & 0 & -\frac{1}{C_o R_L} \end{bmatrix} \tag{5.27a}$$

where

$$s_1^+(t) = s(t), s_2^+(t) = \text{sgn}(i_L) \equiv \begin{cases} 1 & i_L > 0 \\ -1 & i_L < 0 \end{cases} \tag{5.27b}$$

The switching function, $s(t)$ is externally controllable; however, $s_2^+(t)$ which represents the diode rectification is internally controlled by the inductor current. These are the same as those shown in Fig. 5.3.

The following parameters used in the simulations are selected:

$$L = 78\,\mu\text{H}, \quad C = 0.20\,\mu\text{F}, \quad V_s = 5.0\,\text{V}$$

Here the frequency and the phasor perturbation simulations are done for various ω_s, ϕ, C_o, and R_L. Large signal operation waveforms are shown in Fig. 5.16. The vertical scale is relative scale, whereas the horizontal scale is absolute scale. From a lot of simulations it is identified that the large signal system behaviors are nearly either first or second order as shown here. Step change in switching frequency or phase is applied to the SRC in a steady state to identify the small signal behaviors. Comparisons of the simulated waveforms (with harmonic noise) with the approximated model waveforms (without harmonic noise) are shown in Figs. 5.17, 5.18, 5.19, 5.20 and 5.21 for the first order model and in Fig. 5.22 for the second order model. By a lot of simulations as well as the above mentioned it is identified that the proposed models contain errors of about 15 % when the quality factor is too small as shown in Fig. 5.20, or when the switching frequency is neither close to nor far from the resonant frequency as shown in Fig. 5.21. The proposed models,

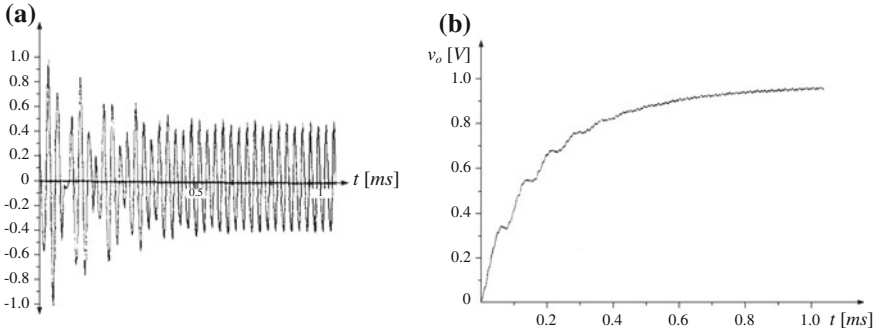

Fig. 5.16 Large signal simulation waveform examples with zero initial conditions. **a** Inductor current. **b** Output voltage

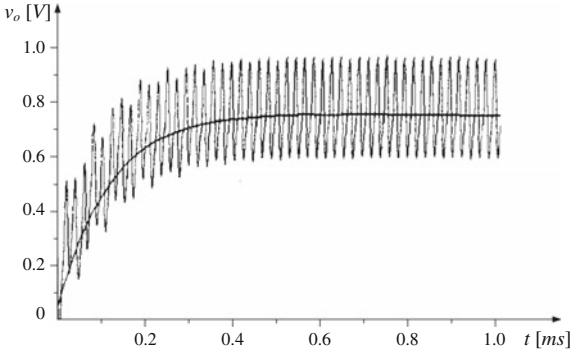

Fig. 5.17 Frequency perturbed output voltage simulation waveforms: first order response $((\omega_s/\omega_r) : 1.654 \rightarrow 1.601,\ \phi : 1.414\ \text{rad},\ C_o : 30\ \mu\text{F},\ R_L : 3\ \Omega)$.

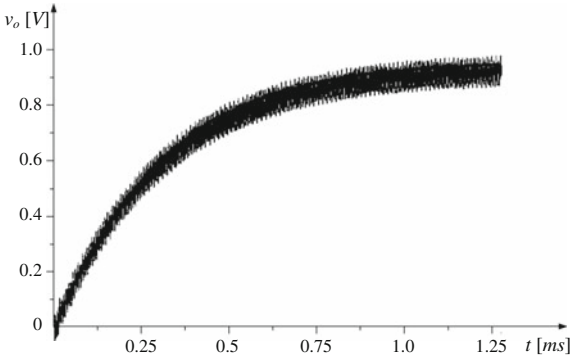

Fig. 5.18 Frequency perturbed output voltage simulation waveforms: first order response $((\omega_s/\omega_r) : 2.482 \rightarrow 2.409,\ \phi : 0.000\ \text{rad},\ C_o : 50\ \mu\text{F},\ R_L : 5\ \Omega)$.

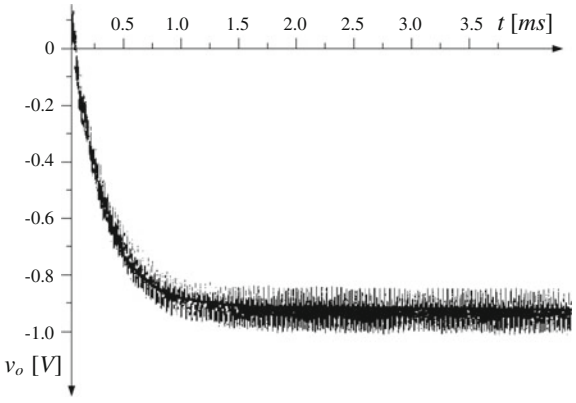

Fig. 5.19 Frequency perturbed output voltage simulation waveforms: first order response $((\omega_s/\omega_r) : 0.709 \rightarrow 0.689,\ \phi : 0.000\ \text{rad},\ C_o : 50\ \mu\text{F},\ R_L : 5\ \Omega)$.

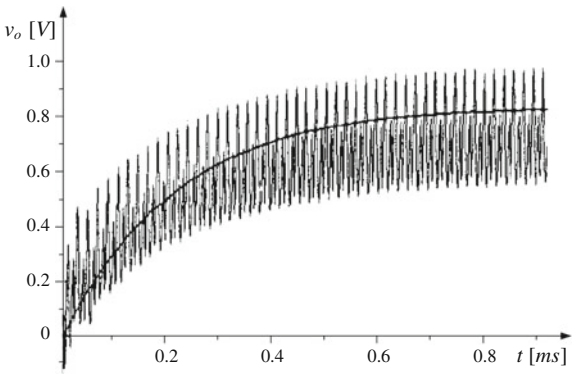

Fig. 5.20 Phase perturbed output voltage simulation waveforms: first order response $((\omega_s/\omega_r) : 1.654,\ \phi : 0.628 \rightarrow 0.597$ rad, $C_o : 20\ \mu$F, $R_L : 10\ \Omega)$.

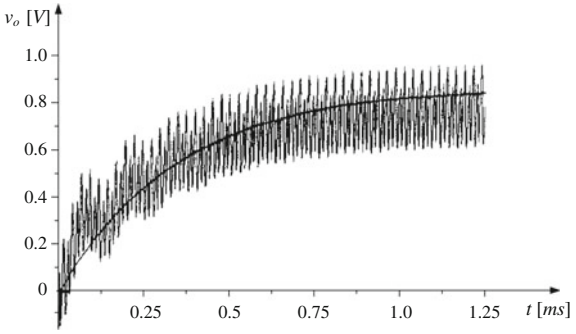

Fig. 5.21 Phase perturbed output voltage simulation waveforms: first order response $((\omega_s/\omega_r) : 1.241,\ \phi : 0.628 \rightarrow 0.597$ rad, $C_o : 100\ \mu$F, $R_L : 3\ \Omega)$.

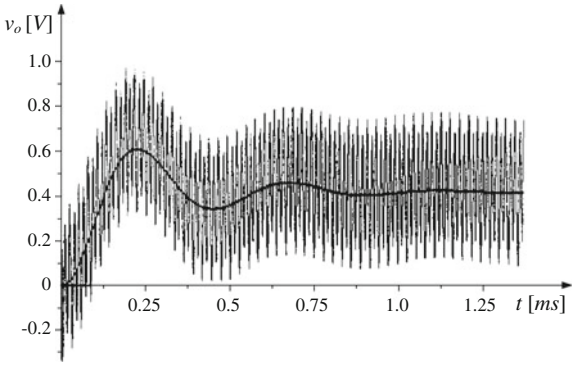

Fig. 5.22 Phase perturbed output voltage simulation waveforms: first order response $((\omega_s/\omega_r) : 1.000,\ \phi : 0.361 \rightarrow 0.314$ rad, $C_o : 20\ \mu$F, $R_L : 6\ \Omega)$.

however, have no problem in practice since the quality factor is usually not smaller than unity and the switching frequency is either close to (for quantum converter) or far from (for frequency control method) the resonant frequency.

5.5 Experiments

The proposed models are to now be experimentally verified for the feasibility test of the practical application. The experimental circuit is selected as a half bridge SRC instead of a full bridge one, however the analytical result of the full bridge SRC valids for the half bridge one either with slight changes in variables as shown in Fig. 5.23.

The parameters are

$$\begin{aligned} L &= 78\ \mu\text{H}, \quad C = 0.24\ \mu\text{F}, \quad V_s = 5.0\ \text{V}, \\ R_s &= 0.40\ \Omega, \quad R_Q = 0.46\ \Omega, \quad R_D = 0.10\ \Omega, \\ L_m &= 130\ \mu\text{H}, \quad V_D = 0.60\ \text{V}, \quad f_r = 36.8\ \text{kHz} \end{aligned}$$

The circuit is constructed on a breadboard and is open loop controlled by the frequency and the phase. The typical experimental output voltage waveforms correspond to the first and the second order models are shown in Figs. 5.24 and 5.25, respectively. Since the second order model is well verified by the literature [14, 15], only the first order model is extensively studied here.

5.5.1 Time Constant Versus Switching Frequency

The time constant of the first order model can be deduced from (5.25b) as

$$\tau \equiv \frac{1}{\omega_c} = \frac{C_o R_L}{1 + \left(\frac{R_L}{X_e}\right)^2} \tag{5.28}$$

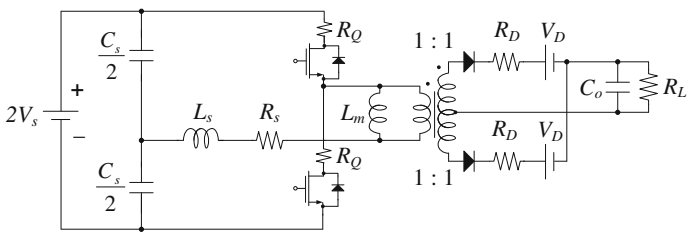

Fig. 5.23 Half-bridge SRC for experiment

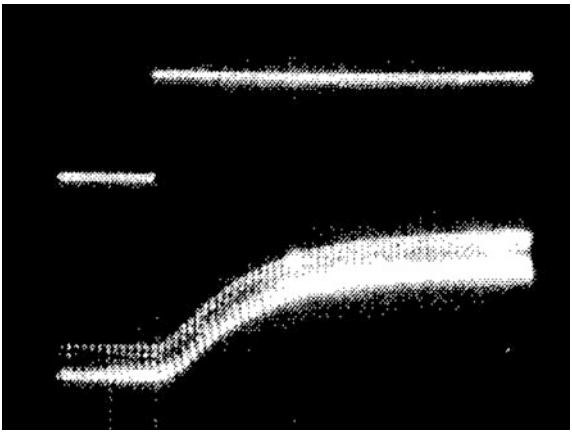

Fig. 5.24 Photograph of frequency perturbed output voltage waveform $((\omega_s/\omega_r) : 0.80,$ $\phi : 0.000$ rad, $C_o : 116$ μF, $R_L : 5\ \Omega,\ 200$ μs/*dev*; *upper*: *frequency input*, *lower*: *voltage output*)

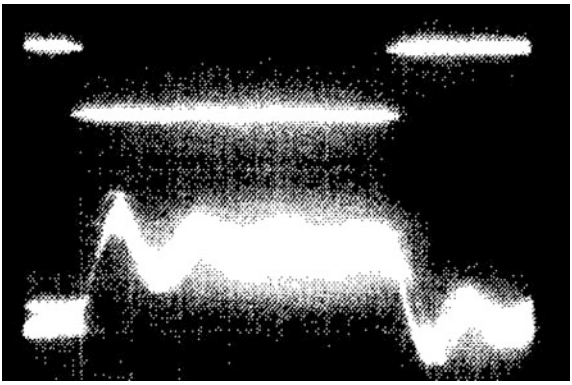

Fig. 5.25 Photograph of phase perturbed output voltage waveform $((\omega_s/\omega_r) : 1.00,$ $\phi : \pi/4$ rad, $C_o : 116$ μF, $R_L : 5\ \Omega, 100$ ms/*dev*; *upper: phase input, lower: voltage output*)

Now this is compared with the measured value for various switching frequencies as shown in Figs. 5.26, 5.27, 5.28 and 5.29. The time constant is less affected by the switching frequency when the load resistance is small as can be predicted by (5.28). A little discrepancy between the predicted and the measured is seemed to be due to the harmonics and parasitic resistances which have not been counted in the model.

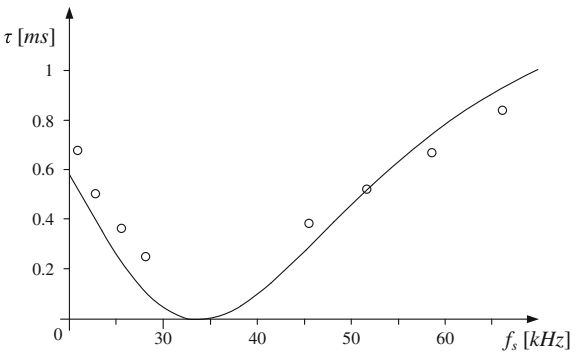

Fig. 5.26 Time constant versus switching frequency; predicted. Measured (C_o : 116 μF, R_L : 22 Ω)

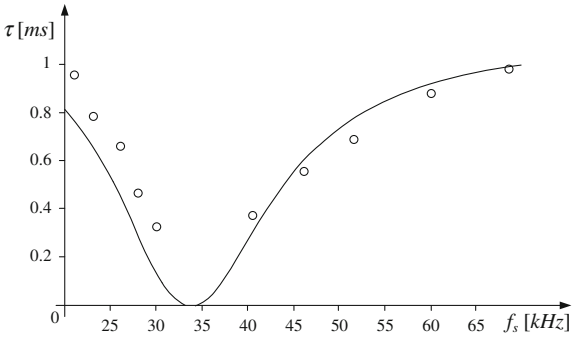

Fig. 5.27 Time constant versus switching frequency; predicted. Measured (C_o : 116 μF, R_L : 10 Ω)

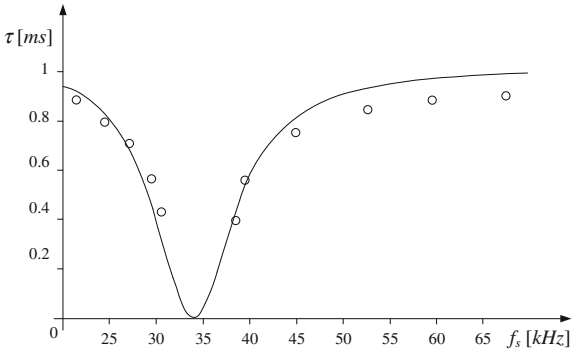

Fig. 5.28 Time constant versus switching frequency; predicted. Measured (C_o : 116 μF, R_L : 5 Ω)

5.5.2 *Time Constant Versus Output Capacitor*

As predicted by (5.28), the system time constant is proportional to the output capacitor as shown in Fig. 5.30 for two different load resistors. This confirms the fact that the system order is dominated by the output filter circuit.

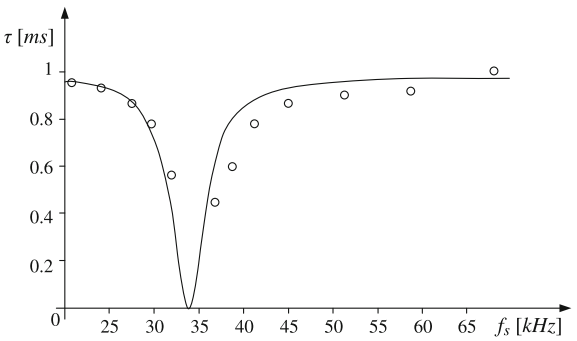

Fig. 5.29 Time constant versus switching frequency; predicted. Measured (C_o : 116 μF, R_L : 2.2 Ω)

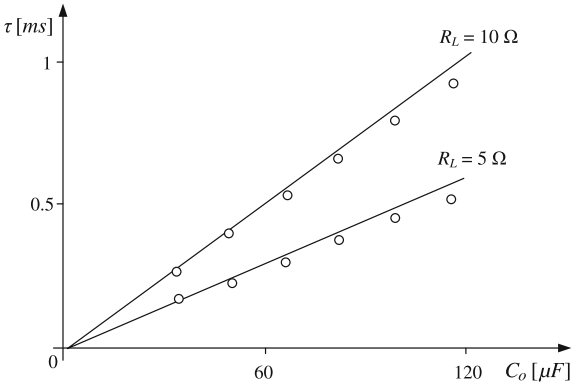

Fig. 5.30 Time constant versus output capacitor; *bold line* is the predicted and *circles* are the measured

5.5.3 Small Signal Phase Gain Versus Phase

To verify the gain of the proposed first order model the phase gain is selected as an example among the three kinds of small signal gains. Figures 5.31 and 5.32 show the phase gains for two different switching frequencies. The gain curves are nearly sinusoid as previously predicted by (5.25b).

5.5.4 Boundary Switching Frequency Versus Output Capacitor

The boundary switching frequency is experimentally measured by finding the critical switching frequency when the overshoot eventually appears in the system response.

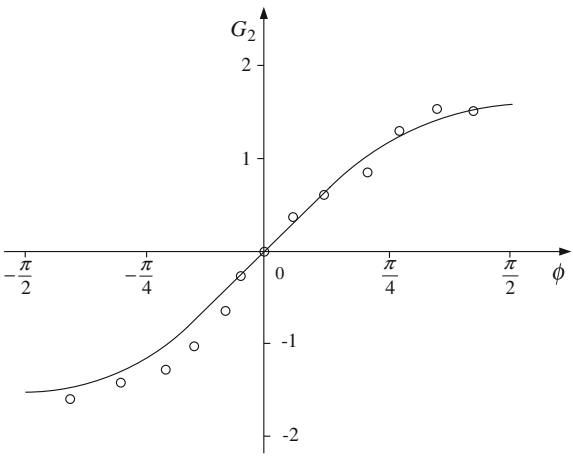

Fig. 5.31 Phase gain versus phase $((\omega_s/\omega_r) : 0.78,$ $C_o : 116\ \mu F,\ \ R_L = 5\ \Omega)$

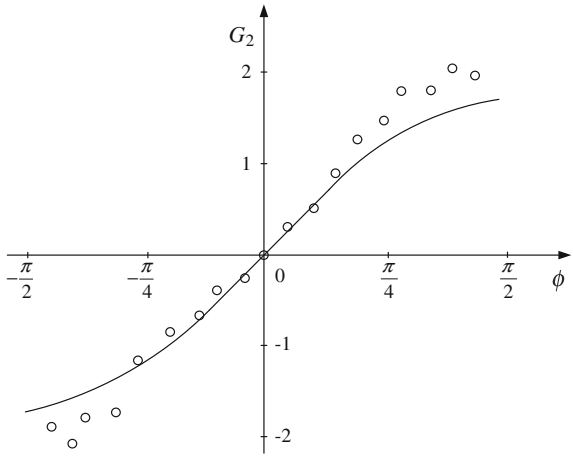

Fig. 5.32 Phase gain versus phase $((\omega_s/\omega_r) : 1.36,$ $C_o : 116\ \mu F,\ \ R_L = 5\ \Omega)$

Applying the approximation used in (5.19a, b, c)–(5.28) and setting the system time constant of (5.20) be the same as the first order time constant of (5.28) yield the following

$$\omega_d \approx \left\{1 + \frac{1}{4Q^2}\left(\frac{\omega_r}{\omega_d}\right)^2\right\}\frac{1}{C_o R_L} \tag{5.29}$$

Unfortunately (5.29) is not an explicit from, hence this cannot be solved by numerical computation. It is verified that (5.29) is enough for the rough prediction of the boundary switching frequency as shown in Figs. 5.33 and 5.34. And it is also identified that the practical SRC whose C_o is normally larger than 100 μF is a first

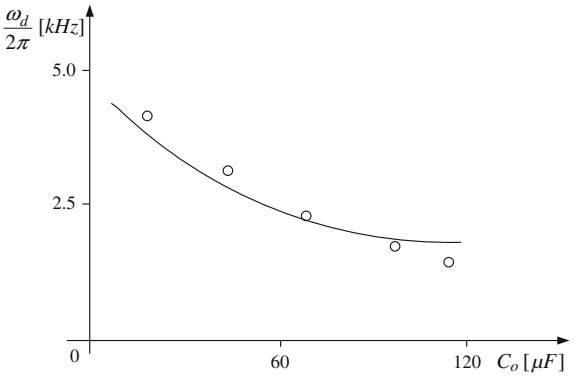

Fig. 5.33 Boundary switching frequency versus output filter: predicted; Measured ϕ : 0.942 rad, R_L : 5 Ω)

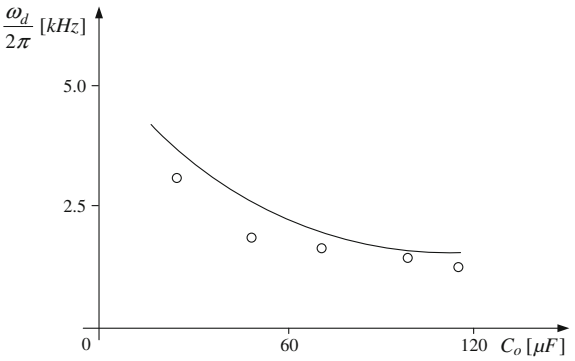

Fig. 5.34 Boundary switching frequency versus output filter: predicted; Measured ϕ : 0.942 rad, R_L : 2.5 Ω)

order system almost everywhere except the narrow switching frequency band within 2 kHz from the resonant frequency, which corresponds to at most 5 % of the resonant frequency.

5.6 Concluding Remarks

Throughout this chapter, the followings are newly explained and verified.

- The phasor transformation is newly proposed and utilized for the DC and AC analyses of the three control methods. So explicit and very simple analytical results are deduced from the equivalent time-invariant circuits obtained by the phasor transformation.
- The analytical results are verified by both the simulations and the experiments with good agreement with the theories. A little discrepancy between the theories and the experiments may arise no problem since this occurs at the region not used in practice.

- The time constant and the gain expressions have been widely explored. The system is modeled as the second order when ω_s is close to ω_r, whereas it is modeled as the first order when ω_s, deviates from ω_r. Furthermore the system order depends on load capacitor and resistor.
- The boundary switching frequency where the system order changes is estimated and verified by experiments that the system is practically first order almost everywhere except the very narrow frequency band near ω_r

It can be concluded that the phasor transformation is one of the basic and powerful analysis techniques for single phase AC systems, especially for the SRC.

References

1. Rim CT, Cho GH (1990) Phasor transformation and its application to the DC/AC analyses of frequency/phase controlled series resonant converters (SRC). IEEE Trans Power Electron 5 (2):201–211
2. Vorperian V, Cuk S (1982) A complete DC analysis of the series resonant converter. In: IEEE power electronics specialists conference record, pp 85–100
3. Vorperian V, Cuk S (1983) Small signal analysis of resonant converters. In: IEEE power electronics specialists conference record, pp 269–282
4. Witulski AF, Erickson RW (1985) Steady-state analysis of the series resonant converter. IEEE Trans Aerosp Electron AES-21(6):791–799
5. Witulski AF, Erickson RW (1987) Small signal AC equivalent circuit modeling of the series resonant converter. In: IEEE power electronics specialists conference record, pp 693–704
6. Freeland S, Middlebrook RD (1987) A unified analysis of converters with resonant switches. In: IEEE power electronics specialists conference record, pp 20–30
7. King RJ, Stuart TA (1985) Small-signal model of the series-resonant converter. IEEE Trans Aerosp Electron AES-21(3):301–319
8. Verghese GC, Elbuluk ME, Kassakian JG (1986) A general approach to sampled-data modeling for power electronic circuits. IEEE Trans Power Electron PE-1(2):76–89
9. Divan DM (1987) Design considerations for very high frequency resonant DC/DC converters. IEEE Trans Power Electron PE-2(1):45–54
10. Steigerwald RL (1988) A comparison of half-bridge resonant converter topologies. IEEE Trans Power Electron PE-3(2):174–182
11. Vorperian V (1989) Approximate small-signal analysis of the series and the parallel resonant converters. IEEE Trans Power Electron PE-4(1):15–24
12. Pitel IJ (1986) Phase-modulated resonant power conversion techniques for high-frequency link inverters. IEEE Trans Ind Appl IA-22(6):1044–1051
13. Rim CT, Hu DY, Cho GH (1988) The graphical DQ transformation of general power switching converters. In: IEEE-IAS conference record, pp 940–945
14. Joung GB, Rim CT, Cho GH (1989) Integral cycle-mode control of the series resonant converter. IEEE Trans Power Electron PE-4(1):83–91
15. Joung GB, Rim CT, Cho GH (1988) Modeling of quantum series resonant converters-controlled by integral cycle mode. In: IEEE-IAS conference record, pp 821–826

Chapter 6
Applications of Phasor Transformation to AC Circuits and Phasor Detectors

The detection of amplitude and phase information in single phase AC systems is quite challenging due to the lack of quadrature component, which is available in multi-phase AC systems. Phasor transformation can be used to the analysis of single phase AC systems only if the quadrature component is acquired. To fetch a reliable quadrature component from single phase AC systems containing harmonic noises, a derivative quadrature generator with appropriate filters is explained in this chapter. A low pass filter (LPF) optimizing the reductions of total harmonic distortion (THD) and response time of sensed signals is presented, surveying generalized n-th order filters. A lot of this chapter is written based on the original paper of mine [1].

6.1 Introduction

There are many single phase AC power applications such as single phase AC power grid, renewable energy sources, single phase AC converters, and various resonant converters. Fast and precise controls of them, however, are very often impeded by the slow and unreliable amplitude and phase information, i.e. the phasor of sensed voltage or current signals. For example, the power grids connected to sensitive loads such as network computers, data centers, and semiconductor facilities require fast and reliable detections of phasor to switch over power source swiftly [2, 3]. This is why there are several phasor detector literatures for single phase AC systems [4–8]. To obtain the amplitude and phase information of a phasor from a sensed signal v_s, the quadrature component v_β orthogonal to a direct one v_α should be obtained first, then these variables in the rotary frame are transformed to the DQ variables in the stationary frame, as shown in Fig. 6.1.

C.T. Rim, *Phasor Power Electronics*, KAIST Research Series,
DOI 10.1007/978-981-10-0536-7_6

In three phase AC power systems, the DQ information can be easily extracted from their balanced three phase abc variables by appropriate DQ transformations. Ideally, there are no time delay due to the DQ transformation and no need for noise filtering to obtain the DQ information. In the single phase AC power systems, however, there are several issues to be considered concerning the generation of quadrature component. The first issue is the harmonic noise of the sensing signal. For instance, the third and fifth harmonics are dominant and difficult to reduce in most cases. When the noise is not reasonably canceled out in the α-β quadrature generator of Fig. 6.1, the control process using this signal cannot be accurate. The second issue is the response of the quadrature generator for an abrupt change of v_s. In the on-line electric vehicle (OLEV) system [9–12] of 20 kHz operating frequency, for example, fast moving vehicles are considered as rapidly changing loads. To achieve a proper control for regulating voltage and current fluctuation within a few cycles, quite fast quadrature generator of sub milliseconds is essential.

There are a few conventional schemes for the quadrature generation: transport delay [13], Hilbert transformation [14], inverse Park transformation [15], second order generalization integrators (SOGI) [16–18], and the capacitor voltage and current method [19]. Most conventional methods contains follow problems: frequency dependency, high complexity, nonlinearity, and lack of filtering ability. Although a better result have been reported by SOGI which is the latest scheme, a trade-off issue between a dynamic system response and a filtering performance still exists [20, 21].

In this chapter, a new quadrature generator which does not use integrator but use a differentiator to acquire quadrature component from the sensing signal v_s is proposed, which is especially well suited for the single phase AC system requiring fast response time. The pre-processor of the differentiator, composed of a low pass filter (LPF) and an all pass filter (APF), are used to increase the noise immunity. Section 6.2 introduces the concept of the derivative quadrature generator and its design flow. The implementation of the quadrature generator and its experimental verifications are described in Sect. 6.3.

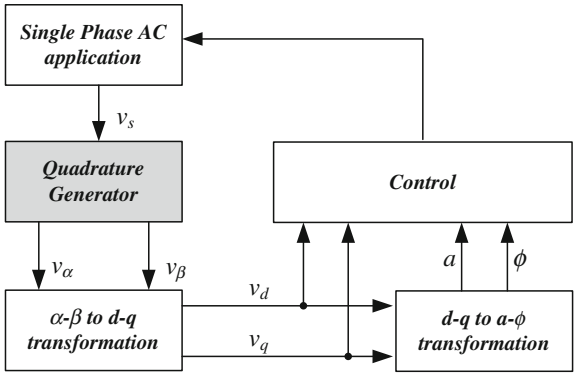

Fig. 6.1 Proposed single phase AC system with a phasor detector

6.2 Design of the Derivative Quadrature Generator

6.2.1 *Derivative or Integral Method for Quadrature Generator*

The orthogonal component against a sinusoidal signal can be obtained by using an integrator or a differentiator. The integrator, however, has the offset problem due to the initial value, which generates the offset error when the sensing signal is abruptly changed at the nonzero point, as shown in Fig. 6.2. So it is difficult to use the integrator for the quadrature generator. Therefore, the differentiator which does not have the offset problem, as shown in Fig. 6.2, was preferred in this book, even though it has the impulse output noise problem for a step load change.

The input v_s of the proposed derivative quadrature generator consists of v_f and v_h which are the fundamental and harmonic components of v_s, respectively, as shown in Fig. 6.3. The LPF attenuates the harmonic components v_h, but it causes a phase shift in v_f. To compensate this phase shift, the APF is adopted; hence, the phase of the output v_α of the APF becomes identical to v_f.

The dynamic phasor of v_α can be defined, in general, as follows [22].

$$v_\alpha = \mathrm{Im}\{ae^{j(\omega_s t+\phi)}\} = \mathrm{Im}\{(ae^{j\phi})e^{j\omega_s t}\}, \tag{6.1}$$

where $ae^{j\phi}$ is the phasor of v_α in which a and ϕ are the time varying amplitude and phase information, respectively. The angular frequency of the signal ω_s is, however, assumed to be constant in this chapter.

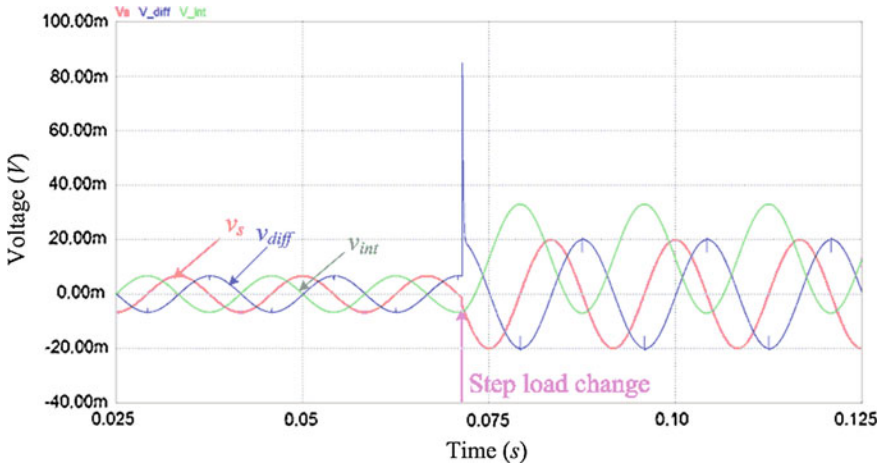

Fig. 6.2 Simulation results for a derivative (v_{diff}) and an integral (v_{int}) method to obtain the orthogonal component of a sensed signal (v_s)

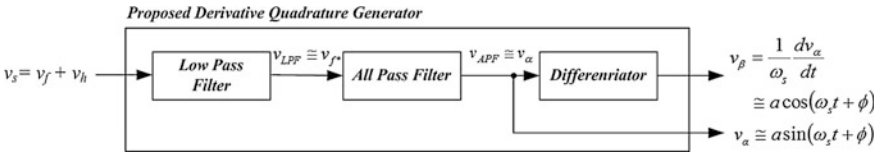

Fig. 6.3 Proposed derivative quadrature generator

Then, the differentiator output v_β can be derived as follows.

$$v_\beta \equiv \frac{1}{\omega_s}\frac{dv_\alpha}{dt} = \frac{1}{\omega_s}\mathrm{Im}\left\{\left(\frac{da}{dt} + j\frac{d\phi}{dt}a + j\omega_s a\right)e^{j(\omega_s t+\phi)}\right\} \tag{6.2}$$

In the quasi steady state, the time derivative terms in (6.2) become diminish as follows.

$$\frac{da}{dt} \cong 0, \frac{d\phi}{dt} \cong 0 \tag{6.3}$$

Therefore, v_α and v_β are approximately expressed as follows.

$$v_\alpha = \mathrm{Im}\left\{ae^{j(\omega_s t+\phi)}\right\} = a\sin(\omega_s t + \phi) \tag{6.4}$$

and

$$v_\beta \cong \mathrm{Im}\left\{jae^{j(\omega_s t+\phi)}\right\} = a\cos(\omega_s t + \phi) \tag{6.5}$$

6.2.2 Selection of Low Pass Filter

The differentiator amplifies high frequency noises in general. To reduce the high frequency noises, the LPF should be used. Because the response time and harmonic noise are important system parameters of the quadrature generator, the system order and cutoff frequency of the LPF should be carefully selected.

Because it is hardly possible to determine the response time of the LPF higher than the 3rd order system analytically, it was determined by simulations for a given transfer function $H_n(s)$, where a generalized form is as follows.

$$H_n(s) = \frac{\omega_c^n}{(s-p_1)(s-p_2)\cdots(s-p_n)}, \quad n = 1, 2, \tag{6.6}$$

where ω_c is the cutoff frequency for the n-th order LPF. The Butterworth filter, which was adopted in this book because of its flat frequency response, has the pole p_k as follow [23]:

$$p_k = \omega_c e^{j\frac{(2k+n-1)}{2n}\pi}, \quad k = 1, 2, \ldots, n \tag{6.7}$$

As shown in Fig. 6.4, the rising time is inversely proportional to the cutoff frequency of the LPF in general, and it is higher for a higher system order LPF.

Another important system parameter is the THD of v_β, which is determined by the characteristics of the LPF, APF, and differentiator, as shown in Fig. 6.3. To reduce the high frequency noise which is amplified by the differentiator, the LPF has to sufficiently attenuate the high frequency noise. In other words, the system order of the LPF should be higher than two, as identified from Fig. 6.5.

Because the low order harmonic components such as the 3rd and 5th harmonics are critical for the performance of the quadrature generator, 10 % of the 3rd and 5th harmonics are included in the simulations for various LPFs. Figure 6.5 shows that the harmonic reduction for higher system order than three is not significant. It is identified that there are trade-off relationships between the rising time and the THD characteristics by using simulation results in Figs. 6.4 and 6.5. Selecting optimal cutoff frequency and system order of the LPF, therefore, highly depends on every applied

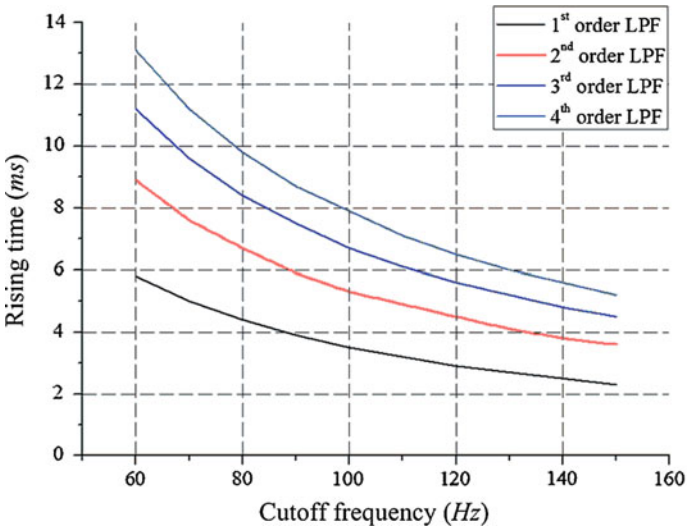

Fig. 6.4 Simulation results for the rising time of different system order LPFs according to various cutoff frequencies in step response

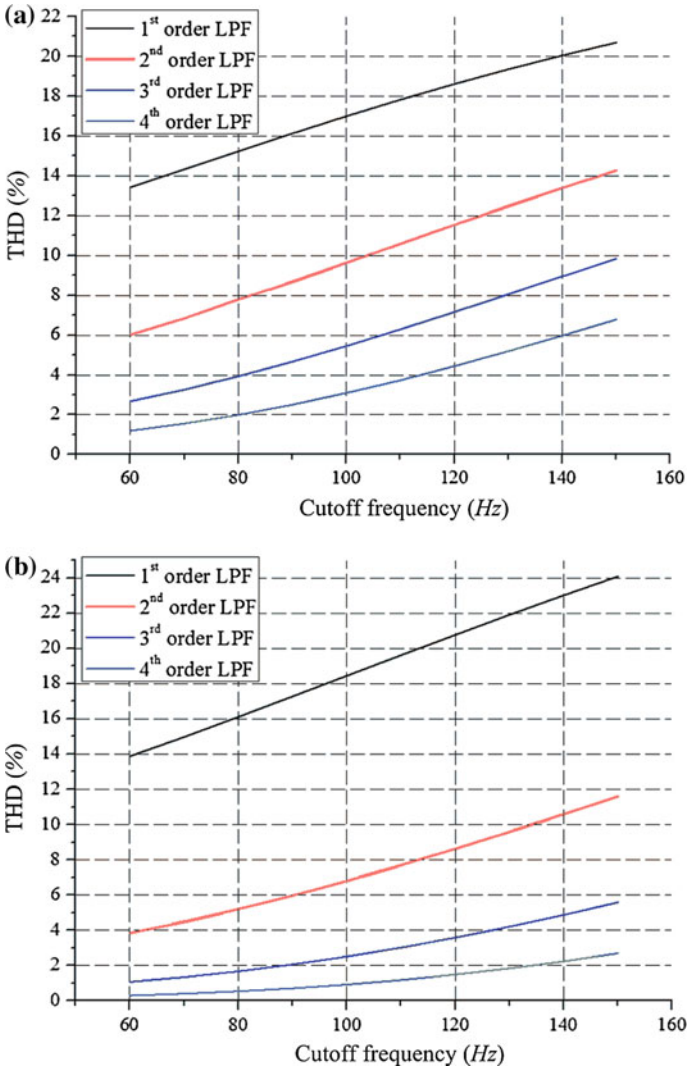

Fig. 6.5 Simulation results for the THD of v_β of different system order LPFs according to various cutoff frequencies. **a** When v_s includes 10 % of 3rd order harmonic. **b** When v_s includes 10 % of 5th order harmonic

system which requires different rising time and THD performance. For the single phase 60 Hz AC systems which has low order harmonic components, a 3rd system order LPF with above 100 Hz cutoff frequency, which has reasonably short rising time and fine harmonic reduction ability, is proper, as shown in Figs. 6.4 and 6.5.

Before heading to the next step which is an APF design, the 3rd system order LPF with 120 Hz cutoff frequency is selected for satisfying two system parameters.

The rising time and the THD of v_β for selecting the LPF are respectively assumed as less than half cycle of 60 Hz, i.e. 8.33 *ms*, and 6 %.

Two bode plots for input v_{f*} and output v_α of APF are shown in Fig. 6.6. As shown in Fig. 6.6a, the LPF occurs the phase shift of v_f, while it diminish the harmonic components. To compensate this phase difference between v_f and v_{f*}, the APF is designed. The transfer function $H_{APF}(s)$ of the APF is derived as

$$H_{APF}(s) = \frac{s - \omega_s}{s + \omega_s}, \tag{6.8}$$

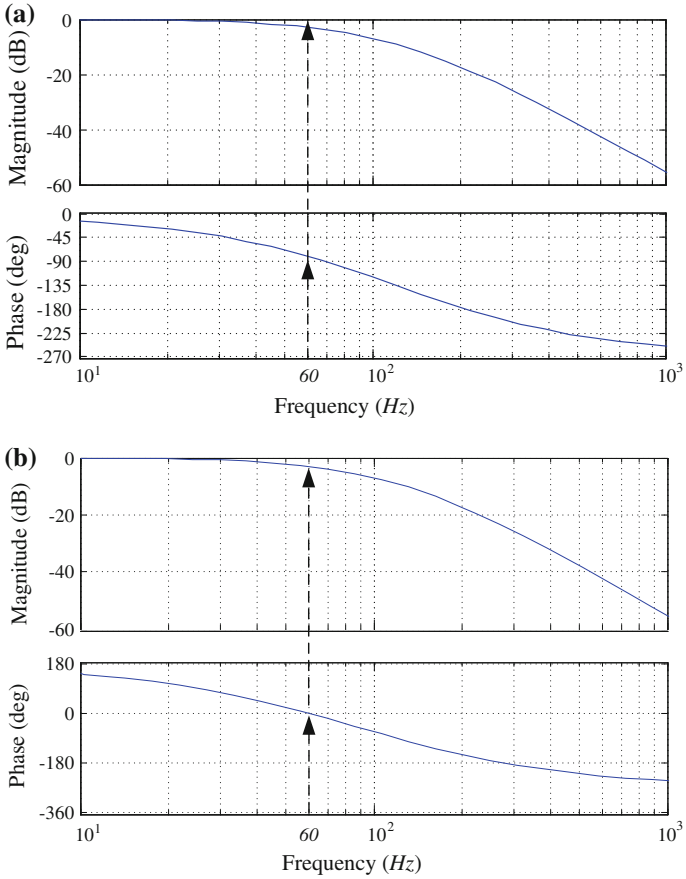

Fig. 6.6 Simulation results for the phase correction of the APF for the 3rd order LPF example. **a** The input of the APF v_{f*} (120 Hz cutoff frequency). **b** The output of the APF v_α, which has been phase-corrected

where ω_s is the target frequency that makes 90° phase shift [24]. By adding the APF after the LPF, the phase of v_α at 60 Hz is corrected to become in phase with v_s, as shown in Fig. 6.5b.

By organizing the proposed quadrature generator with the selected LPF, APF, and differentiator, the two orthogonal signals are generated as outputs. The each transfer function for v_α and v_β can be derived as

$$H_\alpha(s) = H_3(s) \times H_{APF}(s) \tag{6.9}$$

$$H_\beta(s) = H_3(s) \times H_{APF}(s) \times H_{diff}(s), \tag{6.10}$$

where the transfer function $H_{diff}(s)$ of the differentiator is defined by ω_s which is the frequency that the magnitude intersects with 0-dB line as

$$H_{diff}(s) = \frac{s}{\omega_s}. \tag{6.11}$$

Compared to the SOGI which is one of the conventional schemes introduced in [14], the (6.9) and (6.10) show the same transfer functions for v_α and v_β when the system order of LPF is two. By changing the system order of LPF, the proposed derivative quadrature generator can modulate the noise reduction rate as against the SOGI.

6.2.3 *Amplitude and Phase Detection and Simulation Results*

The time-varying amplitude a and phase ϕ of the v_s can be derived from (6.4)–(6.5) as follows.

$$a \cong \sqrt{v_\alpha^2 + v_\beta^2} = \sqrt{v_d^2 + v_q^2} \tag{6.12}$$

$$\phi = \tan^{-1}\frac{v_q}{v_d} \tag{6.13}$$

where the v_d and v_q is defined as

$$\begin{pmatrix} v_d \\ v_q \end{pmatrix} = \begin{pmatrix} \cos\omega_s t & -\sin\omega_s t \\ \sin\omega_s t & \cos\omega_s t \end{pmatrix} \begin{pmatrix} v_\alpha \\ v_\beta \end{pmatrix}. \tag{6.14}$$

The v_d and v_q are calculated as

$$v_d = a \sin\phi \tag{6.15}$$

$$v_q = a \cos\phi, \tag{6.16}$$

where $\omega_s t$ is the angle difference between DQ and α-β reference frames.

The simulation for verifying the designed quadrature generator is conducted when the v_s includes 10 % of 3rd order harmonic component as shown in Fig. 6.7. Under the step resistive load change, moreover, the amplitude a follows the change of v_s well.

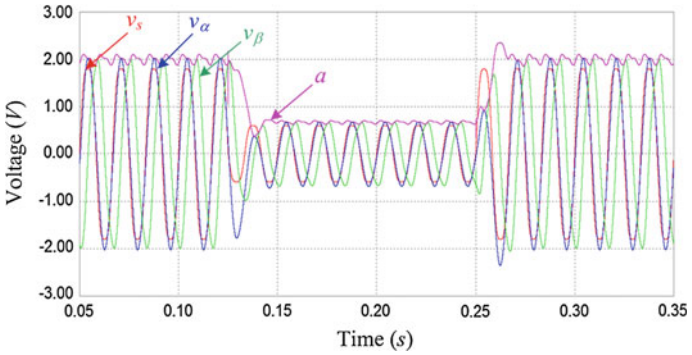

Fig. 6.7 Simulation results of proposed derivative quadrature generator

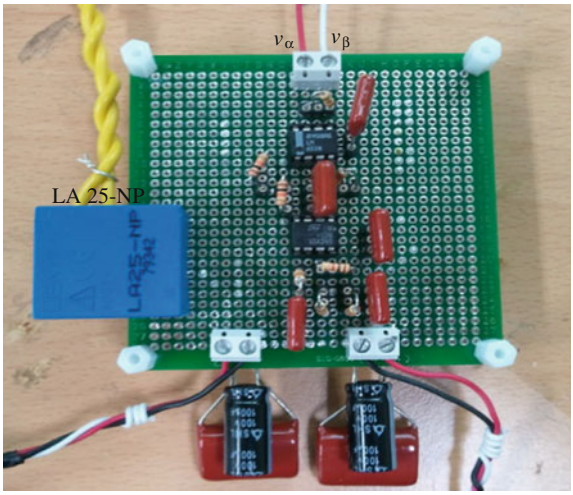

Fig. 6.8 The implementation of the quadrature generator

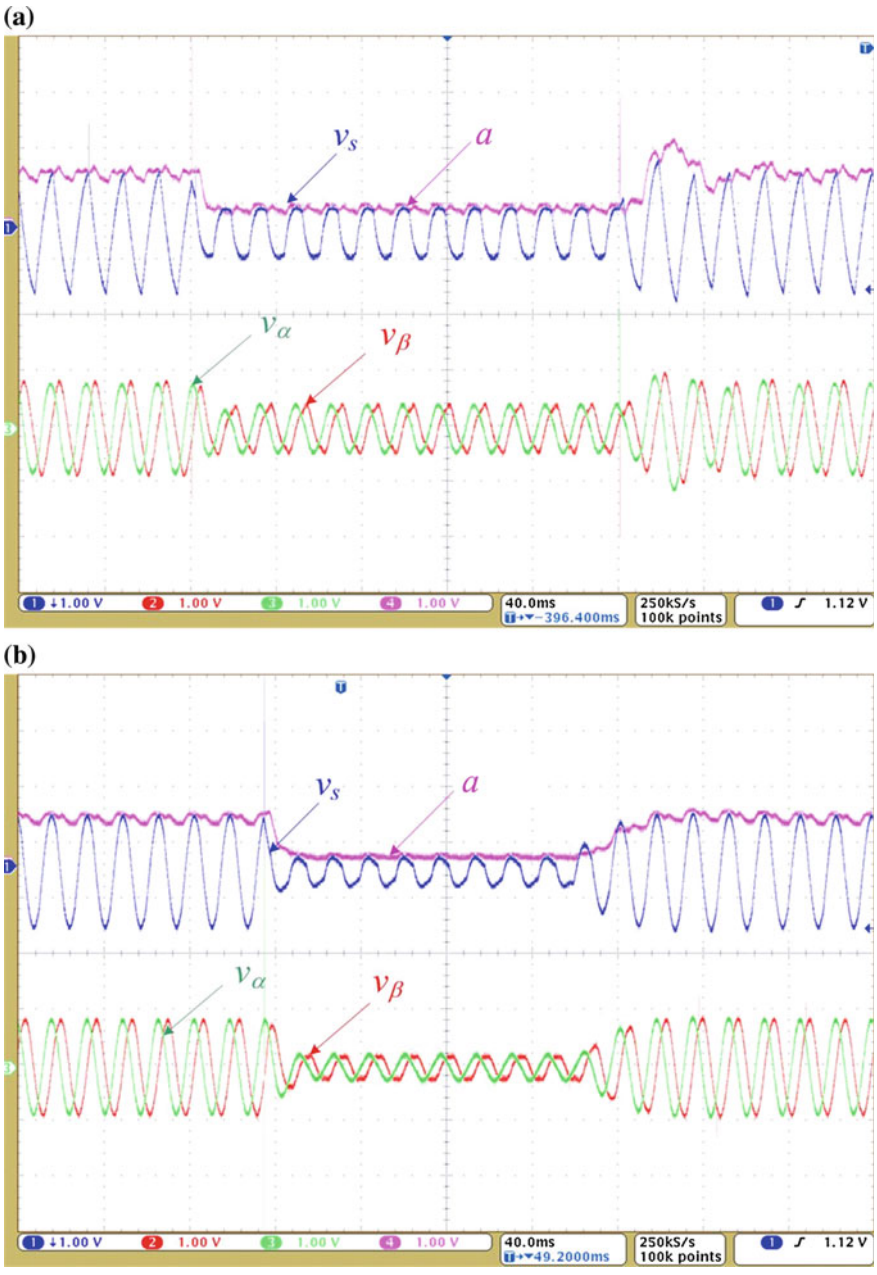

Fig. 6.9 Experimental results of the proposed derivative quadrature generator. **a** Experimental waveforms for high THD case. **b** Experimental waveforms for low THD case

6.3 Experimental Verification with a 60 Hz Single Phase Inverter

The proposed derivative quadrature generator was built based on the proposed design procedure and verified with 60 Hz single phase inverter. The derivative quadrature generator was implemented by using a LA 25-NP current transducer, several analog operational amplifier, and passive elements for organizing the selected LPF, APF, and differentiator, as shown in Fig. 6.8.

To verify the performance of the proposed derivative quadrature generator, each experiment was conducted for the high THD case and low THD case as shown in Fig. 6.9.

For the two THD cases, the v_s was manipulated to have high THD of 9.33 % and low THD of 2.77 % by combining 3rd and 5th order harmonic components. The THDs of sensed load current signal v_s, and the two orthogonal signals from the derivative quadrature generator v_α and v_β were measured by a WT1600 digital power meter, as summarized in Tables 6.1 and 6.2.

The noise immunity abilities were verified by the measured THDs which are well matched with the simulation results introduced in Sect. 6.2. From the experimental results of high THD case, it is also identified that the system order and cutoff frequency of LPF should be re-designed when the other applied system requires low THD of v_β which is less than 6.39 %.

The rising and falling times were measured for verifying the dynamic response of the proposed phase detector, and the both rising and falling times were found to be less than a half cycle for a step change input signal, as shown in Fig. 6.10.

Table 6.1 The measured THDs for high THD case

	v_s	v_α	v_β
3rd (%)	8.32	2.08	6.15
5th (%)	3.14	0.37	1.51
THD (%)	9.33	2.12	6.39

Table 6.2 The measured THDs for low THD case

	v_s	v_α	v_β
3rd (%)	2.77	0.72	2.09
5th (%)	1.18	0.11	0.46
THD (%)	3.16	0.79	2.2

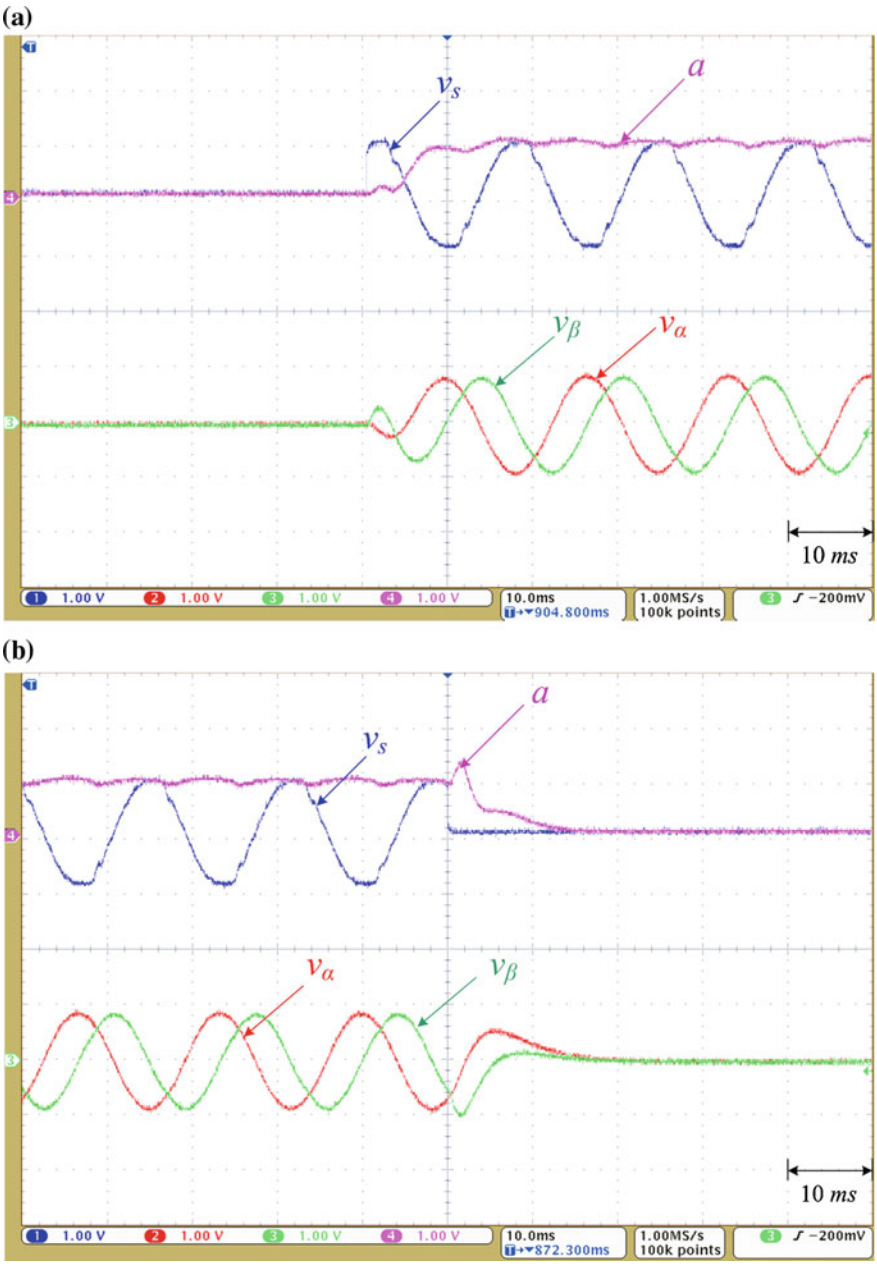

Fig. 6.10 Experimental results for dynamic system responses. **a** Experimental waveforms for rising time (6.8 ms). **b** Experimental waveforms for falling time (7.7 ms)

6.4 Concluding Remarks

In this chapter, a new quadrature generator for single phase AC power systems based on the differentiator is presented. The proposed quadrature generator has fast dynamic response by using the differentiator, and it has good noise immunity by adopting the 3rd system order LPF. The design procedure for the quadrature generator shows the better noise immunity characteristic can be obtained by trading off the system response time. The performance of proposed quadrature generator and its design procedure has been validated by the experimental results.

References

1. Choi BH, Lee SW, Yeo IY, Rim CT (2012) Fast and reliable phasor detectors for single phase AC systems by derivative quadrature generation. In: ECCE-Asia 2012, pp 609–614
2. Thapar A, Saha TK, Dong ZY (2004) Investigation of power quality categorisation and simulating it's impact on sensitive electronic equipment. In: Power engineering society general meeting, IEEE, vol 1, pp. 528–533
3. Matsushita K et al (1996) Study for the performance of high speed switchgear for protection of in-house generation system. In: Industrial and commercial power systems technical conference, pp 91–95
4. Thacker T, Boroyevich D, Burgos R, Fei W (2011) Phase-locked loop noise reduction via phase detector implementation for single-phase systems. IEEE Trans Ind Electron 58(6):2482–2490
5. Shinnaka S (2008) A robust single phase PLL system with stable and fast tracking. IEEE Trans Ind Appl 44(2):624–633
6. Choi JW, Kim YK, Kim HG (2006) Digital PLL control for sing-phase photovoltaic system. In: IEE proceedings electric power applications, vol 153, no 1, pp 40–46
7. Shinnaka S (2011) A novel fast-tracking D-estimation method for single-phase signals. IEEE Trans Power Electron 26(4):1081–1088
8. Saitou N, Matsui M, Shimizu T (2003) A control strategy of single-phase active filter using a novel DQ transformation. Ind Appl Conf IAS 2:1222–1227
9. Huh J, Rim SW, Lee WY, Cho GH, Chun CT (2011) Narrow-width inductive power transfer system for online electrical vehicles. IEEE Trans Power Electron 26(12):3666–3679
10. Huh J, Lee SW, Park CB, Cho GH, Rim CT (2010) High performance inductive power transfer system with narrow rail width for on-line electric vehicles. In: Energy conversion congress and exposition (ECCE), pp 647–651
11. Huh J, Lee WY, Cho GH, Lee BH, Rim CT (2011) Characterization of novel inductive power transfer systems for on-line electric vehicles. In: Applied power electronics conference and exposition (*APEC*), pp 1975–1979
12. Lee SW et al (2010) On-line electric vehicle using inductive power transfer. In: Energy conversion congress and exposition (ECCE), pp 1598–1601
13. Silva SM, Lopes BM, Filho BJC, Campana RP (2004) Performance evaluation of PLL algorithms for single-phase grid-connected systems. Ind Appl Conf 4:2259–2263
14. Saitou M, Simizu T (2002) Generalized theory of instantaneous active and reactive powers in single-phase circuits based on Hilbert transform. In: IEEE Power Electronics Specialists Conference (PESC), pp 1419–1424
15. Silva SM, Arruda LN, Filho BJC (2000) Wide bandwidth single and three-phase PLL structures for frid-tied PV systems. In: Photovoltaic Specialists Conference, pp 1660–1663

16. Ciobotaru M, Teodorescu R, Blaabjerg F (2006) A new single-phase PLL structure based on second order generalized integrator, In: IEEE power electronics specialists conference (PESC), pp 1–6
17. Xiaomin Y, Merk W, Stemmler H, Allemeling J (2002) Stationary-frame generalized integrators for current control of active power filters with zero steady-state error for current harmonics of concern under unbalanced and distorted operating conditions. IEEE Trans. Ind Appl 38(2):523–532
18. Teodorescu R, Blaabjerg F, Borup U, Liserre M (2004) A new control structure for grid-connected LCL PV inverters with zero steady-state error and selective harmonic compensation. In: Applied power electronics conference and exposition (APEC), pp 580–586
19. Chung SK, Shin HB, Lee HW (2005) Precision control of single-phase PWM inverter using PLL compensation. In: IEE proceedings electric power applications, vol 152, no 2, pp 1350–2352
20. Nicastri A, Nagliero A (2010) Comparison and evaluation of the PLL techniques for the design of the grid-connected inverter systems. In: IEEE international symposium on industrial electronics (ISIE), pp 3865–3870
21. Ferreira RJ, Araujo RE, Pecas Lopes JA (2011) A comparative analysis and implementaion of various PLL techniques applied to single-phase grids. In: International youth conference on energetics (IYCE), pp 1–8
22. Rim Chun T (2011) Unified general phasor transformation for AC converters. IEEE Trans Power Electron 26(9):2465–2475
23. Zhongshen L (2007) Design and analysis of improved butterworth low pass filter. In: International conference on electronic measurement and instruments, pp 1729–1732
24. Budak A (1978) Circuit theory fundamentals and application. Prentice-Hall

Chapter 7
Application of Phasor Transformation to Static Analyses of LED Drivers

In this chapter, another example of applying the static phasor transformation to an LED driver is explained. This chapter is useful to see an aspect of modern LED drivers. Innovative passive LED drivers that can reduce the total harmonic distortion (THD) significantly by LC parallel resonance are suggested in this chapter. Using an inductor and three capacitors, called LC3, novel characteristics such as high efficiency and power factor (PF) with extremely long life time are achieved. The proposed LED drivers have a temperature-robust characteristic because their power is hardly changed by temperature, selecting the number of LED in series ns appropriately so that the LED power variation due to temperature change in LED can be zero. For the universal use of the proposed LED drivers in various countries with different source voltages and frequencies, circuit configurations applicable to 110/220 V and/or 50/60 Hz are proposed. To analyze the power and PF of the proposed LED driver, the phasor transformation was firstly applied to a non-linear diode rectifier modeling. Nevertheless, this non-linear switching, the proposed analyses agreed well with simulation and experiment results. A prototype LED driver showed a very high power efficiency of 95.2 % at 70 W, meeting PF and THD regulations for source voltage variation of ±6 % of 220 V, though a reasonably small filter was used. A lot of this chapter is written based on our paper [1].

7.1 Introduction

Since LEDs have higher efficacy than that of fluorescent lamps as well as much longer lifetimes [2–7], conventional lamps are being replaced with LEDs. The change of lamps to LEDs, however, has been slow because of the high cost of LEDs and their drivers as well as the short lifetimes of the drivers [8]. It is quite important for LED drivers to have a longer lifetime than LEDs so that the LED lamps can operate for more than 50,000 h. LED drivers, in general, should be able to regulate or control LED power level, guarantee high input power factor (PF) and

C.T. Rim, *Phasor Power Electronics*, KAIST Research Series,
DOI 10.1007/978-981-10-0536-7_7

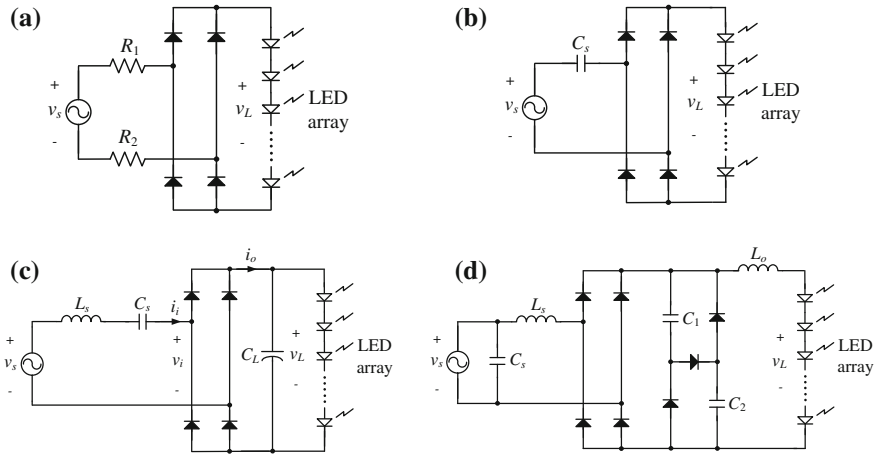

Fig. 7.1 Conventional passive LED drivers, showing long lifetime but sensitivity to LED temperature. **a** A resistor-type LED driver [30]. **b** A capacitor-type LED driver [31]. **c** An LC-series-resonance-type LED driver [32]. **d** A valley-fill-type LED driver [33]

low total harmonic distortion (THD). For example, the PF should be greater than 0.9 for LED power ≥5 W according to Energy Star Requirement for Solid [9], and the THD should satisfy the IEC 61000-3-2 class C standard [10]. Conventionally, switch-mode-power-supply(SMPS)-type LED drivers, which typically include active switches, control ICs, and passive circuit elements, have been widely used to meet the requirements [11–29]. They usually provide LEDs with constant currents by PWM switching techniques with a feedback control. The SMPS-type LED drivers, however, typically have low power efficiencies, which result in large power loss and high junction temperature of the switching devices. Together with DC electrolytic capacitors, this high junction temperature shortens the lifetime of the conventional LED drivers.

In order to overcome these drawbacks, passive-type LED drivers that consist of just passive components, such as inductors, capacitors, and diodes, have been recently proposed [30–35], as shown in Fig. 7.1. One of the simplest passive LED drivers is the resistor-type LED driver, composed of a bridge diode, a resistor, and a capacitor [30], as shown in Fig. 7.1a. The LED power variation is mitigated by the resistor; however, the power efficiency is inevitably deteriorated due to the power dissipation in the resistor. A more simplified and efficient one is the capacitor-type LED driver, which consists of a capacitor and a bridge diode [31]. Because no resistive element is used in this circuit, very high power efficiency of 98 % can be easily achieved [31]. However, due to the use of a capacitor only, the PF is as low as 0.71. To solve this problem, the LC-series-resonance-type LED driver, as shown in Fig. 7.1c, was proposed [32]. The LC resonant frequency of this circuit is tuned close to the source frequency in order to achieve good PF and THD characteristics. The LC filter size, however, should be very large due to the low source frequency of

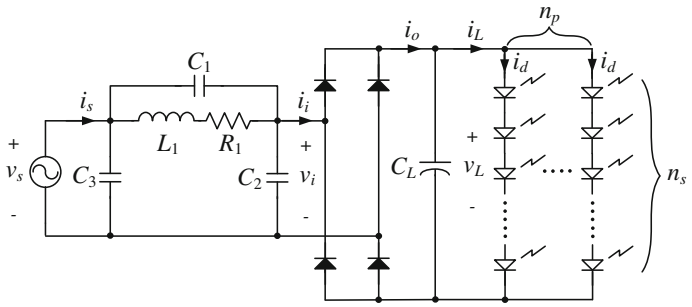

Fig. 7.2 The proposed LC^3 LED driver, which is quite insensitive to LED temperature, meeting PF and THD requirements

50 or 60 Hz. A valley-fill-type LED driver, as shown in Fig. 7.1d, was also proposed [33] in order to remove electrolyte capacitors.

Large-size capacitors should be used for the valley-fill filter to avoid flickering. Furthermore, a large number of passive components including two bulky inductors causes a cost increase and high power loss, i.e. relatively low power efficiency of 93.6 % [33]. These passive LED drivers mentioned so far usually have long life-times and high power efficiency because passive circuit elements are quite robust and free from high frequency switching loss. In some cases, however, PF and THD may not be satisfied by the use of passive elements only [30, 31]. In addition, the LED power may change due to high operating temperature and variation of source voltage because there is no means of regulating the LED power.

In this chapter, compact passive LC^3 LED drivers that achieve low THD and high PF by using LC parallel resonance are newly proposed, as shown in Fig. 7.2. An optimum number of LED array in series is appropriately selected such that the LED power becomes temperature-robust. Furthermore, the LED drivers can operate at both 50 and 60 Hz as well as either 110 or 220 V. The proposed LED drivers are analyzed by the powerful phasor transformation techniques [36–41], which were even applied to wireless power transfer systems [42–44], but their application to the non-linear switching case occurs for the first time in this paper. Experimental verification of the phasor transformation for the proposed LED driver showed good agreements with simulations and designs.

7.2 Static Analysis of the Proposed LED Driver

The proposed LED driver is illustrated in Fig. 7.2, where the source side filters L_1, C_1, and C_2 together with the number of LED array in series n_s determine the line PF, THD in source current i_s, and LED load power P_L. The source side capacitor C_3 is just for PF compensation whereas the load side electrolyte capacitor C_L is for smoothing the LED array voltage v_L. The LED array is composed of n_p number of

parallel sub-arrays, as shown in Fig. 7.2. The steady state behaviors of the proposed LED driver will be analyzed in this chapter by neglecting high-order switching harmonics, and appropriate designing of circuit parameters will be provided. The internal resistance of L_1 is considered as R_1, but the ESRs of capacitors are omitted from consideration throughout this chapter. The characteristics of all the LEDs are assumed to be identical, and temperature distribution over the LED array is even. The source voltage is given and assumed to be fixed. All the circuit parameters are assumed to be ideal unless otherwise specified.

7.2.1 *Equivalent Circuit Modeling of the Proposed LED Driver*

As shown in Fig. 7.3, each LED in an array can be replaced with a dynamic resistance r_d and a DC voltage source V_d [17]. According to the general equivalence of a converter with a time-varying transformer [36, 37], the full bridge diode rectifier can be replaced with a time-varying transformer, whose turn-ratio is a switching function $s(t)$ at the source frequency [37], as shown in Fig. 7.3a, b. Only the fundamental components of voltages and currents of the circuit are considered, and all harmonics are neglected from consideration in this chapter, and it is assumed that input and output filters moderately attenuate the switching harmonics.

In order to analyze the proposed circuit, the well-known phasor transformation [36–41] is applied to the time-varying fundamental component equivalent circuit of Fig. 7.3, as shown in Fig. 7.4. Then a time-invariant complex circuit with α [36] is obtained.

A simplified static circuit, neglecting dynamic behavior, is derived for the static analysis, as shown in Fig. 7.4. In the phasor transformation, the rectified current at the DC output side should include only real value in general and should not contain any imaginary components [38]. Therefore, the input current of the auto-transformer I_i ($= I_L/\alpha$) should be also real in case the phase reference is tuned to the diode rectifier. In the phasor transformation, the selection of a reference phase

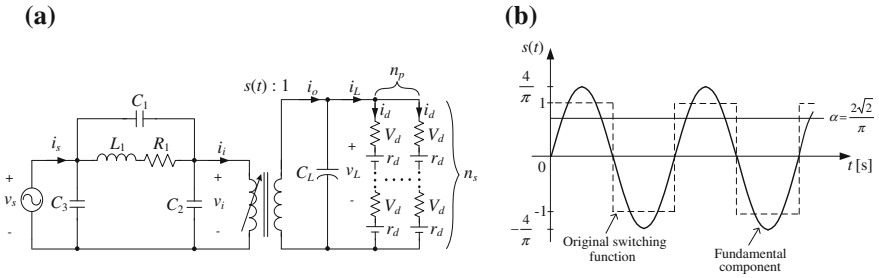

Fig. 7.3 Large signal AC equivalent circuit of Fig. 7.2 replacing each LED with a linear approximated model. **a** A time-varying fundamental component equivalent circuit. **b** Switching waveforms of an ideal time-varying transformer

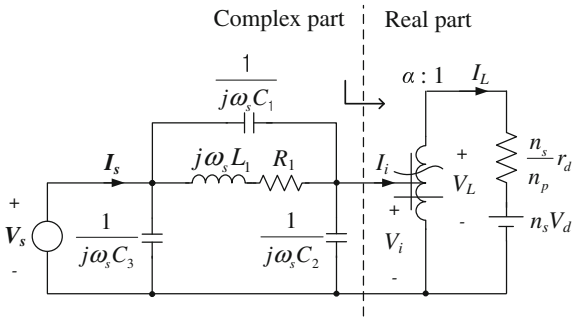

Fig. 7.4 A static phasor circuit, where the rectified current I_L is always real

may be arbitrary; hence, the phase of the rectifier is set to zero for simplicity of analysis, and the phase of source voltage ϕ_s is unknown at the moment. Throughout this chapter, the bridge diode is assumed to be lossless and ideal, with a fixed turn-ratio of α.

The remaining work is to find the source voltage $\boldsymbol{V_s}$ and the source current $\boldsymbol{I_s}$ of a complex variable so that I_i can be real, where the magnitude V_s is given and the magnitude I_s, the phase ϕ_s, and ϕ_s' should be determined. $\boldsymbol{V_s}$ and $\boldsymbol{I_s}$ can be defined as follows:

$$\boldsymbol{V_s} \equiv V_s e^{j\phi_s} \tag{7.1}$$

$$\boldsymbol{I_s} \equiv I_s e^{j\phi_s'}. \tag{7.2}$$

Let us determine ϕ_s first. By reflecting the turn-ratio of auto-transformer to an equivalent circuit seen from left part, Fig. 7.4 can be converted to Fig. 7.5a. In Fig. 7.5, the $\boldsymbol{Z_1}$, $\boldsymbol{Z_2}$, $\boldsymbol{Z_3}$, R_e, and V_e are defined as follows:

$$\boldsymbol{Z_1} = (j\omega_s L_1 + R_1) // \frac{1}{j\omega_s C_1}, \quad \boldsymbol{Z_2} = \frac{1}{j\omega_s C_2}, \quad \boldsymbol{Z_3} = \frac{1}{j\omega_s C_3} \tag{7.3}$$

$$R_e = \alpha^2 \frac{n_s}{n_p} r_d, \quad V_e = \alpha n_s V_d. \tag{7.4}$$

By applying the Thevenin's theorem to the left part of the circuit of Fig. 7.5a, a simplified static circuit is finally obtained, as shown in Fig. 7.5b, where $\boldsymbol{V_t}$ and $\boldsymbol{Z_t}$ are derived as follows:

$$\boldsymbol{V_t} = \boldsymbol{V_s} \frac{\boldsymbol{Z_2}}{\boldsymbol{Z_1} + \boldsymbol{Z_2}} \equiv (V_s e^{j\phi_s}) \cdot (\gamma e^{j\phi_\gamma}) = V_t e^{j\phi_t} \tag{7.5a}$$

$$\because V_t = \gamma V_s, \quad \phi_t = \phi_s + \phi_\gamma \tag{7.5b}$$

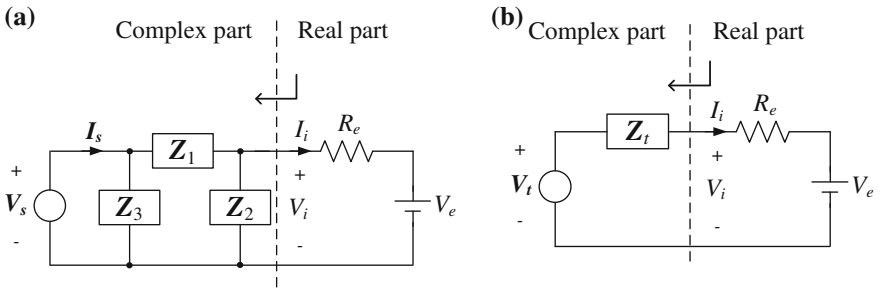

Fig. 7.5 A simplified final static circuit of the proposed LED driver. **a** Equivalent static circuit of Fig. 7.4 eliminating the auto-transformer. **b** Simplified final static circuit of (*a*)

$$\mathbf{Z_t} = \mathbf{Z_1}//\mathbf{Z_2} = \frac{R_1 + j\omega_s L_1}{1 - \omega_s^2 L_1(C_1 + C_2) + j\omega_s R_1(C_1 + C_2)}. \tag{7.6}$$

In (7.5a, b), γ and ϕ_γ are defined as follows:

$$\gamma = \left|\frac{\mathbf{Z_2}}{\mathbf{Z_1} + \mathbf{Z_2}}\right| = \sqrt{\frac{(1 - \omega_s^2 L_1 C_1)^2 + (\omega_s C_1 R_1)^2}{\{1 - \omega_s^2 L_1(C_1 + C_2)\}^2 + \omega_s^2 R_1^2 (C_1 + C_2)^2}} \tag{7.7a}$$

$$\phi_\gamma = \angle\frac{\mathbf{Z_2}}{\mathbf{Z_1} + \mathbf{Z_2}} = \tan^{-1}\frac{\omega_s C_1 R_1}{1 - \omega_s^2 L_1 C_1} - \tan^{-1}\frac{\omega_s R_1(C_1 + C_2)}{1 - \omega_s^2 L_1(C_1 + C_2)}. \tag{7.7b}$$

It is identified from (7.5b) that ϕ_s can be obtained if ϕ_t is determined, where ϕ_γ is readily calculated from (7.7b) for the given L_1, R_1, C_1, and C_2. In order to determine the ϕ_t, the phasor diagram for Fig. 7.5b is illustrated, as shown in Fig. 7.6, where ϕ_{ve} should be the same as ϕ_{ze} in order to make I_i have only a real part, which is the condition for the diode rectified current, as follows:

$$\begin{aligned} I_i &= \frac{\mathbf{V_t} - V_e}{\mathbf{Z_t} + R_e} = \frac{\mathbf{V_{te}}}{\mathbf{Z_{te}}} = \frac{V_{te}e^{j\phi_{ve}}}{Z_{te}e^{j\phi_{ze}}} = \frac{V_{te}}{Z_{te}} \quad (\because \phi_{ve} = \phi_{ze}) \\ &\because \mathbf{V_{te}} \equiv \mathbf{V_t} - V_e \equiv V_{te}e^{j\phi_{ve}}, \quad \mathbf{Z_{te}} \equiv \mathbf{Z_t} + R_e \equiv Z_{te}e^{j\phi_{ze}}. \end{aligned} \tag{7.8}$$

Therefore, ϕ_{ve} is determined as follows:

$$\phi_{ve} = \phi_{ze} = \tan^{-1}\frac{\omega_s[L_1\{1 - \omega_s^2 L_1(C_1 + C_2)\} - R_1^2(C_1 + C_2)]}{R_1 + R_e[\{1 - \omega_s^2 L_1(C_1 + C_2)\}^2 + \omega_s^2 R_1^2(C_1 + C_2)^2]}. \tag{7.9}$$

As identified from Fig. 7.6a, now ϕ_t can be determined because ϕ_{ve}, V_e, and V_t have already been determined from (7.9), (7.4), and (7.5b), respectively. Applying the cosine law of a triangle to Fig. 7.6a results in the following.

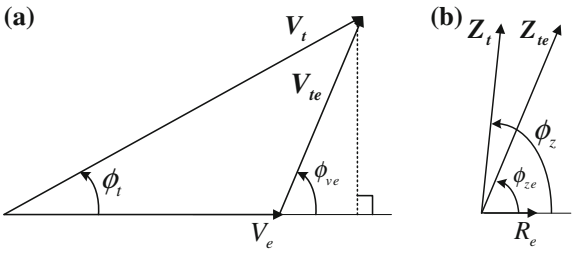

Fig. 7.6 Phasor diagrams for the simplified static circuit of Fig. 7.5b. **a** Phasor diagram of V_e, $\boldsymbol{V_t}$, and $\boldsymbol{V_{te}}$. **b** Phasor diagram of R_e, $\boldsymbol{Z_t}$, and $\boldsymbol{Z_{te}}$

$$\cos\phi_t = \frac{V_t^2 + V_e^2 - V_{te}^2}{2V_tV_e}, \tag{7.10}$$

where V_{te} can be determined from the right-angle triangle in Fig. 7.6a as follows:

$$\begin{aligned} V_t^2 &= (V_{te}\sin\phi_{ve})^2 + (V_e + V_{te}\cos\phi_{ve})^2 \\ &\Rightarrow V_{te} = -V_e\cos\phi_{ve} + \sqrt{V_t^2 - V_e^2\sin^2\phi_{ve}}. \end{aligned} \tag{7.11}$$

From (7.9) to (7.11), ϕ_t is eventually determined as follows:

$$\phi_t = \cos^{-1}\left(\frac{V_e}{V_t}\sin^2\phi_{ve} + \cos\phi_{ve}\sqrt{1 - \left(\frac{V_e}{V_t}\sin\phi_{ve}\right)^2}\right). \tag{7.12}$$

Finally, ϕ_s can be determined from (7.7b) and (7.12) as follows:

$$\phi_s = \phi_t - \phi_\gamma. \tag{7.13}$$

Now all the variables in Figs. 7.4, 7.5 and 7.6 are completely determined, which finishes the equivalent circuit modeling of the proposed LED driver.

7.2.2 Power Factor (PF)

Now the source current phasor ϕ_s' of (7.2) in the steady state can be readily determined in order to calculate the PF because all the variables including ϕ_s have been determined in the previous section. To find the source current $\boldsymbol{I_s}$, the auto-transformer in Fig. 7.4 is substituted with the current source I_i, as shown in Fig. 7.7, which is already determined from (7.8). Because this circuit is linear, $\boldsymbol{I_s}$

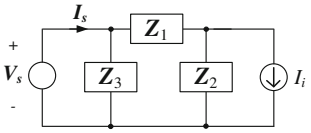

Fig. 7.7 An equivalent static circuit of Fig. 7.4, substituting the auto-transformer with a current source I_i

can be derived by the superposition of the responses from the voltage source $\boldsymbol{V_s}$ and current source I_i as follows:

$$\boldsymbol{I_s} \equiv I_s e^{j\phi_s'} = \frac{\boldsymbol{V_s}}{\boldsymbol{Z_1}+\boldsymbol{Z_2}} + \frac{\boldsymbol{V_s}}{\boldsymbol{Z_3}} + \frac{\boldsymbol{Z_2}}{\boldsymbol{Z_1}+\boldsymbol{Z_2}} I_i = \frac{V_s}{Z_a} e^{j(\phi_s-\phi_a)} + j\omega_s C_3 V_s e^{j\phi_s} + \gamma I_i e^{j\phi_\gamma} \equiv I_{sr} + jI_{si}$$

$$\because \boldsymbol{Z_a} \equiv \boldsymbol{Z_1}+\boldsymbol{Z_2} = Z_a e^{j\phi_a}, \quad I_s = \sqrt{I_{sr}^2 + I_{si}^2}, \quad \phi_s' = \tan^{-1}(I_{si}/I_{sr}), \tag{7.14}$$

where γ and ϕ_γ are already defined in (7.7a, b), and Z_a and ϕ_a are found as follows:

$$Z_a \equiv |\boldsymbol{Z_a}| = |\boldsymbol{Z_1}+\boldsymbol{Z_2}| = \frac{|\boldsymbol{Z_1}+\boldsymbol{Z_2}|}{|\boldsymbol{Z_2}|}|\boldsymbol{Z_2}| = \frac{|\boldsymbol{Z_2}|}{\gamma} = \frac{1}{\omega_s C_2 \gamma} \tag{7.15a}$$

$$\phi_a \equiv \angle(\boldsymbol{Z_1}+\boldsymbol{Z_2}) = \angle\left(\frac{\boldsymbol{Z_1}+\boldsymbol{Z_2}}{\boldsymbol{Z_2}}\boldsymbol{Z_2}\right) = \angle\left(\frac{\boldsymbol{Z_1}+\boldsymbol{Z_2}}{\boldsymbol{Z_2}}\right) + \angle\boldsymbol{Z_2} = -\phi_\gamma - \frac{\pi}{2}. \tag{7.15b}$$

From (7.15a, b), I_s and ϕ_s' of (7.14) can be eventually calculated, though the complicated analytical expressions for I_{sr} and I_{si} are not shown here.

Finally, PF can be determined from (7.13) and (7.14) as follows:

$$PF = \cos(\phi_s - \phi_s'). \tag{7.16}$$

7.2.3 Power and Efficiency

Now the source power P_s and load power P_L can be determined from the analytical results of the previous sections.

As shown in Fig. 7.5, the P_L can be calculated from R_e, V_e, and I_i, which are determined by (7.4) and (7.8), respectively, as follows:

$$P_L \equiv V_L I_L \cong \alpha V_L I_i = I_i^2 R_e + V_e I_i. \tag{7.17}$$

In (7.17), the assumption that the diode rectifier is lossless has been adopted, which can be identified by comparing Fig. 7.4 to Fig. 7.5.

In order to derive the power efficiency of the overall circuit, the source power P_s is calculated from (7.1), (7.14), and (7.16), as follows:

$$P_s = \mathrm{Re}\{\boldsymbol{V_s}\boldsymbol{I_s^*}\} = V_s I_s \cos(\phi_s - \phi_s'). \tag{7.18}$$

Therefore, the power efficiency of the proposed LED driver can be determined from (7.17) and (7.18) as follows:

$$\eta = \frac{P_L}{P_s}. \tag{7.19}$$

7.2.4 Harmonic Reduction by LC Parallel Resonance

The diode rectifier generates switching harmonic currents i_i, as shown in Fig. 7.2. In the steady state, the kth harmonic component of the source current I_{sk}, as shown in Fig. 7.8, can be analyzed if a corresponding kth switching harmonic component of the diode rectifier I_{ik} is given. In particular, the 3rd and 5th harmonics are dominant and must be diminished by filters. In Fig. 7.8, the internal resistance of the inductor R_1 is ignored because the impedance of L_1 becomes much larger than R_1 at the high harmonic frequencies.

The proposed parallel resonant circuit composed of L_1 and C_1 increases its LC tank impedance significantly at the harmonic frequency so that the contribution of the diode harmonic current to the source current can be mitigated. This harmonic current reduction ratio is obtained as follows:

$$G_I(jk\omega_s) \equiv \frac{I_{sk}}{I_{ik}} = \left|\frac{\boldsymbol{Z_{2k}}}{\boldsymbol{Z_{1k}} + \boldsymbol{Z_{2k}}}\right| = \left|\frac{1 - k^2\omega_s^2 L_1 C_1}{1 - k^2\omega_s^2 L_1 (C_1 + C_2)}\right|, \tag{7.20}$$

where, $\boldsymbol{Z_{1k}}$ and $\boldsymbol{Z_{2k}}$ are given as

$$\boldsymbol{Z_{1k}} = jk\omega_s L_1 // \frac{1}{jk\omega_s C_1}, \quad \boldsymbol{Z_{2k}} = \frac{1}{jk\omega_s C_2}. \tag{7.21}$$

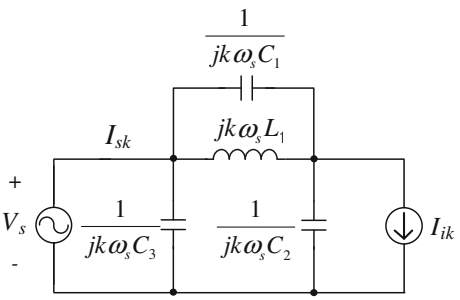

Fig. 7.8 Simplified equivalent static circuit considering the kth harmonic current I_{ik} generated from the diode rectifier

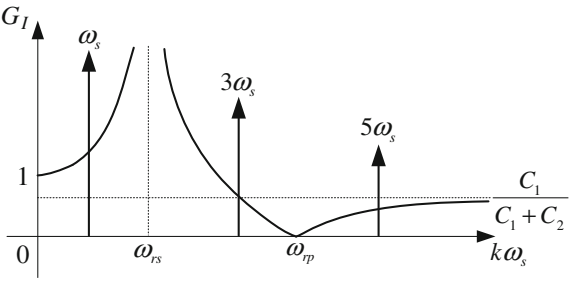

Fig. 7.9 The harmonic current reduction ratio of the proposed parallel resonant filter

In (7.20), there are two resonance angular frequencies ω_{rs} and ω_{rp}, as shown in Fig. 7.9, which correspond to a series resonance and parallel resonance, respectively, as follows:

$$\omega_{rs} = \frac{1}{\sqrt{L_1(C_1+C_2)}} \equiv k_1\omega_s \tag{7.22a}$$

$$\omega_{rp} = \frac{1}{\sqrt{L_1C_1}} \equiv k_2\omega_s, \tag{7.22b}$$

where k_1 and k_2 are corresponding multiples of the source frequency ω_s. It is identified from (7.22a, b) that ω_{rp} is always larger than ω_{rs} and they can be separated from each other by an appropriate selection of C_1 and C_2.

As identified from Fig. 7.9, G_I has a large gain at ω_{rs}, whose frequency should be avoided in order not to amplify the switching harmonic currents I_{ik}. Because the switching harmonic current I_{ik} includes only odd components, ω_{rp} is chosen between the 3rd and 5th harmonics in order to get the benefit of the parallel resonance harmonic suppression. Therefore, the design boundary conditions for the filters are finally determined, considering harmonic patterns and filter size, as follows:

$$\omega_s < \omega_{rs} = k_1\omega_s < 3\omega_s \quad \rightarrow \quad 1 < k_1 < 3 \tag{7.23a}$$

$$3\omega_s < \omega_{rp} = k_2\omega_s < 5\omega_s \quad \rightarrow \quad 3 < k_2 < 5. \tag{7.23b}$$

7.3 Designs for Frequency- and Voltage-Versatile LED Drivers

7.3.1 Baseline Design of the Temperature-Robust LED Driver

For a given set of design conditions for V_s, P_L, PF, and THD as an example, as shown in Table 7.1, the circuit parameters L_1, C_1, C_2, C_3, and n_s shall be determined to complete the baseline design of the proposed LED driver, as shown in Fig. 7.2.

Table 7.1 Design conditions and circuit parameters for the baseline design of temperature-robust LED drivers

Given design conditions		Selected circuit parameters	
Parameters	Values	Parameters	Values
V_s	220 V (±6 %)	L_1	1.07 H
$P_{L,max}$	60 W	C_1	0.4 μF
PF	>0.93 (>0.90)	C_2	0.4 μF
THD	<27 % (=30 % × PF)	C_3	1.3 μF
$\partial P_L/\partial n_s$	0	$n_{s,max}$	70

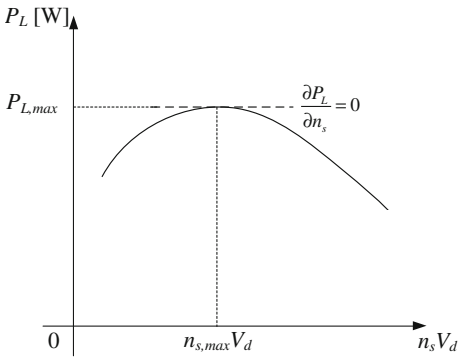

Fig. 7.10 The characteristic of P_L with respect to n_s, where a temperature-robust point exists

One more design condition for determining the five circuit parameters for the four given design conditions is the temperature robustness of P_L. It is assumed that the operating frequency of the baseline LED driver is fixed to 60 Hz.

As the LED array starts to operate, its temperature slowly increases, which results in a decrease in the forward voltage drop V_d of an LED. Therefore, the load power P_L should be insensitive to this LED voltage change. To find this temperature-robust point against the change of V_d, the characteristics of P_L with respect to n_s, whose contribution to the LED array open voltage n_sV_d is the same as V_d, are investigated, as shown in Fig. 7.10. As the number of LED in series n_s is either too small or too large, the voltage or current of the LED array becomes very small, which results in lower power P_L. Therefore, there could be a maximum power point at which $\partial P_L/\partial n_s = 0$, as shown in Fig. 7.10.

The internal resistance of the inductor R_1 is temporarily excluded from the baseline design because it is rather negligible to design the proposed LED driver; hence, R_1 is assumed to be zero at the moment. The turn-ratio of the equivalent auto-transformer of the diode rectifier, as shown in Fig. 7.4, α is selected as 0.80 throughout the chapter, which will be explained in the Discussions chapter. From Figs. 7.2, 7.3 and 7.4, the P_L can be determined in terms of the multiples of the power of an LED power P_d as follows:

$$P_L = V_L I_L = P_d n_p n_s \tag{7.24a}$$

$$\because P_d \equiv (V_d + I_d r_d) I_d \tag{7.24b}$$

Then, the appropriate n_s for the given P_L and P_d can be determined from (7.24a, b), provided that n_p is determined, as follows:

$$n_s = \frac{P_L}{P_d n_p} \tag{7.25}$$

In (7.25), the n_s cannot be arbitrarily large because V_L should not be larger than the peak source voltage as follows:

$$V_L = n_s(V_d + I_d r_d) < \sqrt{2} V_s \quad \rightarrow \quad n_s < \frac{\sqrt{2} V_s}{V_d + I_d r_d}. \tag{7.26}$$

For example, the LED A0P7EFCKLNP4 selected for our designs and experiments has the following parameters: V_d = 2.8 V and r_d = 4.0 Ω at the nominal LED current I_d = 70 mA. Then, the nominal dissipated power of an LED becomes P_d = 0.2156 W. From (7.25) and (7.26), the boundary condition for n_p can be determined, in general, as follows:

$$n_s = \frac{P_L}{P_d n_p} < \frac{\sqrt{2} V_s}{V_d + I_d r_d} \quad \rightarrow \quad n_{p,\min} \equiv \frac{P_L}{P_d} \frac{V_d + I_d r_d}{\sqrt{2} V_s} < n_p. \tag{7.27}$$

It is found from (7.27) that $n_{p,\min} = 2.75$ for the selected LED array; hence, n_p should be either 3 or 4. From (7.25), n_s becomes 93 for n_p = 3 and n_s becomes 70 for n_p = 4. Now, L_1, C_1, C_2, and C_3 can be determined in order to satisfy the design conditions in Table 7.1. For $P_{L,max}$ = 60 W, it is found that the inductor size, which is the major cost driver, is minimized when n_p = 4 and $n_{s,max}$ = 70. It is not possible to analytically determine the temperature robustness point of $P_{L,max}$ and the THD. Accordingly, the four circuit parameters were appropriately determined by numerical calculations to meet the design conditions, as shown in Figs. 7.11 and 7.12, where the PF and P_L were calculated from (7.16) and (7.17) and the THD was calculated by a PSIM simulation. As a result, an optimum parameter set of L_1 = 1.07 H, C_1 = 0.4 μF, C_2 = 0.4 μF, and C_3 = 1.3 μF was selected to satisfy the given design conditions.

As identified from Fig. 7.11a, the temperature robust point was obtained for L_1 = 1.07 H, C_1 = 0.4 μF at $n_{s,max}$ = 70. The PF is well over 0.93 when C_3 = 1.3 μF, where the PF is 3 %, which is marginally higher than the requirement of 0.90. The THD reaches its minimum of 9.4 %, which is well below the requirement of 27.0 %, when C_1 = 0.4 μF. If the size of C_1 is of concern, C_1 could be further reduced to 0.1 μF, where the THD is still as low as 13.5 %.

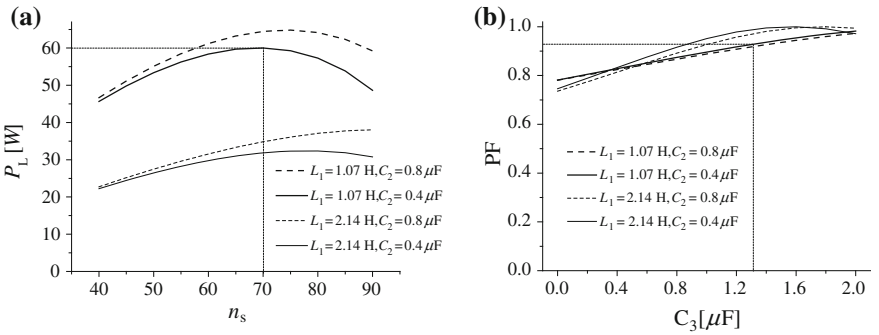

Fig. 7.11 The calculation results of the P_L and the PF for satisfying the given design conditions of temperature-robust point design at 60 Hz. **a** P_L. **b** PF

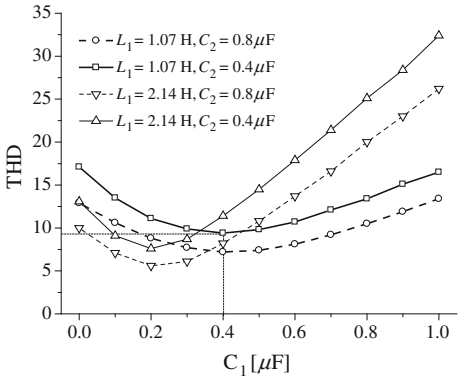

Fig. 7.12 The simulation results of the THD for satisfying the given design conditions of temperature-robust point design at 60 Hz

Based on the determined optimum circuit parameters, k_1 and k_2 in (7.22a, b) were calculated as 2.86 and 4.05, respectively, and it was found that they satisfy the design boundary conditions of (7.23a, b).

7.3.2 *Design of a Frequency-Compatible LED Driver*

In order to make a universal LED driver that can be used for both 50 and 60 Hz, a frequency-compatible LED driver, which is the same circuit as in Fig. 7.2, is proposed in this chapter. The power, PF, and THD should not be significantly changed regardless of the operating frequency change. The new design conditions and circuit parameters L_1, C_1, C_2, C_3, and n_s, which are not necessarily the same as those of the previous baseline design, are specified in Table 7.2. The temperature-robust condition of $\partial P_L/\partial n_s = 0$ for the baseline design is no longer valid for this frequency-compatible design because this condition cannot be

Table 7.2 Design conditions and circuit parameters for the frequency compatible design of LED drivers

Given design conditions		Selected circuit parameters	
Parameters	Values	Parameters	Values
V_s	220 V (±6 %)	L_1	1.59 H
$P_{L,com}$	60 W	C_1	0.3 μF
PF	>0.93 (>0.90)	C_2	1.6 μF
THD	<27 % (=30 % × PF)	C_3	0.1 μF
$\partial P_L/\partial n_s$	Minimized	$n_{s,com}$	95

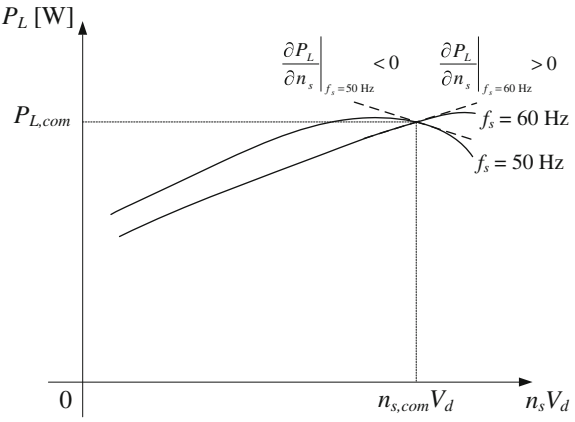

Fig. 7.13 The characteristic of P_L with respect to n_s, where the temperature-robustness is even at the compatible operating point

simultaneously met for both 50 and 60 Hz. Instead, the characteristics for both frequencies over temperature variation are minimized. Though not perfectly zero, the overall temperature variation effect can be minimized when $\partial P_L/\partial n_s|_{fs=60\text{Hz}} = -\partial P_L/\partial n_s|_{fs=50\text{Hz}}$, as shown in Fig. 7.13. In similar with the previous section, a set of the five circuit parameters were appropriately found by numerical calculations using (7.16)–(7.17) and the PSIM simulation, which are L_1 = 1.59 H, C_1 = 0.3 μF, C_2 = 1.6 μF, C_3 = 0.1 μF, and $n_{s,com}$ = 95. Because $n_{s,com}$ is predetermined, n_p is calculated from (7.24a, b) as 2.93, which is quantized to be n_p = 3. In addition, k_1 and k_2 in (7.22a, b) are calculated as 1.83 and 4.61 for 50 Hz, and 1.53 and 3.84 for 60 Hz, respectively, which also satisfy the design boundary conditions of (7.23a, b).

For the selected circuit parameters, the characteristics are shown in Figs. 7.14 and 7.15, where the P_L and PF were calculated from (7.16) and (7.17) and the THD was calculated by a PSIM simulation. As shown in Fig. 7.14b, the PF is 0.963 and 0.931 for 50 and 60 Hz, respectively, which meet the design condition, PF > 0.93. The simulated THD are 6.6 and 4.2 % for 50 and 60 Hz, respectively, which is well below the design condition of 27 %.

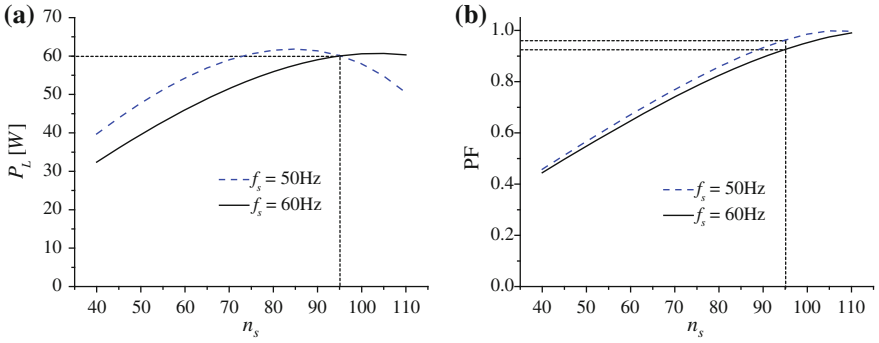

Fig. 7.14 The calculation results of the P_L and PF for satisfying the given design conditions of frequency-compatible design. **a** P_L. **b** PF

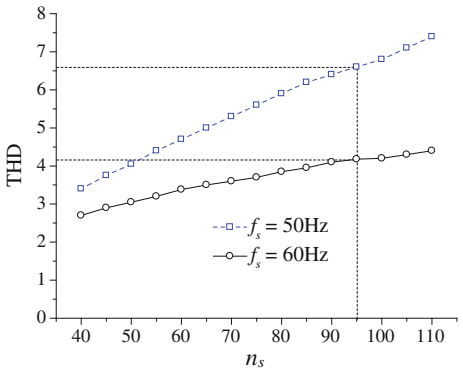

Fig. 7.15 The simulation results of the THD for satisfying the given design conditions of frequency compatible design

7.3.3 *Design of a Voltage-Compatible LED Driver*

The proposed baseline LED driver design can be applied to the design of voltage compatible LED drivers, as shown in Fig. 7.16, where the source voltage can be changed by two times, such as 100/200 V and 110/220 V. The LED power P_L can remain unchanged against the V_s change by a set of appropriate mechanical switching of SW_1, SW_2, and SW_3, as shown in Table 7.3. Each LED array is designed so that it can operate at lower source voltage such as $V_s = 110$ V. The LED array 1 and LED array 2 are connected in series when $V_s = 220$ V. For implementation convenience and reducing manufacturing cost, the inductor of each baseline design of Fig. 7.2 has been merged to a transformer of this voltage-compatible LED driver, as shown in Fig. 7.16. All the currents of the circuit elements of each LED driver in Fig. 7.16 will remain unchanged if all the impedances of the circuit parameters are halved for the halved source voltage; hence, the dissipated power of each LED driver is accordingly halved. The circuit parameters

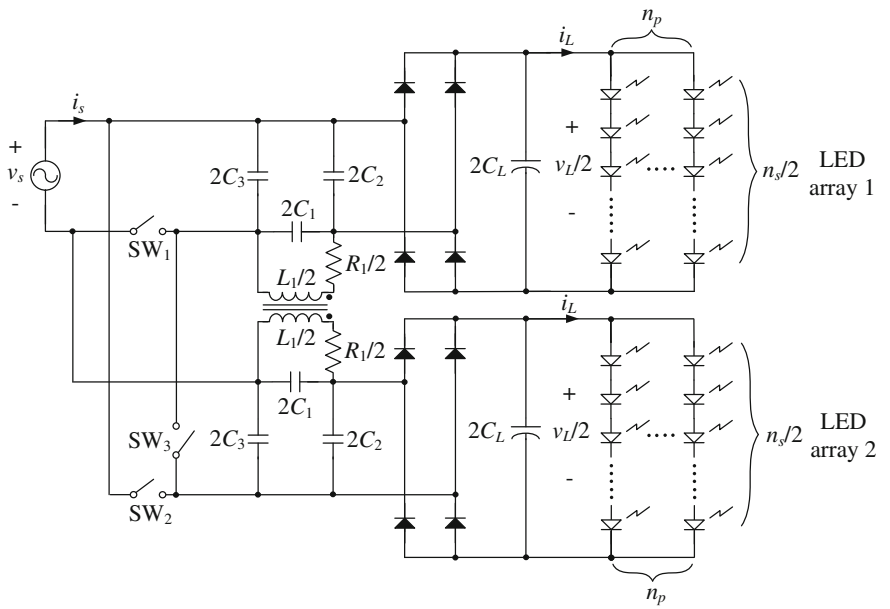

Fig. 7.16 The proposed voltage-compatible LED driver, where all the circuit parameters except v_s are the same as those of the baseline LED driver of Fig. 7.2

Table 7.3 The switch conditions for 110 V/220 V of the voltage-compatible LED driver

Case	SW$_1$	SW$_2$	SW$_3$	V_s
Parallel	On	On	Off	110 V
Series	Off	Off	On	220 V

Table 7.4 Design conditions and circuit parameters for the voltage-compatible LED driver

Given design conditions		Selected circuit parameters	
Parameters	Values	Parameters	Values
V_s	110/220 V (±6 %)	L_1	0.54 H
$P_{L,max}$	60 W	C_1	0.8 μF
PF	>0.93 (>0.90)	C_2	0.8 μF
THD	<27 % (=30 % × PF)	C_3	2.6 μF
$\partial P_L/\partial n_s$	0	$n_{s,max}$	35

of the voltage compatible LED driver for the same design condition of the baseline LED driver are listed in Table 7.4. Comparing Table 7.4 to Table 7.1, L_1 and $n_{s,max}$ are halved, whereas C_1, C_2, and C_3 are doubled in order to provide the same power of P_L = 60 W.

7.4 Experimental Verifications

The design results for the baseline LED driver among those of the three proposed LED drivers will be experimentally verified due to the page limit and similarity of the characteristics. Instead, the experimental results will be compared in detail to the simulation results as well as the calculated results.

7.4.1 Fabrications and Measurements

As shown in Fig. 7.17, an experimental kit was fabricated in accordance with the proposed design, as listed in Table 7.1. Because the proposed LED driver can be used for a street light application, whose power level is as high as 60–70 W, a slightly large-sized inductor poses no serious problem. The internal resistance R_1 of the fabricated inductor was measured as 13 Ω, which has been used throughout this chapter for simulation and theoretical calculations. The fabricated inductor current rating is 530 mA, which was determined by simulation and found to be quite sufficient for the experiments. The DC capacitor, which affects the flickering of LED light, was also determined by simulation as 100 μF. The total weight of the prototype LED driver was measured as 960 g, where the weight of the inductor is 930 g, and the highest temperature of it in the steady state was 40 °C at the ambient temperature of 30 °C.

The waveforms of v_s, i_s, v_L, i_L, and P_L at $n_s = 70$ for the prototype baseline LED driver are shown in Fig. 7.18. As anticipated, the source current i_s involves minimal harmonic current, and the fluctuations of the LED current i_L and LED power P_L are not significant, which can be further reduced by increasing the DC capacitance if needed.

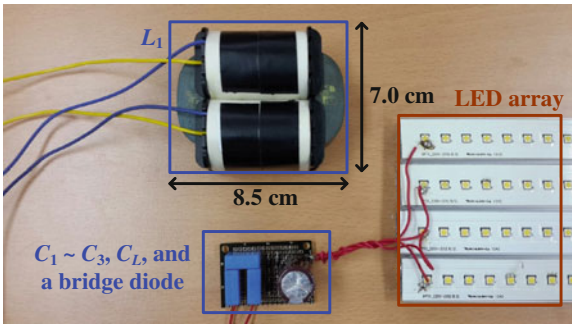

Fig. 7.17 An experimental prototype of the proposed baseline LED driver, operating at 220 V and 60 Hz

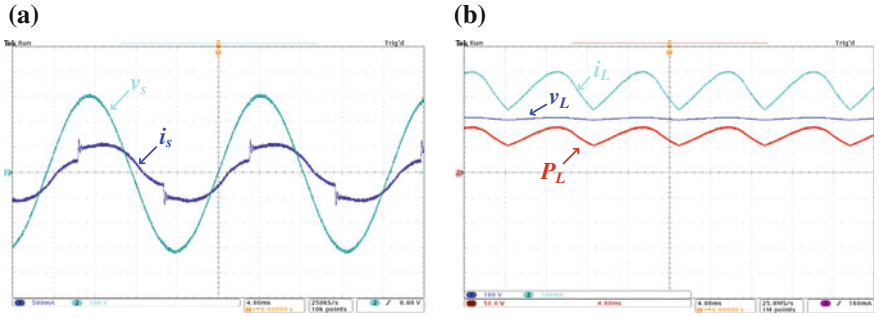

Fig. 7.18 The experimental waveforms of the proposed baseline LED driver for n_s = 70 at 220 V and 60 Hz. **a** The waveforms of v_s and i_s. **b** The waveforms of v_L, i_L, and P_L

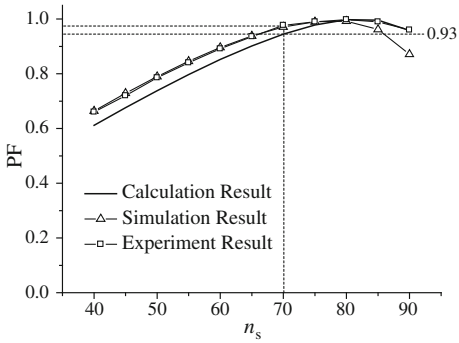

Fig. 7.19 The experimental results of the PF compared to the simulation and calculation results at 220 V and 60 Hz

7.4.2 Power Factor and THD

To verify the design for PF, the experimental results as well as the simulation and calculation results are shown in Fig. 7.19. Even though there are slight discrepancies between them, the calculation result matches well with the simulation and experiment results; the measured PF at n_s = 70 is 0.977, which is much better than anticipated. The discrepancy mainly comes from the selection of α = 0.80 that was used for the design, which will be discussed in detail in Sect. 7.5. The harmonic characteristics of the source current i_s were also measured by a WT1600 power meter, as shown in Fig. 7.20. The THD was measured as 10.5 %, which is quite close to the simulation result of 9.4 %, and each harmonic component is well below the IEC61000-3-2 class C standard.

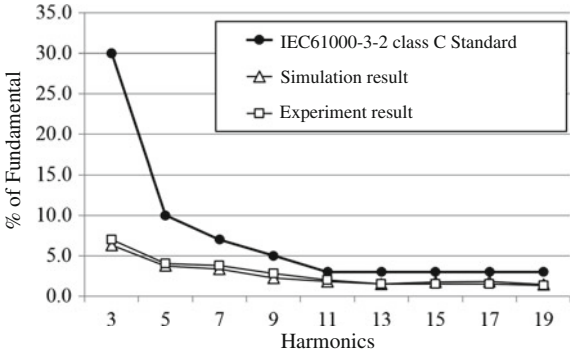

Fig. 7.20 Experimental results of harmonics compared to the simulation results for n_s = 70 at 220 V and 60 Hz

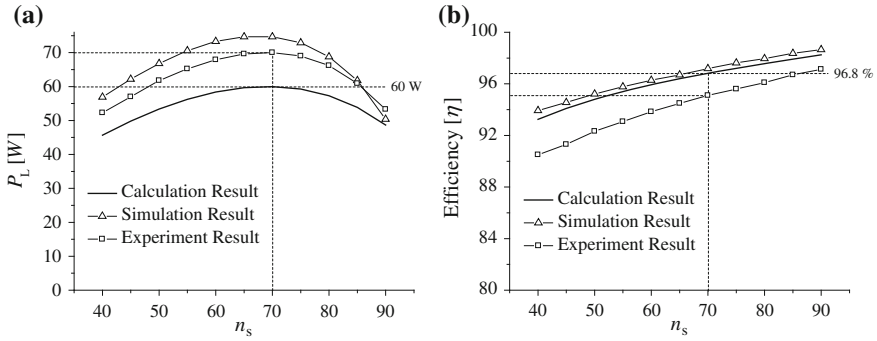

Fig. 7.21 The experimental results of the P_L and efficiency compared to the simulation and calculation results at 220 V and 60 Hz. **a** P_L. **b** Power efficiency

7.4.3 *Power and Efficiency*

To verify the design for power and efficiency, the experimental results as well as the simulation and calculation results are shown in Fig. 7.21. The experiment result of P_L has a maximum point, which corresponds to the temperature-robust point, at n_s = 70; this matches well with the calculation, as shown in Fig. 7.21a. The measured power level at n_s = 70, however, is 70 W, which is about 10 W larger than the calculated power level. The simulation result is relatively similar with the experiment one. The power efficiency, as shown in Fig. 7.21b, shows that the measured value is 95.2 % at n_s = 70, which is a little lower than the calculated and simulation results.

Though not perfectly matched with each other, it is clear that the tendencies of the characteristics with respect to the n_s are all the same and that the calculation results as well as the simulation results help the design.

Table 7.5 Measured results for source voltage variation (V_s = 220 V ± 6 %)

Measured parameters	Source voltage (V_s)		
	206 V_{rms}	220 V_{rms}	233 V_{rms}
P_s (W)	64.9	73.5	83.2
P_L (W)	61.9	70.0	79.0
PF	0.991	0.977	0.953
THD (%)	10.9	10.5	10.0
Efficiency (%)	95.4	95.2	95.0

7.4.4 Source Voltage Variation

For a fixed source voltage of V_s = 220 V, the proposed LED driver satisfies all the design conditions of the LED power level, PF, and THD, as shown in Table 7.1. One of the limitations of the proposed passive LED drivers is no power control capability against the source voltage variation. Therefore, the proposed LED drivers should be used for the applications where the source voltage is regulated. Fortunately, V_s is generally well regulated within ±6 % in most advanced countries because it is the global standard of source voltage variation regulation.

The measured parameters for the source voltage variation of 206–233 V are summarized in Table 7.5, where both the PF and THD meet the design conditions, even though no feedback circuit is involved. The change of LED power is less than ±13 %, which is acceptable because the brightness change of LED lighting as a result of this power change is not a problem in many applications. The overall efficiencies were always kept above 95.0 %, which is quite high compared to conventional LED drivers for street lights.

7.5 Discussions on the Design Verifications by Experiments

Through the experiments, the proposed designs based on the phasor analyses are identified to be quite useful, considering the nonlinearities of the diode rectifier and LEDs. However, the discrepancies between the experiment, simulation, and calculation results need to be further explained in this section.

One of the discrepancies may come from the limitations in LED modeling, i.e., the LED model used for both PSIM simulations and calculations is a linear-approximated LED model, where r_d and V_d of an LED in Fig. 7.4 are always constant regardless of the LED current. In practice, the r_d and V_d highly depend on the LED current, and the discrepancy due to the r_d and V_d becomes more dominant when the LED current deviates from a nominal LED current of 70 mA in this chapter. Furthermore, the simulation results in this chapter did not include the conduction loss of a bridge diode.

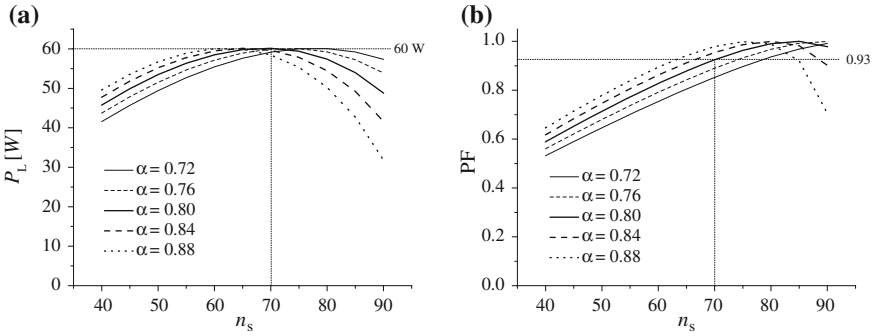

Fig. 7.22 The calculated values of the P_L and PF with respect to n_s for curve fitting of α. **a** P_L. **b** PF

Another important source of the discrepancies is the non-linear characteristic of the auto-transformer of Fig. 7.4, where the equivalent turn-ratio is also assumed to be constant ($\alpha = 0.80$) regardless of the change of n_s and switching conditions. To ensure the linearity of the turn-ratio, the diode rectifier should operate in the continuous conduction mode (CCM), and it becomes $\alpha = 2\sqrt{2}/\pi \cong 0.90$ [36]. In order to make a diode rectifier operate in the CCM, the input and output sides of it should have different sources, as shown in Fig. 7.1c, where a current source (an inductor) is at the input side of the bridge diode and a voltage source (a capacitor) is at the output side of it. The diode currents of the proposed LED drivers are, however, not continuous; therefore, they may operate in the discontinuous conduction mode (DCM). As identified from Fig. 7.2, the output current of the bridge diode i_o does not flow until the input voltage v_i reaches to the rectified voltage v_L; hence, the effective turn-on period of a switching function is reduced, which results in the decrease of α. It must be extremely complicated to find an expression for this highly non-linear parameter α by analysis; instead, such an expression has been found by curve fitting the P_L-n_s and PF-n_s curves, as shown in Fig. 7.22.

As identified from Fig. 7.21, the temperature-robust point was found as $n_s = 70$ through both simulations and experiments. As identified from Fig. 7.22, the best curve fitting is found when $\alpha = 0.80$ for both the P_L and PF; this is why this value has been used in calculation throughout the chapter. It should be noted, however, that the best curve fitting value of $\alpha = 0.80$ may not be valid for other design disciplines.

7.6 Conclusion

The proposed passive-type LED drivers, which have just one inductor and three capacitors, called LC^3, are found to be temperature-robust and highly efficient. The measured THD was as low as 10.5 %, and the PF was as high as 0.977 at the

nominal operating condition. The measured power efficiency was 95.2 %, and the temperature increase of the LED driver was merely 10 °C, which are quite acceptable characteristics for the 70 W street light LED drivers in addition to the inherent extremely long lifetime of the proposed passive LED drivers. The proposed phasor analysis for the non-linear diode rectifier and LEDs was effective in the design of the LED drivers, which is generally applicable in other areas. Design examples for the 50/60 Hz compatible and 110/220 V compatible LED drivers showed the usefulness of the proposed phasor analysis.

References

1. Lee ES, Cheon JP, Choi BH, Lim GC, Kim BC, Rim CT (2015) Temperature-robust LC3 passive LED drivers with low THD, high efficiency and PF, and long life. J Emerg Sel Top Power Electron 3(3):829–840
2. Tsao JY (2004) Solid-state lighting: lamps, chips, and materials for tomorrow. IEEE Circuits Devices Mag 20(3):28–37
3. Steigerwald DA et al (2002) Illumination with solid state lighting technology. IEEE J Sel Top Quant Electron: 310–320 (Apr)
4. Wendt M, Andriesse J-W (2006) LEDs in real lighting applications: from niche markets to general lighting. In: Proceedings of IEEE industry applications conference, pp 2601–2603
5. (Ron) Hui SY, Qin YX (2009) A general photo-electro-thermal theory for light emitting diode (LED) systems. IEEE Trans Power Electron 24(8): 1967–1976
6. Cheng YK, Cheng KWE (2006) General study for using LED to replace traditional lighting devices. In: Proceedings of IEEE international conference on power electronics systems and applications (ICPESA), pp 173–177
7. Streubel K et al (2002) High brightness AlGaInP light-emitting diodes. IEEE J Sel Types Quant Electron 8(2):321–332
8. Hong S-S et al (2010) A new cost-effective current-balancing multi-channel LED driver for a large screen LCD backlight units. J Power Electron (JPE) 10(4):351–356
9. (2008) ENERGY STAR program requirements for solid state lighting luminaires, Eligibility Criteria—Version 1.1
10. IEC 61000-3-2 class C standard (2009) Limits for harmonic current emissions (equipment input current ≤ 16A per phase)
11. van der Broeckl et al (2007) Power driver topologies and control schemes for LEDs. In: Proceedings of IEEE applied power electronics conference and exposition (APEC), Feb 2007, pp 1319–1325
12. Chern T-L et al (2010) High power factor flyback converter for LED driver with boundary conduction mode control. In: Proceedings of IEEE industrial electronics and applications (ICIEA), June 2010, pp 2088–2093
13. Ye Z, Greenfeld F, Liang Z (2008) Design considerations of a high power factor SEPIC converter for high brightness white LED lighting applications. In: Proceedings of IEEE power electronics specialists conference (PESC), June 2008, pp 2657–2663
14. Wang B, Ruan X, Yao K, Ming X (2010) A method of reducing the peak-to-average ratio of LED current for electrolytic capacitor-less AC–DC drivers. IEEE Trans Power Electron 25(3):592–601
15. Aguilar D, Henze CP (2010) LED driver circuit with inherent PFC. In: Proceedings of IEEE applied power electronics conference and exposition (APEC), Feb 2010, pp 605–610

16. Tian Fu P, Huang Jen C, Shih Jen C, Shih Yen C (2007) An improved single-stage flyback PFC converter for high-luminance lighting LED lamps. In: Proceedings of international conference on electronic measurement and instruments (ICEMI), Aug 2007, pp 212–215
17. Yu L, Yang J (2009) The topologies of white LED lamps' power drivers. In: Proceedings of IEEE power electronics systems and applications (PESA): 1–6 (May)
18. Hu Q, Zane R (2011) Minimizing required energy storage in off-line LED drivers based on series-input converter modules. IEEE Trans Power Electron 26(10):2887–2895
19. Wu H, Ji S, Lee FC, Wu X (2011) Multi-channel constant current (MC^3) LLC resonant LED driver. In: Proceedings of IEEE energy conversion congress and exposition (ECCE), Sept 2011, pp 2568–2575
20. Elias Demian A Jr et al (2007) Microcontroller-based quadratic buck converter used as led lamp driver. In: Proceedings of IEEE European conference on power electronics and applications, Sept 2007, pp 1–6
21. Ali M et al (2010) A single stage SEPIC PFC converter for LED street lighting applications. In: Proceedings of IEEE international conference on power and Energy (PECon), Nov 2010, pp 501–506
22. Jiaying L, Xiaobo W (2009) A PWM controller IC for LED driver used to multiple DC-DC topologies. In: Proceedings of IEEE Asia-Pacific power and energy engineering conference (APPEEC), Mar 2009, pp 1–4
23. Hu Q, Zane R (2010) A 0.9 PF LED driver with small LED current ripple based on series-input digitally-controlled converter modules. In: Proceedings of IEEE applied power electronics conference and exposition (APEC), Feb 2010, pp 2314–2320
24. Ye Z, Greenfeld F, Liang Z (2009) Single-stage offline SEPIC converter with power factor correction to drive high brightness LEDs. In: Proceedings of IEEE applied power electronics conference and exposition (APEC), Feb 2009, pp 546–553
25. Hu Y, Huber L, Jovanovi MM (2012) Single-stage, universal-input AC/DC LED driver with current-controlled variable PFC boost inductor. IEEE Trans Power Electron 27(3):1579–1588
26. Xie X, Wang J, Zhao C, Lu Q, Liu S (2012) A novel output current estimation and regulation circuit for primary side controlled high power factor single-stage flyback LED driver. IEEE Trans Power Electron 27(11):4602–4612
27. Alonso JM, Viña J, Vaquero DG, Martínez G, Osorio R (2012) Analysis and design of the integrated double buck–boost converter as a high-power-factor driver for power-LED lamps. IEEE Trans Ind Electron 59(4):1689–1697
28. Hu Q, Zane R (2010) LED driver circuit with series-input-connected converter cells operating in continuous conduction mode. IEEE Trans Power Electron 25(3):574–582
29. Hu Y, Jovanovic MM (2008) A novel LED driver with adaptive drive voltage. In: Proceedings of IEEE applied power electronics conference and exposition (APEC), Feb 2008, pp 565–571
30. Seoul Semiconductor Co., Ltd. (2012) Luminous device. Korea Patent 10-1142939, 27 Apr 2012
31. Lee BH, Kim HJ, Kim BC, Rim CT (2010) The development of low-cost AC power LED driver using capacitor. In: Proceedings of 2010 summer KIPE conference, pp 426–427
32. Optomind Inc. (2012) Direct connection-type L.E.D. lighting apparatus. Korea Patent 10-2012-0094901, 29 Aug 2012
33. (Ron) Hui SY, Li SN, Tao XH, Chen W, Ng WM (2012) A novel passive offline LED driver with long lifetime. IEEE Trans Power Electron 25(10):2665–2672
34. Chen W (2010) A comparative study on the circuit topologies for offline passive light-emitting diode (LED) drivers with long lifetime & high efficiency. In: Proceedings of IEEE energy conversion congress and exposition (ECCE), Sept 2010, pp 724–730
35. Lee BH, Kim HJ, Rim Chun T (2011) Robust passive LED driver compatible with conventional rapid-start ballast. IEEE Trans Power Electron 26(12):3694–3706
36. Rim CT, Cho GH (1990) Phasor transformation and its application to the DC/AC analyses of frequency/phase controlled series resonant converters (SRC). IEEE Trans Power Electron 5(2):201–211

37. Rim CT, Hu DY, Cho GH (1990) Transformers as equivalent circuits for switches: general proofs and D-Q transformation-based analysis. IEEE Trans Ind Appl 26(4):777–785
38. Rim CT (2011) Unified general phasor transformation for AC converters. IEEE Trans Power Electron 26(9):2465–2475
39. Park CB, Lee SW, Rim CT () Static and dynamic analyses of three-phase rectifier with LC input filter by Laplace phasor transformation. In: Proceedings of IEEE energy conversion congress and exposition (ECCE), Sept 2012, pp 1570–1577
40. Lee S, Choi B, Rim CT (2013) Dynamics characterization of the inductive power transfer system for online electric vehicles by Laplace phasor transform. IEEE Trans Power Electron 28(12):5902–5909
41. Rim CT, Cho GH (1989) New approach to analysis of quantum rectifier-inverters. IEEE Electron Lett 25(25):1744–1745
42. Huh J, Lee WY, Choi SY, Cho GH, Rim CT (2013) Frequency-domain circuit model and analysis of coupled magnetic resonance systems. J Power Electron 13(2):275–286
43. Choi S, Huh J, Lee WY, Lee SW, Rim CT (2013) New cross-segmented power supply rails for roadway powered electric vehicles. IEEE Trans Power Electron 28(12):5832–5841
44. Park C, Lee S, Cho G-H, Choi S-Y, Rim CT (2013) Two-dimensional inductive power transfer system for mobile robots using evenly displaced multiple pick-ups. IEEE Trans Ind Appl 50(1):558–565

Part IV
Multi-phase AC Circuits and Circuit DQ Transformation

In this part, the circuit DQ transformation, which I had developed for multi-phase AC converters and power systems, is explained. Contrary to the single phase AC circuits, multi-phase AC circuits may utilize the well-known DQ-transformation techniques. Equational DQ-transformations, however, are not preferred for practical applications due to complicated manipulations and lack of physical insights. Therefore, a circuit DQ-transformation is introduced in this part with application examples.

Chapter 8
Circuit DQ-Transformation

As explained in the previous chapters, the equivalent circuits for the switches in DC-DC, DC-AC, AC-DC, and AC-AC converters are proved to be time-varying transformers. This result is used in this chapter for the analyses of AC-DC-AC converters, an eighth-order current source rectifier-inverter, and a buck-boost inverter, with fruitful physical insight. The circuit D-Q transformation is introduced in this chapter for the analyses of general AC converters such as inverters, rectifiers, and cycloconverters, which include the time-varying transformers. Gyrators, new power circuit elements, appear in the DQ transformed inductors and capacitors of the AC converters. Few equational manipulations are required to determine the steady-state operating points and the small signal gains of the converters. The analysis results for the rectifier-inverter show that the circuit has self-short-circuit protection capability and strong immunity to parasitic inductor resistances. A lot of this chapter is written based on the original paper of mine [1].

8.1 Introduction

Dealing with switches has been an important issue in the power electronics industry since they can turn linear time-invariant systems into nonlinear time-varying systems [2, 3]. Simplifying or eliminating switching action is the main problem in modeling switching systems [3–8]. One successful method is the state-space averaging technique [7]. This approach is well-established for the DC-DC converters. A trial for the extension of this concept to the DC-AC converters is found in [8], where the time-varying nature of the switching systems is eliminated by equational DQ transformation. The equational approach is limited, however, to low-order systems having fewer than four reactive elements since manipulating matrices with order higher than four is very difficult.

C.T. Rim, *Phasor Power Electronics*, KAIST Research Series,
DOI 10.1007/978-981-10-0536-7_8

Another useful method is to replace the switches with equivalent circuits [9, 10]. DC ideal transformers are found to be equivalent circuits for the switches in DC-DC converters: the first trial for this work is found in [9], and the three-terminal equivalent transformer is found in [10]. The cumbersome equational manipulations are minimized by this method. The fact that a certain ac-AC switching converter has a property similar to a transformer which changes frequency, voltage, current, phase, and power factor is discussed in [11]. Up to now, however, general proofs for the equivalence of all switches with transformers and the analyses of AC converters (DC-AC, AC-DC, and AC-AC converters) based on the results have not been found; otherwise, surely the analytical capability of power converters could have increased drastically, and the efforts at finding appropriate models could have been reduced.

In this chapter this property of switches as transformers is strictly proved in general and is then extended to all switching converters. A new circuit DQ transformation suit for the analysis of AC converters is also suggested. High-order AC switching systems such as eighth-order system can be modeled as easily as a few third-order systems. Thus the use of cumbersome equations or matrix manipulations is minimized or eliminated. Analytical examples are shown for an eighth-order current-source rectifier-inverter and a buck-boost inverter.

8.2 Circuit DQ Transformation (Three-Phase Rectifier-Inverter Example)

Those circuits that contain the time-varying transformers cannot be analyzed by the numerous powerful circuit analyses techniques such as Laplace transform until they are transformed to the appropriate time-invariant circuits. As is well known, sinusoidal time-varying systems can be changed to time-invariant systems by the DQ transformation. However this method is inappropriate for multi switch high-order switching systems since they often include a couple of high-order matrices that are impossible to handle. One possible solution, proposed in this chapter, is to draw the DQ transformed circuits and apply circuit analysis techniques rather than manipulate the cumbersome equations.

In this section the circuit to analyze is divided into five kinds of AC subcircuits and a DC subcircuit, and DQ transformation is applied to the individual AC subcircuits. This makes it possible to regard the complex multi switching system as a few partitioned simple switching systems. The resultant circuits are then combined into one. Finally, this circuit is perturbed for AC analysis and simplified for DC analysis. The modeling procedure is shown for a sufficiently complex converter example, the rectifier-inverter shown in Fig. 8.1; the switching frequency of the primary rectifier part is ω_1 and that of the secondary inverter part is ω_2. Throughout this chapter, it is assumed that the circuit is balanced, which means that all the circuit parameters are same for each phase. For the case of unbalanced multi-phase

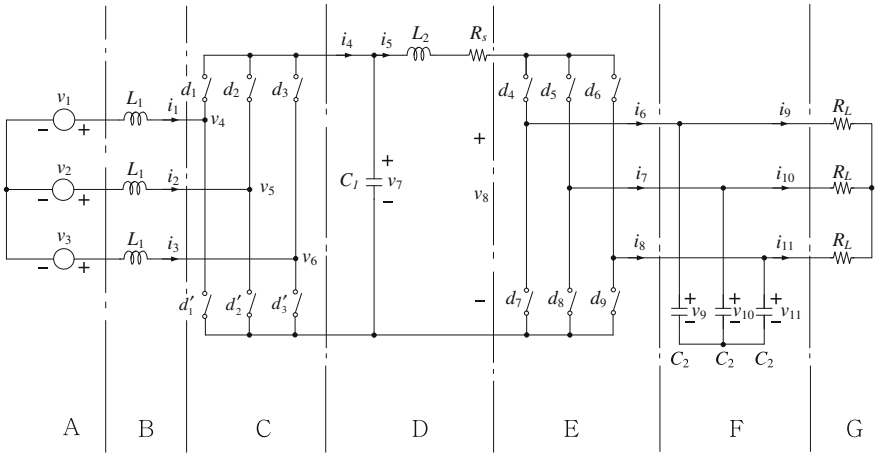

Fig. 8.1 Three-phase rectifier-inverter circuit

AC circuits, other literatures dealing with decomposition of a general unbalanced AC circuit to positive sequence and negative sequence rotating balanced AC circuits and a DC offset circuit [12].

8.2.1 Circuit Partitioning

The first step is to divide the original circuit into several subcircuits. It is found that there are six kinds of subcircuits in the switching system. They are the time-varying transformer set, the voltage (or current) source set, the inductor set, the capacitor set, the resistor set (these are AC subcircuits), and the DC subcircuit. Then the independent partitioned circuits are obtained, regarding the adjacent voltages or currents as external sources (Fig. 8.2).

8.2.2 Subcircuit DQ Transformations

There are five kinds of AC subcircuits. The equivalent *DQ* transformed circuits are obtained assuming all elements are balanced.

1. ***Time-Varying Transformer Sets***: There are two kinds of DC-AC (or ac-DC) converters; voltage-source inverter (VSI) and CSI (or, equivalently, current- and voltage-source rectifier). The DQ transformations of the VSI and CSI transformers are shown in Figs. 8.3 and 8.4, respectively. These procedures are proved as follows, assuming the switching harmonics are negligible. Thus the switching functions are pure sinusoidal.

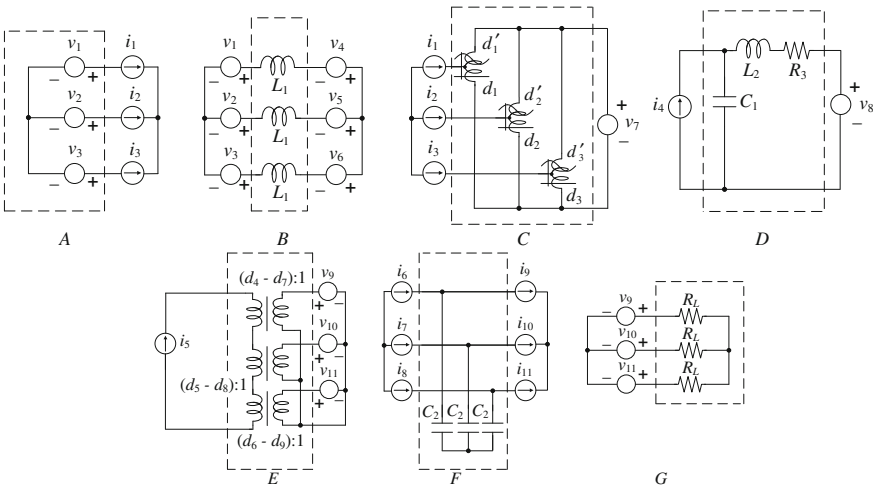

Fig. 8.2 Partitioned circuits

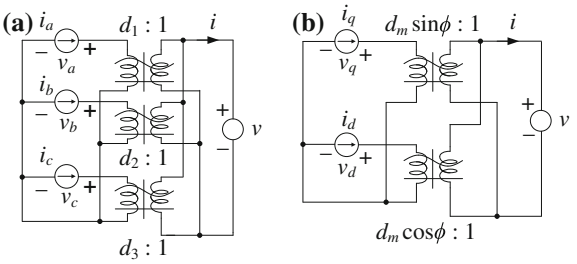

Fig. 8.3 DQ transformation of VSI transformer set. **a** Original circuit. **b** DQ transformed circuit

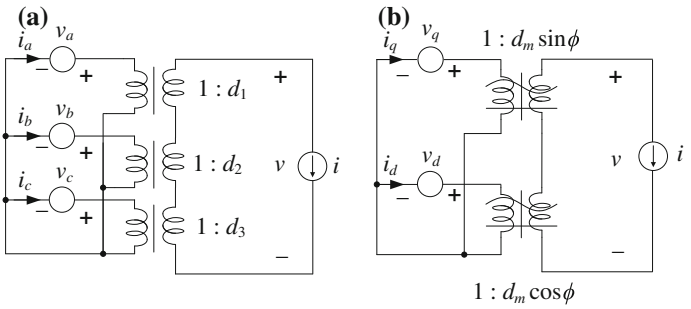

Fig. 8.4 DQ transformation of CSI transformer set. **a** Original circuit. **b** DQ transformed circuit

Proof

$$v = \boldsymbol{D}^T v_{abc} = \boldsymbol{D}^{\boldsymbol{T}} \boldsymbol{K}^{-1} v_{qd0}$$

$$\boldsymbol{i_{abc}} = \boldsymbol{D}\boldsymbol{i} = \boldsymbol{K}^{-\boldsymbol{1}} \boldsymbol{i_{qd0}} \tag{8.1a}$$

$$\boldsymbol{i} = \boldsymbol{D}^{\boldsymbol{T}} \boldsymbol{i_{abc}} = \boldsymbol{D}^{\boldsymbol{T}} \boldsymbol{K}^{-\boldsymbol{1}} \boldsymbol{i_{qd0}}$$

$$v_{abc} = \boldsymbol{D}v = \boldsymbol{K}^{-1} v_{qd0} \tag{8.2b}$$

where

$$\boldsymbol{D} = \begin{bmatrix} d_1 \\ d_2 \\ d_3 \end{bmatrix} = d_m \sqrt{\frac{2}{3}} \begin{bmatrix} \sin(\omega t + \phi) \\ \sin(\omega t - \frac{2}{3}\pi + \phi) \\ \sin(\omega t + \frac{2}{3}\pi + \phi) \end{bmatrix}$$

$$\boldsymbol{v_{abc}} = \begin{bmatrix} v_a \\ v_b \\ v_c \end{bmatrix} \quad \boldsymbol{v_{qd0}} = \begin{bmatrix} v_q \\ v_d \\ v_0 \end{bmatrix}$$

$$\boldsymbol{i_{abc}} = \begin{bmatrix} i_a \\ i_b \\ i_c \end{bmatrix} \quad \boldsymbol{i_{qd0}} = \begin{bmatrix} i_q \\ i_d \\ i_0 \end{bmatrix}$$

$$\boldsymbol{K} = \sqrt{\frac{2}{3}} \begin{bmatrix} \cos(\omega t) & \cos(\omega t - \frac{2}{3}\pi) & \cos(\omega t - \frac{2}{3}\pi) \\ \sin(\omega t) & \sin(\omega t - \frac{2}{3}\pi) & \sin(\omega t + \frac{2}{3}\pi) \\ \frac{1}{\sqrt{2}} & \frac{1}{\sqrt{2}} & \frac{1}{\sqrt{2}} \end{bmatrix}$$

$$\boldsymbol{K}^{-1} = \sqrt{\frac{2}{3}} \begin{bmatrix} \cos(\omega t) & \sin(\omega t) & \frac{1}{\sqrt{2}} \\ \cos(\omega t - \frac{2}{3}\pi) & \sin(\omega t - \frac{2}{3}\pi) & \frac{1}{\sqrt{2}} \\ \cos(\omega t + \frac{2}{3}\pi) & \sin(\omega t + \frac{2}{3}\pi) & \frac{1}{\sqrt{2}} \end{bmatrix} \tag{8.3}$$

Applying (8.3) to (8.2), it is found that

$$v = d_m(v_q \sin\phi + v_d \cos\phi)$$

$$i_q = d_m \sin\phi \, i$$

$$i_d = d_m \cos\phi \, i \tag{8.4a}$$

$$i = d_m(i_q \sin\phi + i_d \cos\phi)$$

$$v_q = d_m \sin\phi\, v$$

$$v_d = d_m \cos\phi\, v \tag{8.4b}$$

The *DQ* transform is selected as the power-invariant transformation, since this does not change the coefficients. The circuit reconstructions of (8.4a) and (8.4b) are Figs. 8.3b and 8.4b, respectively. Note that the time-varying nature of the transformer is removed by the DQ transformation, as expected.

2. ***Three-Phase Voltage (or Current) Source***:

The *DQ* transformed circuit is shown in Fig. 8.5, where the instantaneous power is not changed by this transform.

Proof

$$v_{qd0} = \boldsymbol{K}\boldsymbol{v}_{\boldsymbol{abc}} = V_m \begin{bmatrix} \sin\phi_1 \\ \cos\phi_1 \\ 0 \end{bmatrix}$$

$$i_{qd0} = \boldsymbol{K}\boldsymbol{i}_{\boldsymbol{abc}} = I_m \begin{bmatrix} \sin\phi_2 \\ \cos\phi_2 \\ 0 \end{bmatrix} \tag{8.5}$$

where

$$\boldsymbol{v}_{\boldsymbol{abc}} = \sqrt{\frac{2}{3}} V_m \begin{bmatrix} \sin(\omega t + \phi_1) \\ \sin(\omega t - \frac{2}{3}\pi + \phi_1) \\ \sin(\omega t + \frac{2}{3}\pi + \phi_1) \end{bmatrix}$$

$$\boldsymbol{i}_{\boldsymbol{abc}} = \sqrt{\frac{2}{3}} I_m \begin{bmatrix} \sin(\omega t + \phi_2) \\ \sin(\omega t - \frac{2}{3}\pi + \phi_2) \\ \sin(\omega t + \frac{2}{3}\pi + \phi_2) \end{bmatrix} \tag{8.6}$$

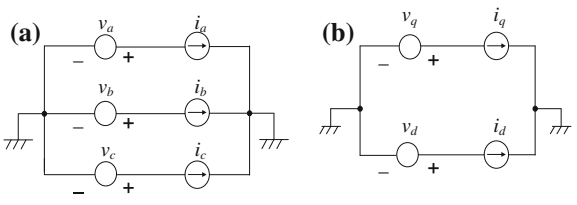

Fig. 8.5 DQ transformation of voltage (or current) source set. **a** Original circuit. **b** DQ transformed circuit

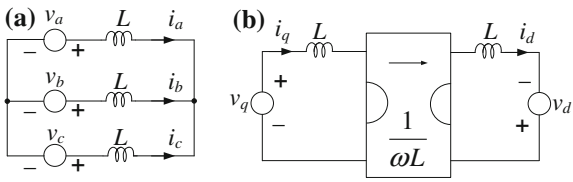

Fig. 8.6 DQ transformation of inductor set. **a** Original circuit. **b** DQ transformed circuit

3. ***Three-phase Inductor Set*: The DQ transformed circuit is shown in Fig. 8.6.**

Proof

$$\boldsymbol{L}\dot{\boldsymbol{i}}_{\boldsymbol{abc}} = \boldsymbol{v}_{\boldsymbol{abc}} \tag{8.7}$$

Substituting i_{abc} with that in (8.6) and taking the derivative, (8.11) becomes

$$L[(\dot{\boldsymbol{K}}^{-1})\boldsymbol{i}_{\boldsymbol{qd0}} + \boldsymbol{K}^{-1}\dot{\boldsymbol{i}}_{\boldsymbol{qd0}}] = v_{abc} \tag{8.8}$$

or

$$\begin{aligned} L\dot{\boldsymbol{i}}_{\boldsymbol{qd0}} &= -L\boldsymbol{K}(\dot{\boldsymbol{K}}^{-1})\boldsymbol{i}_{\boldsymbol{qd0}} + \boldsymbol{K}\boldsymbol{v}_{\boldsymbol{abc}} \\ &= -L\omega \begin{bmatrix} 0 & 1 & 0 \\ -1 & 0 & 0 \\ 0 & 0 & 0 \end{bmatrix} \boldsymbol{i}_{\boldsymbol{qd0}} + \boldsymbol{v}_{\boldsymbol{qd0}} \end{aligned} \tag{8.9}$$

This means that

$$\begin{aligned} L\dot{i}_q &= -\omega L i_d + v_q \\ L\dot{i}_d &= -\omega L i_q + v_d \\ L\dot{i}_0 &= v_0 = 0; \textit{balanced condition}. \end{aligned} \tag{8.10}$$

The circuit reconstruction of (8.10) is Fig. 8.6b. Note that a gyrator is newly introduced. An interesting fact is that the *DQ* variables of inductor sets are electrically coupled by the gyrator through the inductors are not magnetically coupled in fact. The 0 axis variable can be excluded from our discussion since the sources are balanced.

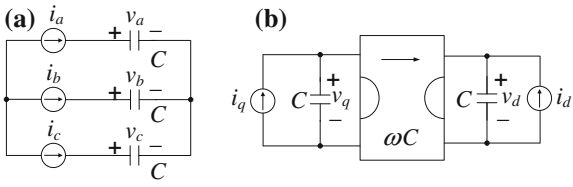

Fig. 8.7 DQ transformation of capacitor set. **a** Original circuit. **b** DQ transformed circuit

4. ***Three-phase Capacitor Set***: The DQ transformed circuit is shown in Fig. 8.7.

Proof

$$C\dot{\boldsymbol{v}}_{\boldsymbol{abc}} = \boldsymbol{i}_{\boldsymbol{abc}} \tag{8.11}$$

Considering v_{abc} in (8.4), (8.11) becomes

$$C[(\dot{\boldsymbol{K}}^{-1})\boldsymbol{v}_{\boldsymbol{qd0}} + \boldsymbol{K}^{-1}\boldsymbol{v}_{\boldsymbol{qd0}}] = \boldsymbol{i}_{\boldsymbol{abc}} \tag{8.12}$$

or

$$\begin{aligned} C\,\dot{\boldsymbol{v}}_{\boldsymbol{qd0}} &= -C\boldsymbol{K}(\dot{\boldsymbol{K}}^{-1})\boldsymbol{v}_{\boldsymbol{qd0}} + \boldsymbol{K}\boldsymbol{i}_{\boldsymbol{abc}} \\ &= -C\omega \begin{bmatrix} 0 & 1 & 0 \\ -1 & 0 & 0 \\ 0 & 0 & 0 \end{bmatrix} \boldsymbol{v}_{\boldsymbol{qd0}} + \boldsymbol{i}_{\boldsymbol{qd0}} \end{aligned} \tag{8.13}$$

This means

$$\begin{aligned} C\dot{v}_q &= -\omega C v_d + i_q \\ C\dot{v}_d &= -\omega C v_q + i_d \\ C\dot{v}_0 &= i_0 = 0; \textit{balanced condition}. \end{aligned} \tag{8.14}$$

The circuit reconstruction of (8.14) is Fig. 8.7b. A gyrator is also introduced as with the inductor set, and the 0 axis variable is eliminated.

5. ***Three-phase Resistor Set***: The *DQ transformed* circuit is shown in Fig. 8.8.

Proof

$$\boldsymbol{v}_{\boldsymbol{qd0}} = \boldsymbol{K}\boldsymbol{v}_{\boldsymbol{abc}} = \boldsymbol{K}\boldsymbol{R}\boldsymbol{i}_{\boldsymbol{abc}} = \boldsymbol{R}\boldsymbol{i}_{\boldsymbol{qd0}} \tag{8.15}$$

The 0 axis variable is omitted since those of other circuits are not used.

The 0 axis variables are excluded for both the balanced sources and balanced initial conditions. The values are always kept zero under these both conditions.

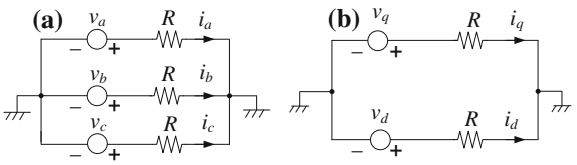

Fig. 8.8 DQ transformation of resistor set. **a** Original circuit. **b** DQ transformed circuit

8.2.3 Circuit Reconstruction

The DQ transformed subcircuits of Fig. 8.1 is shown in Fig. 8.9. The reconstructions are done simply by connecting the adjacent ports that have the same variables as shown in Fig. 8.10. Note that DC side subcircuit D is unchanged. The circuit shown in Fig. 8.10 is equivalent to the original one shown in Fig. 8.1 in the sense of the power-invariant DQ transformation. The DC and AC analyses of Fig. 8.1 can be done by the circuits deduced from this DQ transformed circuit.

8.2.4 Circuit Perturbation

The transformer turn-ratio, which corresponds to the duty ratio of the switch, and the gyrator frequency, which corresponds to the switching frequency, are the control signals in the power electronics. To determine the AC transfer functions, the perturbed circuits must be obtained. A detailed circuit perturbation technique can be found in the literature [7].

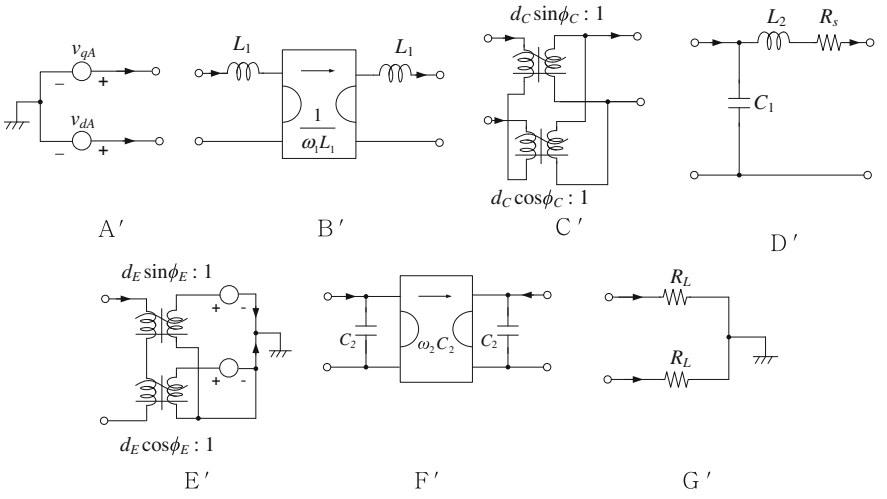

Fig. 8.9 DQ transformed partitioned subcircuits

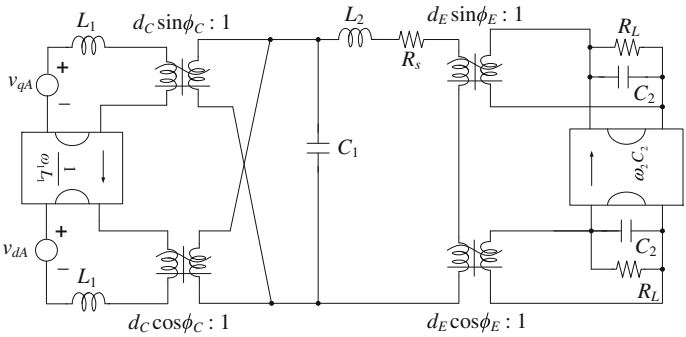

Fig. 8.10 Reconstruction of partitioned circuits

1. ***Transformer Perturbation***: The turn-ratio is perturbed as shown in Fig. 8.18, such that a voltage source and a current source are generated. The negligible bilinear term is eliminated, as shown in Fig. 8.11d.
2. ***Gyrator Perturbation***: The two kinds of gyrators are shown in Figs. 8.12 and 8.13. The switching frequency is perturbed, and thus two sources are generated, neglecting the bilinear terms.

By applying the perturbed transformer and gyrator to the *DQ* transformed circuit of Fig. 8.10, the AC transfer functions can be calculated as functions of the duty ratio, switching frequency, input voltage, etc. This will be shown for the simpler case in the following section for better illustration.

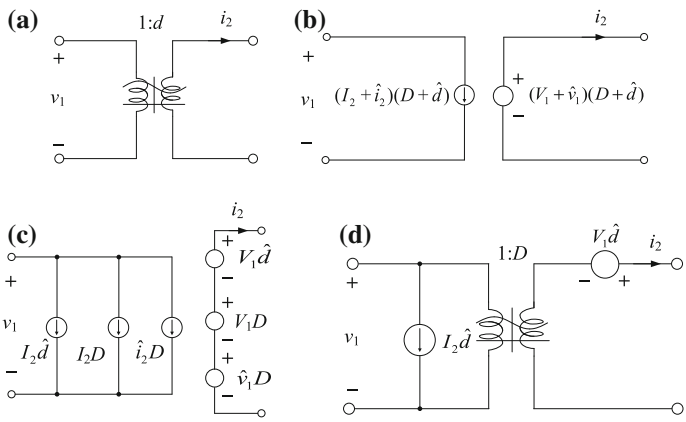

Fig. 8.11 Perturbed transformer. **a** Original. **b** Perturbed. **c** Separated. **d** Final equivalent transformer

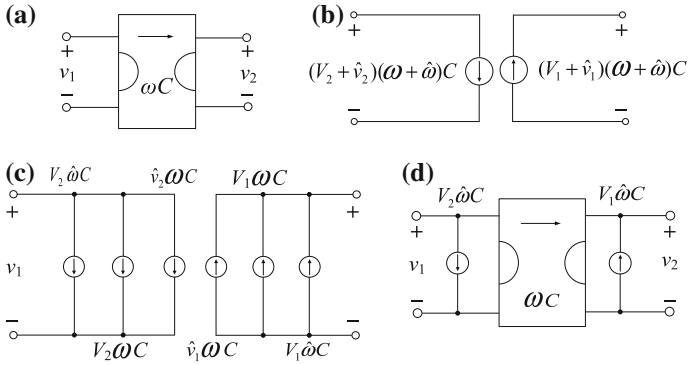

Fig. 8.12 Perturbed capacitive gyrator. **a** Original. **b** Perturbed. **c** Separated. **d** Final equivalent gyrator

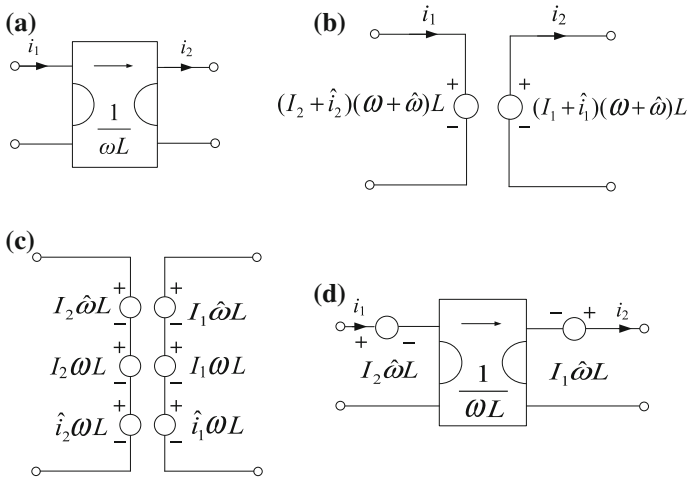

Fig. 8.13 Perturbed inductive gyrator. **a** Original. **b** Perturbed. **c** Separated. **d** Final equivalent gyrator

8.2.5 DC Analysis

The DC operating points can be determined by analyzing Fig. 8.14, which is obtained from Fig. 8.10 by shorting inductors and opening capacitors. The DC voltage gain is calculated from Fig. 8.14 by applying conventional circuit laws as follows:

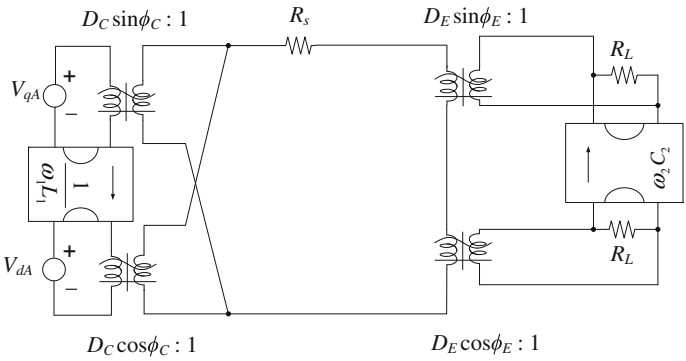

Fig. 8.14 DC circuit of rectifier-inverter circuit

$$G_v = \frac{V_0}{V_s} = \frac{D_c D_E R_L \sin(\phi_1 - \phi_c)}{\omega_1 L_1 \sqrt{1 + (\omega_2 C_2 R_2)^2}} \tag{8.16}$$

Equation (8.16) is of very simple form despite the complexities in the circuit configuration and the inclusions of several conditions such as arbitrary PWM switching patterns and arbitrary input/output frequencies and voltages. It is noteworthy that this voltage gain G_v, is not sensitive to the inductor resistance R_s and the inverter phase ϕ_E, which seem to affect to the gain. It can be seen from Eq (8.16) that as the output voltage decreases either the input or the output frequency increases and that the system has self-short-circuit protection capability since the output voltage becomes zero when R_L is zero notwithstanding the states of the rectifier or the inverter controllers.

8.3 Buck-Boost Inverter Analysis

To compare the proposed technique with the previous one, the buck-boost inverter shown in Fig. 8.15 analyzed in [8], is analyzed again here. The DQ transformed circuit is obtained as shown in Fig. 8.16 by substituting the subcircuits of Fig. 8.15

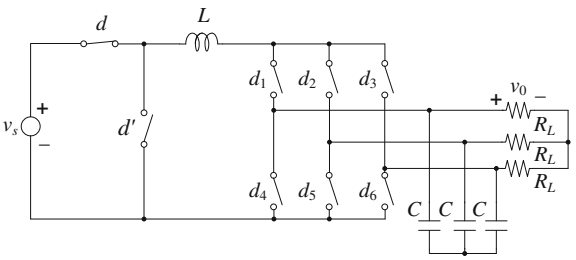

Fig. 8.15 Buck-boost inverter

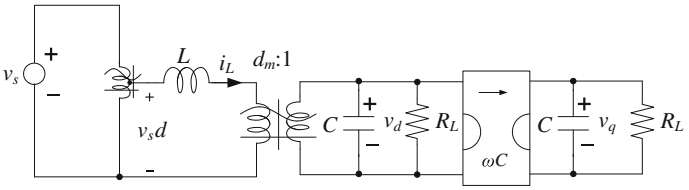

Fig. 8.16 DQ transformed buck-boost inverter

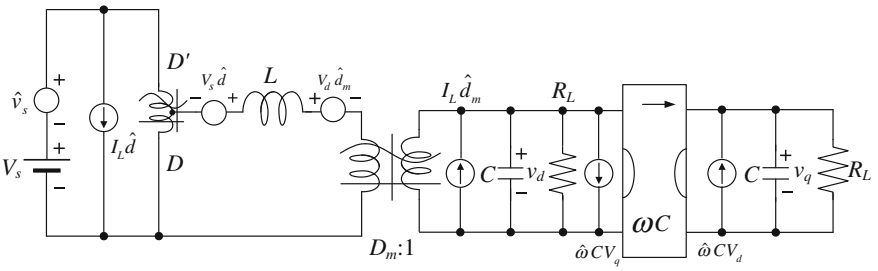

Fig. 8.17 Perturbed buck-boost inverter

with their subcircuits and combining them. The perturbed circuit is Fig. 8.17. The transfer function of $G_d(s)$, which is the perturbed output response against the perturbed duty ratio of the buck converter, is calculated as an example. $G_d(s)$ used in designing the controller that regulates the output voltage by the buck converter; by a few manipulations it is found from

Figure 8.17 as follows:

$$G_d(s) = \frac{\hat{V}_d(s)}{\hat{D}_m(s)} = \frac{G_1(s)}{G_2(s)} \tag{8.17}$$

where

$$\begin{aligned} G_1(s) &= \frac{1}{D_m^2}(1 + sCR_L)(sLI_L - V_d D_m) \\ G_1(s) &= 1 + (R_L C + \frac{\omega^2 LC^2 R_L}{D_m^2} + \frac{L}{D_m^2 R_L})s \\ &\quad + \frac{2LC}{D_m^2}s^2 + \frac{LC^2 R_L}{D_m^2}s^3 \end{aligned} \tag{8.18}$$

Comparing this result with that in [8], it is found that both approaches give the same results.

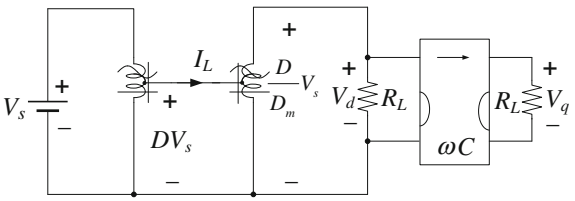

Fig. 8.18 DC circuit of buck-boost inverter

Since the DC circuit can be drawn from Fig. 8.16 as depicted in Fig. 8.18, the voltage gain becomes

$$G_v \equiv \frac{V_o}{V_s} = \frac{\sqrt{V_d^2 + V_q^2}}{V_s} = \frac{D}{D_m}\sqrt{1 + (\omega C R_L)^2}. \tag{8.19}$$

This result is also the same as that in [8]. The modeling procedure is, however, considerably simplified by this new approach. The cumbersome matrix inversions and multiplications, which are in many cases impossible to manipulate by hand, are avoided here. It is apparent that this equivalent circuit model provides more convenience and physical insight than does the equational model.

8.4 Concluding Remarks

The fact that the equivalent circuits for the switches are ideal time-varying transformer is proved in general, and the new circuit DQ transformation technique is identified a simple and useful method in the analysis of AC converters. An eighth-order rectifier-inverter is analyzed by the proposed circuit DQ transformation such that the equivalent circuit is derived and the DC voltage gain is calculated; it could hardly be analyzed by conventional approaches. The rectifier-inverter is found to have self-short-circuit protection capability and robustness in the parasitic inductor resistance. By the comparison with the conventional approach in analyzing the buck-boost inverter, the proposed approach is found to give almost the same results; however, it provides more physical insight with fewer equational manipulations, especially high-order matrix inversion and multiplication that often prevent manual solution. Since the equivalent circuits are composed of traditional electric circuit components only, it can be concluded that the analyses of all linear switching systems become those of the *RLC* filters with transformers and gyrators.

References

1. Rim CT, Hu DY, Cho GH (1990) Transformers as equivalent circuits for switches: General proofs and D-Q transformation-based analysis. IEEE Trans Ind Appl 777–785
2. Wood P (1979) General theory of switching power converters. In: IEEE power electronics specialists conference record, pp 3–10
3. Rim CT, Joung GB, Cho GH (1988) A state space modeling of non-ideal DC-DC converters. In: IEEE power electronics specialists conference record, pp 943–950
4. Verghese GC, Elbuluk ME, Kassakian JG (1986) A general approach to sampled-data modeling for power electronic circuits. IEEE Trans. Power Electron. PE-1(2):76–89
5. Verghese G, Mukherji U (1981) Extended averaging and control procedures. In: IEEE power electronics specialists conference record, pp 329–336
6. Lee FCY, Iwens RP, Yu Y, Triner JE (1979) Generalized computer-aided discrete time-domain modeling and analysis of DC-DC converters. IEEE Trans Ind Electron Contr Instrum IECI-26(2):58–69
7. Middlebrook RD, Cuk S (1976) A general unified approach to modeling switching converter stages, In: IEEE power electronics specialists conference record, pp 18–34
8. Ngo KDT (1986) Low frequency characterization of PWM converter. IEEE Trans Power Electron PE-1(4):223–230
9. Middlebrook RD (1987) Topics in multi-loop regulators and current-mode programming. IEEE Trans Power Electron PE-2(2):109–124
10. Vorperian V, Tymersky R, Lee FCY (1989) Equivalent circuit models for resonant and PWM switches. IEEE Trans Power Electron PE-4(2):205–214
11. Alesina A, Venturini MGB (1981) Solid-state power conversion: a fourier analysis approach to generalized transformer synthesis. IEEE Trans Circuits Syst CAS-28(4):319–330
12. Cespedes M, Sun J (2014) Impedance modeling and analysis of grid-connected voltage-source converters. IEEE Trans Power Electron 29(3):1254–1261

Chapter 9
Application of Circuit DQ Transformation to Current Source Inverter

The circuit DQ transformation is used to analyze a three-phase controlled-current PWM rectifier in this chapter. The DC operating point and AC transfer functions are completely determined. Most features of the converter are clearly interpreted. They are (1) the output voltage can be controlled from zero to maximum, (2) the system is equivalently an ideal current source in the steady state, (3) the system can be described as linear circuits, and (4) the input power factor can be arbitrarily controlled within a certain control range. A lot of this chapter is based on our papers [1, 2]. The circuit DQ transformation is used to analyze a three-phase controlled-current PWM rectifier in this chapter. The DC operating point and AC transfer functions are completely determined. Most features of the converter are clearly interpreted. They are (1) the output voltage can be controlled from zero to maximum, (2) the system is equivalently an ideal current source in the steady state, (3) the system can be described as linear circuits, and (4) the input power factor can be arbitrarily controlled within a certain control range. A lot of this chapter is based on our papers [1, 2].

9.1 Introduction

Aa an excellent DC voltage source of VSI-fed motor drive, the three-phase controlled-current PWM rectifier has been widely studied. Its numerous merits such as sinusoidal input current, power factor adjustment capability, and instantaneous power flow change make it different from the conventional phase controlled rectifier (PCR). Previous works are so much focused on the space vector input current control method [3, 4–6] that the rectified DC voltage should be larger than some value [5, 6], and nonlinear dynamic equation is therefore generated [3, 4–6]. A system control method that is based on the predetermined switching pattern, PWM is sometimes found in the literature [7]. A modeling based on the equational DQ transformation and its application to several control methods of the DC-side

C.T. Rim, *Phasor Power Electronics*, KAIST Research Series,
DOI 10.1007/978-981-10-0536-7_9

capacitor voltage are introduced [8, 9]. However, so far the following important features of the ideal rectifier are not clearly interpreted without the manipulation of complex equations:

1. The rectified DC voltage ranges from zero to its maximum.
2. The rectified DC part is an ideal current source in the steady state.
3. The power factor can be controlled arbitrary only within a certain control range.
4. The system is linear with respect to the source voltage when it is open-loop controlled.
5. Full sets of the DC and linearized AC transfer functions.
6. Open loop control as well as closed-loop control of the system is allowable.

The features are independent of PWM patterns and circuit parameters. In this chapter, they are fully explained based on the recently proposed circuit DQ transformation with great ease in analysis [10]. Some negative aspects of the converter such as large in-rush-current problem and input side harmonic current problem are not described in this chapter, despite their practical importance, in order to highlight on the basic features of the converter.

9.2 Circuit DQ Transformation of the Current Source Inverter

The system shown in Fig. 9.1 is a three-phase controlled current PWM rectifier to be modeled in this section. All circuit elements are LTI (linear time-invariant). All switches and the source voltages are ideal and balanced. The switches operate in the CCM continuous conduction mode). The switch pattern may be either any PWM or six-pulse control, so long as its switching harmonics are not dominant. Now the switched linear time-varying system shown in Fig. 9.1 is to be transformed to an equivalent LTI system by the circuit DQ transformation [10].

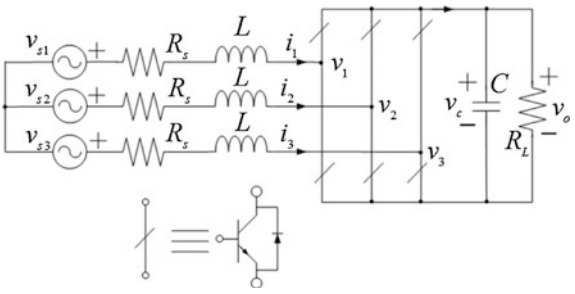

Fig. 9.1 Three-phase controlled-current PWM rectifier

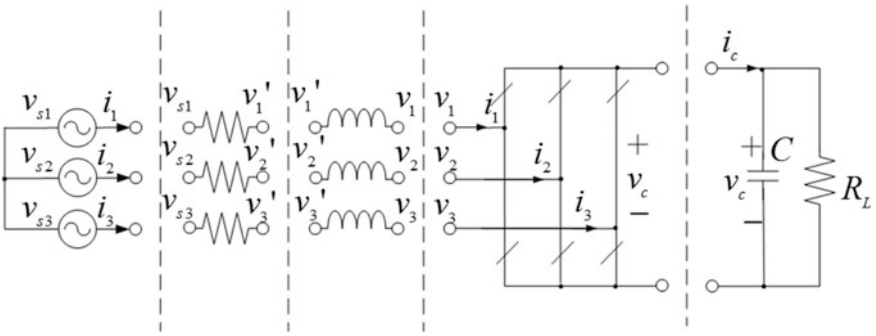

Fig. 9.2 Partitioned circuit

9.2.1 Circuit Partitioning

The original system is too complex to analyze as a whole. It is therefore partitioned to several basic subcircuits that can be analyzed with ease. There are five basic subcircuits in the PWM rectifier. They are voltage source set, resistor set, inductor set, VSI switch set, and DC circuit. The rule of circuit partitioning is to make the original circuit be composed of basic subcircuits only. The results are shown in Fig. 9.2.

9.2.2 Circuit DQ Transformation of Basic Subcircuits

The rotary circuits are now transformed to stationary circuits. The time-varying nature of the switching system is eliminated in this way. The voltage source, switching function, and power invariant DQ transformation matrix are given as follows: (9.1)–(9.4) shown at the bottom of the page, where

$$\boldsymbol{v_{abc}} = \begin{bmatrix} v_{s1} \\ v_{s2} \\ v_{s3} \end{bmatrix} = \sqrt{2/3} V_s \begin{bmatrix} \sin(\omega t + \phi_1) \\ \sin(\omega t - 2\pi/3 + \phi_1) \\ \sin(\omega t + 2\pi/3 + \phi_1) \end{bmatrix} \tag{9.1}$$

$$\boldsymbol{s} = \begin{bmatrix} s_1 \\ s_2 \\ s_3 \end{bmatrix} = \sqrt{2/3} d \begin{bmatrix} \sin(\omega t + \phi_2) \\ \sin(\omega t - 2\pi/3 + \phi_2) \\ \sin(\omega t + 2\pi/3 + \phi_1) \end{bmatrix} \tag{9.2}$$

$$\boldsymbol{K} = \sqrt{2/3} \begin{bmatrix} \sin(\omega t + \phi) & \cos(\omega t - 2\pi/3 + \pi) & \cos(\omega t + 2\pi/3 + \phi) \\ \sin(\omega t + \phi) & \sin(\omega t - 2\pi/3 + \phi) & \sin(\omega t + 2\pi/3 + \phi) \\ 1/\sqrt{2} & 1/\sqrt{2} & 1/\sqrt{2} \end{bmatrix} \tag{9.3}$$

$$\because \quad \boldsymbol{K}^{-1} = \boldsymbol{K}^{T} \tag{9.4}$$

$$\boldsymbol{v} = v_c \boldsymbol{s}, \quad i_c = \boldsymbol{s}^{T} \boldsymbol{i}, \quad \boldsymbol{x}_{qd0} = \boldsymbol{K} \boldsymbol{x}_{abc} \tag{9.5}$$

The voltage source is balanced by the assumption, and the switching function is continuous sinusoidal, assuming that the high-order switching harmonics do not contribute much to the fundamental components. The constant phases of the voltage source, switching function, and DQ transformation matrix are arbitrary, as denoted by (9.1), (9.2), and (9.3).

The modulation index d of (9.2) ranges from zero to 1.56 and is controlled externally. The x of (9.5) denotes any AC voltage or current variables in Figs. 9.1, 9.2, 9.3, 9.4. The voltage and current variables of (9.5) represent the operation of rectifier switches.

The equivalent circuits can be drawn from the DQ variables using conventional circuit elements, such as transformers, gyrators, and inductors.

By this transformation, the inductor set becomes a second-order gyrator-coupled system, and the switch set becomes time-invariant transformers as well. Since all switching harmonics are assumed to be negligible, if only the fundamental component of a switching function is identical, then the dynamic response is just identical regardless of the PWM patterns. The result of the transformation is shown in Fig. 9.3, where all switches vanish.

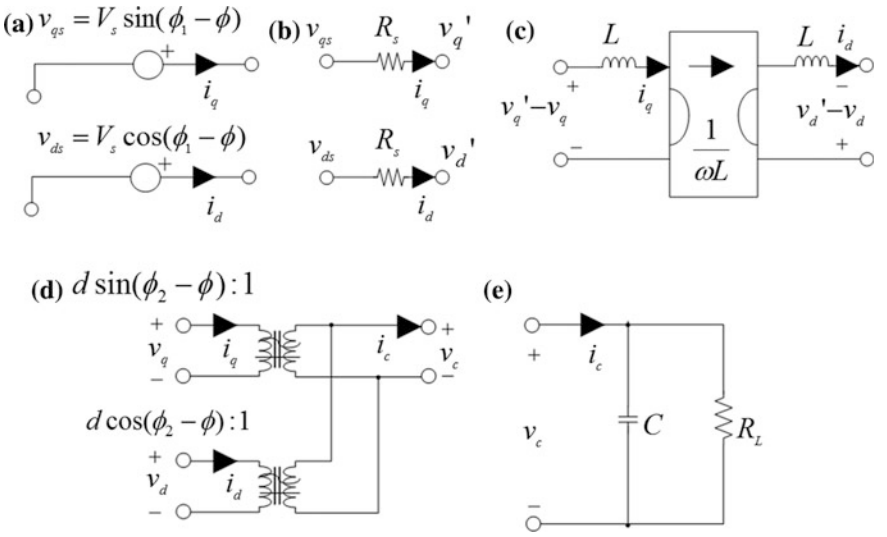

Fig. 9.3 DQ transformed partitioned circuits

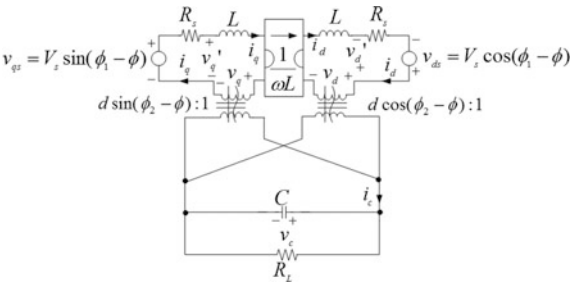

Fig. 9.4 Reconstructed stationary circuit

9.2.3 Circuit Reconstruction

The rule of circuit reconstruction is to connect the adjacent related nodes where the voltage and current variables are the same. The result is shown in Fig. 9.4. The resultant stationary circuit is LTI with respect to the source voltage. Remember that previous works showed the nonlinearity of this system [3–6]. It can be seen that the nonlinearity does not stem from the system elements, such as switches, but from the nonlinear switch control. This circuit can be directly used to find the DC operating points and the dynamic responses.

9.2.4 Circuit Reduction

The stationary circuit shown in Fig. 9.4 can be simplified noticing the fact that the phase of the DQ transform can be set to an arbitrary value. One possible selection is $\phi = \phi_1$. Then v_q becomes zero, as shown in Fig. 9.5.

Another choice is $\phi = \phi_2$. Then one of the transformers vanishes, as shown in Fig. 9.6. It is evident that this selection simplifies the original system much more than the previous one does. Remark that there is no loss of generality throughout the procedures.

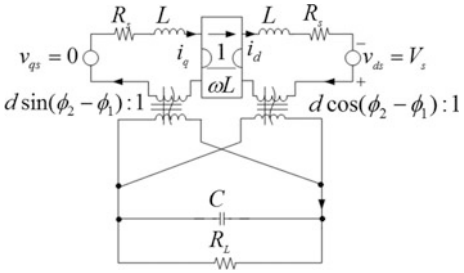

Fig. 9.5 Simplified circuit ($\phi = \phi_1$ case)

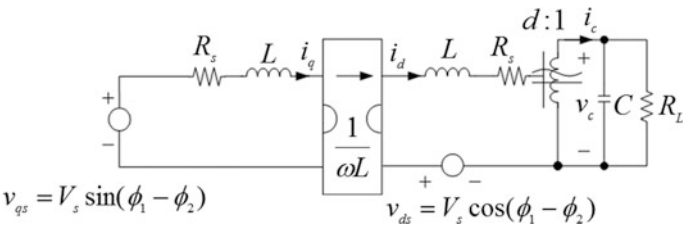

Fig. 9.6 Simplified circuit ($\phi = \phi_2$ case)

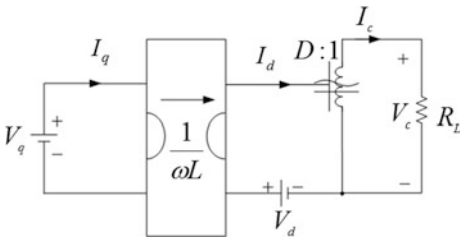

Fig. 9.7 The DC circuit with no source resistance

9.3 DC Analysis

The DC analysis can be performed by the steady-state circuit, as shown in Fig. 9.7, obtained from Fig. 9.6 by shorting the inductors and opening the capacitor. To pay our whole attention to the description of the main features of the system, the parasitic source resistances are omitted.

9.3.1 DC Transfer Function: G_v

It is found from Fig. 9.7 that

$$V_c = I_c R_L = I_d D R_L = \frac{V_q}{\omega_L} D R_L = \frac{V_s \sin \phi_0}{\omega L} D R_L, \tag{9.6}$$

where

$$\begin{aligned} V_q &= V_s \sin(\phi_1 - \phi_2) = V_s \sin \phi_0 \\ V_d &= V_s \cos(\phi_1 - \phi_2) = V_s \cos \phi_0 \end{aligned} \tag{9.7}$$

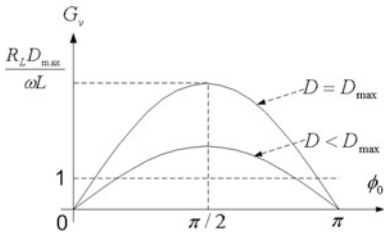

Fig. 9.8 The DC voltage gain

and ϕ_0 is the phase difference between the source voltage and switching function. Then the DC transfer function is found to be

$$G_v = \frac{V_c}{V_s} = \frac{\sin\phi_0}{\omega L} D R_L \tag{9.8}$$

Note that G_v ranges from zero to infinite by controlling ϕ_0 and D. However, this is impeded in practice by current or voltage ratings. Because of this constraint, G_v should be near unity. For given circuit parameters, the maximum DC transfer function is given by

$$G_{v,\max} = \frac{R_L}{\omega L} D_{\max} \tag{9.9}$$

Thus it can be seen that for given $G_{v,\max}$ *and* R_L the source inductor impedance should be smaller than the value determined by (9.9) to establish enough DC output voltage. Equivalently, *RL* should be much larger than the source inductor impedance to guarantee ϕ_0 and D of (9.8) small enough for power factor control.

Figure 9.8 shows the G_v as a function of the phase difference between the source and inverter voltages for different values of the modulation index D. The DC analysis based on the circuit DQ transformation is very straightforward, so we do not have to do any cumbersome equational manipulation.

9.3.2 *Ideal Current Source Characteristics*

The rectified current *Io* is found from Fig. 9.7 and (9.6) as

$$I_0 = I_C = \frac{V_s \sin\phi_0}{\omega L} D \tag{9.10}$$

Note that it is independent of the DC voltage V_s, or load resistor R_L. It is determined by circuit parameters and switching function variables only. Hence it is an ideal current source controlled by the switching function characterized by ϕ_0 and D.

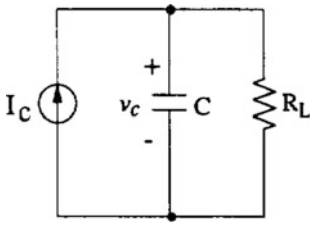

Fig. 9.9 Quasi-steady-state output model

This ideal current source feature is very useful when we construct a quasi-steady-state capacitor voltage controller. In case the system response is very slow, it is possible to approximate the system into a first-order system as shown in Fig. 9.9, since the capacitor is very large in practice. The maximum current is limited by the source impedance. Note the fact that negative current flow is also allowed if the switches were four-quadrant ones. Regeneration occurs instantaneously when the polarity of current is negative while the DC capacitor voltage is kept positive, not in the steady state but in the transient state.

9.3.3 Input Power: P, Q, PF (Resistive Load Case)

The input real power P and reactive power Q are found to be

$$P = V_q I_q + V_d I_d = \frac{V_s^2}{\omega L} a \sin^2 \phi_0 \tag{9.11a}$$

$$Q = V_q I_d + V_d I_q = \frac{V_s^2}{\omega L} (1 - a \sin \phi_0 \cos \phi_0) \tag{9.11b}$$

Where

$$a = \frac{D^2 R_L}{\omega L} \tag{9.12}$$

Then the power factor PF becomes

$$PF = \frac{P}{(P^2 + Q^2)^{1/2}} = \frac{a \sin^2 \phi_0}{\left(1 - a \sin 2\phi_0 + a^2 \sin^2 \phi_0\right)^{1/2}} \tag{9.13}$$

Figures 9.10, 9.11, 9.12 show the P, Q, and PF for different a's, respectively. By proper selection of a and ϕ_0, the P and Q can be controlled as required. For the optimum operation of the system, the power factor should be at its maximum value. It can be seen from Fig. 9.11 that a should be larger than 2 for the unity power factor. In other words, power factor may not be unity when the load resistor is very

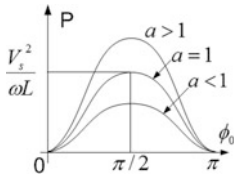

Fig. 9.10 Real power

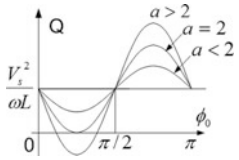

Fig. 9.11 Reactive power

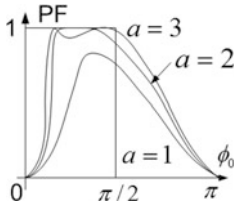

Fig. 9.12 Power factor

small, as can be seen from (9.12) and (9.13). This fact has not been reported before. The unity power factor is obtained when the reactive power is zero. From (9.11b) it can be seen that

$$1 - \frac{2}{a}\sin 2\phi_0 = 0 \quad or \quad \phi_0 = \frac{1}{2}\sin^{-1}\left(\frac{2}{a}\right), \quad a \geq 2 \tag{9.14}$$

Under the unity power factor condition of (9.14), the output capacitor voltage of (9.6) becomes

$$V_c = \frac{V_s R_L}{\omega L} D \sin\left[\frac{1}{2}\sin^{-1}\frac{2\omega L}{D^2 R_L}\right] \approx \frac{V_s}{D}, \quad a \gg 2 \tag{9.15}$$

Hence the output voltage is determined similar with a boost converter under the unity power factor condition. Remark that when the load resistance is much larger than the source inductor impedance, the voltage is not sensitive to the load resistance. On the other hand, power factor becomes its maximum even though it is smaller than unity when the ratio of Q and P is minimum. This is calculated from (9.11a) (9.11b) as follows:

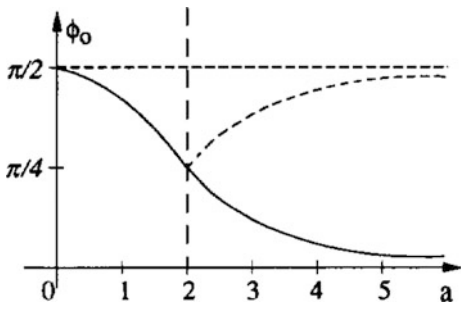

Fig. 9.13 Maximum power factor condition

$$PF = \frac{4a}{a^2+4}, \phi_0 = \sin^{-1}\frac{2}{(a^2+4)^{1/2}}, \quad a<2 \tag{9.16}$$

Figure 9.13 shows the maximum power factor conditions determined by (9.14) and (9.16). There are two possible ϕ_0's when a is larger than 2. The larger one (dotted line) cannot be realized in practice since the output voltage of (9.6) becomes too much larger than the source voltage.

9.3.4 *Input Power: P, Q, PF (No Load Case)*

At no load case, the system may be a reactive power compensator. The DC voltage can be fixed to a certain predetermined value by controlling the rectified current of (9.10). In the steady state, real power and PF are set to zeros by adjusting ϕ_0 to be zero; that is,

$$P = PF = \phi_0 = 0 \tag{9.17}$$

Then reactive power becomes

$$Q = \frac{V_s^2}{\omega L}(1-b), \quad b = \frac{DV_c}{V_s} \tag{9.18}$$

Equation (9.18) shows that the reactive power may be directly controlled by b or equivalently D from negative to positive, as shown in Fig. 9.14. Considering an input side equivalent circuit (9.18) becomes

$$Q = \begin{cases} \frac{V_s^2}{\omega L_{eq}} \leftrightarrow L_{eq} = \frac{L}{1-b}, & b<1 \\ -\omega C_{eq} V_s^2 \leftrightarrow C_{eq} = \frac{b-1}{\omega^2 L}, & b \geq 1 \end{cases} \tag{9.19}$$

The converter is an equivalently variable reluctance linear reactive power compensator (Fig. 9.15).

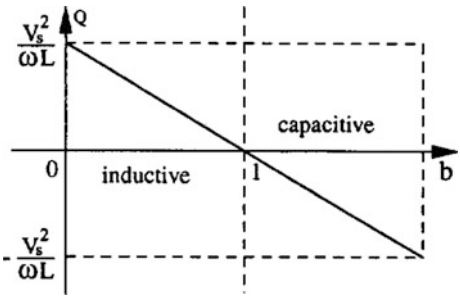

Fig. 9.14 Reactive power

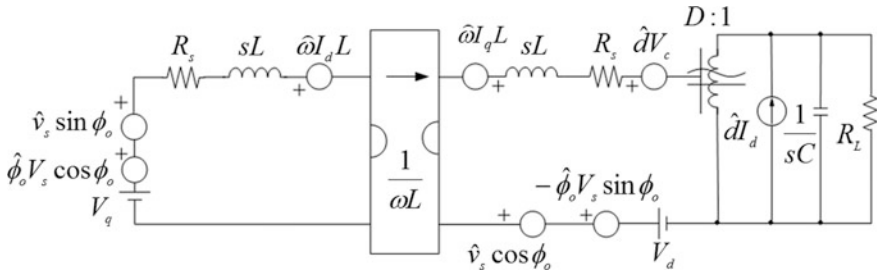

Fig. 9.15 The AC perturbed circuit

9.4 AC Analysis

In this section the specified circuit shown in Fig. 9.6 is analyzed. Though the equivalent circuit shown in Fig. 9.6 is composed of linear elements, this circuit should be perturbed since the circuit is not linear with respect to some variables. Hence the first step is to obtain a perturbed circuit from Fig. 9.6. There are four possible perturbation variables in the system. They are input voltage, and input frequency, phase, and modulation index. Among these, the former two are disturbances and the latter two are control variables. For normal power line, the input frequency is so stable that this may not be a disturbance in this case. Then the AC small-signal perturbed circuit is drawn as shown in Fig. 9.16 [10]. It seems to be very complex to analyze the circuit shown in Fig. 9.16. It is necessary to find a more simplified circuit. Figure 9.17 shows this circuit where sources are integrated and DC source is eliminated. The voltage sources are

$$v_1 = \hat{v}_s \sin\phi_0 + \hat{\phi}_0 V_s \cos\phi_0 - \hat{\omega} I_d L$$
$$v_2 = \hat{v}_s \cos\phi_0 + \hat{\phi}_0 V_s \sin\phi_0 - \hat{\omega} I_q L - \hat{d} V_c$$

$$i_1 = \hat{d}\, I_d \tag{9.20}$$

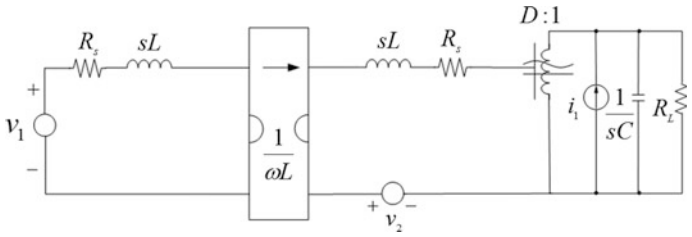

Fig. 9.16 The simplified circuit

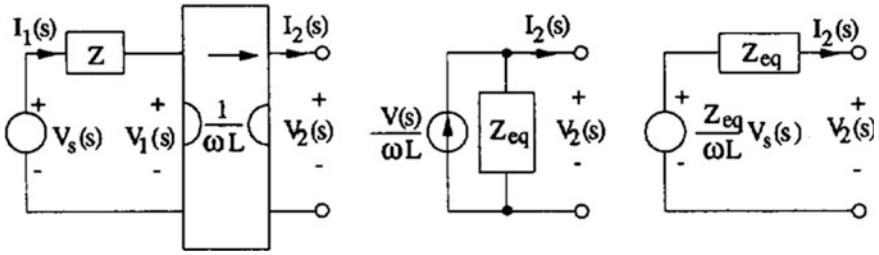

Fig. 9.17 The removal of the gyrator

Now the cumbersome gyrator is to be removed. Considering Norton's Theorem, it can be seen from Fig. 9.17 that

$$I_2(s) = \frac{V_1(s)}{\omega L} = \frac{V_s(s) - I_1(s)Z}{\omega L} = \frac{V_s(s)}{\omega L} - \frac{V_s(s)}{Z_{eq}} \tag{9.21a}$$

$$V_2(s) = \frac{Z_{eq}}{\omega L} V_s(s) - I_2(s)Z_{eq} \tag{9.21b}$$

where

$$Z_{eq} = \frac{(\omega L)^2}{Z} \tag{9.22}$$

Applying the removal processes of the gyrator and the transformer to the circuit of Fig. 9.16, the output voltage can be obtained as follows:

$$V_0(s) = H_1(s)V_1(s) + H_2(s)V_2(s) + H_3(s)I_1(s) \tag{9.23a}$$

or

$$\begin{aligned} V_0(s) = {} & H_1(s)\left\{\hat{V}_s(s)\sin\phi_0 + \hat{\phi}_0(s)V_s\cos\phi_0 - \hat{\omega}_s I_d L\right\} \\ & + H_2(s)\left\{\hat{V}_s(s)\cos\phi_0 + \hat{\phi}_0(s)V_s\sin\phi_0 - \hat{\omega}_s I_q L - \hat{D}(s)V_c\right\} + H_3(s)\left\{\hat{D}(s)I_d\right\} \end{aligned} \tag{9.23b}$$

or

$$V_0(s) = G_v(s)\hat{V}_s(s) + G_\phi(s)\hat{\phi}_0(s) + G_\omega(s)\hat{\omega}(s) + G_d(s)\hat{D}(s) \tag{9.23c}$$

where

$$G_v(s) = \frac{V_0(s)}{\hat{V}(s)} = H_1(s)\sin\phi_0 + H_2(s)\cos\phi_0 \tag{9.24a}$$

$$G_\phi(s) = \frac{V_0(s)}{\hat{\phi}(s)} = [H_1(s)\cos\phi_0 - H_2(s)\sin\phi_0]V_s \tag{9.24b}$$

$$G_\omega(s) = \frac{V_0(s)}{\hat{\omega}(s)} = \left[-H_1(s)I_d + H_2(s)I_q\right]L \tag{9.24c}$$

$$G_d(s) = \frac{V_0(s)}{\hat{D}(s)} = -H_2(s)V_c + H_3(s)I_d \tag{9.24d}$$

and

$$H_1(s) = \frac{G_1(s)}{G_0(s)}, \quad H_2(s) = \frac{G_2(s)}{G_0(s)}, \quad H_3(s) = \frac{G_3(s)}{G_0(s)}. \tag{9.25}$$

We also have

$$\begin{aligned} G_0(s) &= D^2R_L(sL + R_s) + (sR_LC + 1)\cdot\left\{(sL + R_s)^2 + (\omega L)^2\right\} \\ G_1(s) &= \omega LDR_L \\ G_2(s) &= (sL + R_s)DR_L \\ G_3(s) &= \left\{(sL + R_s)^2 + (\omega L)^2\right\}R_L \end{aligned} \tag{9.26}$$

Now the four AC transfer functions are fully determined, completing the AC analysis. The transfer functions are nonlinear to the DC operating points, and the system order is found to be three. The analysis is very simple because of the graphical tool, the circuit DQ transformation.

9.5 Simulation Verification

Previous results are now partially verified by time-domain simulations. Experimental verification is not always superior to the simulation verifications since it can cause unwanted discrepancy to arise. The circuit parameters for simulation are selected as follows:

$$\begin{array}{llll} V_s = 220\,\mathrm{V}, & \omega = 120\pi\,\mathrm{rad/s}, & \phi_0 = 4^\circ & L = 5\,\mathrm{mH} \\ C = 2000\,\mu\mathrm{F} & R_s = 1\,\Omega & R_L = 100\,\Omega & D = 1.0 \end{array} \tag{9.27}$$

To verify the circuit model of Fig. 9.6, the step responses for ϕ_0 are compared, as shown in Figs. 9.18 and 9.19. Figure 9.18 shows the step response of the model of Fig. 9.6, whereas Fig. 9.19 shows that of the original circuit of Fig. 9.1. It can be seen from Fig. 9.19 that the circuit DQ transformed model is very exact, excluding the harmonics.

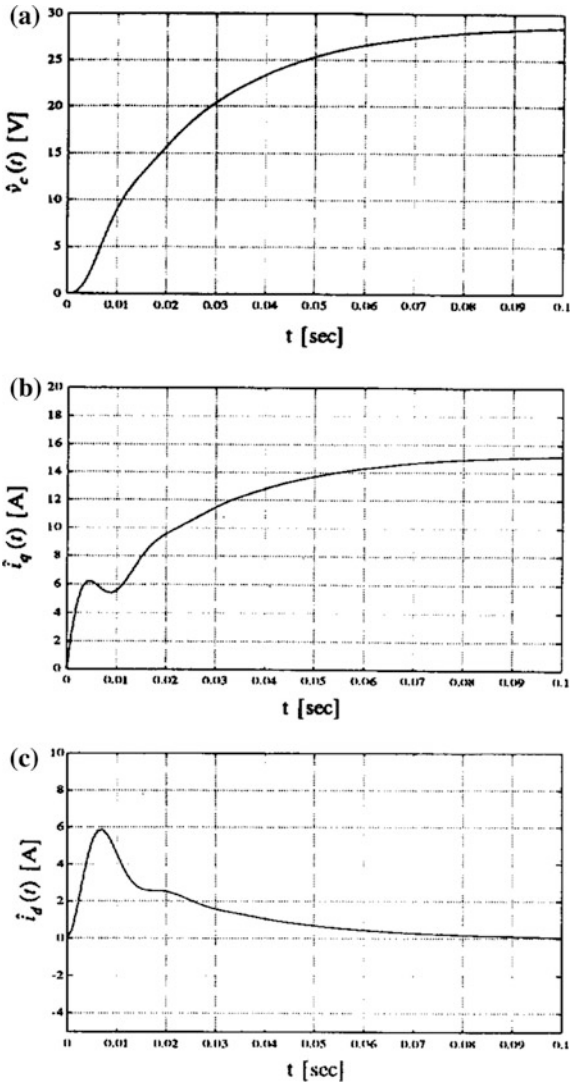

Fig. 9.18 Step responses of the circuit model of Fig. 9.6 (input is $\hat{\phi} = 4u(t)^\circ$) **a** Step response of DC capacitor voltage. **b** Step response of q-axiscurrent. **c** Step response of d-axis current

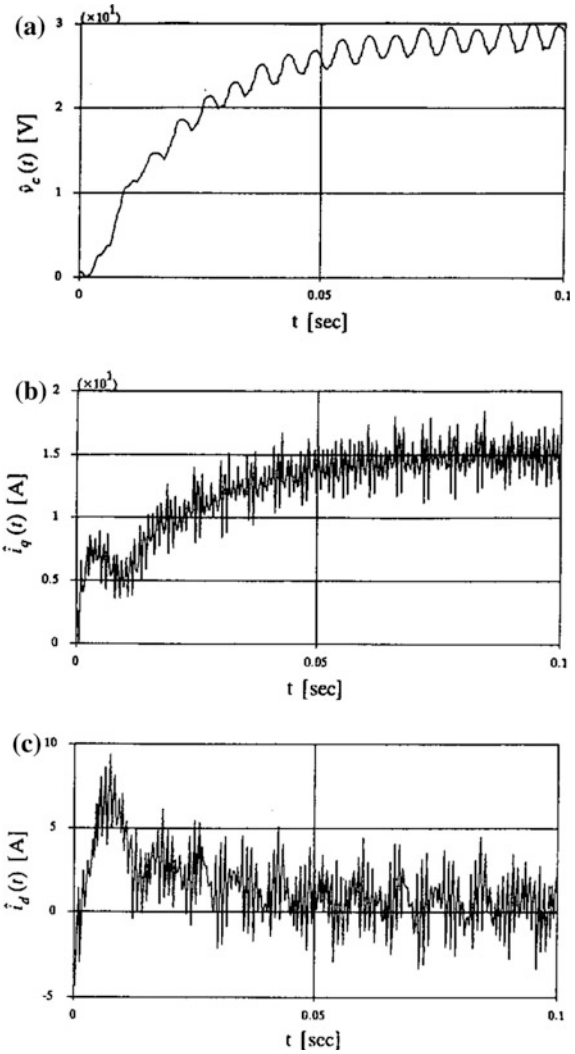

Fig. 9.19 Step responses of the original circuit of Fig. 9.1 (input is $\hat{\phi}_0 = 4u(t)\,^\circ$) **a** Step response of DC capacitor voltage. **b** Step response of q-axiscurrent. **c** Step response of d-axis current

9.6 Concluding Remarks

The rectifier has been completely analyzed. Several new facts are suggested and verified by a recently proposed analysis technique, the circuit DQ transformation, and simulation. The DC voltage can be controlled from zero to its maximum, and the system is a linear ideal current source in the steady state. The power factor is less than unity when a is less than 2, whereas it can be unity when a is larger than 2. The reactive power control capability is described in detail. Four AC small-signal

transfer functions are fully determined without much equational manipulation. It can be concluded that the circuit DQ transformation is a very powerful tool in the analysis of polyphase AC systems.

References

1. Rim CT, Choi NS, Cho GC, Cho GH (1994) A complete DC and AC analysis of three-phase controlled-current PWM rectifier using circuit D-Q transformation. IEEE Trans Power Electron 9(4):390–396
2. Han SB, Choi NS, Chun T, Rim T, Cho GH (1998) Modeling and analysis of static and dynamic characteristics for buck type three-phase PWM rectifier by circuit DQ transformation. IEEE Trans Power Electron 13(2):323–336
3. Ooi BT, Dixon JW, Kulkami AB, Nishimoto M (1988) An integrated AC drive system using a controlled-current PWM rectifier/inverter link. Power Electron PE-3(1):64–71
4. Nishimoto M, Dixon IW, Kulkami AB, Ooi BT (1987) An integrated controlled-current PWM rectifier chopper link for sliding mode position control. IEEE Trans Ind App IA-23(5):894–900
5. Dixon JW, Kulkami AB, Nishimoto M, Ooi BT (1987) Characteristic of a controlled-current PWM rectifier-inverter link. IEEE Trans Indust Appl IA-23(6): 1022–1028
6. Ooi BT, Salmon JC, Dixon JW, Kulkami (1987) A three phase controlled-current PWM converter with lagging power factor. IEEE Trans Indust Appl IA-23(1):78434
7. Wemekinck E, Kawamura A, Hoft R (1987) A high frequency ac/DC converter with unity power factor and minimum harmonic distortion. IEEE PESC Rec 264–270
8. Sugimoto H, Morimoto S, Yano M (1988) A high performance control method of a voltage-type PWM converter. IEEE PESC Rec 360–368
9. Lipo TA (1988) Recent progress in the development of solid-state AC motor drives. IEEE Trans Power Electron PE-3(2):105–117
10. CT Rim, DY, Huh, Cho GH (1988) The graphical DQ transformation of general power switching converters. IEEE IAS Conf Rec 940–945

Part V
Unified General Phasor Transformation

Phasor transformations were at first developed for single phase AC systems, then the circuit DQ transformation was developed for multi-phase AC systems. They should be unified to form a unified general phasor transformation. Furthermore, this model should be able to use for both DC analyses (static phasor transformation) and AC analyses (dynamic phasor transformation or Laplace phasor transformation), which is explained in the subsequent chapters.

More general phasor transformation that embraces the nonlinear switching case of DCM are possible, but this issue is not included in this book this time.

Chapter 10
Static Phasor Transformation

It is highly demanded in power electronics to analyze thousands of numerous converters and power circuits by a unified general theory like the conventional Laplace transform or Fourier transform. It is highly demanded in power electronics to analyze thousands of numerous converters and power circuits by a unified general theory like the conventional Laplace transform or Fourier transform. The 'phasor transformer' concept is explained in this chapter as a candidate of the theory, which comprises of two parts: the 'generalized switched transformer' for all switching converters and the 'general unified phasor transformation' for all AC circuits.

10.1 Introduction

A unified general circuit-oriented phasor transformation with expanded application area encompassing polyphase AC converters, which has previously been covered by the circuit DQ transformation [1, 2], is proposed in this chapter. The proposed transformation drastically simplifies the AC converter analysis: (1) polyphase AC converters are degenerated to single phase converters; (2) the switches in AC converters are replaced with an equivalent transformer with a complex turn-ratio regardless of the numbers of switches and poles; and (3) circuit analyses with a minimal number of equations are possible for high order converters with any degree of complexity, thereby changing the power converter analysis to a conventional circuit analysis [3–25].

C.T. Rim, *Phasor Power Electronics*, KAIST Research Series,
DOI 10.1007/978-981-10-0536-7_10

10.2 Generalized Switched Transformer Models

10.2.1 m-Poly Power Invariant Phasor Transformation (m-PIP)

To obtain simplified and accurate models of AC converters, a generalized power-invariant phasor transformation for the m-poly phase is proposed. The phasor domain circuit is connected to the real domain circuit by 1-to-1 mapping as follows.

$$x(t) = \mathrm{Re}\left\{ \sqrt{\frac{2}{m}} \mathbf{x}(t)\, \mathrm{e}^{j\theta(t)} \right\} \quad \textit{for m-poly phase} \tag{10.1}$$

Equation (10.1) is generally valid for an arbitrary sinusoidal or switching variable in principle, and can be used to describe the modulation in amplitude, frequency, or phase of power systems. However, the phasor $\mathbf{x}(t)$ becomes stationary with no harmonics when the transformation frequency is the same as that of a sinusoidal real variable, $x(t)$. Hence, it is assumed hereafter that the AC converters considered here are operating in sinusoid, and involve no switching harmonics. A harmonic analysis for various PWM switching patterns can be performed with the help of work in previous studies [1, 26].

The term "power-invariant" is used, since the power in a real domain circuit is the same as that in a phasor-transformed domain, as delineated in (10.1). This can be proved conceptually for an m-poly phase circuit, considering that the power is proportional to the square of the voltage or current in the circuit, as follows.

$$P \equiv m\overline{x^2(t)} = m \left\{ \frac{2}{m} |\mathbf{x}|^2 \overline{\cos^2 \theta(t)} \right\} = 2|\mathbf{x}|^2 \frac{1}{2} = |\mathbf{x}|^2 = \mathbf{x} \cdot \mathbf{x}^* \tag{10.2}$$

The total normalized average power of real circuit elements is m times the normalized average power of a real circuit element, and is the same as that of a phasor domain circuit element, as shown in (10.2). It is, however, important to carefully check how the power invariant principle is applied to AC sources, inductors, capacitors, resistors, and switched transformers, as shown in the following section. In (10.1) and (10.2), the phasor represents the rms value, which simplifies the equivalent transformer.

For the single phase case, i.e., $m = 1$, (10.1) becomes the previous phasor transformation in [27]. For the three phase case, i.e., $m = 3$, with fixed transformation frequency, which is the most common application case, (10.1) becomes as follows.

$$x(t) = \mathrm{Re}\left\{ \sqrt{\frac{2}{3}} \mathbf{x}(t)\, \mathrm{e}^{j\omega_s t} \right\} \quad \textit{for 3-phase}, \quad \omega = \omega_s \tag{10.3}$$

Applying (10.3) to a polyphase balanced power system, although the three phase case is shown here, the voltage or current variables in the abc-frame become

$$\begin{bmatrix} x_a \\ x_b \\ x_c \end{bmatrix} \equiv \begin{bmatrix} \mathrm{Re}\{\sqrt{2/3}\mathbf{x_a}\, e^{j\omega_s t}\} \\ \mathrm{Re}\{\sqrt{2/3}\mathbf{x_b}\, e^{j\omega_s t}\} \\ \mathrm{Re}\{\sqrt{2/3}\mathbf{x_c}\, e^{j\omega_s t}\} \end{bmatrix} = \begin{bmatrix} \mathrm{Re}\{\sqrt{2/3}\mathbf{x}\, e^{j\omega_s t}\} \\ \mathrm{Re}\left\{\sqrt{2/3}\mathbf{x}\, e^{j\omega_s t + j\frac{2\pi}{3}}\right\} \\ \mathrm{Re}\left\{\sqrt{2/3}\mathbf{x}\, e^{j\omega_s t - j\frac{2\pi}{3}}\right\} \end{bmatrix} \tag{10.4}$$
$$= \mathrm{Re}\left\{\sqrt{\frac{2}{3}}\mathbf{x}\, e^{j\omega_s t} \begin{bmatrix} 1 \\ e^{j\frac{2\pi}{3}} \\ e^{-j\frac{2\pi}{3}} \end{bmatrix}\right\} \equiv \mathrm{Re}\left\{\sqrt{\frac{2}{3}}\mathbf{x}\, e^{j\omega_s t}\, \boldsymbol{\Phi_1}\right\},$$

where the phase difference matrix is defined as follows.

$$\boldsymbol{\Phi_1} = \begin{bmatrix} 1 \\ e^{j\frac{2\pi}{3}} \\ e^{-j\frac{2\pi}{3}} \end{bmatrix} \tag{10.5}$$

From (10.4), it can be identified that the polyphase variables, regardless of the number of phases, can be described by a phasor. This implies the possibility of degeneration of the polyphase power system to a single phase system.

The m-PIP (m-poly Power Invariant Phasor transformation) unifies a 3-PIP analysis into a 1-PIP analysis. Therefore, employing m-PIP, 3-poly or 6-poly phase power systems can be dealt with in the same manner as for a single phase system.

10.2.2 Application of m-PIP to AC Subcircuits

In general, all converters as well as AC converters are composed of nine categories of subcircuits, as classified in this chapter. They are AC voltage sources, AC current sources, AC inductors, AC capacitors, AC resistors, VSI (Voltage Source Inverter) transformers, CSI (Current Source Inverter) transformers, matrix transformers, and DC subcircuits.

The category of DC subcircuits, while entailing thousands of different configurations, is not segmented further for the purpose of the m-PIP. Rectifiers, meanwhile, are not separately categorized because, from a modeling point of view, they are equivalent to inverters. The VSI is equivalent to the CSR (Current Source Rectifier), and the CSI is equivalent to the VSR (Voltage Source Rectifier), although their current flows are, in most cases, in opposite direction. The most important and complicated subcircuits to be phasor-transformed are the AC inductors, AC capacitors, and AC transformers, as in [27].

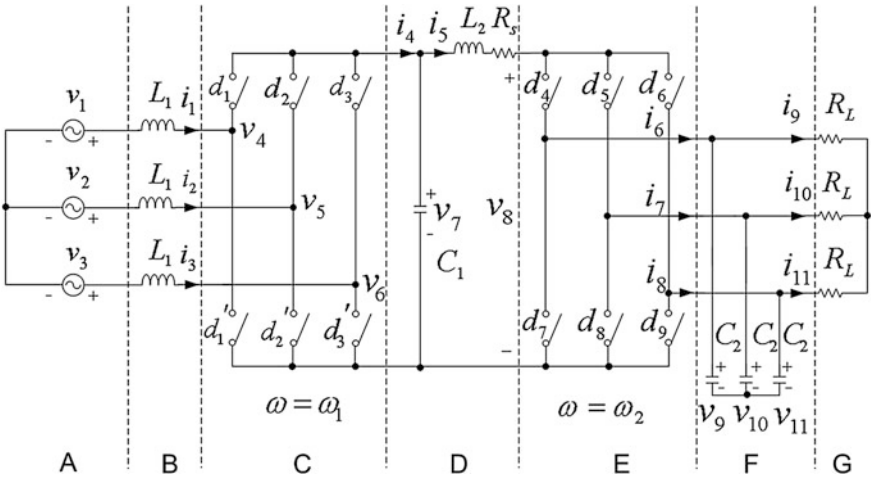

Fig. 1 Three phase rectifier-inverter example to be modeled

The AC converter shown in Fig. 10.1, the same three phase rectifier-inverter example as used in [1], is chosen here for comparison. The converter should be broken into the following subcircuits, which have corresponding subcircuits in the phasor domain. Eight subcircuits need the m-PIP, as outlined below.

1. ***Voltage or Current Sources***: The application of m-PIP to the AC voltage or current sources results in the following, as shown in Fig. 10.2 (upper).

$$\begin{aligned} \boldsymbol{V}_{abc} &\equiv \begin{bmatrix} v_a \\ v_b \\ v_c \end{bmatrix} = \sqrt{\frac{2}{3}} \mathrm{Re}\{ \mathbf{v_p} \, \mathrm{e}^{j\omega_s t} \boldsymbol{\Phi_1} \} \\ \boldsymbol{I}_{abc} &\equiv \begin{bmatrix} i_a \\ i_b \\ i_c \end{bmatrix} = \sqrt{\frac{2}{3}} \mathrm{Re}\{ \mathbf{i_p} \, \mathrm{e}^{j\omega_s t} \boldsymbol{\Phi_1} \} \end{aligned} \tag{10.6}$$

Checking the power relation, the power supplied from the voltage sources in the abc domain is found to be the same as that in the m-phasor domain, as follows.

$$\begin{aligned} P_s &\equiv \overline{v_a i_a} + \overline{v_b i_b} + \overline{v_c i_c} = 3\overline{v_a i_a} (= 3 \, V_{rms} I_{rms} \cos(\phi_V - \phi_I)) \\ &= 3\overline{\sqrt{2/3} \, \mathrm{Re}\{\mathbf{v_p} \mathrm{e}^{j\omega_s t}\} \sqrt{2/3} \, \mathrm{Re}\{\mathbf{i_p} \mathrm{e}^{j\omega_s t}\}} \\ &= \overline{\mathrm{Re}\{\mathbf{v_p} \mathrm{e}^{j\omega_s t} \mathbf{i_p} \mathrm{e}^{j\omega_s t} + \mathbf{v_p} \mathrm{e}^{j\omega_s t} \mathbf{i_p^*} \mathrm{e}^{-j\omega_s t}\}} = \mathrm{Re}\{\mathbf{v_p} \mathbf{i_p^*}\} \end{aligned} \tag{10.7}$$

Similarly, the reactive power supplied from the voltage sources in the abc domain is given as follows.

$$Q_s \equiv 3\, V_{rms} I_{rms} \sin(\phi_V - \phi_I) = \left|\mathbf{v_p i_p^*}\right| \sin(\phi_V - \phi_I) = \mathrm{Im}\{\mathbf{v_p i_p^*}\} \tag{10.8}$$

From (10.7) and (10.8), it is identified that the instantaneous complex power in the m-phasor domain source is simply determined, permitting the time change of phasors in (10.7) and (10.8) as

$$\mathbf{p_s} \equiv P_s + jQ_s = \mathrm{Re}\{\mathbf{v_p i_p^*}\} + j\ \mathrm{Im}\{\mathbf{v_p i_p^*}\} = \mathbf{v_p i_p^*}. \tag{10.9}$$

Hence, the m-phasor domain sources in Fig. 10.2c constitute a subcircuit preserving the power invariance principle.

2. ***Inductors***: The application of m-PIP to the AC inductors results in an inductor with an imaginary resistor, as shown in Fig. 10.2 (middle), where the governing equations are as follows.

$$\begin{aligned} \boldsymbol{V_{abc}} &\equiv \sqrt{\frac{2}{3}}\,\mathrm{Re}\left\{\mathbf{v_p}\, e^{j\omega_s t}\boldsymbol{\Phi_1}\right\} = L\frac{d}{dt}\boldsymbol{I_{abc}} \\ &= L\sqrt{\frac{2}{3}}\,\mathrm{Re}\left\{\frac{d}{dt}\left(\mathbf{i_p}\, e^{j\omega_s t}\,\boldsymbol{\Phi_1}\right)\right\} \\ &= L\sqrt{\frac{2}{3}}\,\mathrm{Re}\left\{\left(\frac{d\mathbf{i_p}}{dt} + j\omega_s \mathbf{i_p}\right) e^{j\omega_s t}\boldsymbol{\Phi_1}\right\} \end{aligned} \tag{10.10}$$

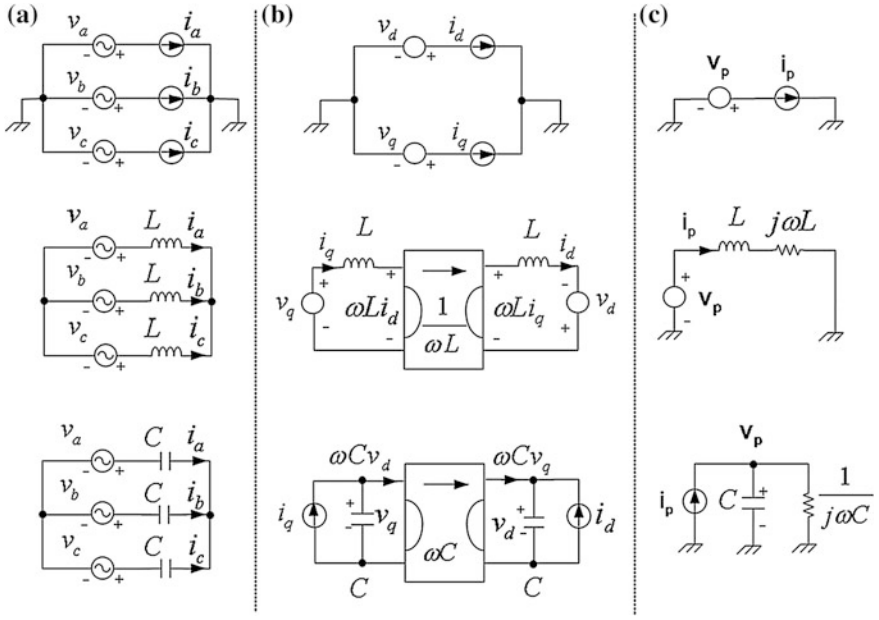

Fig. 2 Comparisons of m-PIP with DQ transformation: voltage/current sources (*upper*), inductors (*middle*), capacitors (*lower*). **a** abc domain. **b** DQ domain. **c** m-phasor domain

In (10.10), the voltage and current definitions of (10.6) are used.
Applying the following equivalence theorem [27],

$$\mathrm{Re}\{\mathbf{x}e^{j\omega_s t}\} = \mathrm{Re}\{\mathbf{y}e^{j\omega_s t}\},\ \omega_s \neq 0 \ \Leftrightarrow\ \mathbf{x} = \mathbf{y}, \tag{10.11}$$

the m-phasor domain inductor subcircuit becomes

$$\mathbf{v_p} = L\frac{d\mathbf{i_p}}{dt} + j\omega_s L\mathbf{i_p}. \tag{10.12}$$

Note that (10.12) has exactly the same form in [27], which gives the single phase inductor case.
The energy relation for the inductors is as follows.

$$E_L \equiv 3\frac{L}{2}\overline{i_a^2} = \frac{3L}{2}\overline{[\sqrt{2/3}\ \mathrm{Re}\{\mathbf{i_p}\,e^{j\omega_s t}\}]^2} = \frac{L}{2}\left|\mathbf{i_p}\right|^2 \tag{10.13}$$

As seen from (10.13), the energy in an m-phasor domain inductor is equal to the sum of the energies for the abc domain; hence, the power, a time derivative of energy, is also invariant.

3. ***Capacitors***: In a similar manner, the application of m-PIP to the AC capacitors results in a capacitor with an imaginary resistor, as shown in Fig. 10.2 (lower), where the corresponding equations are as follows.

$$\begin{aligned}
\boldsymbol{I_{abc}} &\equiv \sqrt{\frac{2}{3}}\,\mathrm{Re}\{\mathbf{i_p}\,e^{j\omega_s t}\,\boldsymbol{\Phi_1}\} = C\frac{d}{dt}\boldsymbol{V_{abc}} \\
&= C\sqrt{\frac{2}{3}}\,\mathrm{Re}\left\{\frac{d}{dt}(\mathbf{v_p}\,e^{j\omega_s t}\,\boldsymbol{\Phi_1})\right\} \\
&= C\sqrt{\frac{2}{3}}\,\mathrm{Re}\left\{\left(\frac{d\mathbf{v_p}}{dt} + j\omega_s\mathbf{v_p}\right)e^{j\omega_s t}\,\boldsymbol{\Phi_1}\right\} \\
&\Leftrightarrow\ \mathbf{i_p} = C\frac{d\mathbf{v_p}}{dt} + j\omega_s C\mathbf{v_p}
\end{aligned} \tag{10.14}$$

The imaginary resistors in Fig. 10.2c must not be simply interpreted as the steady state reactance, since they also play important roles in the dynamic transient state.

4. ***Resistors***: The application of m-PIP to the AC resistors, as shown in Fig. 10.3 (upper), is relatively simple:

$$\begin{aligned}
\boldsymbol{V_{abc}} &\equiv \sqrt{\frac{2}{3}}\,\mathrm{Re}\{\mathbf{v_p}\,e^{j\omega_s t}\,\boldsymbol{\Phi_1}\} = R\boldsymbol{I_{abc}} \\
&= R\sqrt{\frac{2}{3}}\,\mathrm{Re}\{\mathbf{i_p}\,e^{j\omega_s t}\,\boldsymbol{\Phi_1}\} \\
&\Leftrightarrow\ \mathbf{v_p} = R\mathbf{i_p}
\end{aligned} \tag{10.15}$$

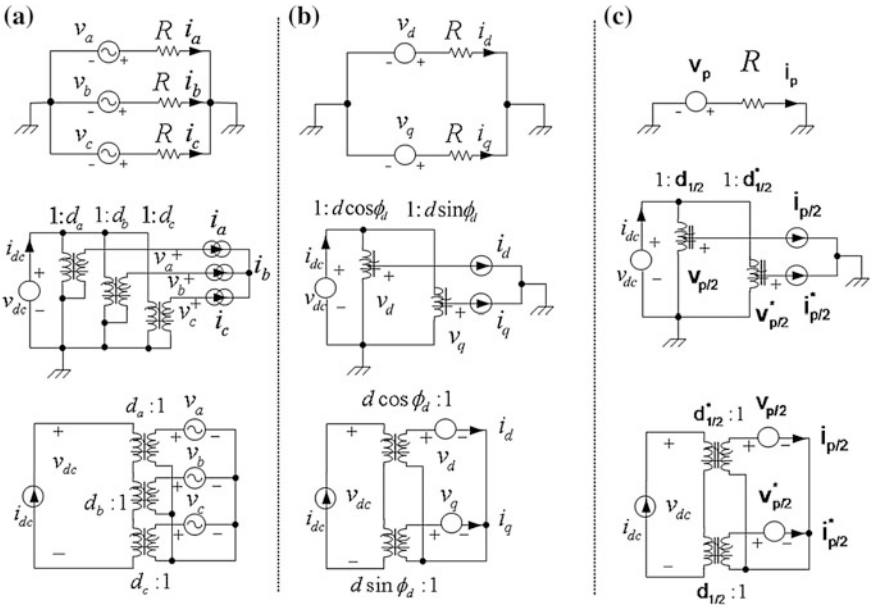

Fig. 3 Comparisons of m-PIP with DQ transformation: resistors (*upper*), VSI transformers (*middle*), CSI transformers (*lower*). **a** abc domain. **b** DQ domain. **c** m-phasor domain

5. ***VSI***: The application of m-PIP to the VSI transformers as, shown in Fig. 10.3 (middle) and delineated in the following, requires extensive caution.

$$\begin{aligned} \boldsymbol{V_{abc}} &\equiv \mathrm{Re}\left\{\sqrt{\frac{2}{3}}\mathbf{v_p}\, e^{j\omega_s t}\, \boldsymbol{\Phi_1}\right\} = v_{dc}\mathbf{d_{abc}} \\ &\equiv v_{dc}\mathrm{Re}\left\{\sqrt{\frac{2}{3}}\mathbf{d}\, e^{j\omega_s t}\, \boldsymbol{\Phi_1}\right\} \\ &= \mathrm{Re}\left\{\sqrt{\frac{2}{3}}v_{dc}\mathbf{d}\, e^{j\omega_s t}\, \boldsymbol{\Phi_1}\right\} \\ &\Leftrightarrow\ \mathbf{v_p} = v_{dc}\,\mathbf{d} \end{aligned} \tag{10.16a}$$

$$
\begin{aligned}
i_{dc} &= i_a d_a + i_b d_b + i_c d_c \\
&= \sum_{k=0}^{2} \mathrm{Re}\left\{\sqrt{\frac{2}{3}}\mathbf{i_p}\, e^{j\omega_s t + j\frac{2\pi}{3}k}\right\}\mathrm{Re}\left\{\sqrt{\frac{2}{3}}\mathbf{d}\, e^{j\omega_s t + j\frac{2\pi}{3}k}\right\} \\
&= \frac{1}{3}\sum_{k=0}^{2} \mathrm{Re}\left\{\mathbf{i_p}\, e^{j\omega_s t + j\frac{2\pi}{3}k}\,\mathbf{d}^*\, e^{-j\omega_s t - j\frac{2\pi}{3}k} + \mathbf{i_p}\, e^{j\omega_s t + j\frac{2\pi}{3}k}\,\mathbf{d}\, e^{j\omega_s t + j\frac{2\pi}{3}k}\right\} \\
&= \frac{1}{3}\sum_{k=0}^{2} \mathrm{Re}\left\{\mathbf{i_p}\,\mathbf{d}^* + \mathbf{i_p}\,\mathbf{d}\, e^{j2\omega_s t + j\frac{4\pi}{3}k}\right\} = \mathrm{Re}\{\mathbf{i_p}\,\mathbf{d}^*\}.
\end{aligned}
\tag{10.16b}
$$

Only the AC voltage term is considered in the VSI transformer modeling, and the DC offset voltage in the VSI output, which is not of importance in AC power conversion, is omitted from (10.16a) and Fig. 10.3a (middle). The DC current in (10.16b) contains no sinusoidal harmonics for the balanced m-poly phase. This, however, no longer holds for the single phase case, where the harmonic current disappears in the model by considering the average DC current [27].

It is not straightforward to build a complex transformer with a complex turn-ratio of $\mathbf{d}$ from (10.16a, b), since (10.16a) involves "real part operation." Equation (10.16a, b) should be modified as follows to find appropriate equivalent circuits in the m-phasor domain.

$$
\begin{aligned}
&\mathbf{v_p} = v_{dc}\,\mathbf{d} \Leftrightarrow \frac{\mathbf{v_p}}{\sqrt{2}} = v_{dc}\,\frac{\mathbf{d}}{\sqrt{2}} \Leftrightarrow \mathbf{v_{p/2}} \equiv \frac{\mathbf{v_p}}{\sqrt{2}} = v_{dc}\,\frac{\mathbf{d}}{\sqrt{2}} \equiv v_{dc}\mathbf{d_{1/2}} \\
&i_{dc} = \mathrm{Re}\{\mathbf{i_p}\,\mathbf{d}^*\} = \frac{\mathbf{i_p}\,\mathbf{d}^* + \mathbf{i}_\mathbf{p}^*\,\mathbf{d}}{2} = \frac{\mathbf{i_p}}{\sqrt{2}}\frac{\mathbf{d}^*}{\sqrt{2}} + \frac{\mathbf{i}_\mathbf{p}^*}{\sqrt{2}}\frac{\mathbf{d}}{\sqrt{2}} \equiv \mathbf{i_{p/2}}\,\mathbf{d}_\mathbf{1/2}^* + \mathbf{i}_\mathbf{p/2}^*\,\mathbf{d_{1/2}}
\end{aligned}
\tag{10.17}
$$

The circuit realization of (10.17) is shown in Fig. 10.3c (middle), where the voltages and currents in the m-phasor domain are the power-halved phasors, as first introduced in [28]. The double bar of the transformer in Fig. 10.3c describes the complex turn-ratio.

In order to cope with the scale factor $1/\sqrt{2}$ in (10.17), the following power-halved m-PIP should be applied for the previous R, L, and C subcircuits.

$$
x(t) = \mathrm{Re}\{\frac{2}{\sqrt{m}}\mathbf{x_{1/2}}(t)\, e^{j\theta(t)}\} \quad for\ m-poly\ phase \tag{10.18}
$$

In the power-halved phasor domain, equivalent circuits are apparently unchanged, but the values of the voltage and current become "power-halved" compared with (10.1).

This can be clarified if the impedance and power are examined. The ratio of the phasor voltage and current in (10.17) is unchanged for the power-halved phasor, which means the impedances of the circuits connected to the VSI are not changed by the scale factor of m-PIP, as follows:

$$\mathbf{z_p} \equiv \frac{\mathbf{v_p}}{\mathbf{i_p}} = \frac{\mathbf{v_p}/\sqrt{2}}{\mathbf{i_p}/\sqrt{2}} = \frac{\mathbf{v_{p/2}}}{\mathbf{i_{p/2}}}, \tag{10.19}$$

where the circuit impedance determined by the complex conjugate voltage and current part in Fig. 10.3c is found to be

$$\frac{\mathbf{v}^*_{\mathbf{p/2}}}{\mathbf{i}^*_{\mathbf{p/2}}} = \frac{\mathbf{v}^*_{\mathbf{p}}}{\mathbf{i}^*_{\mathbf{p}}} = \mathbf{z}^*_{\mathbf{p}}. \tag{10.20}$$

The power delivered from the DC side to the VSI is also preserved by both m-PIP and power-halved m-PIP as follows.

$$\begin{aligned} P_{VSI} &\equiv v_{dc} i_{dc} = v_{dc} \mathrm{Re}\{\mathbf{i_p}\,\mathbf{d}^*\} = v_{dc}\frac{\mathbf{i_p}\,\mathbf{d}^* + \mathbf{i}^*_{\mathbf{p}}\,\mathbf{d}}{2} \\ &= \frac{\mathbf{i_p}\,v_{dc}\mathbf{d}^* + \mathbf{i}^*_{\mathbf{p}}\,v_{dc}\mathbf{d}}{2} = \frac{\mathbf{i_p}\,\mathbf{v}^*_{\mathbf{p}} + \mathbf{i}^*_{\mathbf{p}}\,\mathbf{v_p}}{2} = \mathrm{Re}\left\{\mathbf{v_p}\mathbf{i}^*_{\mathbf{p}}\right\} \end{aligned} \tag{10.21a}$$

$$\begin{aligned} P_{VSI1/2} &\equiv v_{dc} i_{dc} = v_{dc}\mathrm{Re}\{\mathbf{i_p}\,\mathbf{d}^*\} = v_{dc}(\mathbf{i_{p/2}}\,\mathbf{d}^*_{\mathbf{1/2}} + \mathbf{i}^*_{\mathbf{p/2}}\,\mathbf{d_{1/2}}) \\ &= \mathbf{i_{p/2}}\,v_{dc}\mathbf{d}^*_{\mathbf{1/2}} + \mathbf{i}^*_{\mathbf{p/2}}\,v_{dc}\mathbf{d_{1/2}} = \mathbf{i_{p/2}}\mathbf{v}^*_{\mathbf{p/2}} + \mathbf{i}^*_{\mathbf{p/2}}\mathbf{v_{p/2}} = 2\mathrm{Re}\{\mathbf{v_{p/2}}\mathbf{i}^*_{\mathbf{p/2}}\} \\ &= \mathrm{Re}\{\mathbf{v_{p/2}}\,\mathbf{i}^*_{\mathbf{p/2}} + \mathbf{v}^*_{\mathbf{p/2}}\mathbf{i_{p/2}}\} = \mathrm{Re}\{\mathbf{v_{p/2}}\mathbf{i}^*_{\mathbf{p/2}}\} + \mathrm{Re}\{\mathbf{v}^*_{\mathbf{p/2}}\mathbf{i_{p/2}}\} \end{aligned} \tag{10.21b}$$

In the power-halved phasor case of (10.21b), the total power is the sum of the two complex transformers in Fig. 10.3c (middle). It can be seen from (10.21a, b) that the power is unchanged by phasor transformation method thus far, as the power is calculated for all the corresponding phasor voltages and currents.

6. ***CSI***: The application of m-PIP to the CSI transformers in Fig. 10.3 (lower) is very similar with the VSI case, as given below.

$$\begin{aligned} \boldsymbol{I_{abc}} &\equiv \mathrm{Re}\left\{\sqrt{\frac{2}{3}}\mathbf{i_p}\,\mathrm{e}^{j\omega_s t}\,\boldsymbol{\Phi_1}\right\} = i_{dc}\mathbf{d_{abc}} \\ &\equiv i_{dc}\mathrm{Re}\left\{\sqrt{\frac{2}{3}}\mathbf{d}\,\mathrm{e}^{j\omega_s t}\,\boldsymbol{\Phi_1}\right\} \\ &= \mathrm{Re}\left\{\sqrt{\frac{2}{3}}i_{dc}\mathbf{d}\,\mathrm{e}^{j\omega_s t}\,\boldsymbol{\Phi_1}\right\} \\ &\Leftrightarrow\ \mathbf{i_p} = i_{dc}\,\mathbf{d} \end{aligned} \tag{10.22a}$$

$$
\begin{aligned}
v_{dc} &= v_a d_a + v_b d_b + v_c d_c \\
&= \sum_{k=0}^{2} \mathrm{Re}\left\{ \sqrt{\frac{2}{3}} \mathbf{v_p}\, \mathrm{e}^{j\omega_s t + j\frac{2\pi}{3}k} \right\} \mathrm{Re}\left\{ \sqrt{\frac{2}{3}} \mathbf{d}\, \mathrm{e}^{j\omega_s t + j\frac{2\pi}{3}k} \right\} \\
&= \frac{1}{3} \sum_{k=0}^{2} \mathrm{Re}\left\{ \mathbf{v_p}\, \mathrm{e}^{j\omega_s t + j\frac{2\pi}{3}k} \mathbf{d}^{*} \mathrm{e}^{-j\omega_s t - j\frac{2\pi}{3}k} + \mathbf{v_p}\, \mathrm{e}^{j\omega_s t + j\frac{2\pi}{3}k} \mathbf{d}\, \mathrm{e}^{j\omega_s t + j\frac{2\pi}{3}k} \right\} \\
&= \frac{1}{3} \sum_{k=0}^{2} \mathrm{Re}\left\{ \mathbf{v_p}\, \mathbf{d}^{*} + \mathbf{v_p} \mathbf{d}\, \mathrm{e}^{j2\omega_s t + j\frac{4\pi}{3}k} \right\} = \mathrm{Re}\left\{ \mathbf{v_p}\, \mathbf{d}^{*} \right\}
\end{aligned}
\tag{10.22b}
$$

In a similar fashion with (10.17), the "real part operation" of (10.22b) can be dealt with as follows.

$$
\begin{aligned}
&\mathbf{i_p} = i_{dc}\mathbf{d} \Leftrightarrow \frac{\mathbf{i_p}}{\sqrt{2}} = i_{dc}\frac{\mathbf{d}}{\sqrt{2}} \Leftrightarrow \mathbf{i_{p/2}} \equiv \frac{\mathbf{i_p}}{\sqrt{2}} = i_{dc}\frac{\mathbf{d}}{\sqrt{2}} \equiv i_{dc}\mathbf{d_{1/2}} \\
&v_{dc} = \mathrm{Re}\{\mathbf{v_p}\mathbf{d}^{*}\} = \frac{\mathbf{v_p}\mathbf{d}^{*} + \mathbf{v}_{\mathbf{p}}^{*}\mathbf{d}}{2} = \frac{\mathbf{v_p}}{\sqrt{2}}\frac{\mathbf{d}^{*}}{\sqrt{2}} + \frac{\mathbf{v}_{\mathbf{p}}^{*}}{\sqrt{2}}\frac{\mathbf{d}}{\sqrt{2}} \equiv \mathbf{v_{p/2}}\mathbf{d}_{\mathbf{1/2}}^{*} + \mathbf{v}_{\mathbf{p/2}}^{*}\mathbf{d_{1/2}}
\end{aligned}
\tag{10.23}
$$

10.2.3 Construction of m-PIP Circuit

Substituting the m-PIP subcircuits of the previous section with the original partitioned circuits in Fig. 10.1, the m-PIP circuit can be constructed, in accordance with [1], as shown in Fig. 10.4. The input and output AC circuits contain complex conjugate subcircuits due to VSI and CSI transformers. The source and output voltages are power-halved values, and hence they must be multiplied by $\sqrt{2}$ to obtain the rms values of the original circuit in Fig. 10.1.

Comparing the m-phasored circuit of Fig. 10.4 with the DQ transformed circuit [1], the former is greatly simplified, since there is no gyrator coupling between the d-axis and q-axis in [1]. Figure 10.4 can also be compared with the graphical phasor transformation [2], where a similar complex conjugate circuit concept is used; however, more complex transformers are required in some cases.

Analyzing the circuit including four complex transformers in Fig. 10.4 still remains complicated, although obtaining the m-phasored circuit including the conjugate circuit is easy. It is thus necessary to further simplify Fig. 10.4 rather than analyze it, while retaining the accuracy and generality of the model.

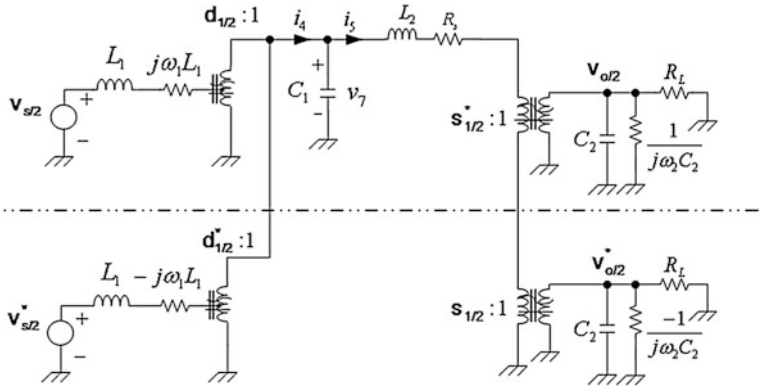

Fig. 4 Equivalent three phase rectifier-inverter circuit in the m-phasor domain (*lower* part circuit is the complex conjugate of the *upper* part AC circuit)

10.2.4 Simplified m-PIP Circuit with Dummy Sources

For simplification of the circuit, we should first return to (10.16a, b) or (10.22a, b) in order to deal with the "real part operation." By introducing appropriate imaginary current or voltage sources, the VSI or CSI can be represented as a single transformer, respectively.

The VSI case is shown first, introducing a dependent imaginary current source as follows.

$$\begin{aligned} \mathbf{v_p} &= v_{dc}\mathbf{d} \\ i_{dc} &= \mathrm{Re}\{\mathbf{i_p}\mathbf{d}^*\} = \mathbf{i_p}\mathbf{d}^* - j\ \mathrm{Im}\{\mathbf{i_p}\mathbf{d}^*\} \equiv \mathbf{i_p}\mathbf{d}^* - ji_d \end{aligned} \tag{10.24}$$

For the CSI case, by introducing a dependent imaginary voltage source, the following is derived.

$$\begin{aligned} \mathbf{i_p} &= i_{dc}\mathbf{d} \\ v_{dc} &= \mathrm{Re}\{\mathbf{v_p}\mathbf{d}^*\} = \mathbf{v_p}\mathbf{d}^* - j\ \mathrm{Im}\{\mathbf{v_p}\mathbf{d}^*\} \equiv \mathbf{v_p}\mathbf{d}^* - jv_d \end{aligned} \tag{10.25}$$

The circuit realization of (10.24) or (10.25) includes only a complex transformer, although the imaginary sources are still included in Fig. 10.5, where the circuit variables are no longer power-halved m-phasor.

The system order of the simplified m-phasored circuit in Fig. 10.5 is 4, which is halved from the 8th order original circuit in Fig. 10.1. The imaginary sources are not counted in the system order because they are dependent variables.

The merit of this simplification is straightforward: the circuit analysis is now conventional if the imaginary source effect can be appropriately dealt with.

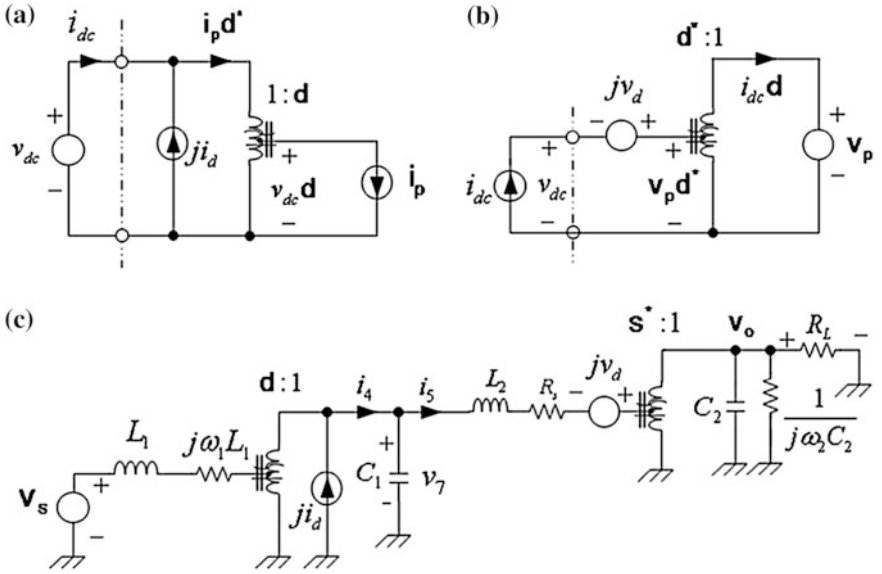

Fig. 5 Simplified m-phasored circuits introducing imaginary sources (the *left* parts of **a** and **b** are real, and the *right* parts are complex). **a** Simplified VSI (*upper left*). **b** Simplified CSI (*upper right*). **c** Simplified three-phase-rectifier-inverter (*lower*)

10.2.5 Simplified m-PIP Circuit Analysis for Controlled Sources

In most practical applications, the DC input voltage of VSI (or the DC output voltage of CSR) and the DC input current of CSI (or the DC output current of VSR) are controlled to have certain desired values. The analysis for this case is drastically simplified, as shown in Fig. 10.6, where there is no imaginary source effect on the circuits because of the controlled source.

For the controlled case, the CSR output voltage and the CSI input current become an ideal voltage source (v_7) and an ideal current source (i_5), respectively, as shown in Fig. 10.6.

The DC circuit shown in Fig. 10.6b can be used for a steady state analysis of the converter as follows.

$$\begin{aligned} I_4 &= \mathrm{Re}\{\mathbf{I_s D^*}\} = \mathrm{Re}\left\{\frac{\mathbf{V_s} - V_7\mathbf{D}}{j\omega_1 L_1}\mathbf{D}^*\right\} = \mathrm{Re}\left\{\frac{\mathbf{V_s D^*}}{j\omega_1 L_1} - \frac{V_7 D^2}{j\omega_1 L_1}\right\} \\ &= \mathrm{Re}\left\{\frac{\mathbf{V_s D^*}}{j\omega_1 L_1}\right\} = \frac{\mathrm{Im}\{\mathbf{V_s D^*}\}}{\omega_1 L_1} = \frac{V_s D \sin(\phi_s - \phi_D)}{\omega_1 L_1} \end{aligned} \tag{10.26}$$

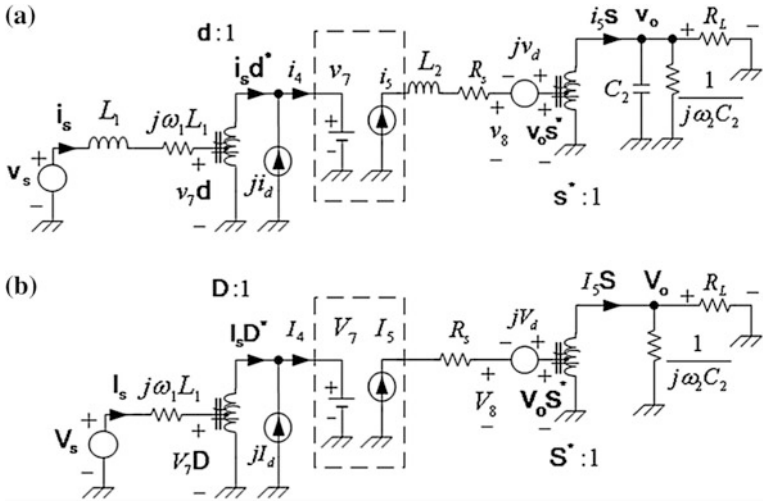

Fig. 6 Simplified m-phasored circuit for controlled sources case (the *dotted box* represents the controlled sources). **a** Dynamic circuit (*upper*) **b** Steady state circuit (*lower*)

It is verified that (10.26) is exactly the same result as that obtained from the circuit DQ transformation [29], which is an ideal current source characteristic independent of the CSR output voltage. Note that the imaginary source is never separately considered in the calculation; instead the condition that no imaginary current should flow into the DC circuit is adopted.

Similarly, the output circuit of Fig. 10.6b is analyzed as

$$\begin{aligned} V_8 &= \mathrm{Re}\{\mathbf{V_o S}^*\} = \mathrm{Re}\left\{I_5 \mathbf{S}\left(R_L // \frac{1}{j\omega_2 C_2}\right)\mathbf{S}^*\right\} \\ &= \mathrm{Re}\left\{I_5 S^2 \frac{R_L}{1 + j\omega_2 C_2 R_L}\right\} = \frac{I_5 S^2 R_L}{1 + (\omega_2 C_2 R_L)^2}. \end{aligned} \tag{10.27}$$

Equation (10.27) can be verified from previous works of [1, 2], and [28].

The source power characteristics from Fig. 10.6b can also be calculated as follows.

$$\begin{aligned} \mathbf{P_s} \equiv P_s + jQ_s &= \mathbf{V_s I_s^*} = \mathbf{V_s}\left(\frac{\mathbf{V_s} - V_7\mathbf{D}}{j\omega_1 L_1}\right)^* = \mathbf{V_s}\frac{\mathbf{V_s^*} - V_7\mathbf{D}^*}{-j\omega_1 L_1} \\ &= \frac{V_s^2 - V_7\mathbf{V_s D}^*}{-j\omega_1 L_1} = \frac{V_s^2 - V_7[\mathrm{Re}\{\mathbf{V_s D}^*\} + j\ \mathrm{Im}\{\mathbf{V_s D}^*\}]}{-j\omega_1 L_1}. \end{aligned} \tag{10.28}$$

where the real power and reactive power are, respectively,

$$\begin{aligned} P_s &= \frac{V_7\ \mathrm{Im}\{\mathbf{V_s}\mathbf{D}^*\}}{\omega_1 L_1} = V_7 \frac{V_s D \sin(\phi_s - \phi_D)}{\omega_1 L_1} = V_7 I_4 \\ Q_s &= \frac{V_s^2 - V_7 \mathrm{Re}\{\mathbf{V_s}\mathbf{D}^*\}}{\omega_1 L_1} = \frac{V_s^2 - V_7 V_s D \cos(\phi_s - \phi_D)}{\omega_1 L_1}. \end{aligned} \tag{10.29}$$

It is verified again that (10.29) is exactly the same result as [29].

Besides the controlled VSI and CSI cases, any resonant converters having ideal DC voltage or current sources can be analyzed by this simplified method.

10.2.6 Simplified m-PIP Circuit Analysis by Real Part Operation

It is appropriate to find a general method to exclude the effect of imaginary sources in Fig. 10.5, where there is no more controlled source. A key issue is how to eliminate the complex transformers without any loss of generality of the model.

A generalized approach to transform the m-phasor domain circuit into a DC side circuit is proposed, as shown in Fig. 10.7. In general, the m-phasor domain circuit can be degenerated into a Thevenin circuit (or a Norton circuit if wanted) composed of an equivalent voltage source and an equivalent impedance.

For the VSI circuit of Fig. 10.7a, the DC current is found to be

$$\begin{aligned} I_{dc} &= \mathrm{Re}\left\{\left(\mathbf{I_s} - \frac{V_{dc}\mathbf{D}}{\mathbf{Z_s}}\right)\mathbf{D}^*\right\} = \mathrm{Re}\{\mathbf{I_s}\mathbf{D}^*\} - V_{dc}\mathrm{Re}\left\{\frac{D^2}{\mathbf{Z_s}}\right\} \\ &\equiv I_n - \frac{V_{dc}}{Z_n}, \end{aligned} \tag{10.30}$$

where

$$I_n = \mathrm{Re}\{\mathbf{I_s}\mathbf{D}^*\} = I_s D \cos(\phi_s - \phi_D), \quad Z_n = \frac{\mathrm{Re}\{\mathbf{Z_s}\}}{D^2}. \tag{10.31}$$

For the CSI circuit of Fig. 10.7b, the DC voltage is found to be

$$\begin{aligned} V_{dc} &= \mathrm{Re}\{(\mathbf{V_o} + I_{dc}\mathbf{Z_o}\mathbf{D})\mathbf{D}^*\} = \mathrm{Re}\{\mathbf{V_o}\mathbf{D}^*\} + I_{dc}\mathrm{Re}\{D^2\mathbf{Z_o}\} \\ &\equiv V_t + I_{dc}Z_t, \end{aligned} \tag{10.32}$$

where

$$V_t = \mathrm{Re}\{\mathbf{V_o}\mathbf{D}^*\} = V_o D \cos(\phi_o - \phi_D), \quad Z_t = D^2\mathrm{Re}\{\mathbf{Z_o}\}. \tag{10.33}$$

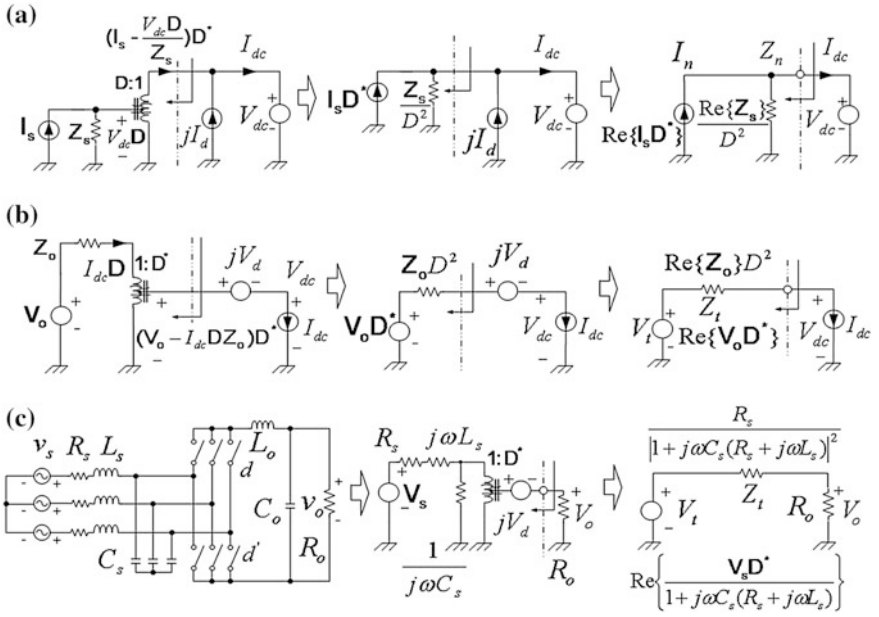

Fig. 7 Real part operation on the AC m-phasor circuits from DC domain. **a** Norton equivalent circuit example of VSI (*upper*). **b** Thevenin equivalent circuit example of CSI (*middle*). **c** Application example for the VSR with LC input filters (*lower*)

As seen from (10.30)–(10.33), the procedure to obtain an equivalent circuit for any given circuit represented as a Thevenin or Norton circuit in Fig. 10.7 is two-fold. First, we eliminate the complex transformer. We then take the real part of the source and impedance. The imaginary dependent sources disappear simply by performing this real part operation. There is no preference between the Thevenin and Norton circuits, although one of them is used for example.

The proposed method is applicable to more complicated AC circuit, as shown in Fig. 10.7c for example, as long as the circuit is in a steady state. The analysis of the circuit can be finished in minutes by manual calculation.

It is found for this VSR case that the source impedance from the DC side is ideally zero, and the output voltage V_o is independent of R_o in the case where $R_s = 0$. Without the help of the proposed m-PIP theory, it would not be easy to predict that the LC filter reactance does not deteriorate the ideal voltage characteristics of the VSR.

Application of a small signal perturbation to the equivalent m-phasor models to obtain the dynamic response is omitted here, since the method is the same as that described in [27].

Application of the real part operation to a complex Laplace transform domain in order to find the dynamic state operation is remained for further work.

10.3 General Unified Phasor Transformation Models

10.3.1 Application of m-PIP to Matrix Transformer

The matrix converters are ac-AC converters, where no DC link exists. The application of the proposed m-PIP has been shown for the m-poly phasored subcircuits in the previous chapter except the matrix transformers. An example matrix converter with 9 switches and 9 reactive elements, representing a typical case, is shown in Fig. 10.8a.

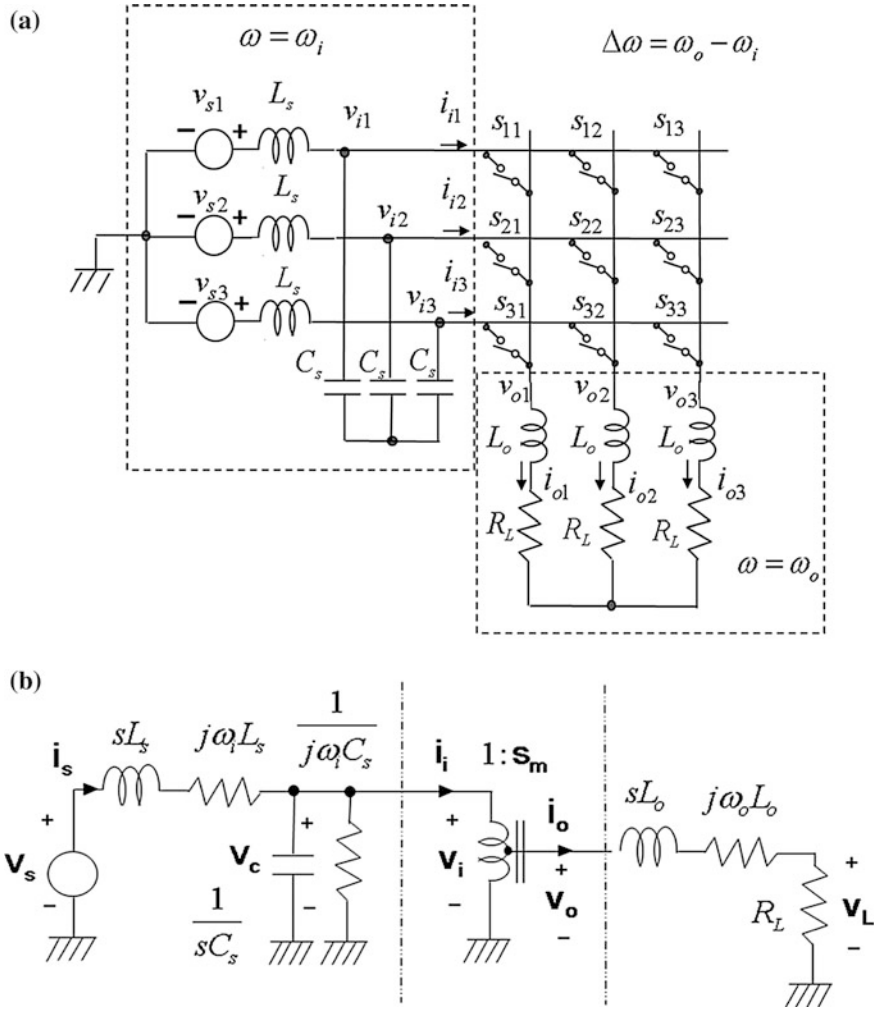

Fig. 8 Three phase matrix converter example. **a** Original circuit. **b** m-phasor equivalent circuit

The m-PIP is applied to the input and output part circuits with different transformation frequencies as follows.

$$x(t) = \mathrm{Re}\left\{ \sqrt{\frac{2}{3}}\mathbf{x}(t)\, \mathrm{e}^{j\omega_i t} \right\} \quad \textit{for input part} \;\; \omega = \omega_i \tag{10.34a}$$

$$x(t) = \mathrm{Re}\left\{ \sqrt{\frac{2}{3}}\mathbf{x}(t)\, \mathrm{e}^{j\omega_o t} \right\} \quad \textit{for output part} \;\; \omega = \omega_o \tag{10.34b}$$

For the matrix switching transformer, the input and output current and voltage are determined by a switching function, i.e., the turn-ratio of an equivalent switching transformer.

Considering the fundamental sinusoidal component, they become

$$\begin{aligned}
\boldsymbol{V_0} &\equiv \mathrm{Re}\left\{ \sqrt{\frac{2}{3}}\mathbf{v_o}\, \mathrm{e}^{j\omega_o t}\, \boldsymbol{\Phi_1} \right\} = \boldsymbol{S^t V_i} \\
&\equiv \mathrm{Re}\left\{ \frac{2}{3}\mathbf{s_m}\, \mathrm{e}^{j(\omega_o-\omega_i)t}\, \boldsymbol{\Phi_3^*} \right\} \mathrm{Re}\left\{ \sqrt{\frac{2}{3}}\mathbf{v_i}\, \mathrm{e}^{j\omega_i t}\, \boldsymbol{\Phi_1} \right\} \\
&= \sqrt{\frac{2}{3}}\frac{1}{3}\mathrm{Re}\left\{ \mathbf{s_m}\, \mathrm{e}^{j(\omega_o-\omega_i)t}\, \boldsymbol{\Phi_3^*}\mathbf{v_i}\, \mathrm{e}^{j\omega_i t}\, \boldsymbol{\Phi_1} + \mathbf{s_m}\, \mathrm{e}^{j(\omega_o-\omega_i)t}\, \boldsymbol{\Phi_3^*}\mathbf{v_i^*}\, \mathrm{e}^{-j\omega_i t}\, \boldsymbol{\Phi_1^*} \right\} \\
&= \sqrt{\frac{2}{3}}\frac{1}{3}\mathrm{Re}\left\{ \mathbf{s_m v_i}\, \mathrm{e}^{j\omega_o t}\, \boldsymbol{\Phi_3^*}\boldsymbol{\Phi_1} + \mathbf{s_m v_i^*}\, \mathrm{e}^{j(\omega_o-2\omega_i)t}\, \boldsymbol{\Phi_3^*}\boldsymbol{\Phi_1^*} \right\} \\
&= \mathrm{Re}\left\{ \sqrt{\frac{2}{3}}\mathbf{s_m v_i}\, \mathrm{e}^{j\omega_o t}\, \boldsymbol{\Phi_1} \right\} \;\Leftrightarrow\; \mathbf{v_o} = \mathbf{s_m v_i},
\end{aligned} \tag{10.35}$$

where

$$\boldsymbol{S} \equiv \frac{2}{3}\mathrm{Re}\left\{ S_m \mathrm{e}^{j\phi_m} \begin{bmatrix} \mathrm{e}^{j(\omega_o-\omega_i)t} & \mathrm{e}^{j(\omega_o-\omega_i)t+j\frac{2\pi}{3}} & \mathrm{e}^{j(\omega_o-\omega_i)t-j\frac{2\pi}{3}} \\ \mathrm{e}^{j(\omega_o-\omega_i)t-j\frac{2\pi}{3}} & \mathrm{e}^{j(\omega_o-\omega_i)t} & \mathrm{e}^{j(\omega_o-\omega_i)t+j\frac{2\pi}{3}} \\ \mathrm{e}^{j(\omega_o-\omega_i)t+j\frac{2\pi}{3}} & \mathrm{e}^{j(\omega_o-\omega_i)t-j\frac{2\pi}{3}} & \mathrm{e}^{j(\omega_o-\omega_i)t} \end{bmatrix} \right\} \tag{10.36a}$$

$$\begin{aligned}
\because \boldsymbol{\Phi_3^*}\boldsymbol{\Phi_1} &= \begin{bmatrix} 1 & \mathrm{e}^{-j\frac{2\pi}{3}} & \mathrm{e}^{j\frac{2\pi}{3}} \\ \mathrm{e}^{j\frac{2\pi}{3}} & 1 & \mathrm{e}^{-j\frac{2\pi}{3}} \\ \mathrm{e}^{-j\frac{2\pi}{3}} & \mathrm{e}^{j\frac{2\pi}{3}} & 1 \end{bmatrix} \begin{bmatrix} 1 \\ \mathrm{e}^{j\frac{2\pi}{3}} \\ \mathrm{e}^{-j\frac{2\pi}{3}} \end{bmatrix} = 3\begin{bmatrix} 1 \\ \mathrm{e}^{j\frac{2\pi}{3}} \\ \mathrm{e}^{-j\frac{2\pi}{3}} \end{bmatrix} = 3\boldsymbol{\Phi_1} \\
\boldsymbol{\Phi_3^*}\boldsymbol{\Phi_1^*} &= \begin{bmatrix} 1 & \mathrm{e}^{-j\frac{2\pi}{3}} & \mathrm{e}^{j\frac{2\pi}{3}} \\ \mathrm{e}^{j\frac{2\pi}{3}} & 1 & \mathrm{e}^{-j\frac{2\pi}{3}} \\ \mathrm{e}^{-j\frac{2\pi}{3}} & \mathrm{e}^{j\frac{2\pi}{3}} & 1 \end{bmatrix} \begin{bmatrix} 1 \\ \mathrm{e}^{-j\frac{2\pi}{3}} \\ \mathrm{e}^{j\frac{2\pi}{3}} \end{bmatrix} = \begin{bmatrix} 0 \\ 0 \\ 0 \end{bmatrix},
\end{aligned} \tag{10.36b}$$

and

$$
\begin{aligned}
\boldsymbol{I_i} &\equiv \mathrm{Re}\left\{\sqrt{\frac{2}{3}}\mathbf{i_i}\, e^{j\omega_i t}\,\boldsymbol{\Phi_1}\right\} = \boldsymbol{S I_o} \\
&\equiv \mathrm{Re}\left\{\frac{2}{3}\mathbf{s_m}\, e^{j(\omega_o-\omega_i)t}\,\boldsymbol{\Phi_3}\right\}\mathrm{Re}\left\{\sqrt{\frac{2}{3}}\mathbf{i_o}\, e^{j\omega_o t}\,\boldsymbol{\Phi_1}\right\} \\
&= \sqrt{\frac{2}{3}}\frac{1}{3}\mathrm{Re}\left\{\mathbf{s_m} e^{j(\omega_o-\omega_i)t}\,\boldsymbol{\Phi_3}\mathbf{i_o}\, e^{j\omega_o t}\,\boldsymbol{\Phi_1} + \mathbf{s_m^*} e^{j(\omega_i-\omega_o)t}\,\boldsymbol{\Phi_3^*}\mathbf{i_o}\, e^{j\omega_o t}\,\boldsymbol{\Phi_1}\right\} \\
&= \sqrt{\frac{2}{3}}\frac{1}{3}\mathrm{Re}\left\{\mathbf{s_m i_o}\, e^{j(2\omega_o-\omega_i)t}\,\boldsymbol{\Phi_3}\,\boldsymbol{\Phi_1} + \mathbf{s_m^* i_o}\, e^{j\omega_i t}\,\boldsymbol{\Phi_3^*}\,\boldsymbol{\Phi_1}\right\} \\
&= \mathrm{Re}\left\{\sqrt{\frac{2}{3}}\mathbf{s_m^* i_o}\, e^{j\omega_i t}\,\boldsymbol{\Phi_1}\right\} \;\Leftrightarrow\; \mathbf{i_i} = \mathbf{s_m^* i_o},
\end{aligned}
\tag{10.37}
$$

where

$$
\boldsymbol{\Phi_3}\,\boldsymbol{\Phi_1} = \begin{bmatrix} 1 & e^{j\frac{2\pi}{3}} & e^{-j\frac{2\pi}{3}} \\ e^{-j\frac{2\pi}{3}} & 1 & e^{j\frac{2\pi}{3}} \\ e^{j\frac{2\pi}{3}} & e^{-j\frac{2\pi}{3}} & 1 \end{bmatrix}\begin{bmatrix} 1 \\ e^{j\frac{2\pi}{3}} \\ e^{-j\frac{2\pi}{3}} \end{bmatrix} = \begin{bmatrix} 0 \\ 0 \\ 0 \end{bmatrix}. \tag{10.38}
$$

The circuit realization of (10.35) and (10.37) is merely a complex transformer [27]. The scale factor, 2/3 of the matrix switching function, matches the 3-PIP applied here. No restriction on the frequency, phase, or magnitude is imposed on the input, output, and switching matrix. Note that no real part operation is needed for the matrix transformer. Hence, the analysis of the matrix converter will be quite simple and straightforward.

10.3.2 Analysis of Matrix Converter

By substituting the equivalent complex transformer with the matrix converter in Fig. 10.8a, the most simplified equivalent circuit without loss of accuracy or generality is obtained, as shown in Fig. 10.8b. The 9 matrix switches are substituted with a complex transformer, and the 9th order system is degenerated into the 3rd order. This system order reduction stems from the coupling between abc phases and the balanced circuit topology, which results in a reduced number of independent variables.

The single complex transformer in Fig. 10.8b can be compared with a graphical phasor transformation [2], where two complex transformers are used for the same purpose among the total five transformers.

Another case of a graphical phasor transformation for a matrix converter analysis [30] requires three complex transformers for dq0 axes in general. One complex transformer is required for the special case where the input phase is zero, which is not necessary in this chapter.

The power between the matrix transformer is investigated using (10.35) and (10.37), as follows.

$$\mathbf{p_i} \equiv \mathbf{v_i i_i^*} = \mathbf{v_o s_m^{-1}} (\mathbf{i_o s_m^*})^* = \mathbf{v_o s_m^{-1} i_o^* s_m} = \mathbf{v_o i_o^*} \equiv \mathbf{p_o} \tag{10.39}$$

It is found from (10.39) that the reactive power as well as the real power is preserved through the matrix power conversion. This result is not obvious, since the input and output frequencies and phases are arbitrary. On the contrary, the VSI or the CSI preserves only the real power, as discussed in the previous chapter. Utilizing the property of preserving reactive power of the matrix converter, an effective reactive power generator can be constructed by increasing the output frequency to a sufficiently high level so as to reduce the AC capacitor size for a given reactive power.

The dynamic operation of the converter can be found by applying the Laplace transform to Fig. 10.8b. The Thevenin equivalent circuit for the left part of Fig. 10.8b becomes

$$\begin{aligned} &\mathbf{V_{th1}}(s) = \frac{\mathbf{Z_2}(s)}{\mathbf{Z_1}(s) + \mathbf{Z_2}(s)} \mathbf{V_s}(s), \quad \mathbf{Z_{th1}}(s) = \mathbf{Z_1}(s) /\!/ \mathbf{Z_2}(s) \\ &\because \mathbf{Z_1}(s) = sL_s + j\omega_i L_s, \quad \mathbf{Z_2}(s) = \frac{1}{sC_s + j\omega_i C_s}. \end{aligned} \tag{10.40}$$

Using (10.40), the Thevenin equivalent circuit for the middle part of Fig. 10.8b, where the complex transformer is eliminated, becomes

$$\mathbf{V_{th2}}(s) = \mathbf{V_{th1}}(s)\mathbf{S_m}, \quad \mathbf{Z_{th2}}(s) = \mathbf{Z_{th1}}(s) S_m^2. \tag{10.41}$$

Using (10.41), the Thevenin equivalent circuit for the right part of Fig. 10.8b finally becomes

$$\mathbf{V_L}(s) = \frac{R_\mathbf{L}}{\mathbf{Z_{th2}}(s) + \mathbf{Z_o}(s) + R_\mathbf{L}} \mathbf{V_{th2}}(s) \quad \because \mathbf{Z_o}(s) = sL_o + j\omega_o L_o. \tag{10.42}$$

The dynamic and steady state voltage transfer functions can be calculated from (10.40)–(10.42), respectively, as follows.

$$\mathbf{G_V}(s) \equiv \frac{\mathbf{V_L}(s)}{\mathbf{V_s}(s)} = \frac{\mathbf{Z_2}(s)}{\mathbf{Z_1}(s) + \mathbf{Z_2}(s)} \cdot \frac{\mathbf{S_m} R_L}{\{\mathbf{Z_1}(s) /\!/ \mathbf{Z_2}(s)\} S_m^2 + \mathbf{Z_o}(s) + R_L} \tag{10.43}$$

$$G_V \equiv \left|\frac{\mathbf{V_L}(0)}{\mathbf{V_s}(0)}\right| = \frac{1}{1-\omega_i^2 L_s C_s} \cdot \frac{S_m R_L}{\left|\{j\omega_i L_s // (j\omega_i C_s)^{-1}\} S_m^2 + j\omega_o L_o + R_L\right|}$$
$$= \frac{1}{1-\omega_i^2 L_s C_s} \cdot \frac{S_m R_L}{\sqrt{R_L^2 + \{\omega_o L_o + \omega_i L_s S_m^2/(1-\omega_i^2 L_s C_s)\}^2}} \tag{10.44}$$

As seen from (10.43) and (10.44), quite explicit solutions are obtained without cumbersome high order matrix manipulation. In contrast, such matrix manipulation is inevitable when the real value solution is sought by decoupling complex phasors into sine and cosine components [29], or a small signal response is required [30].

It is noteworthy from (10.44) that the voltage gain of the matrix converter is independent of the phase difference between the source voltage and the matrix switching function, which is not the case of CSR in (10.31) or VSR in (10.33).

10.3.3 Verification by Simulation

The m-PIP model in Fig. 10.8b is tested by a numerical simulation, where the complex state equation for the model is established as follows.

$$\begin{aligned} L_s \dot{\mathbf{i}}_\mathbf{s} &= \mathbf{v_s} - j\omega_i L_s \mathbf{i_s} - \mathbf{v_c} \\ C_s \dot{\mathbf{v}}_\mathbf{c} &= \mathbf{i_s} - j\omega_i C_s \mathbf{v_c} - \mathbf{s_m^*} \mathbf{i_o} \\ L_o \dot{\mathbf{i}}_\mathbf{o} &= \mathbf{s_m} \mathbf{v_c} - (j\omega_o L_o + R_L)\mathbf{i_o} \\ \Rightarrow \mathbf{v_L} &= R_L \mathbf{i_o} \end{aligned} \tag{10.45}$$

Since the complex circuit simulation by computers is not available yet, (10.45) is numerically calculated by an Excel sheet, which takes a few seconds to finish one iteration of the simulation, for the parameters:

$$\begin{aligned} &\mathbf{V_s} = 100 \angle \frac{\pi}{6}, \quad \mathbf{S_m} = 0.50 \angle \frac{\pi}{4}, \quad f_i = 60 \text{ Hz}, \quad f_o = 200 \text{ Hz} \\ &L_s = 5 \text{ mH}, \quad C_s = 390 \text{ μF}, \quad L_o = 1 \text{ mH}, \quad R_L = 4 \text{ Ω} \end{aligned} \tag{10.46}$$

The simulation results for the dynamic states of the phasor model and real time model with zero initial conditions are shown in Fig. 10.9. The phasor model is verified to be quite accurate, having less than 0.1 % error for this simulation case.

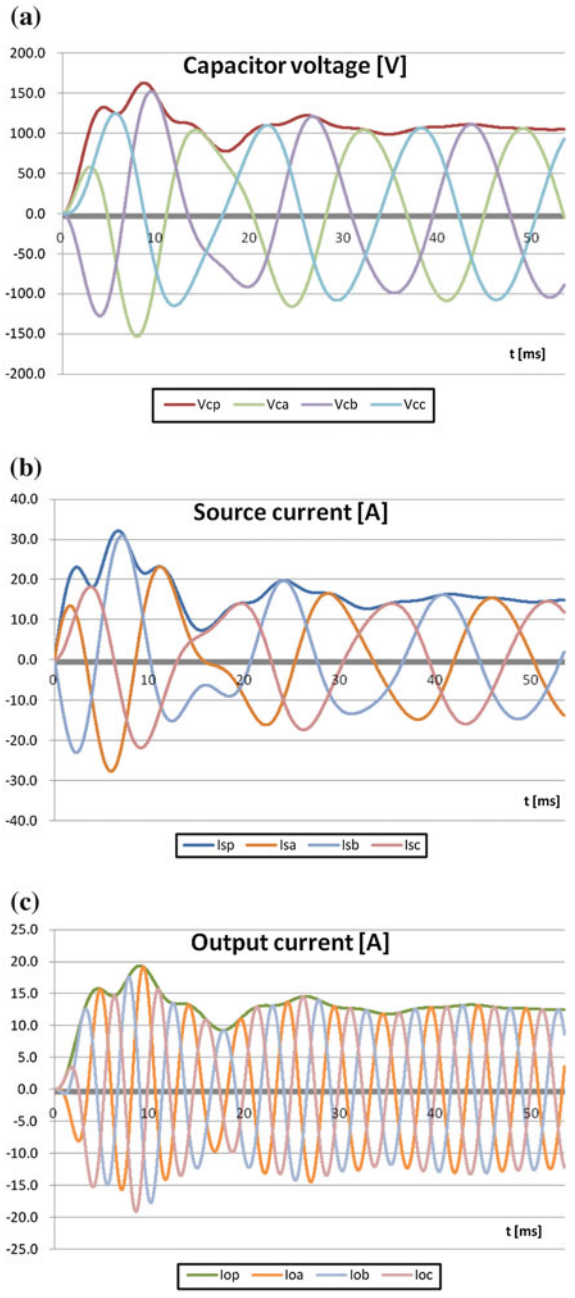

Fig. 9 Numerical simulation for the matrix converter phasor model (the phasor value (*upper*) is $\sqrt{2/3}$ times scaled down to fit the envelopes of the abc values (*below*))

10.4 Concluding Remarks

The analysis of AC time-varying circuits has been one of the fundamental problems in the field of power electronics, and a general solution of the m-PIP theory is provided in this work. This theory is applicable to multi-phase ac-DC, DC-ac, and ac-AC converters as well as to single phase ac-DC, DC-ac, ac-AC converters, and DC-DC resonant converters. Any converter can be substituted with a generalized complex transformer, and the AC balanced subcircuits can be substituted with stationary circuits by the developed theory. The circuit DQ transformation for polyphase converters and the phasor transformation for single phase converters are unified in this chapter.

References

1. Rim CT, Hu DY, Cho GH (1990) Transformers as equivalent circuits for switches: general proofs and DQ transformation-based analyses. IEEE Trans Ind Applicat 26(4):777–785
2. Chen J, Ngo KDT (2001) Graphical phasor analysis of three-phase PWM converters. IEEE Trans Power Electron 16(5):659–666
3. Middlebrook R, Cuk S (1976) A general unified approach to modeling switching power converter stages. IEEE PESC 18–34
4. Rim CT (1990, Feb) Analysis of linear switching systems using circuit transformations. Ph.D. dissertation, KAIST, Seoul
5. Novotny DW (1975) Switching function representation of polyphase inverters. IEEE Ind Applicat Society Conf Rec 823–831
6. Alesina A, Venturini MGB (1981, Apr) Solid-state power conversion: a fourier analysis approach to generalized transformer synthesis. IEEE Trans Circuits Syst CAS-28(4):319–330
7. Vorperian V, Tymersky R, Lee FC (1989, Apr) Equivalent circuit models for resonant and PWM switches. IEEE Trans Power Electron PE-4(2):205–214
8. Sanders SR, Noworolski JM, Liu XZ, Verghese GC (1991) Generalized averaging method for power conversion circuits. IEEE Trans Power Electron 6:251–259
9. White DC, Woodson HH (1959) Electromechanical energy conversion. John Wiley and Sons, New York
10. Ngo KDT (1986, Oct) Low frequency characterization of PWM converter. IEEE Trans Power Electron PE-1:223–230
11. Yin B, Oruganti R, Panda SK, Bhat AKS (2009) A simple single—input-single-output (SISO) model for a three-phase PWM rectifier. IEEE Trans Power Electron 24(3):620–631
12. Vorperian V (1990) Simplified analysis of PWM converters using the model of the PWM switch, part I and part II. IEEE Trans Aerospace Electron Syst 26(3):490–505
13. Mao HC, Boroyevich D, Lee CY (1998) Novel reduced-order small signal model of a three-phase PWM rectifier and its application in control design and system analysis. IEEE Trans Power Electron 13(3):511–521
14. Yin Y, Zane R, Glaser J, Erickson RW (2003, Aug) Small-signal analysis of frequency-controlled electronic ballasts. IEEE Trans Circuits Syst-I: fundamental theory and applications 5(8)
15. Ben-Yaakov S, Glozman S, Rabinovici R (2001) Envelope simulation by spice-compatible models of linear electric circuits driven by modulated signals. IEEE Trans Ind Appl 37 (2):527–533

16. Ye Z, Jain PK, Sen PC (2009) Phasor-domain modeling of resonant inverters for high-frequency AC power distribution systems. IEEE Trans Power Electron 24(4):911–924
17. Rim CT, Choi NS, Cho GC, Cho GH (1994) A complete DC and AC analysis of three-phase controlled-current PWM rectifier using circuit DQ transformation. IEEE Trans Power Electron 9(4):390–396
18. Kwak S, Kim T (2009) An integrated current source inverter with reactive and harmonic power compensators. IEEE Trans Power Electron 24(2):348–357
19. Sun J (2009) Small-signal methods for AC distributed power systems–a review. IEEE Trans Power Electron 24(11):2545–2554
20. Valdivia V, Barrado A, Laazaro A, Zumel P, Raga C, Fernandez C (2009) Simple modeling and identification procedures for "black-box" behavioral modeling of power converters based on transient response analysis. IEEE Trans Power Electron 24(12):2776–2790
21. Sun J, Bing Z, Karimi KJ (2009) Input impedance modeling of multi pulse rectifiers by harmonic linearization. IEEE Trans Power Electron 24(12):2812–2820
22. Barazarte R, Gonzalez G, Ehsani M (2010) Generalized gyrator theory. IEEE Trans Power Electron 25(7):1832–1837
23. Dannehl J, Fuchs F, Thøgersen P (2010) PI state space current control of grid-connected PWM converters with LCL filters. IEEE Trans Power Electron 25(9):2320–2330
24. Bucknall R, Ciaramella K (2010) On the conceptual design and performance of a matrix converter for marine electric propulsion. IEEE Trans Power Electron 25(6):1497–1508
25. Kim S, Yoon Y, Sul S (2010) Pulse width modulation method of matrix converter for reducing output current ripple. IEEE Trans Power Electron 25(10):2620–2629
26. Wood P (1979) General theory of switching power converters. In: IEEE PESC 3–10
27. Rim CT, Cho GH (1990) Phasor transformation and its application to the DC/AC analyses of frequency phase-controlled series resonant converters (SRC). IEEE Trans Power Electron 5:201–211
28. Rim CT (1999) A complement of imperfect phasor transformation. In: Korea power electronics conference, Seoul, pp 159–163
29. Ye Z, Jain PK, Sen PC (2009) Phasor-domain modeling of resonant inverters for high-frequency AC power distribution systems. IEEE Trans Power Electron 24(4):911–924
30. Szczesniak P, Fedyczak Z, Klytta M (2008) Modeling and analysis of a matrix-reactance frequency converter based on buck-boost topology by DQ0 Transformation. In: 13th international power electronics and motion control conference (EPE-PEMC 2008), pp 165–172

Chapter 11
Laplace Phasor Transformation

The phasor transformation is extended to the dynamic analysis of linear AC converters in this chapter. A complex Laplace transformation is adopted in power electronics for the dynamic analysis of phasor transformed circuits. It is verified in general by mathematics that any linear AC converter can be completely analyzed of closed form by the proposed 'Laplace phasor transformation.' Pseudo real Laplacian concept is envisioned to deal with the real part operation in the phasor circuits for DC-AC or AC-DC converters. The system stability of a time-varying AC converter in time domain is proved to be the same as that in complex Laplace domain. A three-phase rectifier with LC filters is fully analyzed and verified by simulations as an example. The proposed transformation is much simpler than the conventional DQ transformation and found to be quite accurate and useful for the design and control of high order AC converters. Lots of this chapter is based on the paper of ours [1].

11.1 Introduction

Power switches in a converter rapidly change the circuit configuration over time; hence, all switching converters are inherently time-varying, and switching harmonics are inevitably generated from the switches. In the history of power electronics, how to deal with the time-varying nature of switching converters has been the most important issue in numerous models and analyses [2–24]. Among them, several modeling techniques have drawn great attention from power electronics specialists, i.e. the switching function based Fourier analysis techniques [2, 4, 5] for fundamental and harmonics analyses in the steady state, the averaging techniques [3, 11] for static and dynamic analyses of DC converters, the DQ transformations [6, 8, 12, 14, 15] for three-phase AC converter analyses, and the circuit transformations [8, 9, 12, 14] for static and dynamic analyses of converters like conventional circuits.

C.T. Rim, *Phasor Power Electronics*, KAIST Research Series,
DOI 10.1007/978-981-10-0536-7_11

The phasor transformation was first introduced [9] for single phase AC converter analyses, where the conventional phasor concept that the magnitude and phase of a sinusoid are constant [25] was substituted with the generalized time-varying phasor. It is applicable to not only single phase DC-AC, AC-DC, and AC-AC converter analyses but also to any resonant converter analyses. This technique has evolved to various forms [26–32] because it makes the analysis of AC converters very easy.

Recently, a unified general circuit-oriented phasor transformation has been developed [33] encompassing polyphase AC converters, which was previously analyzed by the circuit DQ transformation [8, 12, 14] in a very complicated manner. This new phasor transformation drastically simplifies the AC converter analysis so that any balanced polyphase AC converters can be degenerated into single phase converters and multiple switches in the AC converters can be replaced with an equivalent transformer having a complex turn-ratio regardless of the number of switches. The paper [33] shows, however, only the case of static analyses for AC converters in the steady state. The dynamic analyses for phasor transformed AC circuits in the transient state have not been possible in general.

For the convenient dynamic analyses, traditional linear transformations such as Laplace transformations, Fourier transformations, and z-transformations should be applicable to the phasor transformed AC circuits. By the phasor transformations [9, 33], an AC converter is transformed into a circuit that contains imaginary resistors and electronic transformers with complex turn-ratios. Without rigorous verifications, the linear transformations, dealing with only real variables so far, cannot be applied to the complex circuits whose voltages and currents are complex variables in time.

In this chapter, the complex Laplace transformation is introduced first in power electronics for the dynamic analyses of phasor transformed complex circuits. It is verified in general by mathematics that any linear AC converter can be completely analyzed of closed form by the proposed transformation. Pseudo real Laplacian concept is envisioned to deal with the real part operation in the phasor circuits for DC-AC or AC-DC converters. The system stability of a time-varying AC converter in time domain is proved to be the same as that in complex Laplace frequency domain. A three-phase rectifier with LC filters is fully analyzed by the proposed transformation and verified by simulations as an example. The proposed technique is much simpler than the conventional DQ transformation and found to be quite accurate and useful for the design and control of high order AC converters.

Together with the static phasor transformation [33], this circuit oriented dynamic phasor transformation makes it possible to analyze AC converters without cumbersome equations; thus, these techniques are quite essential for high order converter analyses.

Now, a complete analysis flow for any switching converters in power electronics can be established in general, as shown in Fig. 11.1. First, any switching converter could be substituted with corresponding electronic transformer(s) because a switch set is exactly equivalent to a time-varying transformer whose turn-ratio is the switching function [8]. If the switching function is affected by the currents or the voltages of the converter, the system is in the DCM (Discontinuous Conduction

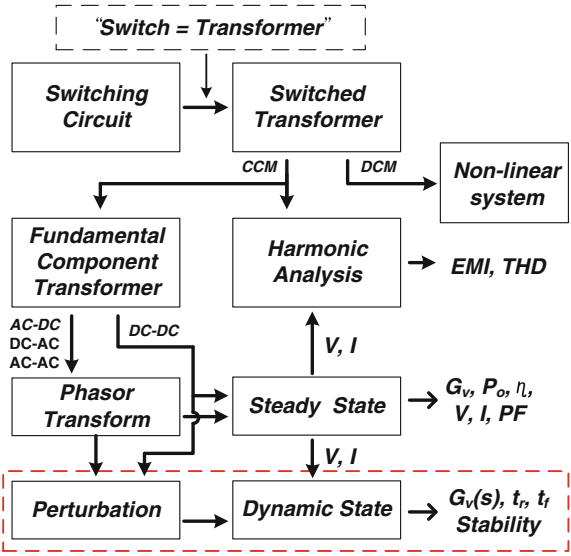

Fig. 11.1 Phasor transformation based analysis flow of switching converters

Mode) and becomes a non-linear system. If the switching function is solely determined by external commands, i.e. turn-on/off duty ratio, the system is in the CCM (Continuous Conduction Mode) and becomes a linear system so far as linear circuit elements are used. The switched transformer in a linear switching system can be averaged for the fundamental component analysis to determine the steady state characteristics, i.e. voltage gain G_V, output power P_o, efficiency η, DC operating points, power factor PF and dynamic state characteristics, i.e. transfer function $G_V(s)$, rising/falling times, and system stability. Harmonic analysis for EMI (Electro Magnetic Interference) and THD (Total Harmonic Distortion) design can be performed by the harmonic voltage/current sources derived from the switched transformer model. The last imperfect part of the phasor transformation based analyses was the dynamic state analysis, as shown in the dotted line box of Fig. 11.1, which has been supplemented by the proposed Laplace phasor transformation.

11.2 Laplace Phasor Transformation for AC Converters

A three-phase rectifier, as shown in Fig. 11.2a, is chosen to show the procedure of applying the complex Laplace transformation to the phasor transformed circuit throughout this chapter. It is assumed that the three-phase rectifier is well balanced and harmonics free because the LC input filters and the output filter can sufficiently diminish switching harmonics so as not to meaningfully affect the fundamental voltage or current components.

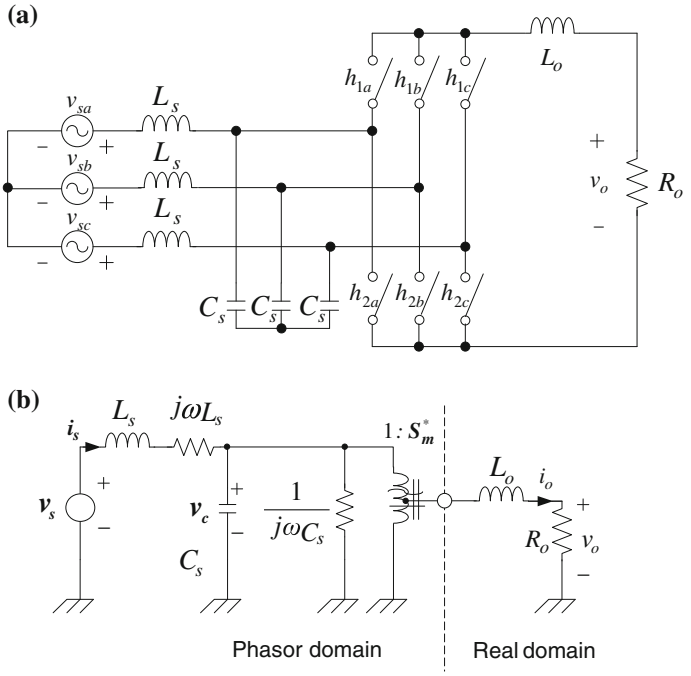

Fig. 11.2 A three-phase rectifier example for the unified general phasor transformation. **a** Original power circuit in real time domain. **b** Phasor transformed circuit in time domain

11.2.1 Application of the Unified General Phasor Transformation to AC Converters

The converter in the rotary time frame, as shown in Fig. 11.2a, can be transformed into a circuit in the stationary time frame, as shown in Fig. 11.2b, by the power-invariant phasor transformation [33]. The system order is drastically degenerated from seven to three, which makes it possible to analyze the circuit by hands. In Fig. 11.2b, it can be seen that the three-phase rectifier acts like a single-phase rectifier and that the six switches are substituted with a complex transformer, which is much simpler than the conventional DQ transformation [6, 8]. The phasor transformed circuit is no longer a time-varying but a time-invariant linear system; hence, conventional circuit theories can be used if carefully applied. For an example, the imaginary resistor no longer means a conventional reactance of AC inductors and capacitors in the steady state [25].

The phasor transformed circuit is, however, not ready to the analysis of dynamics characterization in frequency domain because of three reasons. First, there is no theoretical rationale in applying conventional linear transformations such as Laplace transformation developed for real variables only to the circuit containing complex variables. Second, the real part operation [33] which is the interface of

phasor domain and real domain of a circuit, as depicted in a dotted line with a dummy source in Fig. 11.2b, should be valid for frequency domain. Third, a small signal perturbed model for the complex transformer, as shown in the phasor transformed circuit of Fig. 11.2b, valid for frequency domain should be available.

11.2.2 Introduction of the Complex Laplace Transformation

Among the linear transformations, the Laplace transformation is selected for the frequency domain analysis tool of complex circuits in this chapter since it is most widely used in power electronics, automatic controls, and electric circuits. The Laplace transformation in the complex form was first proposed as a generalized form of the previous Laplace transformation by Poincare [34, 35] as follows:

$$F(s) = \int_0^\infty f(t)\mathrm{e}^{-st}dt, \quad f(t): \text{ complex variable} \tag{11.1}$$

The time domain variable of (11.1) is no longer a real number but a complex number. It is recent years, however, that this concept has been gradually used in engineering areas such as digital signal processing [36] and time-varying control [37–39]. Now, this theory is to be applied to power electronics in which complex circuits are involved. The complex Laplace transformation applied to the phasor transformed complex circuits is called 'Laplace phasor transformation' in this chapter.

It is not straightforward yet to apply (11.1) to complex circuits in a way that can give us same physical meaning such as conventional impedances and system poles and zeroes. To obtain the result of Laplace integration in mathematics is one thing, and to analyze electric circuits based upon the result is another thing, which will be clarified in the following section.

11.2.3 Application of the Complex Laplace Transformation to Phasor Transformed Complex Circuit Elements

Phasor transformed AC circuits, also called complex circuits, can be decomposed into nine circuit elements in the phasor domain, as shown in Fig. 11.3. They are linear time-invariant circuit elements, i.e. phasor voltage sources, phasor current sources, phasored inductors, phasored capacitors, phasored real resistors, phasored imaginary resistors, complex matrix transformers, complex VSI (Voltage Source Inverter) transformers, and complex CSI (Current Source Inverter) transformers. Therefore, if the complex Laplace transformation can be applicable to each

complex circuit element, then any complex circuit composed of the complex circuit elements can be analyzed, in general, by the complex Laplace transformation.

(a) ***Phasored inductor***: First of all, the application of the complex Laplace transformation to a phasor transformed inductor, called a phasored inductor in this chapter, is performed. By comparing the result of conventional Laplace transformation of real form with that of the complex Laplace transformation, the mathematical validation will be confirmed.

The governing time domain equation for a phasored inductor, as shown in Fig. 11.3a ①, is as follows:

$$\boldsymbol{v_L} = L\frac{d\boldsymbol{i_L}}{dt} \tag{11.2}$$

where $\boldsymbol{v_L}$ and $\boldsymbol{i_L}$ are the complex voltage and current of a phasored inductor in time domain, respectively, and L is the inductance of the real value. Since a complex variable can be decomposed into a real part and an imaginary part, (11.2) can be rewritten as follows:

$$v_{Lr} + jv_{Li} = L\left(\frac{di_{Lr}}{dt} + j\frac{di_{Li}}{dt}\right), \quad \because j \equiv \sqrt{-1} \tag{11.3}$$

where $\boldsymbol{v_L}$ and $\boldsymbol{i_L}$ are defined using the real time variables, respectively, as

$$\boldsymbol{v_L} \equiv v_{Lr} + jv_{Li}, \quad \boldsymbol{i_L} \equiv i_{Lr} + ji_{Li} \tag{11.4}$$

Decomposing (11.3) into a real part equation and an imaginary part equation, two sets of independent equations in the real time domain are obtained, as follows:

$$\begin{aligned} v_{Lr} &= L\frac{di_{Lr}}{dt} \\ v_{Li} &= L\frac{di_{Li}}{dt} \end{aligned} \tag{11.5}$$

A conventional Laplace transformation of the form (11.7) can be applied to (11.5) without any mathematical arguments as follows:

$$\begin{aligned} V_{Lr}(s) &= L\{sI_{Lr}(s) - i_{Lr}(0)\} \\ V_{Li}(s) &= L\{sI_{Li}(s) - i_{Li}(0)\} \end{aligned} \tag{11.6}$$

$$F(s) \equiv \int_0^\infty f(t)\mathrm{e}^{-st}dt, \quad f(t): \text{ real variable} \tag{11.7}$$

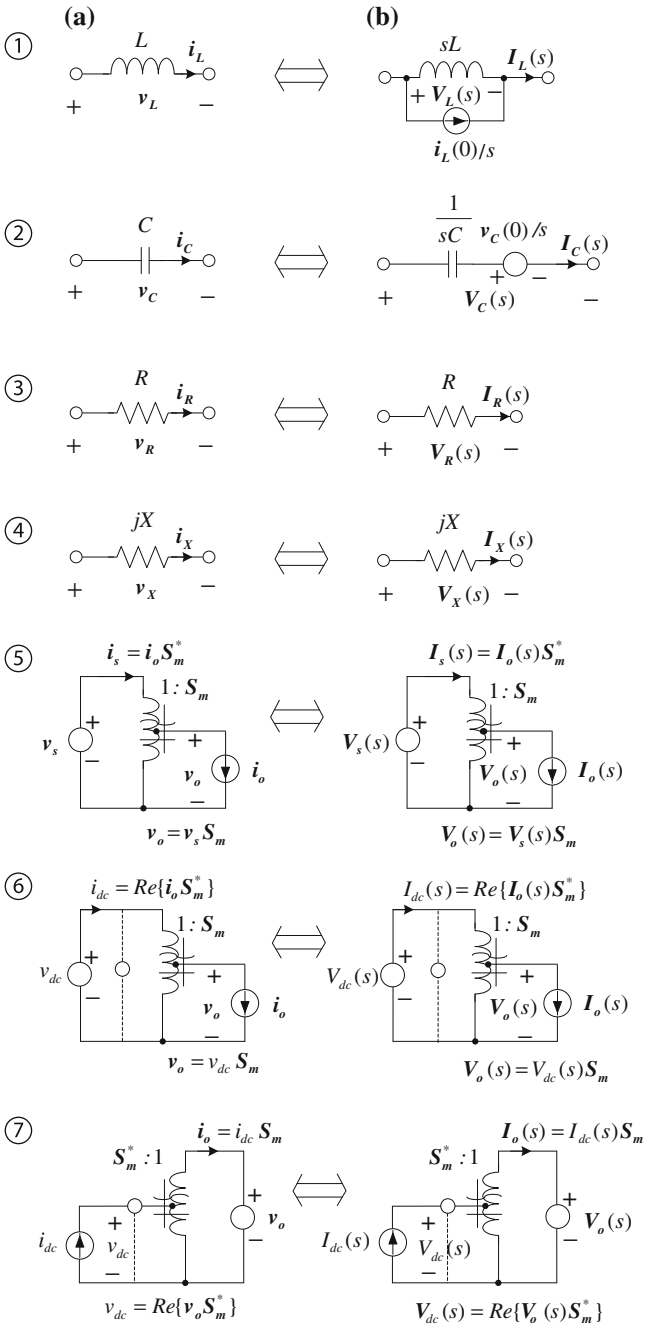

Fig. 11.3 Complex laplace transformation for basic circuit elements of complex circuits. **a** Complex time domain (*left*). **b** Complex laplace transform domain (*right*)

It is found that applying the complex Laplace transformation (11.1)–(11.4) and using (11.6) results in the following relationship:

$$\begin{aligned}
\boldsymbol{V_L}(s) &\equiv \int_0^\infty \boldsymbol{v_L} \mathrm{e}^{-st} dt = \int_0^\infty (v_{Lr} + jv_{Li}) \mathrm{e}^{-st} dt \\
&= \int_0^\infty v_{Lr} \mathrm{e}^{-st} dt + j \int_0^\infty v_{Li} \mathrm{e}^{-st} dt = V_{Lr}(s) + jV_{Li}(s) \\
&= L\{sI_{Lr}(s) - i_{Lr}(0)\} + jL\{sI_{Li}(s) - i_{Li}(0)\} \\
&= sL\{I_{Lr}(s) + jI_{Li}(s)\} - L\{i_{Lr}(0) + ji_{Li}(0)\} \\
&= sL\boldsymbol{I_L}(s) - L\boldsymbol{i_L}(0) \\
&= \int_0^\infty L \frac{d\boldsymbol{i_L}}{dt} \mathrm{e}^{-st} dt
\end{aligned} \tag{11.8}$$

From (11.8), it is noted that the direct application of the complex Laplace transformation (11.1)–(11.2) is equivalent to the application of the conventional Laplace transformation to the real and imaginary parts of a complex variable respectively, as shown in (11.3)–(11.7). In other words, the 'complex Laplace transformation' can be interpreted as the complex sum of two conventional Laplace transformations applied to the real and imaginary parts of a complex variable, independently.

The equivalent circuit in the complex Laplace transformed domain can be obtained, as shown in Fig. 11.3b ①, based on the following equation derived from (11.8):

$$\boldsymbol{I_L}(s) = \frac{\boldsymbol{V_L}(s)}{sL} + \frac{\boldsymbol{i_L}(0)}{s} \tag{11.9}$$

It can be seen from (11.9) that the phasored inductor in frequency domain has the impedance of sL, which is the same as the conventional inductor case. The initial current of (11.9) is, however, of complex form.

It is worthy to note that the voltage and current of the phasored inductor are completely separable into the real and imaginary parts, as shown in (11.5); they are actually independent each other though they are apparently combined into a complex equation, as shown in (11.2), (11.3), and (11.8). Therefore, the complex Laplace transformed voltage and current of (11.8) and (11.9) can be decomposed into real and imaginary parts again. It is convenient, in the decomposition, to regard the Laplacian s as a real value, which will be called 'pseudo real Laplacian' in this chapter. The Laplacian s was regarded as a complex value in the conventional Laplace transformation.

(b) ***Phasored capacitor***: Now, the complex Laplace transformation can be directly applied to the phasored capacitor. The governing time domain equation for a phasored capacitor, as shown in Fig. 11.3a ②, is as follows:

$$\boldsymbol{i_C} = C\frac{d\boldsymbol{v_C}}{dt} \tag{11.10}$$

Applying the complex Laplace transformation (11.1)–(11.10) results in the following Laplace equation.

$$\begin{aligned}\boldsymbol{I_C}(s) &= \int_0^\infty \boldsymbol{i_C} e^{-st} dt = \int_0^\infty C\frac{d\boldsymbol{v_C}}{dt} e^{-st} dt \\ &= sC\boldsymbol{V_C}(s) - C\boldsymbol{v_C}(0) \quad \text{or} \quad \boldsymbol{V_C}(s) = \frac{\boldsymbol{I_C}(s)}{sC} + \frac{\boldsymbol{v_C}(0)}{s}\end{aligned} \tag{11.11}$$

The equivalent circuit of (11.11) in the complex Laplace transformed domain can be obtained, as shown in Fig. 11.3b ②, where the voltage source term represents the initial capacitor voltage and can be removed if it is zero. It can be seen from (11.11) that the phasored capacitor in frequency domain has the admittance of sC, which is the same as the conventional capacitor case.

(c) ***Phasored real resistor***: The application of the complex Laplace transformation to a phasored real resistor, as shown in Fig. 11.3a ③, is straightforward since its governing time domain equation is as follows:

$$\boldsymbol{v_R} = R\boldsymbol{i_R} \tag{11.12}$$

Performing the complex Laplace transformation for (11.12) results in the following Laplace equation.

$$\begin{aligned}\boldsymbol{V_R}(s) &= \int_0^\infty \boldsymbol{v_R} e^{-st} dt = \int_0^\infty R\boldsymbol{i_R} e^{-st} dt \\ &= R\int_0^\infty \boldsymbol{i_R} e^{-st} dt = R\boldsymbol{I_R}(s)\end{aligned} \tag{11.13}$$

The equivalent circuit of (11.13) in the complex Laplace transformed domain is shown in Fig. 11.3b ③. The resistance is unchanged by the Laplace phasor transformation.

(d) ***Phasored imaginary resistor***: The application of the complex Laplace transformation to a phasored imaginary resistor, as shown in Fig. 11.3a ④, is performed for the governing time domain equation, as follows:

$$\boldsymbol{v_X} = jX\boldsymbol{i_X} \tag{11.14}$$

Performing the complex Laplace transformation for (11.14) results in the following Laplace equation.

$$\begin{aligned} \boldsymbol{V_X}(s) &= \int_0^\infty \boldsymbol{v_X} \mathrm{e}^{-st} dt = \int_0^\infty jX\boldsymbol{i_X} \mathrm{e}^{-st} dt \\ &= jX \int_0^\infty \boldsymbol{i_X} \mathrm{e}^{-st} dt = jX\boldsymbol{I_X}(s) \end{aligned} \tag{11.15}$$

The equivalent circuit of (11.15) in the complex Laplace transformed domain is shown in Fig. 11.3b ④. The imaginary resistance is also unchanged by the Laplace phasor transformation.

It is worthy to note from (11.14) and (11.15) that the real part of the voltage is related with the imaginary part of the current by the value of the imaginary resistance X. It is also true for the relationship between the imaginary part of the voltage and the real part of the current. Thus, there are two independent equations in (11.14) and (11.15), respectively. They are, however, different from the phasored inductor, capacitor, and resistor cases, where there is no cross relationship between the real and imaginary parts, as shown in (11.5).

(e) ***Complex matrix transformer***: A complex matrix transformer, as shown in Fig. 11.3a ⑤, is a phasor transformed equivalent circuit element of an AC-AC converter, i.e. a matrix converter, whose governing time domain equation is as follows [33]:

$$\boldsymbol{v_o} = \boldsymbol{v_s}\boldsymbol{S_m}, \quad \boldsymbol{i_s} = \boldsymbol{i_o}\boldsymbol{S_m^*} \tag{11.16}$$

where $\boldsymbol{S_m}$, i.e. $S_m \mathrm{e}^{j\phi_S}$, is a complex turn-ratio representing the voltage conversion ratio S_m and the phase difference ϕ_S between the source and output voltages of the fundamental components. $\boldsymbol{S_m^*}$, i.e. $S_m \mathrm{e}^{-j\phi_S}$, is a complex conjugate of the complex turn-ratio and represents the relationship between the source and the output currents. It should be remarked that the complex turn-ratio includes neither switching harmonics nor time-varying components in this chapter; hence, it is just a time-invariant complex number.

The complex turn-ratios of the complex transformer models in Fig. 11.3 are assumed to have already been perturbed [9]; hence, the transformer models have fixed complex turn-ratios; perturbed voltage sources and current sources are excluded from the models. Under this condition, the application of the complex Laplace transformation to (11.16) results in the following Laplace equation.

$$\begin{aligned} \boldsymbol{V_o}(s) &= \int_0^\infty \boldsymbol{v_o} \mathrm{e}^{-st} dt = \int_0^\infty \boldsymbol{v_s} \boldsymbol{S_m} \mathrm{e}^{-st} dt \\ &= \boldsymbol{S_m} \int_0^\infty \boldsymbol{v_s} \mathrm{e}^{-st} dt = \boldsymbol{V_s}(s) \boldsymbol{S_m}, \\ \boldsymbol{I_s}(s) &= \int_0^\infty \boldsymbol{i_s} \mathrm{e}^{-st} dt = \int_0^\infty \boldsymbol{i_o} \boldsymbol{S_m^*} \mathrm{e}^{-st} dt \\ &= \boldsymbol{S_m^*} \int_0^\infty \boldsymbol{i_o} \mathrm{e}^{-st} dt = \boldsymbol{I_o}(s) \boldsymbol{S_m^*} \end{aligned} \tag{11.17}$$

The equivalent circuit of (11.17) in the complex Laplace transformed domain is shown in Fig. 11.3b ⑤. The complex transformer is unchanged by the proposed Laplace Phasor transformation, i.e. the complex turn-ratios are unchanged for frequency domain as well.

In (11.16) and (11.17), the real and imaginary parts of the voltages or currents are cross-correlated each other, which is the most complicated cases so far.

(f) ***Complex VSI transformer***: A complex VSI transformer, as shown in Fig. 11.3a ⑥, is a phasor transformed equivalent circuit element of a DC-AC voltage source converter, i.e. a voltage source inverter or a current source rectifier, whose governing time domain equation is as follows [33]:

$$\boldsymbol{v_o} = v_{dc} \boldsymbol{S_m}, \quad i_{dc} = Re\{\boldsymbol{i_o} \boldsymbol{S_m^*}\} \tag{11.18}$$

where the cumbersome real part operation is used to describe the fact that there is no complex voltage and current in the real time domain circuits, i.e. the DC side circuits. The dotted line, together with the small circle in Fig. 11.3a ⑥, represents a border line that divides the real domain (left side) and the complex domain (right side), where the small circle denotes the dummy current source [33] to nullify the imaginary current of the complex transformer flowing into the DC side. Except for this real part operator, which is composed of the dotted line and the small circle, the complex transformers in Fig. 11.3⑥ and ⑦ are exactly the same as that in Fig. 11.3⑤.

The $\boldsymbol{S_m}$ of (11.18) is a constant complex turn-ratio, as discussed in the above complex matrix transformer case; hence, the application of the complex Laplace transformation to (11.18) results in the following Laplace equation.

$$\begin{aligned} \boldsymbol{V_o}(s) &= \int_0^\infty \boldsymbol{v_o} \mathrm{e}^{-st} dt = \int_0^\infty v_{dc} \boldsymbol{S_m} \mathrm{e}^{-st} dt \\ &= \boldsymbol{S_m} \int_0^\infty v_{dc} \mathrm{e}^{-st} dt = V_{dc}(s) \boldsymbol{S_m}, \\ I_{dc}(s) &= \int_0^\infty i_{dc} \mathrm{e}^{-st} dt = \int_0^\infty Re\{\boldsymbol{i_o} \boldsymbol{S_m^*}\} \mathrm{e}^{-st} dt \\ &= Re\left\{ \int_0^\infty \boldsymbol{i_o} \mathrm{e}^{-st} dt \boldsymbol{S_m^*} \right\} = Re\{\boldsymbol{I_o}(s) \boldsymbol{S_m^*}\} \end{aligned} \tag{11.19}$$

From (11.19), it should be remarked that the real part operator $Re\{\ \}$ is valid for the complex Laplace transformation only when regarding the Laplacian s as a real number. The equivalent circuit of (11.19) in the complex Laplace transformed domain is shown in Fig. 11.3b ⑥. It is identified from (11.19) that the real part operation is linear and that the complex VSI transformer is unchanged in frequency domain.

(g) ***Complex CSI transformer***: A complex CSI transformer, as shown in Fig. 11.3a ⑦, is a phasor transformed equivalent circuit element of a current source DC-AC converter, i.e. a current source inverter or a voltage source rectifier, whose governing time domain equation is as follows [33]:

$$\boldsymbol{i_o} = i_{dc} \boldsymbol{S_m}, \quad v_{dc} = Re\{\boldsymbol{v_o} \boldsymbol{S_m^*}\}, \tag{11.20}$$

which is analogous to (11.18); the real part operation was used for the same purpose as the complex VSI transformer case. The dotted line, together with the small circle in Fig. 11.3 ⑦, also divides the real domain (left side) and the complex domain (right side), where the small circle denotes the dummy voltage source [33], which is used to nullify the imaginary voltage of the complex transformer at the DC side.

The $\boldsymbol{S_m}$ of (11.20) is also a constant complex turn-ratio; hence, the application of the complex Laplace transformation to (11.20) results in the following Laplace equation:

$$\begin{aligned}\boldsymbol{I_o}(s) &= \int_0^\infty \boldsymbol{i_o} e^{-st} dt = \int_0^\infty i_{dc} \boldsymbol{S_m} e^{-st} dt \\ &= \boldsymbol{S_m} \int_0^\infty i_{dc} e^{-st} dt = I_{dc}(s) \boldsymbol{S_m}, \\ V_{dc}(s) &= \int_0^\infty v_{dc} e^{-st} dt = \int_0^\infty Re\{\boldsymbol{v_o} \boldsymbol{S_m^*}\} e^{-st} dt \\ &= Re\left\{ \int_0^\infty \boldsymbol{v_o} e^{-st} dt \boldsymbol{S_m^*} \right\} = Re\left\{ \boldsymbol{V_o}(s) \boldsymbol{S_m^*} \right\}\end{aligned} \tag{11.21}$$

From (11.21), the real part operator $Re\{\ \}$ is also valid for the complex Laplace transformation only when regarding the Laplacian s as a real number. The equivalent circuit of (11.21) in the complex Laplace transformed domain is shown in Fig. 11.3b ⑦.

The applications of the complex Laplace transformation to the phasor voltage source and the phasor current source are not shown separately here; however, they are inherently included in the above discussions, e.g. in (11.16) and (11.17).

11.2.4 Application of Complex Laplace Transformation to Complex Circuits

The application of the complex Laplace transformation to the individual complex circuit elements shown in Fig. 11.2b assuming zero initial conditions and the reconstruction of them result in a circuit in the frequency domain, as shown in Fig. 11.4. Apparently, the complex Laplace transformation is similar to a conventional Laplace transformation, as can be seen in Fig. 11.4, in which inductors

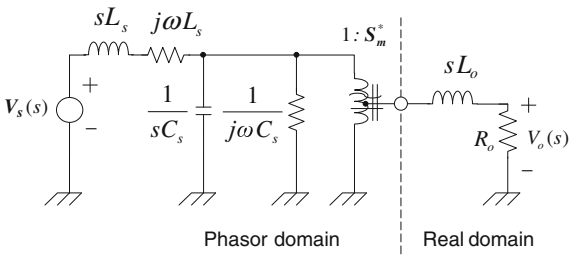

Fig. 11.4 Complex laplace transformed three-phase rectifier

and a capacitor have impedances represented in Laplacian terms. There is, however, no guarantee that the Laplace phasor transformed circuit gives the same poles and zeros as the conventional Laplace transformed circuit does. So, it is not straightforward yet to find the poles and zeros when the real part operator is included in the circuit. Remind that dealing with the real part operation was the biggest issue in the steady state case [33]. Therefore, conventional circuit theories cannot be directly applied to the Laplace phasor transformed circuit of Fig. 11.4 without special cares for the real part operator, nevertheless the similarity of the complex Laplace transformation with the conventional Laplace transformation.

The example three-phase rectifier, shown in Fig. 11.4, is used to demonstrate the analysis procedure where the real part operator is included. Dynamic responses, as well as static responses, can be analyzed by the proposed Laplace phasor transformation. Though this chapter is focusing on the dynamic analysis, the static analysis is also provided here since it is useful to determine the Q point.

11.2.5 Static Analysis of Laplace Phasor Transformed Circuit

In the steady state, inductors are shorted and capacitors are opened for the complex Laplace transformed circuit, as shown in Fig. 11.5a. This is the same as the conventional Laplace transformation case, where $s \rightarrow 0$ in the steady state.

The source voltage $\boldsymbol{V_s}$ is a complex value representing the magnitude and phase of the source voltages, as shown in Fig. 11.2a, and the angular frequency ω is the same as that of the source voltages. Because the circuit including the real part operator is linear, Thevenin theorem can be applied to the Laplace phasor transformed circuit. Thus, a Thevenin equivalent circuit for the left part of the complex transformer, as shown in Fig. 11.5b, can drastically simplify the analysis, where the Thevenin equivalent voltage and impedance are as follows:

$$\boldsymbol{V_{t1}} = \frac{\frac{1}{j\omega C_s}}{j\omega L_s + \frac{1}{j\omega C_s}} \boldsymbol{V_s} = \frac{1}{1 - \omega^2 L_s C_s} \boldsymbol{V_s} \tag{11.22}$$

$$\boldsymbol{Z_{t1}} = \frac{j\omega L_s \frac{1}{j\omega C_s}}{j\omega L_s + \frac{1}{j\omega C_s}} = \frac{j\omega L_s}{1 - \omega^2 L_s C_s} \tag{11.23}$$

Now, the complex transformer in Fig. 11.5b can be eliminated when another Thevenin equivalent circuit for the right part is sought, considering that the complex transformer is linear, as shown in Fig. 11.5c. The Thevenin equivalent voltage is the open circuit voltage shown in Fig. 11.5b, in which no current flows, as follows:

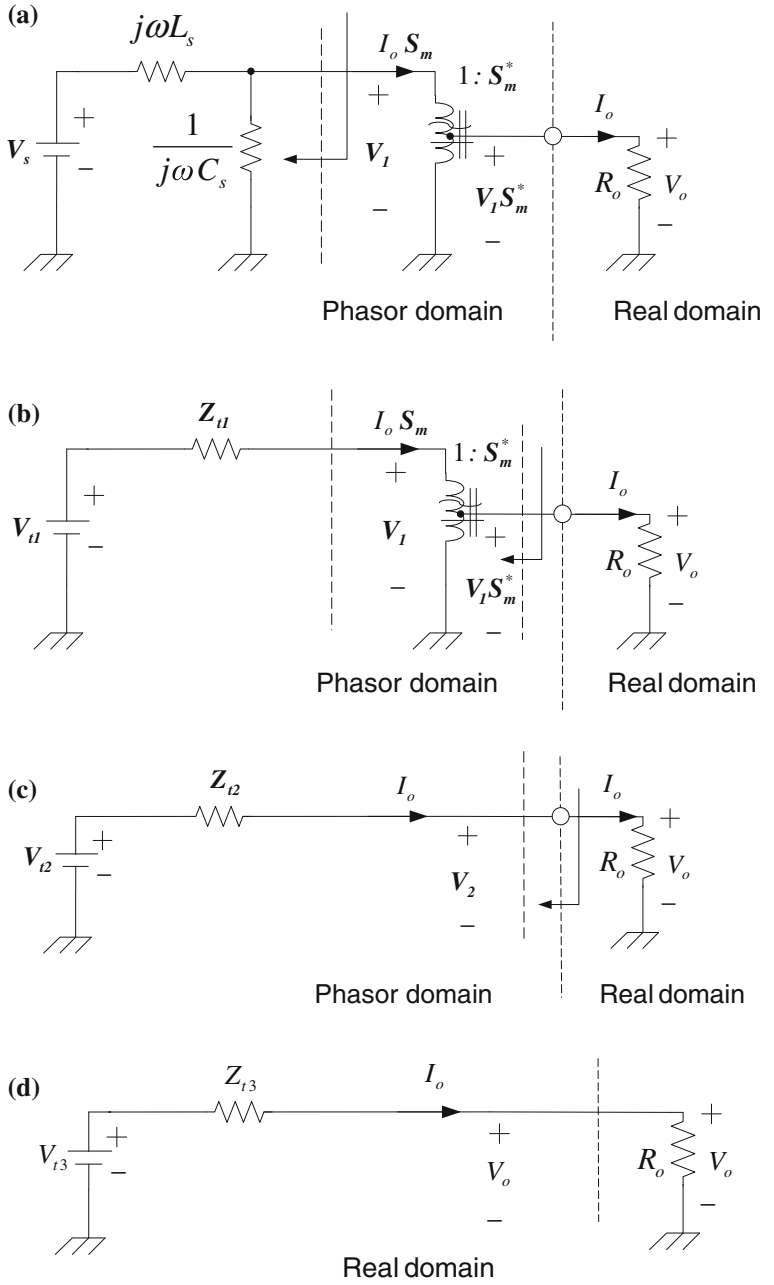

Fig. 11.5 Static equivalent circuits of the three-phase rectifier. **a** Original static circuit. **b** The first Thevenin equivalent circuit for the source side. **c** The second Thevenin equivalent circuit, removing the complex transformer. **d** The third Thevenin equivalent circuit, removing the real part operator

$$\boldsymbol{V_{t2}} = \boldsymbol{V_2}|_{I_o=0} = \boldsymbol{V_1 S_m^*}\big|_{I_o=0} = \boldsymbol{V_{t1} S_m^*} \tag{11.24}$$

The Thevenin equivalent resistance can be calculated from Fig. 11.5b, as follows:

$$\begin{aligned} \boldsymbol{Z_{t2}} &\equiv \frac{\boldsymbol{V_1 S_m^*}}{-I_o}\bigg|_{V_{t1}=0} = \frac{(-I_o \boldsymbol{S_m Z_{t1}})\boldsymbol{S_m^*}}{-I_o} \\ &= \boldsymbol{Z_{t1} S_m S_m^*} = \boldsymbol{Z_{t1}}|\boldsymbol{S_m}|^2 \equiv \boldsymbol{Z_{t1}} S_m^2 \end{aligned} \tag{11.25}$$

Finally, the Fig. 11.5c can be further simplified to remove the cumbersome real part operator with a little caution on the phasor domain and real domain as follows:

$$\begin{aligned} V_o &= Re\{\boldsymbol{V_{t2}} - \boldsymbol{Z_{t2}} I_o\} \\ &= Re\{\boldsymbol{V_{t2}}\} - Re\{\boldsymbol{Z_{t2}}\} I_o \equiv V_{t3} - Z_{t3} I_o \end{aligned} \tag{11.26}$$

where

$$V_{t3} \equiv Re\{\boldsymbol{V_{t2}}\}, \quad Z_{t3} \equiv Re\{\boldsymbol{Z_{t2}}\}. \tag{11.27}$$

From (11.26) and (11.27), it can be seen that the final circuit of Fig. 11.5(d) includes only the real part variables and that a conventional circuit analysis is now possible; hence, the DC output voltage can be calculated from (11.22)–(11.27), as follows:

$$\begin{aligned} V_o &= \frac{R_o}{Z_{t3} + R_o} V_{t3} = \frac{R_o}{Re\{\boldsymbol{Z_{t2}}\} + R_o} Re\{\boldsymbol{V_{t2}}\} \\ &= \frac{R_o}{Re\{\boldsymbol{Z_{t1}} S_m^2\} + R_o} Re\{\boldsymbol{V_{t1} S_m^*}\} \\ &= \frac{R_o}{Re\{\frac{j\omega L_s}{1-\omega^2 L_s C_s}\} S_m^2 + R_o} Re\left\{\frac{\boldsymbol{V_s S_m^*}}{1-\omega^2 L_s C_s}\right\} \\ &= \frac{R_o}{0 + R_o} \frac{Re\{\boldsymbol{V_s S_m^*}\}}{1-\omega^2 L_s C_s} = \frac{Re\{\boldsymbol{V_s S_m^*}\}}{1-\omega^2 L_s C_s} \end{aligned} \tag{11.28}$$

Note that Z_{t3} becomes zero because the real part of (11.23) or (11.25) is zero; hence, the analytical result of (11.28) is very simple. The procedure for DC phasor analysis seems somewhat complicated for this example, which is intentionally illustrated in detail; however, the circuit oriented phasor analysis requires quite few equations and can even be drastically simple, as shown in [33].

11.2.6 Dynamic Analysis of Laplace Phasor Transformed Circuit

The Laplace phasor transformed three-phase rectifier shown in Fig. 11.4 can be analyzed in a fashion similar to that of the above static analysis case for the dynamics characterization, as shown in Fig. 11.6. Because the Laplace phasor transformed circuit shown in Fig. 11.6a is linear, a Thevenin equivalent circuit for the left part of the complex transformer is obtained, as shown in Fig. 11.6(b), in which the Thevenin equivalent voltage and impedance are as follows:

$$\begin{aligned} \boldsymbol{V_{t1}}(s) &= \frac{1/(sC_s + j\omega C_s)}{sL_s + j\omega L_s + 1/(sC_s + j\omega C_s)} \cdot \boldsymbol{V_s}(s) \\ &= \frac{1}{1 + (sL_s + j\omega L_s)(sC_s + j\omega C_s)} \cdot \boldsymbol{V_s}(s) \end{aligned} \tag{11.29}$$

$$\begin{aligned} \boldsymbol{Z_{t1}}(s) &= \frac{(sL_s + j\omega L_s)\frac{1}{sC_s + j\omega C_s}}{(sL_s + j\omega L_s) + \frac{1}{sC_s + j\omega C_s}} \\ &= \frac{sL_s + j\omega L_s}{1 + (sL_s + j\omega L_s)(sC_s + j\omega C_s)} \end{aligned} \tag{11.30}$$

The complex transformer in Fig. 11.6b can be eliminated by finding a Thevenin equivalent circuit for the left side of the real part operator, as shown in Fig. 11.6c. The Thevenin equivalent voltage is the open circuit voltage shown in Fig. 11.6b, at which no current flows, as follows:

$$\boldsymbol{V_{t2}}(s) = \boldsymbol{V_2}(s)|_{I_o(s)=0} = \boldsymbol{V_1}(s)\boldsymbol{S_m^*}\big|_{I_o(s)=0} = \boldsymbol{V_{t1}}(s)\boldsymbol{S_m^*} \tag{11.31}$$

The Thevenin equivalent resistance is calculated from Fig. 6b as follows:

$$\begin{aligned} \boldsymbol{Z_{t2}}(s) &\equiv \left.\frac{\boldsymbol{V_1}(s)\boldsymbol{S_m^*}}{-I_o(s)}\right|_{V_{t1}(s)=0} = \frac{-I_o(s)\boldsymbol{S_m}\boldsymbol{Z}_{t1}(s)\boldsymbol{S_m^*}}{-I_o(s)} \\ &= \boldsymbol{Z_{t1}}(s)\boldsymbol{S_m}\boldsymbol{S_m^*} = \boldsymbol{Z_{t1}}(s)S_m^2 \end{aligned} \tag{11.32}$$

Figure 11.6c is further simplified by removing the real part operator as follows:

$$\begin{aligned} V_3(s) &= Re\{\boldsymbol{V_2}(s)\} = Re\{\boldsymbol{V_{t2}}(s) - Z_{t2}(s)I_o(s)\} \\ &= Re\{\boldsymbol{V_{t2}}(s)\} - Re\{\boldsymbol{Z_{t2}}(s)\}I_o(s) \\ &\equiv V_{t3}(s) - Z_{t3}(s)I_o(s) \end{aligned} \tag{11.33}$$

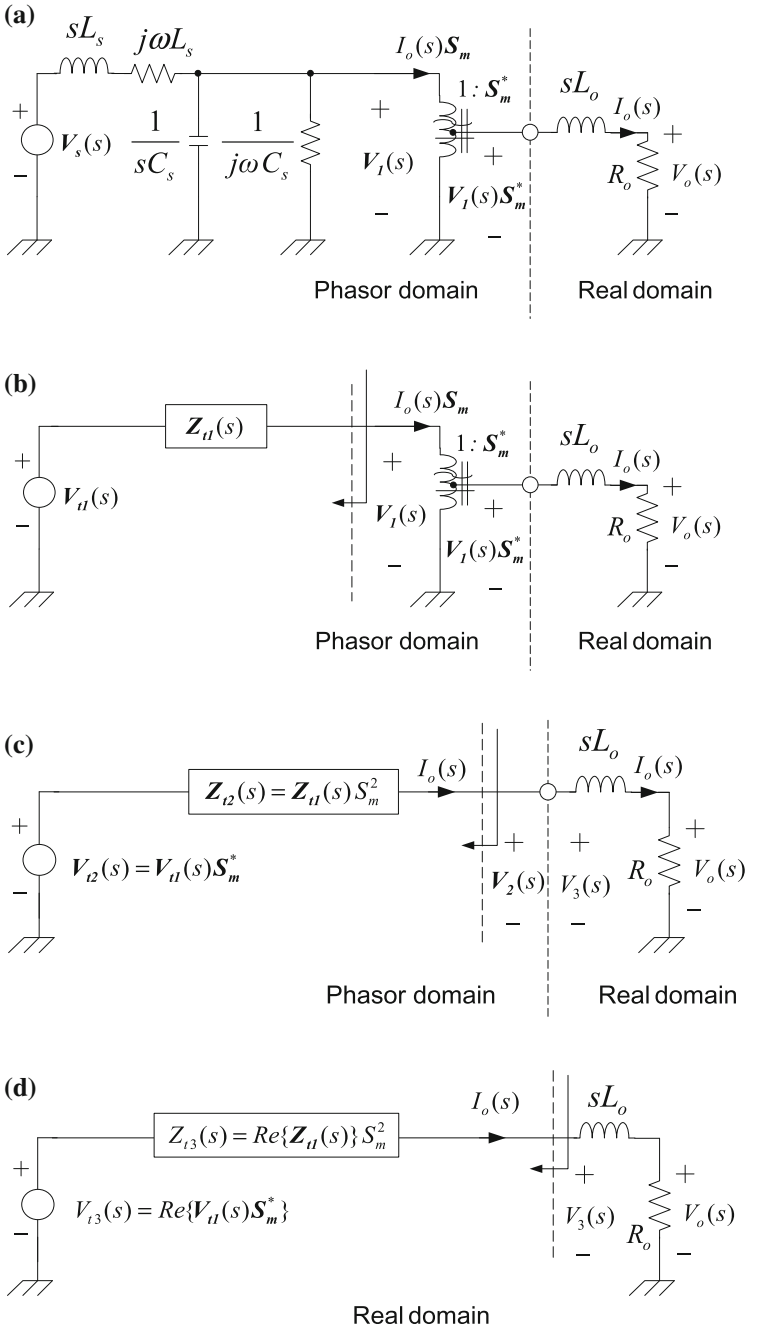

Fig. 11.6 Dynamic equivalent circuits of the three-phase rectifier in the complex laplace domain. **a** Original dynamic circuit. **b** The first Thevenin equivalent circuit for the source side. **c** The second Thevenin equivalent circuit, removing the complex transformer. **d** The third Thevenin equivalent circuit, removing the real part operator

where

$$\begin{aligned} V_{t3}(s) &\equiv Re\{\boldsymbol{V_{t2}}(s)\} = Re\{\boldsymbol{V_{t1}}(s)\boldsymbol{S_m^*}\}, \\ Z_{t3}(s) &\equiv Re\{\boldsymbol{Z_{t2}}(s)\} = Re\{\boldsymbol{Z_{t1}}(s)\}S_m^2 \end{aligned} \tag{11.34}$$

From (11.33) and (11.34), the final circuit of Fig. 11.6d can be drawn; this circuit is in the conventional Laplace transformation domain and no complex variables exist. Thus, the output voltage transfer function can be calculated from (11.29)–(11.34) as follows:

$$\begin{aligned} V_o(s) &= \frac{R_o}{Z_{t3}(s) + sL_o + R_o} V_{t3}(s) \\ &= \frac{R_o}{Re\{\boldsymbol{Z_{t1}}(s)\}S_m^2 + sL_o + R_o} Re\{\boldsymbol{V_{t1}}(s)\boldsymbol{S_m^*}\} \end{aligned} \tag{11.35}$$

where the real part operation of the dynamic case is quite complicated in comparison with the static case of (11.28), as follows:

$$\begin{aligned} &Re\{\boldsymbol{V_{t1}}(s)\boldsymbol{S_m^*}\} = \\ &\frac{Re\{\boldsymbol{V_s}(s)\boldsymbol{S_m^*}\}\{1 + (s^2 - \omega^2)L_sC_s\} + Im\{\boldsymbol{V_s}(s)\boldsymbol{S_m^*}\}2\omega sL_sC_s}{\{1 + (s^2 - \omega^2)L_sC_s\}^2 + 4\omega^2 s^2 L_s^2 C_s^2} \end{aligned} \tag{11.36}$$

$$Re\{\boldsymbol{Z_{t1}}(s)\} = \frac{sL_s\{1 + (s^2 + \omega^2)L_sC_s\}}{\{1 + (s^2 - \omega^2)L_sC_s\}^2 + 4\omega^2 s^2 L_s^2 C_s^2}. \tag{11.37}$$

11.2.7 Introduction of Pseudo Real Laplacian to Deal with the Real Part Operation

It should be noted that the imaginary part operation $Im\{\}$ is used in (11.36) and that the real part operation is not directly applicable to the denominator. Equations (11.36) and (11.37) constitute the key parts of this chapter; hence, how to apply the real part operation for the Laplace phasor transformed circuit is illustrated for this case. Detail procedures for (11.36) and (11.37) are in Appendix (11.61) and (11.62).

As emphasized in the previous chapter, the Laplacian s is regarded as a real number in the real part operations of (11.36) and (11.37). This may be very strange for the readers who are familiar with the idea that the Laplacian s should be a complex number in general. Furthermore, the complex Laplace transformation of (11.1) has been applied to the complex variables, as shown in Fig. 11.3; hence, it can be thought that it might be a complex number. It is worthwhile, at the moment,

to remark on the validity of the proposed real part operation in the complex domain related with the complex Laplace transformation.

Let us begin with a complex Laplace transformed function $\boldsymbol{F}(s)$, assuming that it can be decomposed into two conventional real Laplace transformed functions, $F_r(s)$ and $F_i(s)$, as follows:

$$\boldsymbol{F}(s) = F_r(s) + jF_i(s) \tag{11.38}$$

where

$$\begin{aligned} \boldsymbol{F}(s) &\equiv \int_0^\infty \boldsymbol{f}(t)\mathrm{e}^{-st}dt, \\ F_r(s) &\equiv \int_0^\infty f_r(t)\mathrm{e}^{-st}dt, \quad F_i(s) \equiv \int_0^\infty f_i(t)\mathrm{e}^{-st}dt \end{aligned} \tag{11.39}$$

and

$$\boldsymbol{f}(t) = f_r(t) + jf_i(t), \quad \because f_r(t), f_i(t) \in \mathrm{R}^1 : \text{real}. \tag{11.40}$$

Note that $F_r(s)$ and $F_i(s)$ of (11.39) are of real value if the Laplacian s is a real number because their corresponding time domain functions $f_r(t)$ and $f_i(t)$ are real. So, $F_r(s)$ and $F_i(s)$ become complex values only when the Laplacian s is a complex number. In other words, the nature of complex variables in the conventional Laplace transformed function stems not from the time domain function but from the postulation that the Laplacian s is a complex variable. It can be seen from (11.38) and (11.40) that the real part operation in the complex Laplace transformation is valid for the real Laplacian s, as follows:

$$\begin{aligned} Re\{\boldsymbol{F}(s)\} &= Re\left\{\int_0^\infty \boldsymbol{f}(t)\mathrm{e}^{-st}dt\right\} \\ &= \int_0^\infty Re\{\boldsymbol{f}(t)\}\mathrm{e}^{-st}dt \quad \text{if } s \in \mathrm{R}^1 \\ &= \int_0^\infty f_r(t)\mathrm{e}^{-st}dt = F_r(s) \\ &= Re\{F_r(s) + jF_i(s)\} \quad \text{if } s \in \mathrm{R}^1 \end{aligned} \tag{11.41}$$

It should not be misunderstood, however, from (11.41) that the complex Laplace transformation proposed in this chapter is valid for the real Laplacian s only. What

(11.41) shows is just a way of finding the real part of a complex Laplace function, i.e. it does not necessarily impose the Laplacian s on a real number.

To further clarify this statement, a conventional real Laplace transformed function $F(s)$ of (11.7), which represents one of $F_r(s)$ and $F_i(s)$, is defined as follows:

$$\begin{aligned} F(s) &\equiv \frac{b_0 + b_1 s^1 + b_2 s^2 + \cdots + b_m s^m}{a_0 + a_1 s^1 + a_2 s^2 + \cdots + a_n s^n} = \frac{G_z(s)}{G_p(s)}, \\ &\because \{a_k\} \in R^1, 1 \le k \le n, \{b_k\} \in R^1, 1 \le k \le m, \\ &a_n \neq 0, b_m \neq 0 \\ &G_p(s) = a_0 + a_1 s^1 + a_2 s^2 + \cdots + a_n s^n, \\ &G_z(s) = b_0 + b_1 s^1 + b_2 s^2 + \cdots + b_m s^m \end{aligned} \tag{11.42}$$

It is assumed that $F(s)$ is composed of polynomial functions $G_p(s)$ and $G_z(s)$ with real coefficients, which is the case in a linear system with real variables such as an ordinary electrical circuit. Permitting complex poles p_k and complex zeros z_k, $F(s)$ of (11.42) can be rewritten in the following form.

$$\begin{aligned} F(s) &= \frac{G_z(s)}{G_p(s)}, \\ G_p(s) &= a_n (s - p_0)(s - p_1) \cdots (s - p_n), \\ G_z(s) &= b_m (s - z_0)(s - z_1) \cdots (s - z_m) \end{aligned} \tag{11.43}$$

Note that the complex poles in $G_p(s)$ or the complex zeros in $G_z(s)$ always have their corresponding complex conjugate pairs so that the coefficients can be real, as shown for the following complex pole pair case.

$$\begin{aligned} (s - p_k)(s - p_k^*) &= s^2 - s(p_k + p_k^*) + p_k p_k^* \\ &= s^2 - s \cdot 2Re\{p_k\} + |p_k|^2, \quad 1 \le k \le n \end{aligned} \tag{11.44}$$

The time domain function $f(t)$, which is the inverse Laplace transformation of (11.43), includes no complex value, as defined in (11.7); hence, the complex pole pairs or complex zero pairs do not generate any complex time domain value. In this way, the real Laplace transformed functions $F_r(s)$ and $F_i(s)$, though having complex poles or zeros, are inversely Laplace transformed to the time domain functions of real value only. In a word, what matters is not the nature of Laplacian s but the real coefficients in $F(s)$; hence, the decomposition of the complex Laplace transformed function $\boldsymbol{F}(s)$ into $F_r(s)$ and $F_i(s)$ can be conveniently performed by finding the real and imaginary parts of $\boldsymbol{F}(s)$ regarding s as real, as shown in (11.36) and (11.37). From this viewpoint, the s is called the pseudo real Laplacian for the real part operation or the imaginary part operation in the complex Laplace transformation.

11.2.8 Perturbation Analysis of Laplace Phasor Transformed Circuit

In the previous section, the source voltage $\boldsymbol{V}_s(s)$ was considered only as an input for the purpose of large signal dynamic analysis; however, the complex transformer, as shown in Fig. 11.2b or Fig. 11.6a, is the control driver in most applications. The complex transformer is no longer linear for a time-varying complex turn-ratio $\boldsymbol{s}_m$, though it is linear for the constant $\boldsymbol{S}_m$, as has been discussed so far.

So, a perturbed complex transformer model in the complex Laplace domain neglecting the product of two perturbed variables is, as follows:

$$\begin{aligned}
\boldsymbol{v}_o &\equiv \boldsymbol{V}_o + \hat{\boldsymbol{v}}_o = \boldsymbol{v}_s \boldsymbol{s}_m \equiv (\boldsymbol{V}_s + \hat{\boldsymbol{v}}_s)(\boldsymbol{S}_m + \hat{\boldsymbol{s}}_m) \\
&= \boldsymbol{V}_s \boldsymbol{S}_m + \boldsymbol{V}_s \hat{\boldsymbol{s}}_m + \boldsymbol{S}_m \hat{\boldsymbol{v}}_s + \hat{\boldsymbol{v}}_s \hat{\boldsymbol{s}}_m \cong \boldsymbol{V}_s \boldsymbol{S}_m + \boldsymbol{V}_s \hat{\boldsymbol{s}}_m + \boldsymbol{S}_m \hat{\boldsymbol{v}}_s \\
\boldsymbol{i}_s &\equiv \boldsymbol{I}_s + \hat{\boldsymbol{i}}_s = \boldsymbol{i}_o \boldsymbol{s}_m^* \equiv (\boldsymbol{I}_o + \hat{\boldsymbol{i}}_o)(\boldsymbol{S}_m^* + \hat{\boldsymbol{s}}_m^*) \\
&= \boldsymbol{I}_o \boldsymbol{S}_m^* + \boldsymbol{I}_o \hat{\boldsymbol{s}}_m^* + \boldsymbol{S}_m^* \hat{\boldsymbol{i}}_o + \hat{\boldsymbol{i}}_o \hat{\boldsymbol{s}}_m^* \cong \boldsymbol{I}_o \boldsymbol{S}_m^* + \boldsymbol{I}_o \hat{\boldsymbol{s}}_m^* + \boldsymbol{S}_m^* \hat{\boldsymbol{i}}_o
\end{aligned} \tag{11.45}$$

The small signal perturbed variables, excluding the large signal constant variables from (11.45), as shown in Fig. 11.7a, are as follows:

$$\begin{aligned}
\hat{\boldsymbol{v}}_o &\cong \boldsymbol{V}_s \hat{\boldsymbol{s}}_m + \boldsymbol{S}_m \hat{\boldsymbol{v}}_s \\
\hat{\boldsymbol{i}}_s &\cong \boldsymbol{I}_o \hat{\boldsymbol{s}}_m^* + \boldsymbol{S}_m^* \hat{\boldsymbol{i}}_o
\end{aligned} \tag{11.46}$$

It can be seen from (11.46) that the equations are now linear w.r.t. the perturbed variables with the constant complex coefficients, corresponding to the Q points of

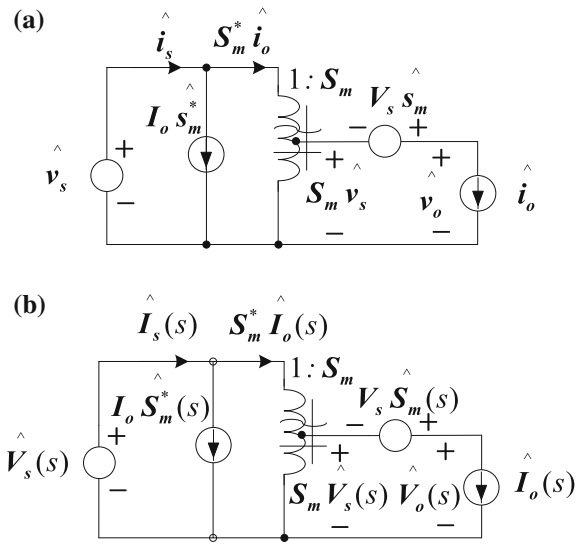

Fig. 11.7 Perturbed complex transformer model. **a** Time domain. **b** Complex laplace domain

the converter; hence, the complex Laplace transformation can be applied to (11.46), resulting in the following Laplace domain equations, as also shown in Fig. 11.7b.

$$\begin{aligned}\hat{\boldsymbol{V}}_{\boldsymbol{o}}(s) &\cong \boldsymbol{V}_{\boldsymbol{s}}\hat{\boldsymbol{S}}_{\boldsymbol{m}}(s) + \boldsymbol{S}_{\boldsymbol{m}}\hat{\boldsymbol{V}}_{\boldsymbol{s}}(s) \\ \hat{\boldsymbol{I}}_{\boldsymbol{s}}(s) &\cong \boldsymbol{I}_{\boldsymbol{o}}\hat{\boldsymbol{S}}^{*}_{\boldsymbol{m}}(s) + \boldsymbol{S}^{*}_{\boldsymbol{m}}\hat{\boldsymbol{I}}_{\boldsymbol{o}}(s)\end{aligned} \tag{11.47}$$

Considering $s_m = s_m e^{j\phi_s}$ and $s_m^* = s_m e^{-j\phi_s}$, the perturbed complex turn-ratios in (11.46) can be further resolved as follows:

$$\begin{aligned}\hat{\boldsymbol{s}}_{\boldsymbol{m}} &= \hat{s}_m e^{j\phi_s} + j\hat{\phi}_s S_m e^{j\phi_s} = (\hat{s}_m/S_m + j\hat{\phi}_s)\boldsymbol{S}_{\boldsymbol{m}} \\ \hat{\boldsymbol{s}}^{*}_{\boldsymbol{m}} &= \hat{s}_m e^{-j\phi_s} - j\hat{\phi}_s S_m e^{-j\phi_s} = (\hat{s}_m/S_m - j\hat{\phi}_s)\boldsymbol{S}^{*}_{\boldsymbol{m}}\end{aligned} \tag{11.48}$$

The complex Laplace transformation for (11.48) results in the following.

$$\begin{aligned}\hat{\boldsymbol{S}}_{\boldsymbol{m}}(s) &= \{\hat{S}_m(s)/S_m + j\hat{\phi}_s(s)\}\boldsymbol{S}_{\boldsymbol{m}} \\ \hat{\boldsymbol{S}}^{*}_{\boldsymbol{m}}(s) &= \{\hat{S}_m(s)/S_m - j\hat{\phi}_s(s)\}\boldsymbol{S}^{*}_{\boldsymbol{m}}\end{aligned} \tag{11.49}$$

The perturbed complex Laplace transformed transformer model of Fig. 11.7b can be applied to Fig. 11.6a for the perturbation analysis, as shown in Fig. 11.8a. The source voltage is also perturbed; hence, there are three independent voltage and current sources in Fig. 11.8a, in which the source side LC filter is substituted with the Thevenin resistance $\boldsymbol{Z}_{\boldsymbol{t1}}(s)$, which is the same as (11.30), and the perturbed Thevenin voltage $\hat{\boldsymbol{V}}_{\boldsymbol{t1}}(s)$ is as follows:

$$\hat{\boldsymbol{V}}_{\boldsymbol{t1}}(s) = \frac{1}{1 + (sL_s + j\omega L_s)(sC_s + j\omega C_s)} \cdot \hat{\boldsymbol{V}}_{\boldsymbol{s}}(s) \tag{11.50}$$

Removing the complex transformer and obtaining the Thevenin open voltage for the three independent sources, a more simplified equivalent circuit is found in Fig. 11.8c, in which the Thevenin resistance $\boldsymbol{Z}_{\boldsymbol{t2}}(s)$ is the same as (11.32) and the perturbed Thevenin voltage $\hat{\boldsymbol{V}}_{\boldsymbol{t2}}(s)$ is as follows:

$$\hat{\boldsymbol{V}}_{\boldsymbol{t2}}(s) = \boldsymbol{S}^{*}_{\boldsymbol{m}}\hat{\boldsymbol{V}}_{\boldsymbol{t1}}(s) - \boldsymbol{S}^{*}_{\boldsymbol{m}}I_o\boldsymbol{Z}_{\boldsymbol{t1}}(s)\hat{\boldsymbol{S}}_{\boldsymbol{m}}(s) + V_1\hat{\boldsymbol{S}}^{*}_{\boldsymbol{m}}(s). \tag{11.51}$$

Finally, removing the real part operator, the Thevenin equivalent circuit is found in Fig. 11.8d, where the Thevenin resistance $\boldsymbol{Z}_{\boldsymbol{t3}}(s)$ is the same as (11.34) and the perturbed Thevenin voltage $\hat{V}_{t3}(s)$ is as follows:

$$\hat{V}_{t3}(s) = Re\{\hat{\boldsymbol{V}}_{\boldsymbol{t2}}(s)\} \tag{11.52}$$

Now, the perturbed output voltage can be obtained by applying conventional real domain circuit analysis to Fig. 11.8d, which is very similar to (11.35), as follows:

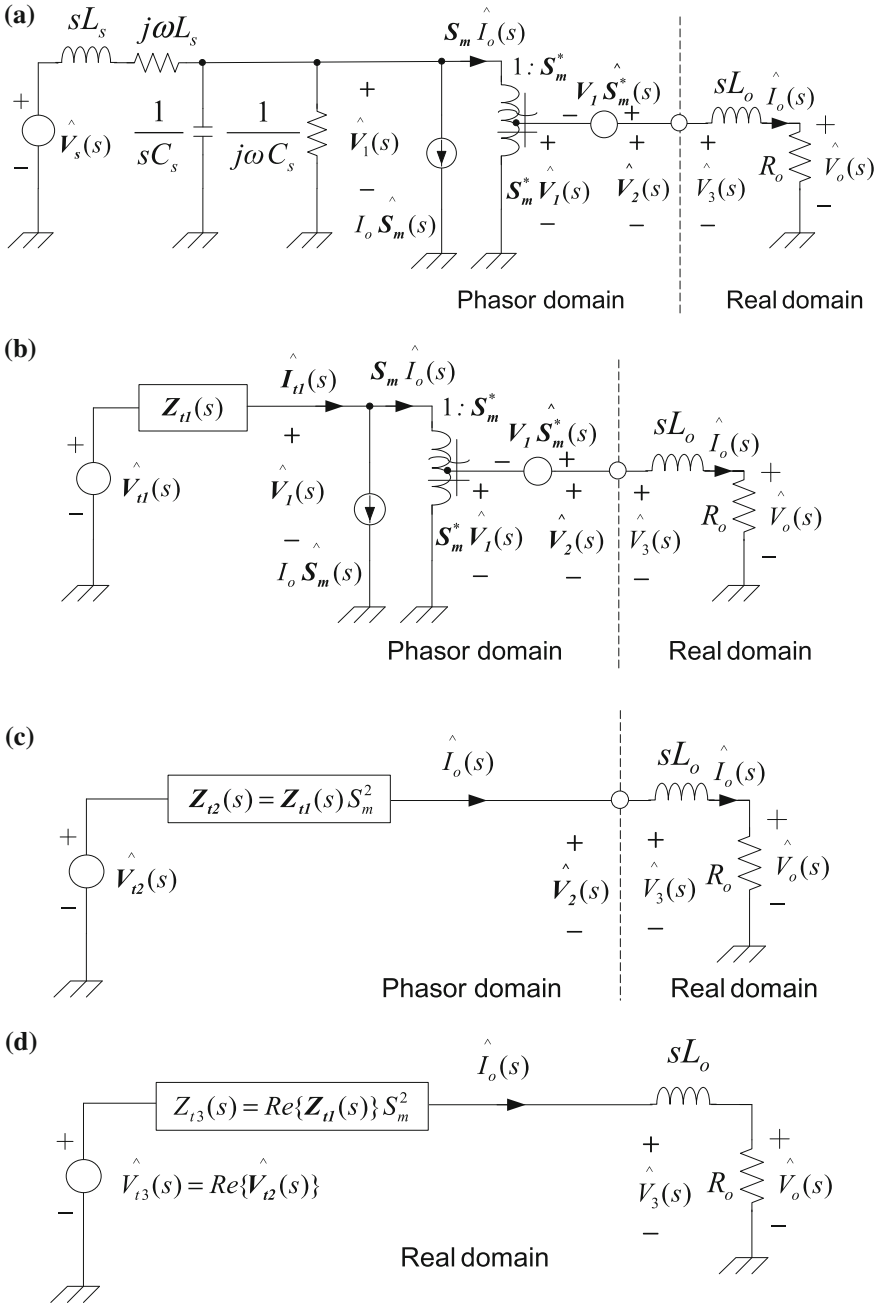

Fig. 11.8 Perturbed circuits of the three-phase rectifier in the complex laplace domain. **a** Original perturbed circuit. **b** The first Thevenin equivalent circuit for the source side. **c** The second Thevenin equivalent circuit, removing the complex transformer. **d** The third Thevenin equivalent circuit, removing the real part operator

$$\begin{aligned}\hat{V}_o(s) &= \frac{R_o}{Z_{t3}(s) + sL_o + R_o}\hat{V}_{t3}(s) \\ &= \frac{R_o}{Re\{\boldsymbol{Z_{t1}}(s)\}S_m^2 + sL_o + R_o} Re\{\hat{\boldsymbol{V}}_{\boldsymbol{t2}}(s)\}\end{aligned} \tag{11.53}$$

where $\mathrm{Re}\{\boldsymbol{Z_{t1}}(s)\}$ is the same as (11.37) and $Re\{\hat{\boldsymbol{V}}_{\boldsymbol{t2}}(s)\}$ can be obtained using (11.49)–(11.51).

$$\begin{aligned}Re\{\hat{\boldsymbol{V}}_{\boldsymbol{t2}}(s)\} &= Re\{\boldsymbol{S}_{\boldsymbol{m}}^{*}\hat{\boldsymbol{V}}_{\boldsymbol{t1}}(s) - \boldsymbol{S}_{\boldsymbol{m}}^{*}I_o\boldsymbol{Z_{t1}}(s)\hat{\boldsymbol{S}}_{\boldsymbol{m}}(s) + \boldsymbol{V_1}\hat{\boldsymbol{S}}_{\boldsymbol{m}}^{*}(s)\} \\ &= Re\{\boldsymbol{S}_{\boldsymbol{m}}^{*}\hat{\boldsymbol{V}}_{\boldsymbol{t1}}(s)\} - I_o Re\Big\{\boldsymbol{S}_{\boldsymbol{m}}^{*}\boldsymbol{Z_{t1}}(s)\{\hat{S}_m(s)/S_m + j\hat{\phi}_S(s)\}\boldsymbol{S_m}\Big\} \\ &\quad + Re\Big\{\boldsymbol{V_1}\{\hat{S}_m(s)/S_m - j\hat{\phi}_S(s)\}\boldsymbol{S}_{\boldsymbol{m}}^{*}\Big\} \\ &= Re\{\boldsymbol{S}_{\boldsymbol{m}}^{*}\hat{\boldsymbol{V}}_{\boldsymbol{t1}}(s)\} - I_o S_m^2\Big[Re\{\boldsymbol{Z_{t1}}(s)\}\hat{S}_m(s)/S_m - \mathrm{Im}\{\boldsymbol{Z_{t1}}(s)\}\hat{\phi}(s)\Big] \\ &\quad + \Big[Re\{\boldsymbol{V_1}\boldsymbol{S}_{\boldsymbol{m}}^{*}\}\hat{S}_m(s)/S_m + Im\{\boldsymbol{V_1}\boldsymbol{S}_{\boldsymbol{m}}^{*}\}\hat{\phi}_S(s)\Big]\end{aligned} \tag{11.54}$$

In similar ways to those used for obtaining (11.36) and (11.37), $Re\{\boldsymbol{S}_{\boldsymbol{m}}^{*}\hat{\boldsymbol{V}}_{\boldsymbol{t1}}(s)\}$ and $Im\{\boldsymbol{Z_{t1}}(s)\}\hat{\phi}_S(s)$ can be found as follows:

$$\begin{aligned}&Re\{\boldsymbol{S}_{\boldsymbol{m}}^{*}\hat{\boldsymbol{V}}_{\boldsymbol{t1}}(s)\} \\ &= \frac{Re\{\boldsymbol{S}_{\boldsymbol{m}}^{*}\hat{\boldsymbol{V}}_{\boldsymbol{s}}(s)\}\{1 + (s^2 - \omega^2)L_sC_s\} + 2Im\{\boldsymbol{S}_{\boldsymbol{m}}^{*}\hat{\boldsymbol{V}}_{\boldsymbol{s}}(s)\}\omega sL_sC_s}{\{1 + (s^2 - \omega^2)L_sC_s\}^2 + 4\omega^2 s^2 L_s^2 C_s^2}\end{aligned} \tag{11.55}$$

$$\begin{aligned}&Im\{\boldsymbol{Z_{t1}}(s)\} \\ &= \frac{Im\{(sL_s + j\omega L_s)\{1 + (s^2 - \omega^2)L_sC_s - j2\omega sL_sC_s\}\}}{\{1 + (s^2 - \omega^2)L_sC_s\}^2 + 4\omega^2 s^2 L_s^2 C_s^2} \\ &= \frac{\omega L_s\{1 - (s^2 + \omega^2)L_sC_s\}}{\{1 + (s^2 - \omega^2)L_sC_s\}^2 + 4\omega^2 s^2 L_s^2 C_s^2}\end{aligned} \tag{11.56}$$

It is important to note that the system analysis results in the Laplace phasor transformation, (11.53)–(11.56) are also valid for the original time-varying converter in time domain, as shown in Fig. 11.2a. In other words, the system stability of a converter is unchanged by the proposed Laplace phasor transformation. It is due to the fact that the phasor transformation [33] is one-to-one mapping transformation from a time-varying real circuit to a time-invariant complex circuit and vice versa; hence, the magnitude and phase of voltage or current is unchanged and preserved through the transformation. A stable system in the Laplace phasor transformed domain must also be stable in the corresponding time domain.

Therefore, the proposed Laplace phasor transformation can be directly used for the design and control of AC converters in the same way the conventional Laplace transformation does for the time-invariant real circuit.

11.3 Simulations of Laplace Phasor Transformed Circuits

The proposed Laplace phasor transformation embraces several new concepts and mathematics; hence, the accuracy and usefulness of the theory for practical situations should be identified. Experimental verifications, though giving physical insights in most cases, are not preferred this time since they are not appropriate for checking the accuracy of a theory. Instead, real time domain numerical simulations using a state equation for Fig. 11.2a, neglecting switching harmonics, were performed for the following circuit parameters, unless otherwise specified.

$$\begin{aligned} &\boldsymbol{V}_s = 440\angle\frac{\pi}{3} \quad \boldsymbol{S_m} = 0.90\angle\frac{\pi}{4} \quad f_s = 60 \text{ Hz} \\ &L_s = 5 \text{ mH} \quad C_s = 300\ \mu F \quad L_o = 3 \text{ mH} \quad R_L = 10\ \Omega \end{aligned} \tag{11.57}$$

A time domain transient response for all zero initial conditions under the circuit parameters of (11.57) is shown in Fig. 11.9, in which the converter is stabilized within 2–3 cycles but undergoes large transient voltage stresses for a step source voltage at $t = 0$.

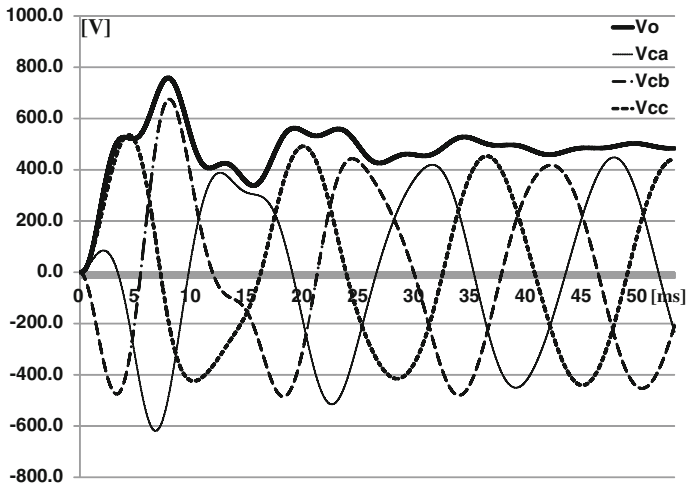

Fig. 11.9 Transient simulation results of the output voltage and input capacitor voltages for the three phase rectifier examples of Fig. 11.2a with the parameters of (11.57)

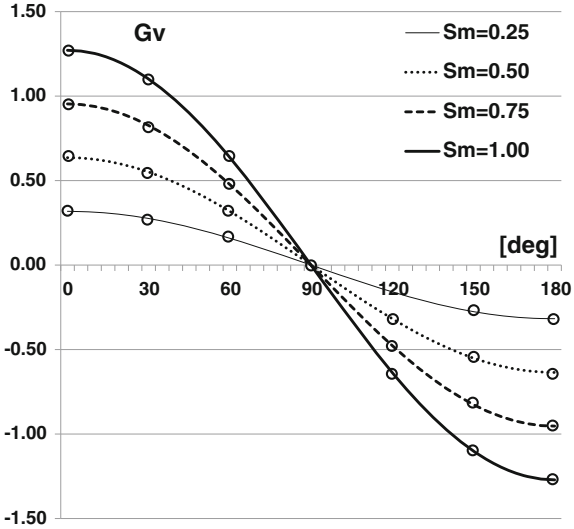

Fig. 11.10 Static simulation results of the DC voltage gain versus the phase difference between the source voltage and the switching function for different turn-ratios shown in Fig. 11.2a, ($\boldsymbol{V_s} = 440\angle\frac{\pi}{3}$ $\boldsymbol{S_m}$: variable $f_s = 60$ Hz $L_s = 5$ mH $C_s = 300$ μF $L_o = 3$ mH $R_L = 10\ \Omega$)

11.3.1 Verifications for the Static Analysis

The DC output voltage analysis result of (11.28) was verified by the time domain simulations for different switching functions, i.e. S_m and ϕ_S. The DC voltage gain should be as follows:

$$\begin{aligned} G_V \equiv \frac{V_o}{V_s} &= \frac{1}{V_s}\frac{Re\{\boldsymbol{V_s}\boldsymbol{S_m^*}\}}{1-\omega^2 L_s C_s} = \frac{1}{V_s}\frac{Re\{V_s e^{j\phi_V} S_m e^{-j\phi_S}\}}{1-\omega^2 L_s C_s} \\ &= \frac{S_m \cos(\phi_V - \phi_S)}{1-\omega^2 L_s C_s} \equiv \frac{S_m \cos\phi_{VS}}{1-\omega^2 L_s C_s} \end{aligned} \tag{11.58}$$

It is verified by the time domain simulation, as shown in Fig. 11.10, that the DC voltage gain of (11.58), as a function of ϕ_{VS}, is well within the 0.1 % error, which is regarded as a simulation error. The DC gain G_V could be negative if the four quadrant AC switches are used in the example circuit shown in Fig. 11.2a.

11.3.2 Verifications for the Dynamic Perturbation Analysis

For simplicity, it is assumed that the source voltage phasor has a zero phase angle, by which the analysis results do not lose generality because the responses will be

relative w.r.t. the source voltage. In this way, the small signal source voltage transfer function, chosen among the transfer functions (11.49)–(11.56), becomes as follows:

$$G_v(s) = \frac{1}{\hat{V}_s(s)} \frac{R_o}{Re\{\boldsymbol{Z}_{t1}(s)\} S_m^2 + sL_o + R_o} Re\{\hat{\boldsymbol{V}}_{t2}(s)\} \Big|_{\hat{S}_m(s)=\hat{\phi}_S(s)=0} \tag{11.59}$$

A detail procedure of (11.59) is available in Appendix.

The amplitude frequency response of the example converter can be obtained from (11.59), as follows:

$$|G_v(\omega_c)| \equiv |G_v(s)|_{s=j\omega_c, \omega=\omega_s}$$
$$= S_m R_o \frac{\left|\cos\phi_S \left\{1 - (\omega_c^2 + \omega_s^2) L_s C_s\right\} - j2 \sin\phi_S \omega_s \omega_c L_s C_s\right|}{\left|j\omega_c L_s \left\{1 + (\omega_s^2 - \omega_c^2) L_s C_s\right\} S_m^2 + (j\omega_c L_o + R_o) \left[\left\{1 - (\omega_c^2 + \omega_s^2) L_s C_s\right\}^2 - 4\omega_s^2 \omega_c^2 L_s^2 C_s^2\right]\right|} \tag{11.60}$$

Note that ω_c is a variable control angular frequency, whereas ω_s is the fixed source voltage angular frequency, and that the frequency response of the complex Laplace transfer function can be calculated by letting $s = j\omega_c$, just as in the conventional Laplace transformation case. Other small signal transfer functions, though not shown here, can also be obtained in ways similar to those used in (11.59) and (11.60).

As shown in Fig. 11.11, this theoretical calculation of the voltage gain (11.60) is well within ±0.1 from the time domain simulation result, in which a small

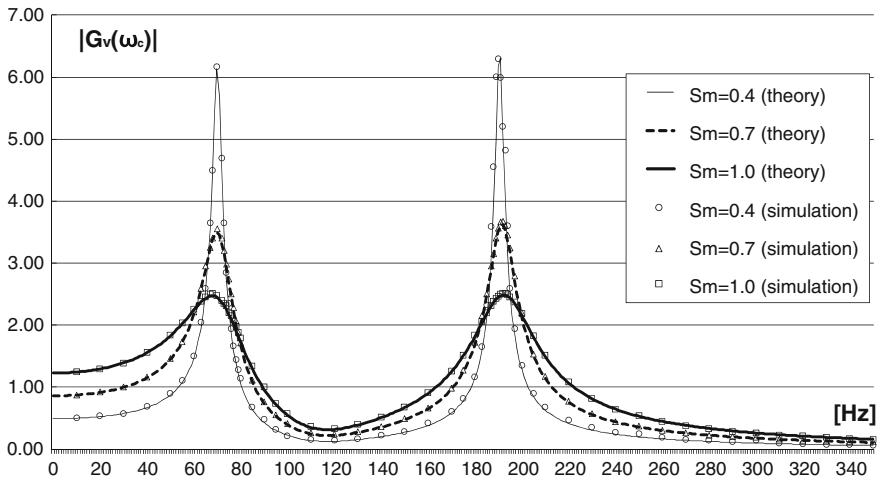

Fig. 11.11 Simulation results for the small signal frequency response of the amplitude gain for the example converter of Fig. 11.2a. ($\boldsymbol{V}_s = 440\angle 0$ $\phi_{VS} = \frac{\pi}{12}$ $f_s = 60$ Hz $L_s = 5$ mH $C_s = 300$ μF $L_o = 3$ mH $R_L = 10\ \Omega$)

perturbation signal was inserted into the source voltage using the circuit parameters of (11.57) except for the turn-ratio. The errors stem from the inaccurate measurements of the simulated output voltages, in which some harmonic ripples remained. It is found that there are two poles at 68–70 Hz and 191–193 Hz, which roughly correspond to the difference between and the addition of the input filter resonance frequency 130 Hz and the source frequency 60 Hz. This can be explained by noting that the modulating control signal over the source voltages generates frequencies of the difference and the addition of each frequency and these frequencies resonate with the input filter.

There are potential applications of the proposed Laplace phasor transformation to the dynamic characterization of AC converters such as renewable energy conversions [40–44], which would not be possible to analyze of close form by the conventional techniques. The AC converters shall be manipulated like conventional circuits by the proposed theory.

11.4 Concluding Remarks

The application of the complex Laplace transformation to a phasor transformed circuit for the dynamics characterization was performed and selectively verified by simulations. Together with the static analysis theory for AC converters [33], the general unified phasor transformation theory is now completed by the proposed Laplace phasor transformation in this chapter. Any linear time-varying AC converters with multiple phases and multiple switches can be substituted with a complex circuit including a complex transformer, and can be thoroughly analyzed by the proposed theory.

The applications of other linear transformations such as Fourier transformation and z-transformation to the phasor transformed circuits will be quite challenging. Furthermore, the extension of the proposed Laplace phasor transformation to the area wherever sinusoidal oscillation occurs, i.e. RF electronic circuits, mechanical vibration controls, and musical instrument designs must be interesting and fruitful. They are left for further works.

Appendix

The real part operations in (11.36) and (11.37) are performed respectively as follows.

$$
\begin{aligned}
Re\{\boldsymbol{V_{tl}}(s)\boldsymbol{S_m^*}\} &= Re\left\{\frac{\boldsymbol{V_s}(s)\boldsymbol{S_m^*}}{1+(sL_s+j\omega L_s)(sC_s+j\omega C_s)}\right\} = Re\left\{\frac{\boldsymbol{V_s}(s)\boldsymbol{S_m^*}}{1+(s^2-\omega^2)L_sC_s+j2\omega sL_sC_s}\right\} \\
&= Re\left\{\frac{\boldsymbol{V_s}(s)\boldsymbol{S_m^*}\{1+(s^2-\omega^2)L_sC_s-j2\omega sL_sC_s\}}{\{1+(s^2-\omega^2)L_sC_s+j2\omega sL_sC_s\}\{1+(s^2-\omega^2)L_sC_s-j2\omega sL_sC_s\}}\right\} \\
&= \frac{Re\{\boldsymbol{V_s}(s)\boldsymbol{S_m^*}\{1+(s^2-\omega^2)L_sC_s-j2\omega sL_sC_s\}\}}{\{1+(s^2-\omega^2)L_sC_s\}^2+4\omega^2s^2L_s^2C_s^2} \\
&= \frac{Re\{\boldsymbol{V_s}(s)\boldsymbol{S_m^*}\}\{1+(s^2-\omega^2)L_sC_s\}+Im\{\boldsymbol{V_s}(s)\boldsymbol{S_m^*}\}2\omega sL_sC_s}{\{1+(s^2-\omega^2)L_sC_s\}^2+4\omega^2s^2L_s^2C_s^2}
\end{aligned}
\tag{11.61}
$$

$$
\begin{aligned}
Re\{\boldsymbol{Z_{tl}}(s)\} &= Re\left\{\frac{sL_s+j\omega L_s}{1+(sL_s+j\omega L_s)(sC_s+j\omega C_s)}\right\} \\
&= \frac{Re\{(sL_s+j\omega L_s)\{1+(s^2-\omega^2)L_sC_s-j2\omega sL_sC_s\}\}}{\{1+(s^2-\omega^2)L_sC_s\}^2+4\omega^2s^2L_s^2C_s^2} \\
&= \frac{sL_s\{1+(s^2-\omega^2)L_sC_s\}+(\omega L_s)2\omega sL_sC_s}{\{1+(s^2-\omega^2)L_sC_s\}^2+4\omega^2s^2L_s^2C_s^2} \\
&= \frac{sL_s\{1+(s^2+\omega^2)L_sC_s\}}{\{1+(s^2-\omega^2)L_sC_s\}^2+4\omega^2s^2L_s^2C_s^2}
\end{aligned}
\tag{11.62}
$$

References

1. Park CB, Lee SW, Rim CT (2012) Static and dynamic analyses of three-phase rectifier with LC input filter by laplace phasor transformation. IEEE ECCE 2012, pp 1570–1577
2. Novotny DW (1975) Switching function representation of polyphase inverters. In: IEEE industrial application society conference record, pp 823–831
3. Middlebrook R, Cuk S (1976) A general unified approach to modeling switching power converter stages. In: IEEE PESC, pp 18–34
4. Wood P (1979) General theory of switching power converters. In: IEEE PESC, pp 3–10
5. Alesina A, Venturini MGB (1981) Solid-state power conversion: A Fourier analysis approach to generalized transformer synthesis. IEEE Trans Circuits Syst CAS-28(4):319–330
6. Ngo KDT (1986) Low frequency characterization of PWM converter. IEEE Trans Power Electron PE-1:223–230
7. Vorperian V, Tymersky R, Lee FC (1989) Equivalent circuit models for resonant and PWM switches. IEEE Trans Power Electron PE-4(2):205–214
8. Rim CT, Hu DY, Cho GH (1990) Transformers as equivalent circuits for switches: general proofs and DQ transformation-based analyses. IEEE Trans Ind Appl 26(4):777–785
9. Rim CT, Cho GH (1990) Phasor transformation and its application to the DC/AC analyses of frequency phase-controlled series resonant converters (SRC). IEEE Trans Power Electron 5:201–211
10. Vorperian V (1990) Simplified analysis of PWM converters using the model of the PWM switch, part I and part II. IEEE Trans Aerospace Electron Syst 26(3):490–505
11. Sanders SR, Noworolski JM, Liu XZ, Verghese GC (1991) Generalized averaging method for power conversion circuits. IEEE Trans Power Electron 6:251–259

12. Rim CT, Choi NS, Cho GC, Cho GH (1994) A complete DC and AC analysis of three-phase controlled-current rectifier using circuit DQ transformation. IEEE Trans Power Electron 9 (4):390–396
13. Mao HC, Boroyevich D, Lee CY (1998) Novel reduced-order small signal model of a three-phase rectifier and its application in control design and system analysis. IEEE Trans Power Electron 13(3):511–521
14. Chen J, Ngo KDT (2001) Graphical phasor analysis of three-phase PWM converters. IEEE Trans Power Electron 16(5):659–666
15. Szczesniak P, Fedyczak Z, Klytta M (2008) Modeling and analysis of a matrix-reactance frequency converter based on buck-boost topology by DQ0 transformation. In: 13th international power electronics and motion control conference (EPE-PEMC 2008), pp 165–172
16. Kwak S, Kim T (2009) An integrated current source inverter with reactive and harmonic power compensators. IEEE Trans Power Electron 24(2):348–357
17. Yin B, Oruganti R, Panda SK, Bhat AKS (2009) A simple single- input-single-output (SISO) model for a three-phase rectifier. IEEE Trans Power Electron 24(3):620–631
18. Sun Jian (2009) Small-signal methods for AC distributed power systems–a review. IEEE Trans Power Electron 24(11):2545–2554
19. Valdivia V, Barrado A, Laazaro A, Zumel P, Raga C, Fernandez C (2009) Simple modeling and identification procedures for "Black-Box" behavioral modeling of power converters based on transient response analysis. IEEE Trans Power Electron 24(12):2776–2790
20. Sun Jian, Bing Zhonghui, Karimi KJ (2009) Input impedance modeling of multi pulse rectifiers by harmonic linearization. IEEE Trans Power Electron 24(12):2812–2820
21. Dannehl J, Fuchs F, Thøgersen P (2010) PI state space current control of grid-connected PWM converters with LCL filters. IEEE Trans Power Electron 25(9):2320–2330
22. Bucknall R, Ciaramella K (2010) On the conceptual design and performance of a matrix converter for marine electric propulsion. IEEE Trans Power Electron 25(6):1497–1508
23. Kim S, Yoon Y, Sul S (2010) Pulse width modulation method of matrix converter for reducing output current ripple. IEEE Trans Power Electron 25(10):2620–2629
24. Barazarte R, González G, Ehsani M (2010) Generalized gyrator theory. IEEE Trans Power Electron 25(7):1832–1837
25. Steinmetz CP (1894) Complex quantities and their use in electrical engineering. In: Proceedings of AIEE international electrical congress. Chicago, IL, pp 33–74
26. Rim CT (1990) A complement of imperfect phasor transformation, In: Korea power electronics conference. Seoul, pp 159–163
27. Ben-Yaakov S, Glozman S, Rabinovici R (2001) Envelope simulation by spice-compatible models of linear electric circuits driven by modulated signals. IEEE Trans Ind Appl 37 (2):527–533
28. Yin Y, Zane R, Glaser J, Erickson RW (2003) Small-signal analysis of frequency-controlled electronic ballasts. IEEE Trans Circ Syst I Fundam Theory Appl 5(8)
29. Ye Z, Jain PK, Sen PC (2009) Phasor-domain modeling of resonant inverters for high-frequency AC power distribution systems. IEEE Trans Power Electron 24(4):911–924
30. Mattavelli P, Stanković AM, Verghese GC (1999) SSR analysis with dynamic phasor model of thyristor-controlled series capacitor. IEEE Trans Power Syst 14:200–208
31. Stanković AM, Sanders SR, Aydin T (2002) Dynamic phasors in analysis of unbalanced polyphase AC machines. IEEE Trans Energy Convers 17(1):107–113
32. de la O Serna JA (2007) Dynamic phasor estimates for power system oscillations. IEEE Trans Instrum Meas 56(5):1648–1657
33. Rim CT (2011) Unified general phasor transformation for AC converters. IEEE Trans Power Electron, to be published. Available: http://ieeexplore.ieee.org/xpls/abs_all.jsp?arnumber=5699928
34. Paley RC, Wiener N (1934) Fourier transforms in the complex domain, vol 19. American Mathematical Society Colloquium Publications
35. Deakin MAB (1992) The ascendancy of the laplace transform and how it came about. Arch Hist Exact Sci 44(3):265–286

36. Steven WS (1997) The scientists & engineers guide to Digital Signal Processing. California Technical Publishing, San Diego, pp 567–604
37. Bayan N, Erfani S (2005) Frequency analysis of linear time-varying systems: a new perspective. In: Proceedings of IEEE Midwest symposium on circuits and systems, pp 1494–1497
38. Bayan N, Erfani S (2007) Laplace transform approach to analysis and synthesis of Bessel type linear time-varying systems. In: Proceedings of IEEE midwest symposium on circuits and systems, pp 919–923
39. Erfani S (2007) Extending laplace and fourier transforms and the case of variable systems: a personal perspective. In: Proceedings of IEEE signal processing long island section. Available: http://www.ieee.li/pdf/viewgraphs/laplace.pdf
40. Billinton R, Gao Y (2008) Multistate wind energy conversion system models for adequacy assessment of generating systems incorporating wind energy. IEEE Trans Energy Convers 23 (1):163–170
41. Dehghan SM, Mohamadian M, Varjani AY (2009) A new variable-speed wind energy conversion system using permanent-magnet synchronous generator and Z-source inverter. IEEE Trans Energy Convers 24(3):714–724
42. Changchien SK, Liang TJ, Chen JF, Yang LS (2009) Novel high step-up DC-DC converter for fuel cell energy conversion system. IEEE Trans Energy Convers 24(3):714–724
43. Lopez O, Freijedo FD, Yepes AG, Fernandez-Comesana P, Malvar J, Teodorescu R, Doval-Gandoy J (2010) Eliminating ground current in a transformer less photovoltaic application. IEEE Trans Energy Convers 25(1):140–147
44. Beltran B, Ahmed-Ali T, Benbouzid MEH (2010) Sliding mode power control of variable-speed wind energy conversion systems. IEEE Trans Ind Elec 57(6):2007–2017

Chapter 12
Dynamics of Inductive Power Transfer Systems

As an example of applying the Laplace phasor transform to a practical problem solving a large signal dynamic model of the inductive power transfer system (IPTS) for on-line electric vehicles (OLEVs) is explained in this chapter. As an example of applying the Laplace phasor transform to a practical problem solving a large signal dynamic model of the inductive power transfer system (IPTS) for on-line electric vehicles (OLEVs) is explained in this chapter.

With the help of the dynamic model, the effect of the output capacitor and load resistance variation on the transient response of the IPTS is analyzed. The maximum pick-up current and the output voltage for an abrupt in-rush of the OLEV are examined by both the proposed analysis and simulations, and verified through good agreement with experiments. Thus, it is found that the voltage and current ratings of the pick-up remain relatively constant regardless of the load resistance. A lot of this chapter is written based on the paper of ours [1].

12.1 Introduction

The depletion of petroleum and the global warming make the electric vehicle (EV) be the most promising means of transport, and various types of EVs such as hybrid electric vehicle (HEV), plug-in HEV (PHEV), and pure EV (PEV) have been developed.

The high price, large size, and relatively short distance per charge of the battery in the EVs, however, make it difficult to commercialize them. To alleviate the battery problems, the roadway-powered EVs (RPEVs) which are based on the inductive power transfer system (IPTS) have been developed [2–12]. Recently, the on-line electric vehicle (OLEV), one of the most advanced RPEVs so far, has been developed and successfully deployed at various public sites [6–8]. Its concept is shown in Fig. 12.1 and the overall schematic of the IPTS is shown in Fig. 12.2.

C.T. Rim, *Phasor Power Electronics*, KAIST Research Series,
DOI 10.1007/978-981-10-0536-7_12

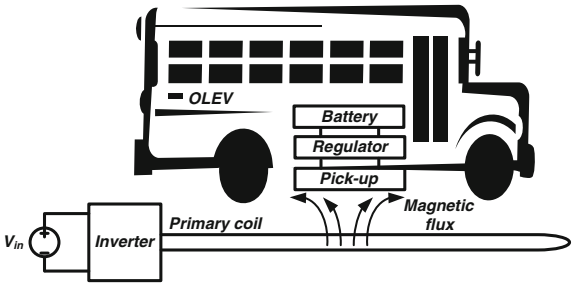

Fig. 12.1 The concept of the OLEV system

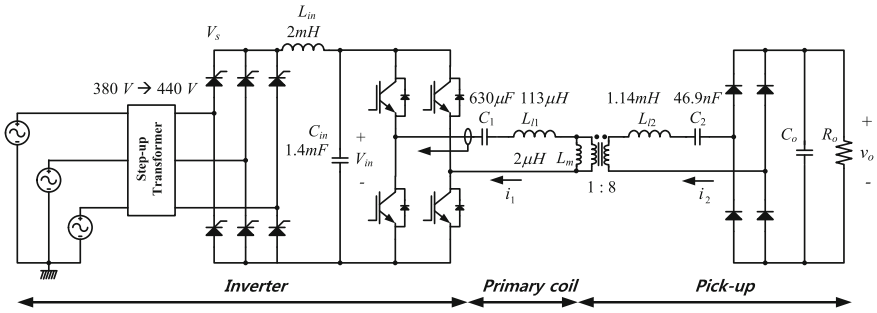

Fig. 12.2 The overall schematic of the IPTS for the OLEV. The on-board regulator and battery is replaced with R_o

To improve the power transfer efficiency, the "fully resonated current source IPTS" was proposed for the OLEV [10–12]. The IPTS constantly controls the primary coil current i_1, and the magnetizing inductance L_m and leakage inductance L_{l2} of the pick-up are resonated with the secondary capacitor C_2. By doing so, the output voltage of the IPTS is nearly constant for various load conditions. The pick-up current, however, is highly fluctuated because of the abrupt in-rush movement of the vehicle and the rapid load current change. The pick-up undergoes severe voltage stress and breakdown may occur in the capacitors during this transient state. One of the worst case scenarios is that the LC resonant tank of the pick-up, i.e. i_2, is maximally energized by the inverter whereas the output voltage is zero; this is a very probable situation in practice when a fast OLEV rushes into the primary coil. At this case, i_2 can be largely fluctuated and its maximum value should be clearly identified in order to design the ratings of the C_2. Hence, not only the static analysis but also the large signal dynamic analysis on i_2 is quite essential for various load conditions and circuit parameters.

To find an appropriate dynamic model, the recently proposed Laplace phasor transform theory [13], which was developed for the dynamic analysis of phasored circuits [14–19], has been adopted in this chapter. The conventional DQ

transformations [20, 21] could be used to analyze AC systems if the system order is less than three, however, it is nearly impossible to obtain the dynamics of the IPTS by the traditional techniques because the system order is very high, as identified from Fig. 12.2. On the other hand, the linear time-invariant dynamic model for a very high order AC system can be easily obtained by the unified general phasor transform [19, 13], and the analysis of the phasor transformed circuit is straightforward because conventional circuit analysis techniques such as Kirchhoff's voltage and current laws, Thevenin's theorem, and Norton's theorem can be applied to the phasored circuits.

In this chapter, the Laplace phasor transform [13] was firstly applied to the practical real system, and the large signal dynamic model for the pick-up current of the OLEV is fully developed.

12.2 Large Signal Dynamic Model for the OLEV IPTS

12.2.1 Operation Principle of the OLEV

The key operation concept of the IPTS for OLEV is to control the primary coil current i_1 as a constant current source, where the C_2 is resonated with $n^2L_m + L_{l2}$ to maximize power transfer. Under this condition, the output voltage V_o in the steady state is equal to $n\omega_s L_m I_1$ [12], where the ω_s is the switching angular frequency and I_1 is the magnitude of the primary coil current i_1 in the steady state. Because the primary current I_1 is constant regardless of the load condition, the output voltage of the IPTS of an OLEV is kept constant; hence, this IPTS can effectively supply wireless power to multiple OLEVs on the primary coil simultaneously.

In addition, the intrinsic resonant frequency ω_i of the $L_m + L_{l1}$ and the C_1 is set to a slightly lower frequency than the inverter switching frequency ω_s so that the IPTS can be always inductive in the primary coil, which results in the zero voltage switching (ZVS) of the inverter [12]. Because the pick-up and primary coil of the IPTS is loosely coupled, the L_m is much lower than the L_{l1}. Therefore, the ω_i does not vary largely in accordance with the number of OLEVs on the primary rail and the air-gap between the pick-up and primary coil; hence, the stable control of the i_1 is possible at the fixed switching frequency.

12.2.2 Large Signal Dynamic Analysis of the Pick-up Current

To develop the large signal model of the pick-up current i_2, the Laplace phasor transform [13] which converts the rotatory AC domain circuit to the stationary phasor domain circuit in the frequency domain is adopted. For example, the Laplace

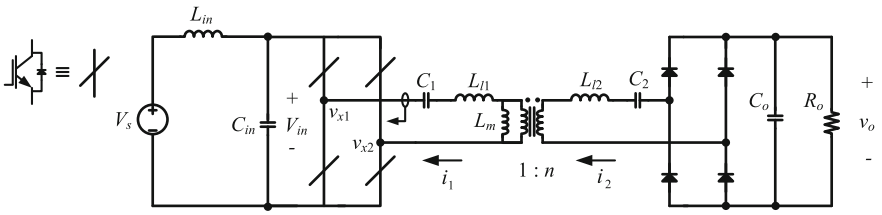

Fig. 12.3 Simplified overall schematic of the IPTS for the OLEV

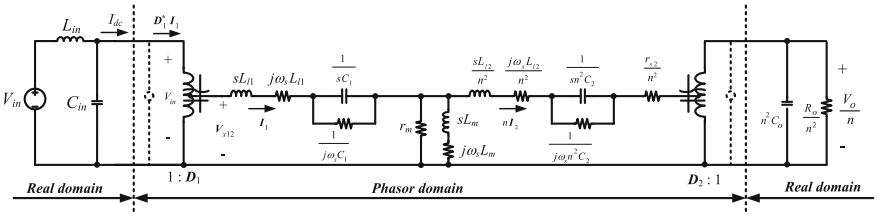

Fig. 12.4 The overall Laplace phasor transformed equivalent circuit of the IPTS from source side, removing the transformer. The *bold letters* indicate the complex variables in the Laplace domain. The $\boldsymbol{D}_1$ and $\boldsymbol{D}_2$ indicate the complex turn ratios of the complex transformers for the inverter and diode rectifier, respectively

phasor transform converts an inductor in the rotatory AC domain shown in Fig. 12.3 can be transformed into an inductor with an imaginary resistor in the stationary phasor domain as shown in Fig. 12.4. The inductor rotatory circuit equation is

$$L_{l1}\frac{di_1}{dt} = v_{L1}, \tag{12.1}$$

where the v_{L1} is the voltage across the inductor. By applying the phasor transformation, the dynamic phasor $\boldsymbol{I}_1$ and $\boldsymbol{V}_{L1}$ can be obtained from

$$i_1 \equiv Re\{\sqrt{2}\boldsymbol{I}_1 e^{j\omega_s t}\}, \quad v_{L1} \equiv Re\{\sqrt{2}\boldsymbol{V}_{L1} e^{j\omega_s t}\}. \tag{12.2}$$

Note that the phasors in (12.2) are not stationary but dynamic so that they are time-varying complex numbers. By applying (12.2) to (12.1), the relationship between the $\boldsymbol{V}_{L1}$ and the $\boldsymbol{I}_1$ is obtained as

$$L_{l1}\frac{d\boldsymbol{I}_1}{dt} + j\omega_s L_{l1}\boldsymbol{I}_1 = \boldsymbol{V}_{L1}. \tag{12.3}$$

Therefore the inductor L_{l1} in the rotatory AC domain converts into inductor L_{l1} with an imaginary resistor $j\omega_s L_{l1}$ in the stationary phasor [19]. By applying the Laplace transformation [13] into the first term of (12.3), the (12.3) can be converted as

$$sL_{l1}\boldsymbol{I}_1 + j\omega_s L_{l1}\boldsymbol{I}_1 = \boldsymbol{V}_{L1}. \tag{12.4}$$

In this way, the other rotatory domain elements can be converted into the stationary domain. The overall phasor transformed circuit of the IPTS for the OLEV is shown in Fig. 12.4. The dotted small circles connect the real domain and the phasor domain, and it is called as "real part operator" [19]. In Fig. 12.4, the complex transformer turn-ratio $\boldsymbol{D}_1$, i.e. $D_1 e^{j\theta_1}$ where D_1 is the voltage conversion ratio and θ_1 is the phase difference between the source voltage V_{in} and the $\boldsymbol{V}_{x12}$, is defined as

$$\boldsymbol{V}_{x12} = V_{in}\boldsymbol{D}_1, \quad I_{dc} = Re(\boldsymbol{I}_1\boldsymbol{D}_1^*), \tag{12.5}$$

where the detailed transform process is explained in [13, 19]. In this process, the real part operator $Re()$ regards the Laplacian 's' as a real number, and it was named 'pseudo real Laplacian' [13]. For example, $Re(sL + R + j\omega L) = sL + R$ is valid for this pseudo real Laplacian. In Fig. 12.4, the r_m indicates the side effects of the coils of the IPTS, which include the iron loss and eddy current loss of the coils. The r_{s2} includes the copper loss of the pick-up coil and the dynamic resistance of the bridge diodes. Because the inverter primary coil current i_1 is constantly controlled by the inverter, it becomes a constant current source, as shown in Fig. 12.5a. In general, the system dynamics of the IPTS is much slower than the switching period of the inverter; hence, the absolute value of Laplacian 's' can be artificially much smaller than the ω_s as follows [16];

$$|s| \ll \omega_s. \tag{12.6}$$

Therefore, the impedance of the pick-up coil $\boldsymbol{Z}_2$ shown in Fig. 12.5a can be derived using (12.6) as

$$\boldsymbol{Z}_2 = \frac{sL_{l2}}{n^2} + \frac{j\omega_s L_{l2}}{n^2} + \frac{1}{sn^2C_2 + j\omega_s n^2 C_2} = \frac{sL_{l2}}{n^2} + \frac{j\omega_s L_{l2}}{n^2} + \frac{1}{j\omega_s n^2 C_2} \cdot \frac{1}{1 + \frac{s}{j\omega_s}}. \tag{12.7}$$

By the condition (12.6), it can be approximately as follows:

$$\begin{aligned} \boldsymbol{Z}_2 &\cong \frac{sL_{l2}}{n^2} + \frac{j\omega_s L_{l2}}{n^2} + \frac{1}{j\omega_s n^2 C_2}\left(1 - \frac{s}{j\omega_s}\right) \\ &= \frac{sL_{l2}}{n^2} + \frac{j\omega_s L_{l2}}{n^2} + \frac{1}{j\omega_s n^2 C_2} + \frac{s}{\omega_s^2 n^2 C_2}. \end{aligned} \tag{12.8}$$

In (12.8), the last term can be expressed as follow:

$$\frac{s}{\omega_s^2 n^2 C_2} = sL_{eq} \tag{12.9}$$

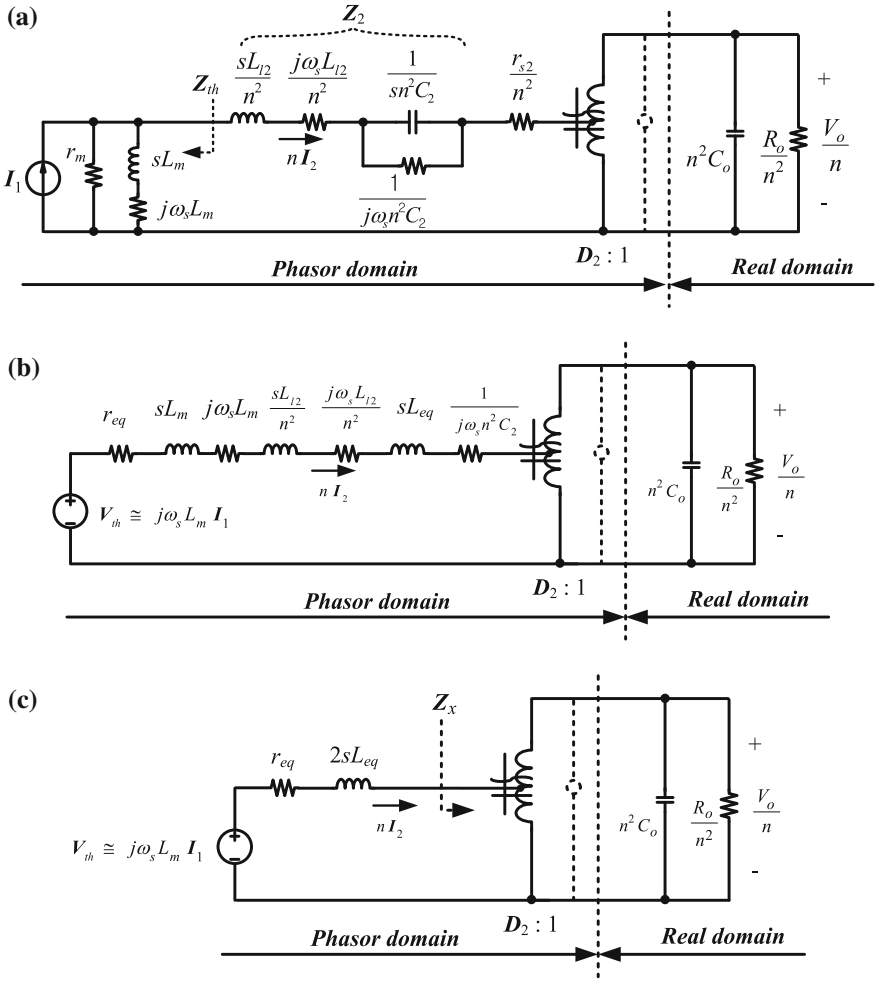

Fig. 12.5 Dynamic equivalent circuits of the IPTS in the complex Laplace domain. **a** Equivalent circuit of the IPTS assuming a constant current source. **b** More simplified and approximated circuit for the source side. **c** The most simplified circuit in the resonant condition

where

$$L_{eq} = \left(L_m + \frac{L_{l2}}{n^2}\right) \cdot \left(\frac{\omega_{r2}}{\omega_s}\right)^2, \quad \omega_{r2} = \frac{1}{\sqrt{(n^2 L_m + L_{l2})C_2}}. \tag{12.10}$$

To apply Thevenin's theorem to the dotted arrow region in Fig. 12.5a, the open circuit equivalent impedance is obtained as follows:

$$\boldsymbol{Z}_{th} = (sL_m + j\omega_s L_m)//r_m = \frac{sL_m + j\omega_s L_m}{1 + \frac{sL_m + j\omega_s L_m}{r_m}}. \tag{12.11}$$

Because the r_m is much larger than the $|j\omega_s L_m|$ or $|sL_m + j\omega_s L_m|$, (12.11) can be approximately represented as

$$\frac{sL_m + j\omega_s L_m}{1 + \frac{sL_m + j\omega_s L_m}{r_m}} \cong (sL_m + j\omega_s L_m)\left(1 - \frac{sL_m + j\omega_s L_m}{r_m}\right). \tag{12.12}$$

By applying the condition (12.6) to (12.12), it can be simplified as follows:

$$\boldsymbol{Z}_{th} \cong sL_m + j\omega_s L_m + \frac{\omega_s^2 L_m^2}{r_m}. \tag{12.13}$$

In addition, the Thevenin voltage source $\boldsymbol{V}_{th}$ shown in Fig. 12.5b is defined as

$$\boldsymbol{V}_{th} = \{(sL_m + j\omega_s L_m)//r_m\}\boldsymbol{I}_1. \tag{12.14}$$

Using (12.11)–(12.13), it can be approximately expressed as follows:

$$\boldsymbol{V}_{th} \cong \left(sL_m + j\omega_s L_m + \frac{\omega_s^2 L_m^2}{r_m}\right)\boldsymbol{I}_1. \tag{12.15}$$

Because $|sL_m + j\omega_s L_m|$ is much larger than $\frac{\omega_s^2 L_m^2}{r_m}$ so far as $r_m \gg \omega_s L_m$, and $|sL_m|$ is much smaller than $|j\omega_s L_m|$, the Thevenin voltage source of (12.15) can be simplified as follows:

$$\boldsymbol{V}_{th} \cong j\omega_s L_m \boldsymbol{I}_1. \tag{12.16}$$

In addition, the equivalent resistance r_{eq} shown in Fig. 12.5b is defined as follows:

$$r_{eq} = \frac{\omega_s^2 L_m^2}{r_m} + \frac{r_{s2}}{n^2}. \tag{12.17}$$

Therefore, the first approximated equivalent circuit is obtained from Fig. 12.5a as shown in Fig. 12.5b.

If the resonant angular frequency ω_{r2} in (12.10) is equal to the switching frequency ω_s, the equivalent inductance L_{eq} is equal to $L_m + \frac{L_{l2}}{n^2}$ and the most simplified equivalent circuit can be obtained, as shown in Fig. 12.5c. In this Fig., the dynamic model of i_2 can be derived from if the $\boldsymbol{Z}_x$ is known. To obtain the $\boldsymbol{Z}_x$, the

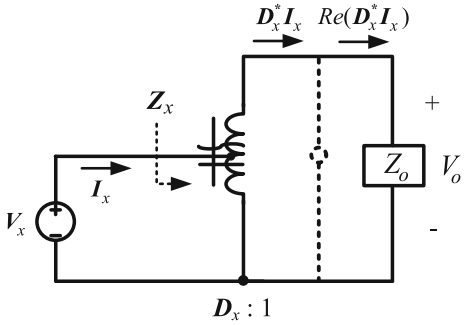

Fig. 12.6 The phasor transformed circuit of the diode rectifier and the output impedance

phasor transformed circuit of the diode rectifier and the output impedance Z_o is shown in Fig. 12.6. Because the diode rectifier is a sort of the current controlled rectifier (CSR), the phase of the test current $\boldsymbol{I}_x$ shown in Fig. 12.6 determines the phase of the complex transformer turn-ratio $\boldsymbol{D}_x$ as follows [16]:

$$\boldsymbol{I}_x = I_x e^{j\theta_x} \rightarrow \boldsymbol{D}_x = D_x e^{j\theta_x}, \quad D_x = \frac{2\sqrt{2}}{\pi} \tag{12.18}$$

Therefore, the test voltage $\boldsymbol{V}_x$ shown in Fig. 12.6 is determined as

$$\boldsymbol{V}_x = V_o \boldsymbol{D}_x, \tag{12.19}$$

and the $\boldsymbol{Z}_x$ shown in Fig. 12.6 is determined as follows:

$$\boldsymbol{Z}_x = \frac{\boldsymbol{V}_x}{\boldsymbol{I}_x} = \frac{V_o \boldsymbol{D}_x}{\boldsymbol{I}_x} = \frac{Re(\boldsymbol{I}_x \boldsymbol{D}_x^*) Z_o \cdot \boldsymbol{D}_x}{\boldsymbol{I}_x} \quad \text{where } Z_o = \frac{R_o}{n^2(1 + sC_o R_o)} \tag{12.20}$$

From (12.18), $\boldsymbol{I}_x \boldsymbol{D}_x^*$ can be derived as

$$\boldsymbol{I}_x \boldsymbol{D}_x^* = I_x e^{j\theta_x} \cdot D_x e^{-j\theta_x} = I_x D_x = Re(\boldsymbol{I}_x \boldsymbol{D}_x^*). \tag{12.21}$$

Applying (12.21) to (12.20), the $\boldsymbol{Z}_x$ is finally determined as

$$\boldsymbol{Z}_x = \frac{\boldsymbol{I}_x \boldsymbol{D}_x^* Z_o \cdot \boldsymbol{D}_x}{\boldsymbol{I}_x} = D_x^2 Z_o. \tag{12.22}$$

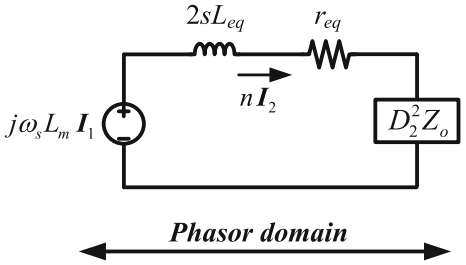

Fig. 12.7 The final simplified phasor transformed circuit of the IPTS

The final equivalent circuit can be derived, as shown in Fig. 12.7, and the phasor $\boldsymbol{I}_2$ can be obtained as

$$\boldsymbol{I}_2 = jG_2 \cdot \frac{1 + sC_oR_o}{\frac{s^2}{\omega_2^2} + \frac{s}{Q_2\omega_2} + 1}\boldsymbol{I}_1 \tag{12.23}$$

where

$$G_2 = \frac{n\omega_s L_m}{D_2^2 R_o + n^2 r_{eq}}, \quad \omega_2 = \frac{1}{n}\sqrt{\frac{D_2^2 R_o + n^2 r_{eq}}{2L_{eq}C_oR_o}}$$

$$Q_2 = \frac{\sqrt{(D_2^2 R_o + n^2 r_{eq})(2L_{eq}C_oR_o)}}{n(2L_{eq} + C_oR_o r_{eq})}, \quad \zeta_2 = \frac{1}{2Q_2} = \frac{n(2L_{eq} + C_oR_o r_{eq})}{2\sqrt{(D_2^2 R_o + n^2 r_{eq})(2L_{eq}C_oR_o)}}, \tag{12.24}$$

and the time domain expression of (12.23) is obtained as

$$\hat{i}_2(t) = G_2\hat{i}_1(t) - G_2\hat{i}_1(t) \cdot \frac{\cosh\frac{\sqrt{(1/4-Q_2^2)\cdot\omega_2 t}}{Q_2} + \frac{Q_2\left(\sinh\frac{\sqrt{(1/4-Q_2^2)\cdot\omega_2 t}}{Q_2}\right)\cdot\left(\frac{\omega_2 - C_oR_oQ_2\omega_2^2}{Q_2} - \frac{\omega_2}{2Q_2}\right)}{\omega_2\sqrt{1/4-Q_2^2}}}{\exp\frac{\omega_2 t}{2Q_2}} \tag{12.25}$$

where

$$\hat{i}_1(t) = \begin{cases} I_1 & t \geq 0 \\ 0 & t < 0 \end{cases}. \tag{12.26}$$

The $\hat{i}_1(t)$ and $\hat{i}_2(t)$ are the envelop time domain variables of the i_1 and i_2 respectively.

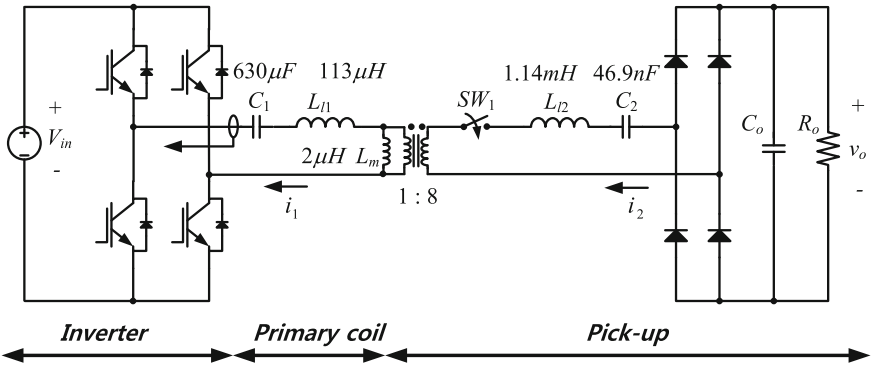

Fig. 12.8 The experiment setup for the pick-up current dynamics study

The presented model is also applicable to develop the small signal dynamic model. Because the turn-ratio of the complex transformer is time-varying when the complex transformer is used as the control driver, the complex transformer is non-linear in that case. Therefore, the linearization by perturbing the control variables is necessary to develop the small signal dynamic model and the detailed process of the perturbation is shown in [13, 17].

12.3 Experimental Verifications

The OLEV system was implemented as shown in Fig. 12.8a. To simplify the experiment, the discrete component L_{l1}, L_m, and L_{l2} were used instead of the real primary rail and the pick-up which are used on the OLEV as shown in Fig. 12.8b, and the values of the inductance L_{l1}, L_m, and L_{l2} were determined by reference [12]. To experiment the pick-up current dynamics, the switch SW_1 shown in Fig. 12.8a was inserted in the pick-up coil and the step response of the pick-up current was measured. The inverter constantly controls the primary coil current i_1. To guarantee the zero voltage switching (ZVS) of the inverter, the resonant frequency of the primary coil was set to slightly lower than the switching frequency 20 kHz of the inverter. To check the resonant conditions of the pick-up coil, the steady state wave forms were measured, as shown in Fig. 12.9. As expected in (12.23), the phase difference between the i_1 and i_2 was about $\pi/2$, as shown in Fig. 12.9. This means the impedance of the $L_m + \frac{L_{l2}}{n^2}$ is successfully canceled by the impedance of the $n^2 C_2$.

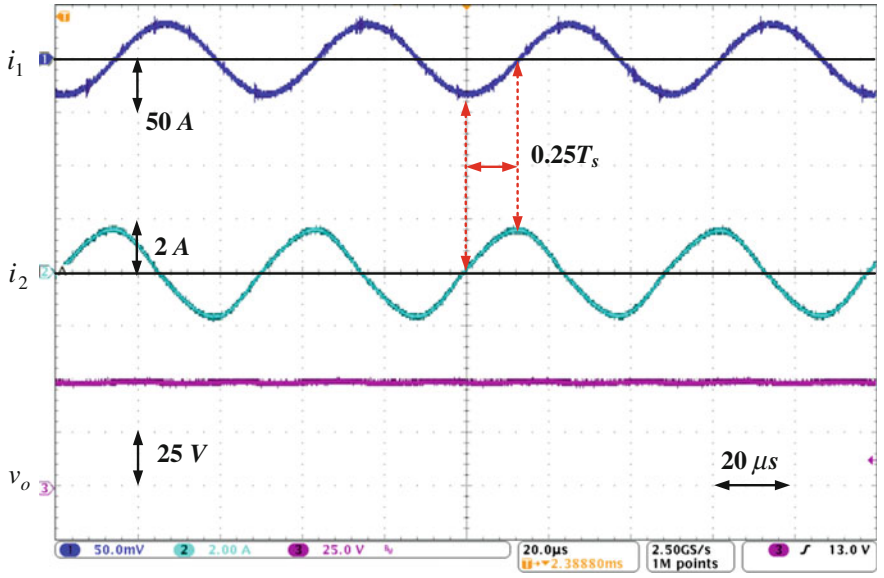

Fig. 12.9 The steady state waveforms for the primary coil current i_1, pick-up current i_2, and the output voltage v_o. The T_s is the period of the switching frequency ω_s

Initially, the SW_1 was open and the i_1 was set to 40 A_{peak}. After the i_1 was stabilized to its steady state value, the SW_1 was turned on and the dynamics of the i_2 was observed for various load conditions, as shown in Fig. 12.10. For comparison, the simulation results and the step response of (12.23) were shown in Fig. 12.11. The step response of (12.23) is well matched with the simulated pick-up current by PSIM. In that process, the r_{eq} was found by comparing the experimental waveforms, and it is about 0.15 Ω. The comparison plot for the maximum and the steady state current of the i_2 is shown in Fig. 12.12.

The experimental results and the step response of (12.23) show that the maximum value of the pick-up current i_2 is varying with the load conditions. The maximum value increases with larger output capacitance for a given output resistance. The remarkable characteristic of the IPTS from the results is that the maximum values of the pick-up current for different output resistances are not significantly changed for a given output capacitor, as shown in Fig. 12.13. This feature is quite advantageous for the robust IPTS development because the rated voltage of the C_{l2} does not largely change by the output resistance.

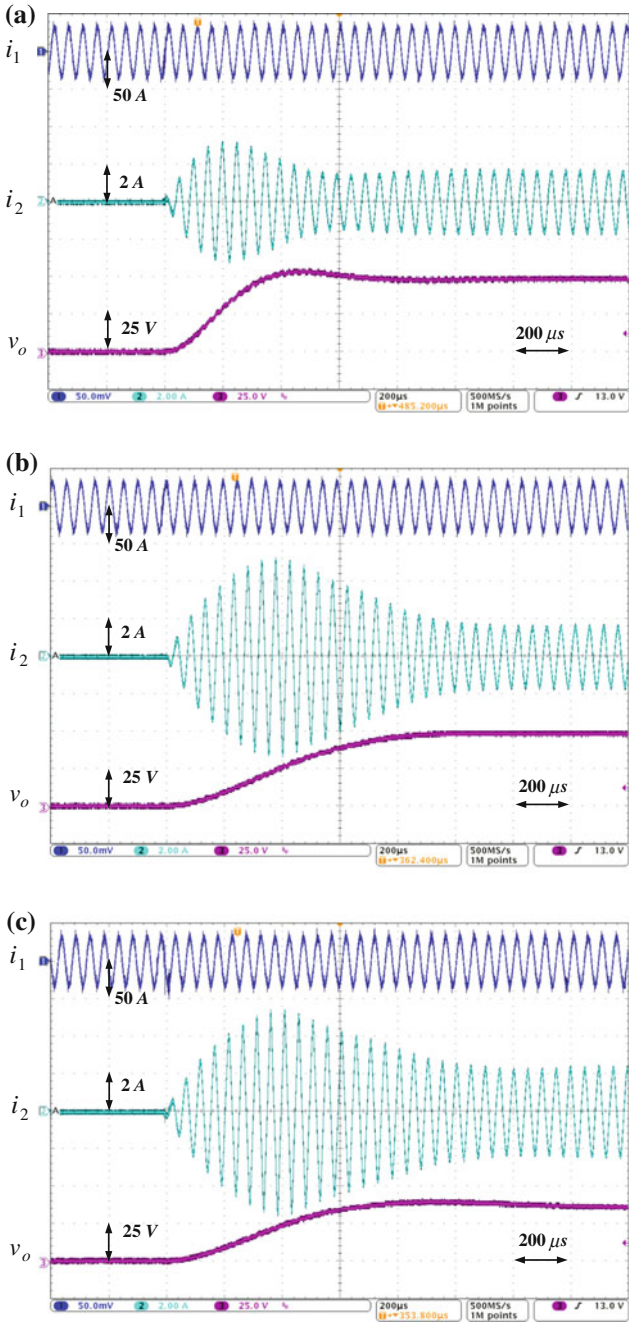

Fig. 12.10 The measured step response of the pick-up current i_2 and the out voltage v_o for various load conditions. **a** $R_o = 50\ \Omega$, $C_o = 6.6\ \mu$F. **b** $R_o = 50\ \Omega$, $C_o = 27.1\ \mu$F. **c** $R_o = 25\ \Omega$, $C_o = 27.1\ \mu$F

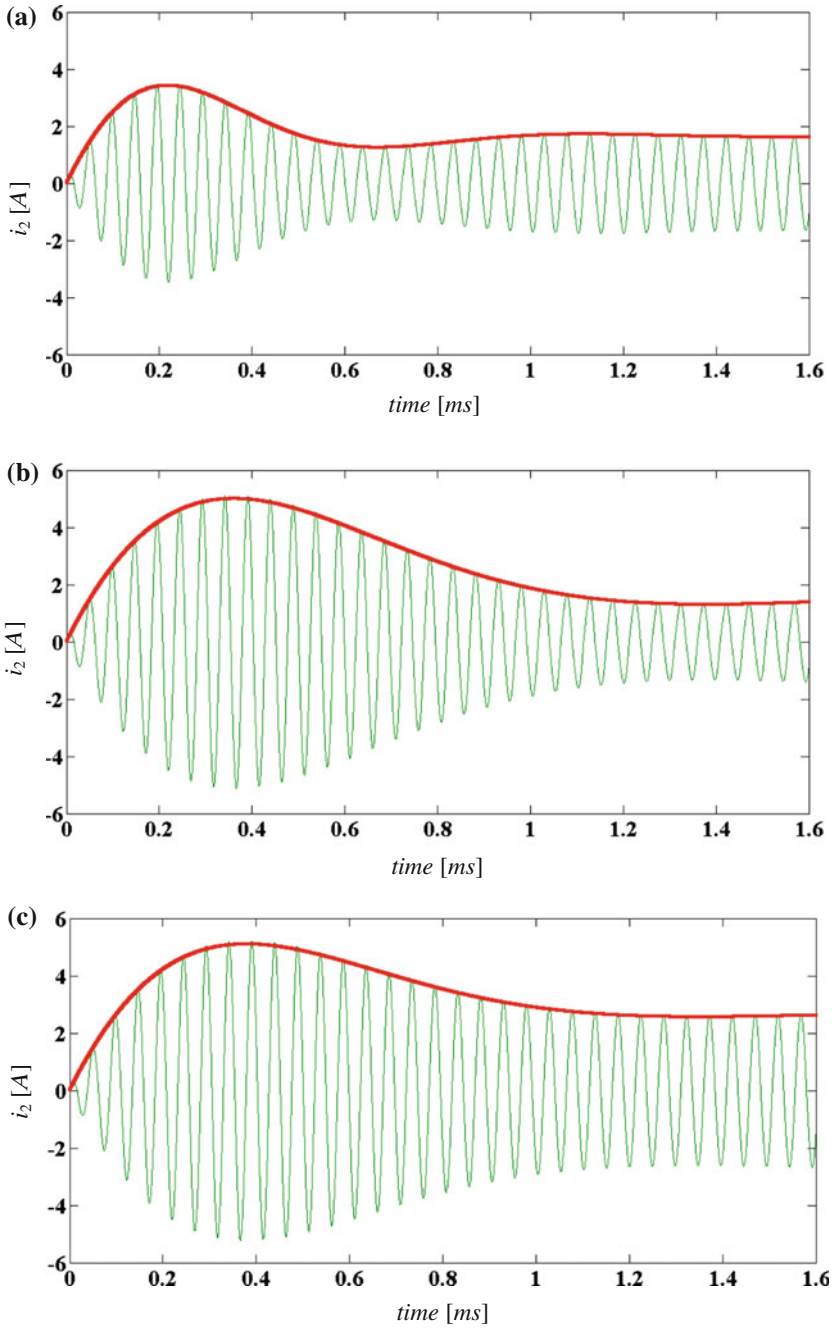

Fig. 12.11 The simulated step response (AC waveform) and the envelop waveform of the step response of (23) for the pick-up current i_2. **a** $R_o = 50\ \Omega$, $C_o = 6.6\ \mu F$. (b) $R_o = 50\ \Omega$, $C_o = 27.1\ \mu F$. **c** $R_o = 25\ \Omega$, $C_o = 27.1\ \mu F$

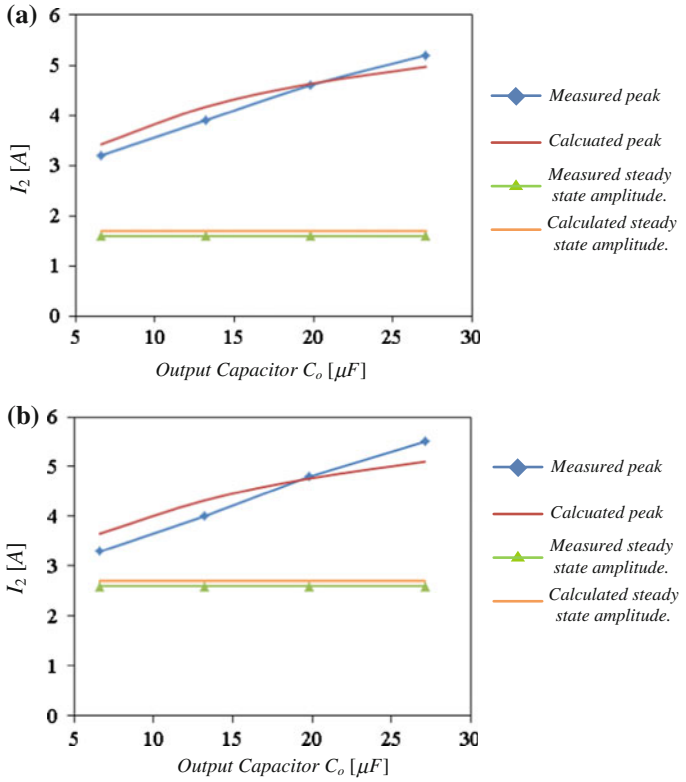

Fig. 12.12 The peak and steady state current values of the pick-up for various output capacitors. **a** R_o = 50 Ω. **b** R_o = 25 Ω

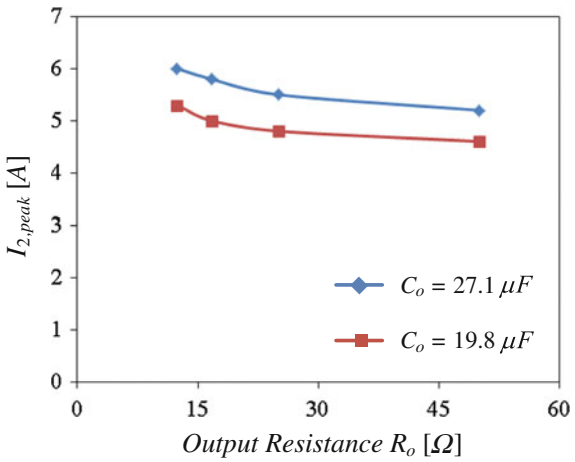

Fig. 12.13 The measured peak current of the pick-up current for various output resistances

12.4 Conclusions

The dynamic model for the IPTS of the OLEV has been fully developed and verified by simulations and experiments in this chapter. By applying the Laplace phasor transform first to the very high order IPTS, a very simple second order equivalent circuit could be obtained. With the help of this novel dynamic model, the maximum pick-up current during the transient state was successfully identified, and found to be relatively unchanged for various load resistances.

References

1. Lee S, Choi B, Rim CT (2013) Dynamics Characterization of the inductive power transfer system for on-line electric vehicles by laplace phasor transform. IEEE Trans Power Electron 28(12):5902–5909
2. Bolger JG, Kirsten FA, Ng LS (1978) Inductive power coupling for an electric highway system. In: Proceedings of IEEE 28th Vehicular Technology Society, vol 28, pp 137–144
3. Green AW, Boys JT (1994) 10 kHz inductively coupled power transfer concept and control. In Proceedings of 5th International Conference IEE Power Electron Variable-Speed Drivers, pp 694–699
4. Elliott GAJ, Boys JT, Green AW (1995) Magnetically coupled systems for power transfer to electric vehicles. In Proceedings of International Conference Power Electronics and Drive Systems, pp 797–801
5. Covic GA, Boys JT, Kissin MLG, LU HG (2007) A three-phase inductive power transfer system for roadway-powered vehicles. IEEE Trans Ind Electron 54(6):3370–3378
6. Lee SW, Huh J, Park CB, Choi NS, Cho GH, Rim CT (2010) On-line electric vehicle using inductive power transfer system. IEEE Energy Conversion Congress and Exposition, pp 1598–1601
7. Suh NP, Cho DH, Rim CT (2010) Design of on-line electric vehicle (OLEV). In: Plenary lecture at the 2010 CIRP Design Conference
8. Huh J, Rim CT (2011) KAIST wireless electric vehicles-OLEV, JSAE Annual Congress, invited paper
9. Lee SW, Lee WY, Huh J, Park CB, Rim CT (2011) Active EMF cancellation method for I-type pick-up of on-line electric vehicles. IEEE Applied Power Electronics Conference & Exposition (APEC), pp 1980–1983
10. Huh J, Lee BH, Lee WY, Cho GH, Rim CT (2011) Characterization of novel inductive power transfer systems for on-line electric vehicles. IEEE Applied Power Electronics Conference and Exposition, pp 1975–1979
11. Huh J, Lee SW, Park CB, Cho GH, Rim CT (2010) High performance inductive power transfer system with narrow rail width for on-line electric vehicles. IEEE Energy Conversion Congress and Exposition, pp 1598–1601
12. Huh J, Lee SW, Lee WY, Cho GH, Rim Chun T (2011) Narrow-width inductive power transfer system for online electrical vehicles. IEEE Trans Power Electron 26(12):3666–3679
13. Park C, Lee S, Cho GH, Rim CT (2012) Static and dynamic analyses of three-phase rectifier with LC input filter by Laplace phasor transformation.IEEE Energy Conversion Congress and Exposition, pp 1570–1577
14. Rim CT (1990) Analysis of linear switching systems using circuit transformations. Ph.D. dissertation, KAIST, Seoul

15. Rim CT, Hu DY, Cho GH (1990) Transformers as equivalent circuits for switches: General proofs and DQ transformation-based analyses. IEEE Trans Ind Appl 26(4):777–785
16. Rim CT, Cho GH (1990) Phasor transformation and its application to the DC/AC analyses of frequency phase-controlled series resonant converters (SRC). IEEE Trans Power Electron 5:201–211
17. Rim CT (1999) A complement of imperfect phasor transformation. Korea Power Electronics Conference, Seoul, pp 159–163
18. Rim CT, Choi NS, Cho GC, Cho GH (1994) A complete DC and AC analysis of three-phase controlled-current PWM rectifier using circuit DQ transformation. IEEE Trans Power Electron 9(4):390–396
19. Rim Chun T (2011) Unified general phasor transformation for AC converters. IEEE Trans Power Electron 26(9):2465–2475
20. White DC, Woodson HH (1959) Electromechanical Energy Conversion. Wiley, New York
21. Ngo KDT (1986) Low frequency characterization of PWM converter. IEEE Transactions on Power Electronics, vol PE-1, pp 223–230

Part VI
Phasored Power Electronics and Beyond

Throughout this book, the phasor model has been identified to be a useful tool for dealing with switching converters. In this last chapter, the applicability of the phasor model to other power electronics areas such as controllers, signal processors, power systems, and motors is explained. Furthermore, the general applicability of the phasor model is shown for other areas including mechanics and musical instruments. Finally, the future uses of power electronics are suggested.

Numerous studies of the application of phasor transformation to fields other than power electronics can be found in the literature. It will be challenging to apply the phasor transformation to quantum mechanics and stochastic processes of signal processing, work that remains for proactive readers and researchers.

Chapter 13
Phasor Transformers in Power Electronics and Beyond

As all switch set of a converter is identified as an electronic transformer with a complex turn-ratio, which is simply referred as 'phasor transformer' in this book, it can be said in general that power electronics deal with phasor transformers. Now the phasor transformers embrace not only converters, but also controllers, processors, power systems, and motors. This assertion that 'power electronics = phasor transformers' can be justified by the fundamental fact that "power electronics processes the power of a system, which results in the changes of amplitude, phase, and frequency of voltages and currents." Ideally, there is no power loss in the general power system, which includes converters, transformers, power lines, and motors. This means that the output power is ideally the same as input power, and that 'the power processor' is 'the phasor transformer.' Of course, this argument is true for a lossy power system, which results in a 'lossy' phasor transformer. DC converters and DC motors are regarded as special cases of phasor transformers with the turn-ratio of zero phase at zero frequency.

In this chapter, the applications of phasor transformation to other power electronics areas except for converters are explained for a few selected issues.

13.1 Complex Controllers and Phasored Signal Processing

A conventional controller in a converter system processes the rare signals coming from outputs and inputs, as shown in Fig. 13.1a.

In case of AC converters, the signals are of sinusoidal waveform, which must be transformed to DQ domain if an envelope control of signal is required, as shown in Fig. 13.2a. If not this case, the abc-to-dq conversion is not needed.

Different from the canonical controller where real variables are used for control, the new phasored controller uses complex variables for control, as shown in Fig. 13.1b. In Fig. 13.2, it is assumed that the three phase AC system is balanced, which means that the phase differences between each phase are the same as each

C.T. Rim, *Phasor Power Electronics*, KAIST Research Series,
DOI 10.1007/978-981-10-0536-7_13

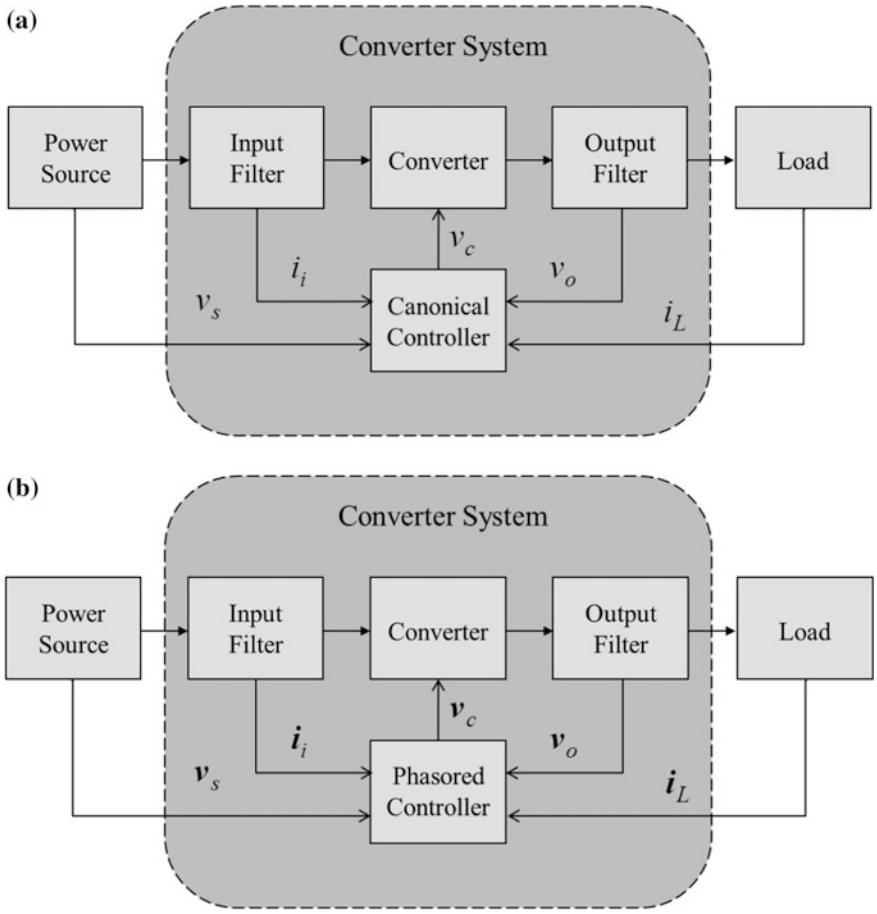

Fig. 13.1 Comparison of a canonical controller with a phasored controller. **a** Canonical controller. **b** Phasored controller

other and the magnitude of each voltage or current is also the same. If this is not the case, one offset term will appear, which will result in three stationary DQ0 variables. A proportional, integral, and derivative (PID) controller is shown in Fig. 13.2, as an example. The PID controller is widely used in industry, and one of the very cumbersome problems with this controller is that two identical PID processors must be used to constitute a canonical PID controller. As we change the gain of one of the D- or Q-PID processor, we must also change the other as follows:

$$v_d' = K_P v_d + K_I \int_0^t v_d dt + K_D \frac{dv_d}{dt}, \tag{13.1a}$$

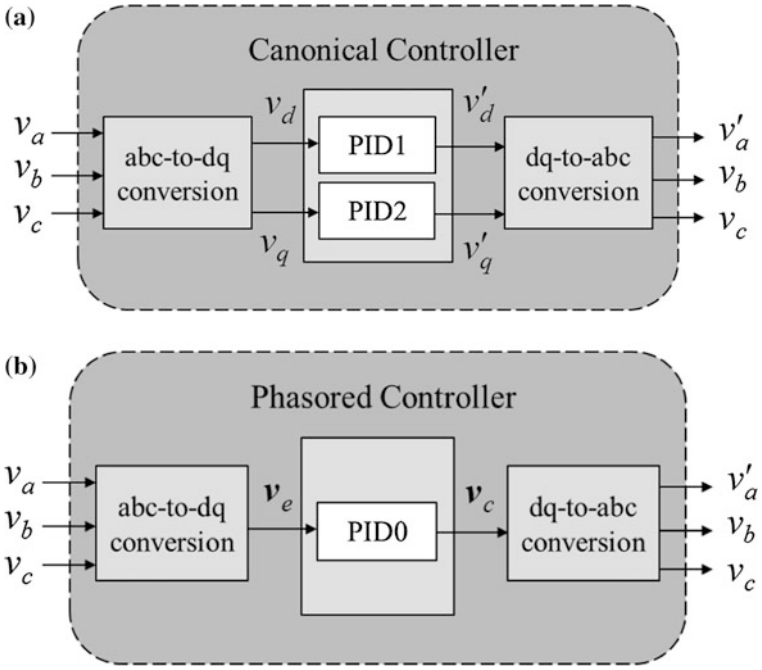

Fig. 13.2 Comparison of a canonical PID controller with a phasored PID controller. **a** Canonical controller. **b** Phasored controller

$$v'_q = K_P v_q + K_I \int_0^t v_q dt + K_D \frac{dv_q}{dt}. \tag{13.1b}$$

This inconvenience can be completely removed if a phasored PID controller is adopted, as shown in Fig. 13.2b. The processing of the complex PID controller becomes as follows:

$$\boldsymbol{v}_c = K_P \boldsymbol{v}_e + K_I \int_0^t \boldsymbol{v}_e dt + K_D \frac{d\boldsymbol{v}_e}{dt}. \tag{13.2}$$

Note from (13.2) that the same PID gains of (13.1a, b) are used.

A new aspect to consider is that the phasored controller should be able to manipulate complex numbers, which is not available in the case of an ordinary processor but available for a modern signal processor handling complex numbers.

Similarly, any signal processing of AC signals can be done by complex signal processors, as done by (13.2).

13.2 Phasored Power Systems and Motors

AC systems including AC power systems such as AC transmission lines, power distribution networks, transformers, and motors can be now studied by the phasor transformation, as shown in Fig. 13.3. A time domain simulation is shown in Fig. 13.3, where the envelope resembles a first order system, which can be explored using the equivalent phasored circuit.

As expected from the equivalent circuit, the system order is not necessarily one but it could be two, though not shown here. Detailed study of this system order change is left for future works for active readers. It is noteworthy that the system order is never six, which is the number of energy storage elements of the power circuit.

As shown in Fig. 13.4, another example is shown for a resonant transformer, also referred to as a 'Tesla coil', which consists of a transformer and capacitors to have resonance circuits. This circuit is also widely used for wireless power transfer, where a loose magnetic coupling is often used. As a step input is applied to this resonant transformer, the dynamic response is quite complicated, but it should be well controlled to stabilize the overall system, minimizing its overshoot and dynamic response time. Although not shown here, a phasor circuit for this resonant transformer is useful for the design of the main circuit and controller.

AC motors such as induction motors and synchronous motors, which are usually expressed in the DQ domain, can be explicitly described in the phasored domain.

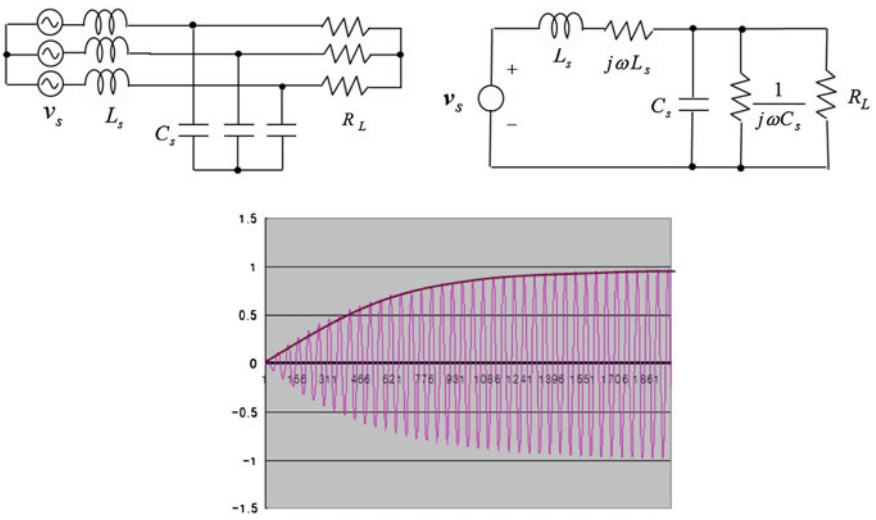

Fig. 13.3 The static and dynamic characteristics of an AC power system (*left*) can be analyzed by its equivalent phasor circuit (*right*). Then, dynamic response can be analyzed (*bottom*)

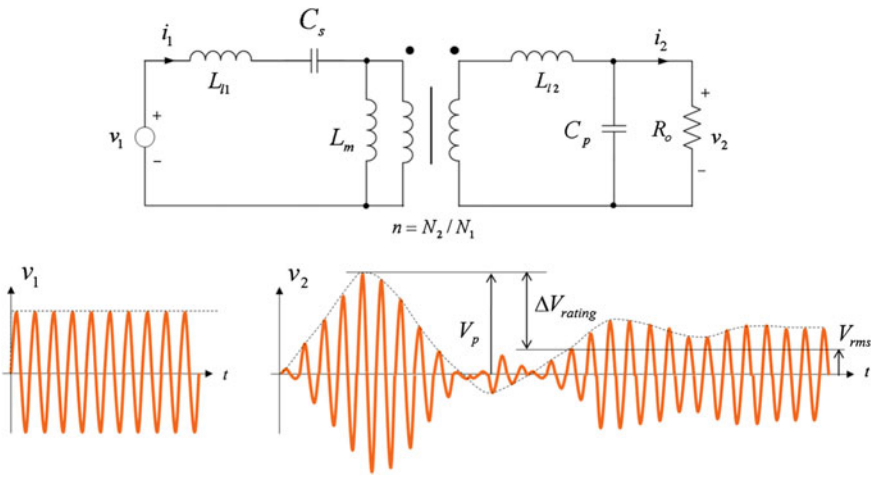

Fig. 13.4 The static and dynamic characteristics of a resonant transformer (*top*) can be analyzed by using its equivalent phasor circuit, from which its envelope can be studied (*below*)

13.3 AC Electronic Filters and RF Circuits

The RF electronic circuit, as shown in Fig. 13.5, can be explored by the phasored circuit to find the dynamics and static behaviors. By the phasor transformation, the LC resonant tank becomes $2C_s$ when it is in parallel resonance, as shown in Fig. 13.5. If the LC resonant tank is in series resonance, its equivalent circuit becomes $2L_s$. With the help of the phasor transformation, the envelope behavior can be completely explored. This equivalent phasored circuit can explain an AM transmitter or receiver, which has a large delayed response when its Q factor is large. The envelope dynamics can be determined by the circuit, which was empirically tuned by an engineer. Moreover, FM and PM modulators can also be studied in this way even though they are of digital signal.

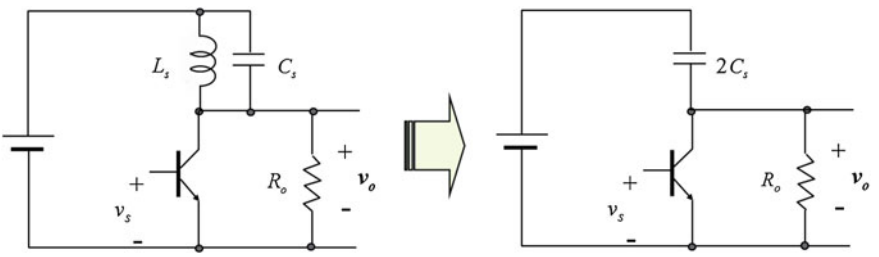

Fig. 13.5 The envelope of an RF electronic filter can be analyzed by its equivalent phasor circuit

13.4 Phasored Mechanics and Musical Instruments

Because a mechanically vibrating system is analogous with an electric circuit, a phasor circuit can be useful for analyzing mechanical systems. There are many mechanical vibrating systems including mechanical resonance in cars, airplanes, and other machines, and oscillation in acoustic systems and musical instruments.

Furthermore, any oscillations including quantum mechanics can be dealt with using the phasor transformation to analyze their dynamics, which is left for future work.

Chapter 14
The Future of Power Electronics

The future of power electronics is estimated using emerging issues and trends widely selected from my academic activities. This estimation is, however, not rigorous but instead some general ideas are offered.

As long as the electronic power switch, i.e., semiconductor switch now, is used for power processing, power electronics will never disappear as presently defined. But there will be endless changes in the future of power electronics because everything changes.

I think that the future of power electronics can be summarized as "NEW FRI" days, as predicted now.

- **"New Advanced Stone Ages"**
- **"Electrification"**
- **"Wireless"**
- **"Filter-less"**
- **"Renewables"**
- **"Innovations"**

These trends of the future of power electronics can be explained as follows:

"New Advanced Stone Age" will come because of low cost power switches

Because semiconductor power switches used in power electronic systems are very expensive and vulnerable to various operating conditions, the number and cost of the power switches are of great concern for the design of a converter. However, power switches are becoming cheaper and better now, and the restrictions of the switches in terms of cost, speed, temperature, and size have been significantly mitigated. In particular, SiC and GaN power switches have reached breakthroughs in cost and performance, making them viable solutions to many applications which would not have been possible but for their advent.

C.T. Rim, *Phasor Power Electronics*, KAIST Research Series,
DOI 10.1007/978-981-10-0536-7_14

"Electrification" will be accelerated by electric vehicles, batteries, smart grids

More vehicles are electrified now than ever, especially in Japan, Norway, and China. The rate of new electric vehicles in markets is over 30 % each year in these countries. Among electric vehicles (EVs), more electrified vehicles such as pure battery EVs and plug-in hybrid EVs are becoming preferred over less electrified vehicles such as hybrid EVs. Rechargeable batteries are widely used due to ever increasing mobile devices. Smart grids are becoming more important as an efficient way of using electric power. Electrification has changed the world for a century and will change the future in the 21st century.

"Wireless" will change future life

Wireless power transfer (WPT) is one of the ways of delivering power in general. Inductive coupling, capacitive coupling, conductive coupling, electromagnetic wave, sound, and light between a transmitter (Tx) and a few receivers (Rx's) are typical methods of WPT. Inductive power transfer (IPT) utilizes inductive coupling between a Tx and an Rx coils and has become the most widespread power transfer method, with power rating ranges from a few mW to several MW. WPT will be crucial for continuous powering or stationary charging to any moveable things such as mobile devices, electric vehicles, drones, and robots. Together with sensors and communication technologies, WPT will be one of three key technologies in the coming internet of things (IoT) and ubiquitous era.

"Filter-less" will cost down power electric systems

As the cost and size of passive filters, i.e., inductors and capacitors, have been of great concern in power electronics, the switching frequency of converters tends to increase, which results in an increase of the operating frequency of filters. In this way the burden of cost and size of filters is mitigated, which is inevitable considering the expensive materials used for filters such as copper, iron, and scarce materials. Recently, less-filter, inductor-less, or even filter-less power electronic systems such as no-dc-link inverters and digital LED drivers have become available, and this 'filter-less' trend will grow in the future.

"Renewables" will continue to grow

Energy will be more important in the future. Due to global warming and air pollution, clean energies such as wind power and solar power together with nuclear power, tidal power, and earth heat power will play more important roles than fossil energies such as oil, coal, gas, and waste energies. In particular, wind power and solar power are attracting more attention from the public and governments even though their initial cost is high, due to ever improving technologies in power electronics and material science.

"Innovations" will not stop in the future

Some experts predict the saturation of technology, i.e., the cease of innovation. However, this will never happen until human beings disappear. The world is not

perfect and ever changing in time and space. Power electronics is a relatively young engineering field compared to its 'mother technologies' such as electronics and electrical and mechanical engineering. Due to the high pressure for new research and developments discussed above, lots of innovations will be made by power electronics in the future. Ultra high speed and high power density motors and actuators, digital lighting, long-range and free-space-charging WPTs, wireless IoTs, electric airplanes, ubiquitous robots, commercially available 50 % efficiency solar cells, auto-piloted personal electric airplanes, and on-line electric vehicles running on electrified smart roads are expected in the coming decades.

Reference Papers of Mine

1. Rim CT, Cho GH (1990) Phasor transformation and its application to the DC/AC analyses of frequency/phase controlled series resonant converters (SRC). IEEE Trans Power Electron 5 (2):201–211
2. Rim CT, Hu DY, Cho GH (1990) Transformers as equivalent circuits for switches: general proofs and D-Q transformation-based analysis. IEEE Trans Ind Appl 26(4):777–785
3. Rim CT, Choi NS, Cho GC, Cho GH (1994) A complete DC and AC analysis of three-phase controlled-current PWM rectifier using circuit D-Q transformation. IEEE Trans Power Electron 9(4):390–396
4. Rim CT (2011) Unified general phasor transformation for AC converters. IEEE Trans Power Electron 26(9):2465–2475
5. Lee S, Choi B, Rim CT (2013) Dynamics characterization of the inductive power transfer system for on-line electric vehicles by Laplace phasor transform. IEEE Trans Power Electron 28(12):5902–5909
6. Choi BH, Lee SW, Yeo IY, Rim CT (2012) Fast and reliable phasor detectors for single phase AC systems by derivative quadrature generation. In: IEEE ECCE-Asia 2012, June 2012, pp 609–614
7. Park CB, Lee SW, Rim CT (2012) Static and dynamic analyses of three-phase rectifier with LC input filter by Laplace phasor transformation. In: IEEE ECCE 2012, Sept 2012, pp 1570–1577
8. Lee ES, Cheon JP, Choi BH, Lim GC, Kim BC, Rim CT (2015) Temperature-robust LC^3 passive LED drivers with low THD, high efficiency and PF, and long life. IEEE J Emerg Sel Top Power Electron 3(3):829–840

C.T. Rim, *Phasor Power Electronics*, KAIST Research Series,
DOI 10.1007/978-981-10-0536-7